

IP2
 FSAR UPDATE

TABLE 10
 FREQUENCY DISTRIBUTION OF 24 HOUR RESULTANT WIND DIRECTIONS
 INDIAN POINT (10 METER LEVEL)

Resultant Wind Direction	No. Obs.	Persistence > 0.9 Aver. SPDS (MPH)		No. Obs.	Persistence > 0.8 < 0.9 Aver. SPDS (MPH)		No. Obs.	Persistence > 0.7 < 0.8 Aver. SPDS (MPH)	
		Result.	Mean		Result.	Mean		Result.	Mean
350-011	4	5.75	6.15	6	4.87	5.62	2	3.90	5.00
012-034	20	4.97	5.22	6	4.05	4.67	4	2.40	3.23
035-056	13	4.81	4.98	8	3.56	4.04	1	2.60	3.40
057-079	5	4.06	4.24	2	2.70	3.15	2	2.30	2.95
080-101	0			0			1	1.50	1.90
102-124	0			0			0		
125-146	0			0			0		
147-169	0			0			1	2.20	2.80
170-191	2	2.90	3.10	1	3.20	3.70	0		
192-214	10	3.38	3.53	5	2.38	2.76	5	2.56	3.44
215-238	3	4.07	4.23	7	2.69	3.11	1	2.00	2.60
237-259	0			3	4.40	5.27	2	3.35	4.40
260-281	0			1	2.40	3.00	2	3.15	4.10
282-304	0			3	3.03	3.70	1	3.70	4.80
305-326	6	4.17	4.48	4	5.15	6.00	3	2.90	3.93
327-349	13	7.82	8.22	8	4.64	5.40	7	3.41	4.51
	76			54			31		
Percent:	25.94			18.43			10.58		

Number of Valid 24-hour Resultants (>17 hours): 293

Percent Valid Data: 97.39

IP2
FSAR UPDATE

TABLE 11
SUMMARY OF TWO-STATION WIND CORRELATIONS PIERMONT (SITE 1) REFERENCED TO SELECTED MONITORING LOCATIONS
(SITE 2)

Month	Station (Site 2)	Total	Number of Observations				North Wind at Piermont Resultant Wind @ Site 2			North Wind at Site 2 Resultant Wind @ Piermont		
			North Winds		Concurrent Winds		Direct.	Speed (mph)	Persist.	Direct.	Speed (mph)	Persist.
			Piermont	Site 2	All Directions	North						
March	South Nyack	588	83	33	70	10	331	3.3	0.90	025	8.5	0.
	Kingsland	481	71	74	133	39	004	6.7	0.96	001	9.2	0.
	Ossining	586	83	25	31	4	327	3.8	0.92	023	7.5	0.
	Iona Island	565	76	16	65	3	327	5.0	0.73	042	9.4	0.
	Indian Point	589	83	67	137	7	035	4.2	0.89	334	9.3	0.
April	South Nyack	567	50	25	63	6	346	1.9	0.65	025	6.6	0.
	Kingsland	490	39	68	145	13	008	3.2	0.79	018	8.1	0.
	Ossining	567	50	28	45	2	316	2.6	0.85	030	8.8	0.
	Iona Island	354	30	21	26	2	308	4.5	0.73	043	11.0	0.
	Indian Point	567	50	58	129	6	020	2.4	0.64	340	8.5	0.
May	South Nyack	359	46	20	33	2	327	3.7	0.84	032	6.8	0.
	Kingsland	67	2	2	9	0	256*	2.1*	0.98*	031*	10.0*	1.
	Ossining	474	68	37	28	4	309	6.4	0.85	036	9.9	0.
	Iona Island	415	66	22	20	2	301	7.3	0.89	052	6.6	0.
	Indian Point	422	50	58	91	26	350	3.5	0.79	356	10.1	0.
June	South Nyack	480	17	19	57	2	332	4.0	0.92	036	8.2	0.
	Kingsland	284	5	2	30	1	301*	5.6*	0.95*	031*	5.4*	0.
	Ossining	480	17	16	41	0	318	7.3	0.90	046	6.7	0.
	Iona Island	368	12	8	16	0	301	8.5	0.88	062*	9.1*	0.
	Indian Point	475	17	28	80	4	326	3.1	0.73	006	5.6	0.
July	South Nyack	744	10	25	114	1	332	2.7	0.92	041	7.9	0.
	Kingsland	724	10	25	98	0	337	2.3	0.55	052	5.7	0.
	Ossining	744	10	37	66	0	326	4.5	0.79	047	6.8	0.
	Iona Island	401	5	9	45	0	302*	10.0*	0.95*	054*	5.7*	0.
	Indian Point	742	10	35	108	1	007	2.3	0.64	358	4.7	0.

* Less than 10 valid data points

IP2
FSAR UPDATE

TABLE 11 (Cont'd)

SUMMARY OF TWO-STATION WIND CORRELATIONS PIERMONT (SITE 1) REFERENCED TO SELECTED MONITORING LOCATIONS
(SITE 2)

Month	Station (Site 2)	Total	Number of Observations				North Wind at Piermont Resultant Wind @ Site 2			North Wind at Site 2 Resultant Wind @ Piermont		
			North Winds		Concurrent Winds		Direct.	Speed (mph)	Persist.	Direct.	Speed (mph)	Persist.
			Piermont	Site 2	All Directions	North						
Aug.	South Nyack	744	24	44	95	1	334	3.0	0.75	058	11.9	0.95
	Kingsland	744	24	52	93	1	313	4.8	0.74	054	11.7	0.92
	Ossining	741	24	58	96	2	336	6.9	0.84	047	10.5	0.87
	Iona Island	679	24	15	80	0	308	4.9	0.66	036	9.8	0.80
	Indian Point	719	24	32	139	3	037	2.5	0.70	332	5.2	0.73
Sept.	South Nyack	513	37	36	63	10	348	2.5	0.88	018	12.6	0.91
	Kingsland	513	37	22	42	3	345	4.6	0.79	026	9.6	0.90
	Ossining	512	36	36	87	9	354	5.0	0.86	010	9.4	0.84
	Iona Island	513	37	10	34	3	322	4.8	0.76	024	11.7	0.91
	Indian Point	501	37	38	102	4	031	3.4	0.83	339	7.2	0.85
Oct.	South Nyack	379	24	28	83	5	335	2.8	0.91	019	10.7	0.92
	Kingsland	379	24	25	64	5	018	3.0	0.73	019	11.4	0.96
	Ossining	379	24	31	69	4	007	4.0	0.85	016	11.8	0.95
	Iona Island	379	24	12	38	3	291	2.8	0.77	016	12.9	0.99
	Indian Point	379	24	24	89	5	031	2.9	0.95	009	7.5	0.86

Table 11 can be summarized in terms of the valid wind direction data from the five designated sites concurrent with wind directions at Piermont (Note: The data from these sites should not be presumed concurrent with each other simultaneously). This summary is shown in Table 12.

IP2
FSAR UPDATE

TABLE 12
CONCURRENCE OF TWO-STATION WIND DIRECTIONS
(Relative to Piermont)

	5 Site Total	% Valid	Percent (Concurrent Data Basis)	
	Concurrent Data	6 Site Basis	All Directions	North Wind
March	2809	62.93	15.52	2.24
April	2545	58.91	16.03	1.14
May	1737	38.91	10.42	1.96
June	2087	48.31	10.73	0.34
July	3355	75.16	12.85	0.06
August	3627	81.25	13.87	0.19
September	2552	59.07	12.85	1.14
October	1895	42.45	18.10	1.16

Since these data are derived from hourly average wind directions, it is again shown that there is little likelihood of sustaining south bound movement of air from Indian Point beyond 15-miles.

3.2.3.5 Summary-Trajectory II Study

A modified version of the generic model TRAJECTORY (Kaplun and Wuebber, 1980) was used as a basis of a study, which involved the use of concurrent hourly average wind data from a network of 13-14 monitoring stations within 20-miles of Indian Point. All but four sites were located on the Hudson River shorelines. Only two sites were used to the north of Indian Point. As with the original study (Kaplun and Wuebber, 1980), emphasis was on the objective creation of the trajectories of air parcels originating hourly at Indian Point with a speed and direction equal to the average wind at the 10 meter level of Indian Point 122 Meter Meteorological Tower.

In the Trajectory II Study (Kaplun and Wuebber, 1981), each parcel of air was tracked for eight consecutive hours after its movement was initiated as dictated by two factors: The movement time interval and the wind velocity at the coordinate end point of the parcel at the end of movement time interval. As in the earlier study a 21 by 21-mile grid pattern of one mile squares was used to generate tabulations of the trajectory segment end-points. While the tabulations assumed each point to be located in the center of each square, the actual coordinates within the squares were used as a starting point for the next hourly trajectory segment. Subsequent movement of a parcel from a given set of coordinates was determined by the appropriate average hourly wind velocity assigned to grid square as determined by a "zone of influence" file. While trajectories were objectively created, the zone of influence file required the subjective assignment of each available wind velocity monitoring site to specific grid squares. The wind velocity for any given hour within these assigned grid squares would be the same as that of the specified control monitoring site.

Influence assignments were based on assessments of local wind patterns (historical and present) with some consideration for obvious meso-scale modification factors: topographic channeling, drainage flow patterns, thermally induced flow patterns, etc.

IP2
FSAR UPDATE

For the purpose of the study, all movements of parcels past the grid boundaries were assumed to continue their movements under the influence of the site whose wind was being used at the time that a boundary was crossed.

When only a few wind monitoring sites are available to cover a large area, movement controlled solely by a single site's non-variant hourly average wind was not a critical factor. As the number of monitoring sites increased and zones of influence became smaller, discrete movement based on a single wind in a given hour increment would allow a parcel to move through a zone of influence without modification of its controlling wind, which could be substantially different in direction and speed than that associated with the by-passed zone. In the TRAJ3 model, as used in this study, parcel end point coordinates at the end of each hour, which had been previously determined by the non-variant wind at the parcel source at the beginning of each hour, were the resultant of 30 discrete movements (two minute intervals) within the hour interval. On this basis, a wind speed of 30 mph was required in order for a parcel to travel with a non-variant wind for more than one mile. A discrete wind velocity was reassigned to a parcel according to its coordinates (zone of influence) at the end of each two minute intervals. In effect, a parcel could, in extreme, alter its direction and speed 30 times in a given hour and not apparently move at all if it were trying to move from one zone of influence to another at a boundary line between zones and the wind in the two zones were in opposition. Such apparent anomalies were found as a matter of routine.

Figure 16 shows the grid system that was used in the Trajectory 2 Study, Indian Point was located at coordinates 7,17. In the development of the trajectories recirculation was allowed. This is a parcel could leave the grid boundaries and be brought back onto the grid at a later time if dictated by a change in the wind at the monitoring site controlling its movement.

In the first hour of movement for the ten months of data, only 390 parcels out of 7,344 (5.3) left the grid system and did not return. Of these 345 (4.7%) were crossings of the northern grid boundary, 40 (0.5%) were crossings of the western grid boundary and 5 (0.1%) were crossings of the southern grid boundary. There were no crossings of the eastern grid boundary. Of the five points crossing the southern boundary, all occurred in December, 1980. To cross the southern boundary a minimum speed of 7.6 M/S (17 mph) was required.

During the ten months (206 days) of record there were only 35 days (11.4%) in which there are no rotation and/or recirculation (flow reversal) characteristics in at least one of the 24 trajectories created daily. This does not take into account any trajectories that may have experienced reversals wholly outside of the grid area.

If flow reversals and rotational trajectories were due solely to synoptic scale meteorological patterns, then randomness would be expected in the starting time occurrence frequency as a diurnal function. The actual pattern observed for those eight hour trajectories, which contained at least one on grid or on-off-on grid flow reversal is shown in Table 13. These results include those reversals of synoptic origin and can be interpreted as consistent with the local average diurnal wind patterns induced by meso-scale phenomena when the following factors are taken into account:

- Nocturnal flow patterns generally north to south with minimal with speeds
- Afternoon flow patterns generally south to north with maximum wind speeds

IP2
FSAR UPDATE

Summaries of the trajectory end-point counts and percentages are shown on a monthly basis in Tables 14 and 15 for selected time increments up to the complete eight hour trajectory. The idealized valley is shown in Figure 16. It is noted that the idealized valley contains 64 out of 441 (14.5%) possible grid box end-point coordinates: ten grid boxes are north of Indian Point; and 54 are on a line with Indian Point and south. With respect to total grid, 84 boxes are to the north and 357 are to the south.

The effect of dominant meso-scale factors are readily discernible in the results. Differences in north and south boundary crossings of trajectory points can be related to the normal seasonal distribution of local wind velocities as well as their diurnal distribution patterns. During the summer season it would take up to six hours of persistent north sector winds from Indian Point to Piermont to generate a south boundary crossing. Such a persistent diurnal time span is improbable. After eight hours, only 6.7 percent of all possible trajectory end-points for all time intervals in July 1980 (5,924 possible) were found to cross the southern boundary (a distance of 17-miles from Indian Point). The highest crossing percentage, 30.7 percent of 5,924 possible, occurred in December, 1980.

IP2
FSAR UPDATE

TABLE 13
Diurnal Distribution of Occurrences of
Eight-Hour Trajectories with On Grid Reversals

Starting Hour	End Hour	Number of Trajectory with Flow Reversals										Total
		Mar	Apr	May	June	July	Aug	Sept	Oct	Nov	Dec	
0100	0900	7	9	13	13	14	9	13	7	7	10	102
0200	1000	11	9	15	9	11	10	15	10	9	6	105
0300	1100	9	11	12	15	14	14	12	12	8	8	115
0400	1200	12	11	18	14	17	13	11	12	6	10	124
0500	1300	10	11	16	17	21	13	14	11	4	9	126
0600	1400	9	11	10	13	19	13	14	11	7	11	118
0700	1500	10	8	9	10	10	12	12	7	9	9	96
0800	1600	6	7	5	10	9	10	14	7	10	7	85
0900	1700	6	10	6	8	11	6	10	4	7	8	76
1000	1800	5	7	10	11	7	8	9	4	9	7	77
1100	1900	6	8	4	4	9	7	9	6	4	5	62
1200	2000	2	8	2	4	10	8	10	5	6	4	59
1300	2100	2	8	4	5	6	5	8	4	5	6	53
1400	2200	3	4	5	5	11	5	7	6	5	6	57
1500	2300	2	7	6	4	12	11	8	6	8	6	70
1600	2400	5	5	7	6	12	11	8	6	10	7	77
1700	0100	7	6	10	9	17	12	9	6	8	8	92
1800	0200	10	7	12	8	16	10	9	9	7	9	97
1900	0300	10	3	14	11	14	8	7	6	7	10	90
2000	0400	12	9	14	7	15	8	6	6	6	8	91
2100	0500	12	8	13	5	8	8	7	7	9	8	85
2200	0600	15	9	12	10	8	6	7	8	6	8	89
2300	0700	10	12	13	8	10	9	8	9	5	9	93
2400	0800	<u>7</u>	<u>5</u>	<u>12</u>	<u>10</u>	<u>13</u>	<u>11</u>	<u>9</u>	<u>8</u>	<u>5</u>	<u>11</u>	<u>91</u>
TOTAL		188	193	242	216	294	227	236	177	167	190	2130
TOTAL POSSIBLE		736	712	736	712	736	736	712	736	712	736	7264
OCCURRENCE (%)		25.5	27.1	32.9	30.3	39.9	30.8	33.1	24.0	23.5	25.8	29.3

IP2
FSAR UPDATE

TABLE 14
SUMMARY OF TRAJECTORY END-POINT COUNTS

	March	April	May	June	July	August	Sept	Oct	Nov	Dec	
Number of Hours/Month	744	720	744	720	744	744	720	744	720	744	
Total Number of End-Points	5924	5732	5924	5732	5924	5924	5732	5924	5732	5924	
<u>Elapsed Time</u>		<u>Number of End-Points</u>									
2 Hours -	Number of Trajectories	742	718	742	718	742	742	718	742	718	742
	Within Grid	490	440	577	559	593	599	498	595	538	513
	In Valley (North of Indian Point)	41	29	49	65	51	57	36	39	30	44
	In Valley (Indian Point and South)	95	94	150	148	305	185	178	204	139	123
	Percent Grid Points in Valley	28.3	28.0	34.5	38.1	60.0	40.4	43.0	40.8	31.4	32.6
4 Hours -	Number of Trajectories	740	716	740	716	740	740	716	740	716	740
	Within Grid	275	244	356	355	433	361	328	371	285	297
	In Valley (North of Indian Point)	20	8	17	34	28	26	15	22	13	17
	In Valley (Indian Point and South)	43	59	118	106	139	146	109	156	97	78
	Percent Grid Points in Valley	22.9	27.5	37.9	39.4	38.6	47.6	37.8	48.0	38.6	32.0
6 Hours -	Number of Trajectories	738	714	738	714	738	738	714	738	714	738
	Within Grid	173	183	257	257	342	277	250	255	175	213
	In Valley (North of Indian Point)	8	5	9	13	20	9	6	16	7	11
	In Valley (Indian Point and South)	18	42	93	91	105	119	80	106	63	46
	Percent Grid Points in Valley	15.0	25.7	39.7	40.5	36.5	46.2	34.4	47.8	40.0	26.8
8 Hours -	Number of Trajectories	736	712	736	712	736	736	712	736	712	736
	Within Grid	121	135	190	194	276	226	199	188	130	160
	In Valley (North of Indian Point)	9	5	6	9	9	3	5	4	6	11
	In Valley (Indian Pint and South)	11	25	73	61	91	87	51	70	47	38
	Percent Grid Points in Valley	16.5	22.2	41.6	36.1	36.2	39.8	28.1	39.4	40.8	30.6
	Total Past South Boundary*	1643	958	1048	636	399	708	657	926	1706	1821
	Percent Past South Boundary	27.7	16.7	17.7	11.1	6.7	12.0	15.0	15.6	29.8	30.7
	Total Past North Boundary*	1013				1676					937
	Percent Past North Boundary	17.1				28.3					15.8

* This count includes all end-points for all time intervals.

IP2
FSAR UPDATE

TABLE 15
SUMMARY OF TRAJECTORY END-POINTS (Percent)

<u>Month</u>	<u>2 Hours</u>			<u>4 Hours</u>			<u>6 Hours</u>			<u>8 Hours</u>		
	<u>Total Traj.</u>	<u>% On Grid</u>	<u>% In Valley</u>	<u>Total Traj.</u>	<u>% On Grid</u>	<u>% In Valley</u>	<u>Total Traj.</u>	<u>% On Grid</u>	<u>% In Valley</u>	<u>Total Traj.</u>	<u>% On Grid</u>	<u>% In Valley</u>
March	742	66.0	18.3	740	37.2	8.5	738	23.4	3.5	736	16.4	2.7
April	718	61.3	17.1	716	34.1	9.4	714	25.6	6.6	712	19.0	4.2
May	742	77.8	26.8	740	48.1	18.2	738	34.8	13.8	736	25.8	10.7
June	718	77.7	29.7	716	49.6	19.5	714	36.0	14.6	712	27.2	9.8
July	742	79.9	48.0	740	58.5	22.5	738	46.3	16.9	736	37.5	13.6
August	742	80.7	32.6	740	48.8	23.2	738	37.5	17.3	736	30.7	12.2
September	718	69.4	29.8	716	45.8	17.3	714	35.0	12.0	712	27.9	7.9
October	742	80.2	32.7	740	50.1	24.1	738	34.6	16.5	736	25.5	10.1
November	718	74.9	23.5	716	39.8	15.4	714	24.5	9.8	712	18.3	7.4
December	742	69.1	22.5	740	40.1	12.8	738	28.9	7.7	736	21.7	6.7
Average		73.7	28.1		45.2	17.1		32.7	11.9		25.0	8.5
Standard Deviation		6.5	8.4		7.0	5.3		6.7	4.6		8.1	3.3

IP2
FSAR UPDATE

In any given month of the ten that were investigated and out of the 7,242 complete eight hour trajectories that were generated, there were a number of basic pattern types. There were those whose sequence of temporal end-points exhibited basic straight line tendencies. These were generally associated with high wind speeds. There were those whose sequence of end-points that rotated in a more or less smooth pattern but they were not usually associated with a meso-scale diurnal rotation or terrain induced deflections. In addition, there were those that exhibited characteristics of recirculation and those in which there were sharp reversals. These were induced by wind velocity changes of synoptic scale origin and/or most frequently they appeared in those trajectories, which included the morning or evening transitional periods, meso-scale induced. In the latter cases, of rotation, recirculation and reversals, the sequences may occur wholly on the grid or on-off-on on the grid.

Examination of details of specific trajectories and concurrent opposing winds suggests that three block regions can be projected in the lower Hudson Valley within the grid system. These regions are:

Peekskill Bay

Haverstraw Bay

Tappan Zee

The reality of the zones of divergence and convergence on a concurrent wind basis were premised on the continuity of air flow movements locally and for air streams that were projected to cross the Hudson River. This latter feature was not uniquely demonstrated with respect to surface (10 meter) level wind velocities. If some local wind patterns were induced by thermal differentials between land and water during periods of weak geostrophic pressure gradients in accordance with sea breeze concepts: during the day air will move from cool water to warm land with return flow aloft; at night, a reverse flow pattern may develop. If this occurred on opposite shorelines of a wide river, concurrently, then there should be vertical motions induced by convergence and divergence in the mid river area or a region of air flow directionally independent of the shoreline circulations. The light wind speeds that were normally found at Croton Point during periods of weak geostrophic flow may result from its proximity to a mid river transition zone. (During periods of strong northwesterly gradients Croton Point had a high frequency of west to west northwest winds implying a cross river flow parallel to South Mountains.)

In addition to the land-water effects in so far as they generate local on-shore and off-shore winds, the effect of nocturnal drainage winds should be considered. The Kingsland Park site was one example. A zone of convergence frequently develops at night between that site and Ossining. This was also apparent from the average diurnal monthly diurnal wind distributions. If only drainage winds are considered, from Figure 4, Ossining would reflect drainage from the Croton River and/or a secondary local river both of which would generate air movements from the north-northeast. Kingsland Park is, however, at the outfall to Gory Brook, while this drains from the north-northeast, it hooks in its final section and outfalls into the Hudson from the southeast. There were no measurements available upon which to alter these directions after the air streams flow into the Hudson River itself. For the objective creation of eight hour trajectories, these winds were presumed to extend into the Hudson River and generate local blocks on a concurrent hourly basis.

The dominance of mesoscale flow factors on surface winds in this study have been demonstrated over and over since local meteorological data have been collected. The

surface wind data sets used for this study are from the most extensive network of concurrent monitoring stations that have ever been deliberately located in the region. These data have been evaluated by many of the routine methodologies common to earlier local studies. All of the data sets were found to exhibit characteristics of complex meso-scale flow fields distortions. The east shore stations were found to share some common characteristics on a daily basis and the same was true for the west shore stations. These characteristics were frequently in opposition to each other. At the same time inland stations had characteristics that were entirely different from either the east or the west shore stations.

The creation and interpretation of eight hour trajectories from these data sets could not be truly separated from the concurrent flow fields on an hourly basis. The eight hour trajectories were a result of the constantly changing concurrent flow field. They were a distinct function of movement interval when based on hourly average wind velocities; and therefore, it may be presumed that in a dynamic flow field they would be equally sensitive to the wind averaging interval itself. As noted earlier, this study did not account for vertical air movement, the trajectories were therefore extremely sensitive to one crucial factor - the assumption of continuity of air movement across the Hudson River without midstream directional distortions.

The results of this study indicated that continued southward movement of air parcels in the Hudson River Valley could not generally be sustained past Piermont, if, in accordance with the data evaluated, Piermont's winds are assumed to be representative of the full width of Hudson River.

3.2.4 January 1, 1979 Through December 31, 1980

3.2.4.1 Data Analyses

In the previous sections, with reference to the Trajectory I and Trajectory II studies, portions of 1979 and 1980 data from the Indian Point Meteorological Tower were analyzed and evaluated with reference to the studies that were in progress. Some of these analyses included references to historical data. In both of these studies it was concluded that the meteorological data being obtained at Indian Point were representative of that site and that any observed variations in wind frequency distributions and diurnal variations were assignable to transient climatological deviations from the norm on, at least, the synoptic-cyclonic scale of meteorological events. There was no indication that any changes could be attributed to local physical or dynamic modification, and/or in monitoring equipment and analyses techniques, which could introduce permanent data bias.

To maximize the recent data analyses, all of 1979 and 1980 have been evaluated and compared to historical data as available. The amount of valid data for these years has been previously tabulated in Table 2.

3.2.4.2 Wind Frequency Distributions

For Climatological perspective, historical comparisons have been made for selected months: March, July and December, between the wind direction, wind frequency distributions at the 10 meter level of the 122 Meter Indian Point Tower and climatological data available from Bridgeport, Connecticut and La Guardia Airport in New York City. These latter sites are within the synoptic-cyclonic scale range of Indian Point. The distributions are shown in Table 16. With respect to March and July, climatological frequency extremes are noted on a nine year basis for La Guardia and a 21 year basis for Bridgeport.

IP2
FSAR UPDATE

The fluctuations of the frequency distributions and the extremes can be associated with the frequency distribution fluctuations at Indian Point when consideration is given to the fact that winds at Indian Point are channeled by the west bank terrain.

Tables 17 and 18 give the percent frequency distribution of wind direction at Indian Point at the on "seasonal" basis for the 10 meter and 122 meter sensor levels. These data are compared to comparable results for 1973-1974 (Kaplin, et. al.1974, Appendix D).

In the summer season (Table 17), there is a frequency shift at the 10 meter level from SW and SSW in 1974 to SSW and S in the 1979-1980 period. This shift (with a directional bias) can be related to a similar shifting pattern at Bridgeport and La Guardia as found for July in Table 15. This shift tendency is also found implied at the 122 meter level. There is no reason to expect that these pattern changes are permanent.

For the winter season (Table 18) there is a recent bias of wind frequencies to the NNW ad N sectors at both the 10 meter and 122 meter levels at Indian Point. These shifts have their counterpart in the March and December distributions of Table 16.

It is concluded that the wind velocity data that has been collected in recent years is consistent with the data base for FSAR 2 at all measurement levels when normal climatological variations are considered.

IP2
FSAR UPDATE

TABLE 16A
HISTORICAL COMPARISONS OF
WIND FREQUENCY DISTRIBUTIONS
MARCH

	Indian Point			LaGuardia			Bridgeport		
	1974	1979	1980	1974	1979	1980	1974	1979	1980
N	.120	.078	.125	.044	.137*	.085	.044	.083	.077
NNE	.108	.093	.104	.032	.038	.016**	.012	.020	.040
NE	.115	.174	.173	.109	.105	.085	.097	.031	.052
ENE	.019	.039	.057	.085	.032	.061	.069	.043	.097
E	.008	.011	.030	.000**	.013	.024	.020##	.095	.061
ESE	.004	.009	.007	.008**	.013	.008**	.008	.018	.031
SE	.011	.004	.011	.008**	.023	.032	.016	.035#	.004##
SSE	.027	.014	.016	.040	.044*	.032	.012	.031#	.016
S	.057	.094	.085	.085	.199*	.145	.036	.082#	.069
SSW	.051	.133	.091	.036	.035	.057	.040	.051	.040
SW	.045	.065	.046	.052	.018	.024	.085	.057	.069
WSW	.020	.042	.024	.028	.024	.028	.057	.035	.032
W	.036	.049	.039	.089	.069	.048	.113	.065	.113
WNW	.076	.047	.024	.137	.097	.077	.145	.077	.101
NW	.124	.065	.034	.165	.079	.182*	.133	.097	.137
NNW	.129	.085	.134	.081	.066	.081	.093	.134	.048
CALM	.000	.000	.000	.000	.008	.016	.020	.047#	.012

* 9 Year High (1972-1980)
 ** 9 Year Low (1972-1980)
 ## 21 Year Low (1960-1980)
 # 21 Year High (1960-1980)

IP2
FSAR UPDATE

TABLE 16B
HISTORICAL COMPARISONS OF
WIND FREQUENCY DISTRIBUTIONS
JULY

	Indian Point			LaGuardia			Bridgeport		
	1974	1979	1980	1974	1979	1980	1974	1979	1980
N	.034	.066	.047	.093*	.036	.044	.129#	.030	.028##
NNE	.141	.112	.111	.032	.035	.040	.057	.012##	.016
NE	.148	.104	.158	.057	.059	.052	.028	.015	.012##
ENE	.054	.085	.073	.048	.055	.040##	.020	.028	.032
E	.026	.044	.045	.020	.013	.016	.069	.082	.057
ESE	.011	.019	.022	.012	.013	.008	.016	.054	.024
SE	.020	.013	.022	.044*	.031	.032	.048	.020	.016
SSE	.024	.028	.026	.016**	.032	.040	.020	.022	.020
S	.053	.079	.085	.081**	.184	.161	.073	.102	.129
SSW	.110	.212	.123	.069	.085	.073	.052##	.079	.113
SW	.129	.097	.094	.061**	.095	.133*	.085	.157	.125
WSW	.044	.028	.050	.081	.063	.040**	.154	.114	.109
W	.047	.038	.061	.149*	.073	.073	.145#	.105	.117
WNW	.043	.024	.031	.089	.063	.081	.048	.057	.052
NW	.034	.026	.024	.073	.067	.093	.004##	.069	.069
NNW	.015	.015	.031	.057	.043	.052	.048	.026	.069
CALM	.000	.000	.000	.020	.051	.020	.004	.030	.012

* 9 Year High (1972-1980)
 ** 9 Year Low (1972-1980)
 # 21 Year High (1960-1980)
 ## 21 Year Low (1960-1980)

IP2
FSAR UPDATE

TABLE 16C
HISTORICAL COMPARISONS OF
WIND FREQUENCY DISTRIBUTIONS
DECEMBER

	Indian Point			LaGuardia			Bridgeport		
	1973	1979	1980	1973	1979	1980	1973	1979	1980
N	.068	.101	.082	.081	.044	.093	.101	.058	.048
NNE	.172	.071	.148	.077	.016	.044	.048	.019	.057
NE	.162	.067	.124	.081	.046	.065	.097	.030	.040
ENE	.041	.023	.061	.040	.046	.044	.044	.031	.020
E	.015	.018	.023	.020	.013	.008	.024	.035	.012
ESE	.004	.004	.011	.016	.009	.004	.016	.013	.000
SE	.004	.008	.016	.024	.011	.000	.024	.015	.004
SSE	.015	.030	.023	.040	.008	.004	.024	.012	.024
S	.033	.100	.070	.093	.047	.056	.044	.023	.016
SSW	.048	.091	.081	.040	.058	.056	.048	.020	.024
SW	.049	.042	.057	.061	.122	.081	.048	.040	.069
WSW	.019	.042	.024	.044	.071	.044	.028	.093	.085
W	.026	.108	.031	.089	.206	.081	.141	.233	.157
WNW	.044	.094	.057	.149	.144	.121	.141	.238	.157
NW	.126	.120	.070	.069	.078	.157	.101	.066	.153
NNW	.074	.062	.114	.069	.059	.133	.044	.036	.097
CALM	.016	.000	.000	.008	.022	.008	.024	.038	.036

IP2
FSAR UPDATE

TABLE 17
COMPARISON OF PERCENT WIND FREQUENCY DISTRIBUTIONS – SUMMER

Wind Direction	10 Meter Level				122 Meter Level			
	1974	1979	1980	1979-80	1974	1979	1980	1979-80
N	3.66	5.53	7.15	6.34	6.54	7.25	8.19	7.72
NNE	10.71	10.27	10.07	10.17	10.67	11.22	10.27	10.74
NE	15.89	12.58	13.68	13.13	6.40	4.85	5.31	5.08
ENE	6.20	7.46	7.78	7.62	2.41	1.88	2.26	2.07
E	2.85	2.68	3.27	2.97	1.83	1.88	1.60	1.74
ESE	1.59	1.59	1.97	1.78	1.66	1.00	1.28	1.14
SE	2.20	1.31	1.77	1.54	2.91	1.61	1.83	1.72
SSE	2.85	2.52	2.09	2.30	2.88	2.40	2.86	2.63
S	8.47	13.28	9.05	11.17	13.04	18.49	14.20	16.36
SSW	11.86	17.39	12.75	15.07	9.82	12.74	9.95	11.35
SW	12.23	9.14	8.17	8.65	10.64	10.22	8.32	9.28
WSW	3.63	3.26	4.08	3.67	5.56	5.14	5.21	5.18
W	3.08	4.28	4.95	4.62	4.44	4.12	5.24	4.68
WNW	2.61	2.74	3.88	3.31	4.17	3.85	4.37	4.11
NW	3.19	2.43	3.65	3.04	5.05	6.84	7.71	7.27
NNW	2.41	2.77	3.59	3.18	3.79	5.71	8.28	6.99
VAR.	6.51	0.00	0.00	0.00	1.56	0.00	0.00	0.00
CALM	0.07	0.00	0.00	0.00	0.14	0.00	0.00	0.00
MISS.	0.03	0.77	2.09	1.43	6.50	0.79	3.13	1.96
NO VALID HOURS	2951	4411	4407	8818	2952	4413	4373	8786
% HRS IN DISTR	100.	99.9	99.8	99.8	100.	99.9	99.0	99.5

IP2
FSAR UPDATE

TABLE 18
COMPARISON OF PERCENT WIND FREQUENCY DISTRIBUTIONS - WINTER

Wind Direction	10 Meter Level				122 Meter Level			
	1974	1979	1980	1979-80	1974	1979	1980	1979-80
N	7.19	10.73	11.90	11.32	7.23	11.15	10.97	11.06
NNE	13.67	10.34	10.05	10.20	13.67	13.22	14.33	13.78
NE	12.22	11.45	15.11	13.29	5.63	4.79	4.90	4.85
ENE	4.75	5.90	6.30	6.10	1.93	1.80	1.79	1.79
E	1.59	2.86	3.02	2.94	1.60	1.45	1.79	1.62
ESE	0.95	0.71	0.85	0.78	1.16	0.92	1.65	1.29
SE	0.99	0.67	1.26	0.96	1.36	1.75	1.44	1.60
SSE	1.81	1.98	1.49	1.73	1.79	1.82	1.76	1.79
S	6.44	6.50	5.63	6.06	8.67	10.57	8.26	9.41
SSW	7.39	8.11	7.65	7.88	8.25	8.64	8.04	8.34
SW	5.76	6.24	5.72	5.98	9.36	5.87	5.59	5.73
WSW	2.58	4.31	3.04	3.67	3.51	3.18	3.37	3.27
W	3.32	4.77	4.01	4.39	2.94	3.78	4.14	3.96
WNW	5.42	5.90	4.62	5.26	5.08	6.24	5.24	5.74
NW	11.88	9.63	7.10	8.36	14.01	14.56	13.46	14.01
NNW	8.80	8.80	12.07	10.44	10.42	10.27	13.28	11.78
VAR.	4.23	0.00	0.00	0.00	1.18	0.00	0.00	0.00
CALM	0.66	0.00	0.00	0.00	0.04	0.00	0.00	0.00
MISS.	2.80	1.11	0.18	0.64	5.50	0.00	0.00	0.00
NO VALID HOURS	4967	4341	4368	8709	4924	4342	4368	8710
% HRS IN DISTR	97.6	99.9	100.	100.	96.8	100.0	100.	100.

3.2.4.3 Diurnal Wind Direction Distributions

Seasonal diurnal distributions of the resultant wind directions for the combined 1979-1980 data period are shown in comparison to the 1973-1974 data collection period in Table 19 and in Figures 17 and 18.

The diurnal patterns with the exception of the summer season at the 122 meter level from the 2300 to 0900 are nearly identical for the 1979-80 data set and the historical 1973-74 data set. The deviation of the 122 meter level during the nocturnal hours is also consistent when considered with respect to the summer wind frequency shift at the 122 meter level to a sharply defined south wind maximum.

It is concluded on the basis of the diurnal wind distributions that the patterns at all levels are consistent with the data base for FSAR 2 at all measurement levels with consideration for normal climatological variations.

3.2.4.4 Wind Speed Distributions

All variable valid wind speeds at the 10 meter and 122 meter levels have been evaluated on a seasonal basis to determine their diurnal characteristics and the cumulative probability distributions. The results of these analyses are shown in Tables 20 and 21 for the summer season and Tables 22 and 23 for the winter season. For visual comparison, the diurnal variability is shown in Figure 19. The probability distributions are shown in Figure 20. In this latter Figure, the annual cumulative probabilities have been included. These curves were generated by combining the cumulative points in Tables 20-23.

The maximum average diurnal wind speeds from this data set can be compared with those of the 1973-1974 season as shown below in Table 24. There are no significant differences.

IP2
FSAR UPDATE

TABLE 19
COMPARISON OF DIURNAL RESULTANT WIND DIRECTIONS

Time	10 Meter Level				122 Meter Level			
	Summer		Winter		Summer		Winter	
	1974	1979-80	1973-74	1979-80	1974	1979-80	1973-74	1979-80
0100	051	034	357	359	351	300	327	329
0200	054	036	358	002	008	313	328	333
0300	050	036	359	003	007	321	329	334
0400	042	043	360	004	355	325	334	335
0500	048	048	001	003	004	327	335	335
0600	050	041	000	007	007	331	336	337
0700	042	040	001	007	011	338	339	338
0800	017	023	357	004	012	341	340	338
0900	337	348	352	356	350	334	337	339
1000	293	302	343	351	317	312	336	336
1100	258	269	335	344	260	279	325	331
1200	246	259	329	336	241	272	320	325
1300	246	247	327	336	248	261	319	321
1400	246	249	323	333	246	260	316	316
1500	233	246	322	332	233	251	313	316
1600	228	244	316	336	221	245	306	315
1700	230	233	321	337	223	239	307	312
1800	226	237	327	340	222	239	303	313
1900	232	245	330	345	233	239	308	317
2000	290	346	340	348	248	250	313	320
2100	049	033	345	355	259	263	315	325
2200	049	018	347	358	277	276	319	329
2300	055	033	351	358	297	282	321	331
2400	045	037	354	360	317	287	321	330

IP2
FSAR UPDATE

Job Number: 01-4122-00

TABLE 20
YORK RESEARCH CORPORATION
ONE RESEARCH DRIVE, STAMFORD, CONNECTICUT 06906
CLIENT: CON EDISON CO. OF NY
SITE: INDIAN POINT (10M)
PARAMETER: WIND SPEED (SUMMER SEASON)
UNITS: MPH

DIURNAL ANALYSIS
MAY 1, 79,80 - OCT. 31, 79,80

OBSERV #	PARAM AVG	PARAM STD DEV	MAX VALUE	RANGE	VALID PTS
1	2.775	1.643	10.500	10.000	362
2	2.748	1.634	9.000	8.500	362
3	2.780	1.643	10.000	9.500	362
4	2.805	1.713	10.000	9.400	362
5	2.748	1.615	9.500	8.900	359
6	2.813	1.790	10.000	9.500	358
7	2.936	1.867	13.000	12.500	358
8	3.103	1.806	12.000	11.400	363
9	3.323	1.899	10.500	9.900	363
10	3.481	1.663	10.000	9.400	361
11	3.809	1.712	10.500	9.900	362
12	3.969	1.618	10.000	9.400	363
13	4.133	1.801	14.000	13.400	363
14	4.104	1.825	12.000	11.000	362
15	4.019	1.833	12.500	11.500	361
16	3.825	1.804	13.000	12.400	359
17	3.562	1.759	12.000	11.400	360
18	3.076	1.641	9.000	8.500	361
19	2.669	1.609	12.000	11.500	362
20	2.593	1.634	10.000	9.500	361
21	2.706	1.763	12.000	11.500	361
22	2.702	1.752	10.000	9.500	361
23	2.710	1.744	10.000	9.500	361
24	2.694	1.684	10.000	9.500	362
TOTAL	3.171	1.802	14.000	13.500	8669

CUMULATIVE PROBABILITY DISTRIBUTION
MAY 1, 79, 80 - OCT 31, 79, 80

CATEGORY OP. LIMIT	CATEGORY POINTS	CATEGORY PERCENT	CUMULATIVE POINTS < LIMIT	CUMULATIVE PERCENT < LIMIT
0.500	39	0.4	39	0.450
1.000	1177	13.6	1216	14.025
2.000	1996	23.0	3212	37.047
3.000	1977	22.8	5189	59.850
5.000	2474	28.5	7663	88.385
7.000	772	8.9	8435	97.290
9.000	181	2.1	8616	99.377
12.000	48	0.6	8664	99.931
16.000	5	0.1	8669	99.988
23.000	0	0.0	8669	99.988
30.000	0	0.0	8669	99.988
40.000	0	0.0	8669	99.988
50.000	0	0.0	8669	99.988
70.000	0	0.0	8669	99.988

NUMBER OF VALID DATA POINTS = 8669
NUMBER OF MISSING DATA POINTS = 163
REPRESENTING 98.2-PERCENT VALID DATA

IP2
FSAR UPDATE

Job Number: 01-4122-00

TABLE 21
YORK RESEARCH CORPORATION
ONE RESEARCH DRIVE, STAMFORD, CONNECTICUT 06906
CLIENT: CON EDISON CO. OF NY
SITE: INDIAN POINT (122M)
PARAMETER: WIND SPEED (SUMMER SEASON)
UNITS: MPH

DIURNAL ANALYSIS
MAY 1, 79,80 - OCT. 31, 79,80

OBSERV #	PARAM AVG	PARAM STD DEV	MAX VALUE	RANGE	VALID PTS
1	7.821	5.161	30.000	29.500	357
2	7.595	5.070	24.000	23.500	356
3	7.581	5.153	26.000	25.400	355
4	7.413	5.097	27.000	26.500	356
5	7.233	5.043	32.000	31.400	353
6	7.436	5.383	35.000	34.500	354
7	7.499	5.616	47.000	48.400	355
8	7.332	5.442	47.000	48.400	359
9	7.717	5.320	38.000	37.400	360
10	8.086	5.399	33.000	32.000	362
11	8.881	5.312	30.000	28.500	361
12	9.595	5.217	28.000	26.000	359
13	10.232	5.394	40.000	39.000	358
14	10.409	5.450	36.000	34.500	359
15	10.762	5.485	30.000	28.000	357
16	11.087	5.397	32.000	31.000	355
17	11.262	5.184	31.000	30.400	353
18	10.764	4.780	25.000	23.500	354
19	10.266	4.919	33.000	32.000	354
20	9.879	5.015	28.000	27.000	354
21	9.256	5.022	27.000	28.400	356
22	8.781	5.299	28.000	27.400	356
23	8.383	5.140	28.000	27.400	356
24	8.070	4.944	26.000	25.500	357
TOTAL	8.888	5.388	47.000	46.500	8556

CUMULATIVE PROBABILITY DISTRIBUTION
MAY 1, 79, 80 - OCT 31, 79, 80

CATEGORY OP. LIMIT	CATEGORY POINTS	CATEGORY PERCENT	CUMULATIVE POINTS < LIMIT	CUMULATIVE PERCENT < LIMIT
0.500	7	0.1	7	0.082
1.000	169	2.0	176	2.057
2.000	511	6.0	687	8.029
3.000	638	7.5	1325	15.484
5.000	1303	15.2	2628	30.712
7.000	1205	14.1	3833	44.794
9.000	1132	13.2	4965	58.023
12.000	1565	18.3	6530	76.312
16.000	1258	14.7	7788	91.013
23.000	652	7.6	8440	98.633
30.000	99	1.2	8539	99.790
40.000	15	0.2	8554	99.965
50.000	2	0.0	8556	99.988
70.000	0	0.0	8556	99.988

NUMBER OF VALID DATA POINTS = 8556
NUMBER OF MISSING DATA POINTS = 276
REPRESENTING 98.9-PERCENT VALID DATA

IP2
FSAR UPDATE

Job Number: 01-4122-00

TABLE 22
YORK RESEARCH CORPORATION
ONE RESEARCH DRIVE, STAMFORD, CONNECTICUT 06906
CLIENT: CON EDISON CO. OF NY
SITE: INDIAN POINT (10M)
PARAMETER: WIND SPEED (WINTER SEASON)
UNITS: MPH

DIURNAL ANALYSIS
NOV 1, 79, 80 - APR 30, 79, 80

OBSERV #	PARAM AVG	PARAM STD DEV	MAX VALUE	RANGE	VALID PTS
1	4.508	2.958	21.000	20.500	362
2	4.462	2.940	14.000	13.500	362
3	4.524	3.163	18.000	17.500	362
4	4.453	3.043	16.000	15.500	361
5	4.298	2.886	15.000	14.400	361
6	4.292	2.961	15.000	14.500	362
7	4.461	3.102	18.000	17.500	363
8	4.556	3.141	15.000	14.400	363
9	4.906	3.212	17.000	16.400	363
10	5.153	3.182	16.000	15.400	363
11	5.310	3.050	16.000	15.500	361
12	5.556	2.995	16.000	15.400	362
13	5.731	3.163	18.000	17.400	362
14	5.702	3.240	16.500	15.900	362
15	5.589	3.109	17.000	16.400	361
16	5.336	3.243	20.000	19.400	360
17	5.030	3.084	20.000	19.500	360
18	4.671	2.858	15.000	14.400	360
19	4.611	2.906	16.000	15.500	361
20	4.502	2.883	15.000	14.400	361
21	4.500	2.972	16.000	15.400	362
22	4.457	2.970	16.000	15.400	361
23	4.381	2.855	16.000	15.400	361
24	4.398	2.874	18.000	17.500	362
TOTAL	4.808	3.088	21.000	20.500	8678

CUMULATIVE PROBABILITY DISTRIBUTION
NOV 1, 79, 80 - APR 30, 79, 80

CATEGORY OP. LIMIT	CATEGORY POINTS	CATEGORY PERCENT	CUMULATIVE POINTS < LIMIT	CUMULATIVE PERCENT < LIMIT
0.500	18	0.2	18	0.207
1.000	788	9.1	806	9.287
2.000	1332	15.3	2138	24.634
3.000	1178	13.6	3316	38.207
5.000	2122	24.4	5438	62.657
7.000	1591	18.3	7029	80.989
9.000	841	9.7	7870	90.679
12.000	614	7.1	8484	97.753
16.000	181	2.1	8665	99.839
23.000	13	0.1	8678	99.988
30.000	0	0.0	8678	99.988
40.000	0	0.0	8678	99.988
50.000	0	0.0	8678	99.988
70.000	0	0.0	8678	99.988

NUMBER OF VALID DATA POINTS = 8678
NUMBER OF MISSING DATA POINTS = 34
REPRESENTING 99.6-PERCENT VALID DATA

IP2
FSAR UPDATE

Job Number: 01-4122-00

TABLE 23
YORK RESEARCH CORPORATION
ONE RESEARCH DRIVE, STAMFORD, CONNECTICUT 06906
CLIENT: CON EDISON CO. OF NY
SITE: INDIAN POINT (122M)
PARAMETER: WIND SPEED (WINTER SEASON)
UNITS: MPH

DIURNAL ANALYSIS
NOV 1, 79, 80 - APR 30, 79, 80

OBSERV #	PARAM AVG	PARAM STD DEV	MAX VALUE	RANGE	VALID PTS
1	10.919	6.869	49.000	48.500	359
2	10.669	5.562	38.000	37.400	359
3	10.636	6.799	40.000	39.400	358
4	10.297	6.804	37.500	36.900	358
5	10.075	6.354	34.000	33.400	358
6	9.832	6.485	32.000	31.500	358
7	9.902	6.811	44.000	43.500	356
8	10.283	7.067	38.000	37.400	356
9	10.525	6.978	36.000	35.400	358
10	10.596	7.032	37.000	36.400	360
11	11.086	6.961	36.000	35.000	362
12	11.828	7.011	34.000	33.500	362
13	12.309	7.218	48.000	47.000	362
14	12.530	7.250	45.000	44.400	362
15	12.727	7.184	43.000	42.000	362
16	12.635	6.992	40.000	38.500	362
17	12.302	6.778	42.000	41.000	361
18	11.921	6.035	32.000	31.400	361
19	11.645	6.061	32.000	31.400	360
20	11.398	6.093	37.000	36.400	360
21	11.106	6.216	40.000	39.400	360
22	10.658	6.206	39.000	38.400	358
23	10.488	6.182	36.000	35.000	358
24	10.551	6.178	41.000	40.500	359
TOTAL	11.124	6.726	49.000	48.500	4629

CUMULATIVE PROBABILITY DISTRIBUTION
NOV 1, 79, 80 - APR 30, 79, 80

CATEGORY OP. LIMIT	CATEGORY POINTS	CATEGORY PERCENT	CUMULATIVE POINTS < LIMIT	CUMULATIVE PERCENT < LIMIT
0.500	6	0.1	6	0.070
1.000	105	1.2	111	1.286
2.000	418	4.8	529	6.130
3.000	458	5.3	987	11.437
5.000	910	10.5	1897	21.981
7.000	895	10.4	2792	32.352
9.000	1009	11.7	3801	44.044
12.000	1622	18.8	5423	62.839
16.000	1518	17.6	6941	80.429
23.000	1230	14.3	8171	94.681
30.000	372	4.3	8513	98.992
40.000	78	0.9	8621	99.896
50.000	8	0.1	8629	99.988
70.000	0	0.0	8629	99.988

NUMBER OF VALID DATA POINTS = 8629
NUMBER OF MISSING DATA POINTS = 83
REPRESENTING 99.0-PERCENT VALID DATA

IP2
FSAR UPDATE

TABLE 24
MAXIMUM DIURNAL WIND SPEEDS (MPH)

<u>Season</u>	<u>Level (M)</u>	<u>1973-1974</u>	<u>1979-1980</u>
Summer	10	4.0	4.1
Summer	120	11.0	11.3
Winter	10	5.0	5.7
Winter	122	13.0	12.7

The median wind speeds extracted from Figure 20 at the 50 percent probability level are 1.1 M/S, 1.7 M/S and 1.4 M/S at the 10 meter level for the summer season, winter season, and annual basis, respectively. At the 122 meter level, these values are 3.4 M/S, 4.4 M/S and 3.9 M/S on the summer, winter and annual basis, respectively. These values bracket those presented by Kaplin and Laznow (1972) for the IP3 Tower. Corrected for exposure elevation no significant change would be expected between the two sets of values.

The variation of winds during the 1979-1980 season are consistent with data obtained during the 1973-1974 operational period. There is no reason to expect any significant variations with respect to the meteorology as used in FSAR 2.

3.2.4.5 Wind Velocities and Atmospheric Stability

3.2.4.5.1 Joint Frequency Distribution of Wind Direction and Stability

Stability categorizations as referenced in this study are in accordance with NRC Pasquill Tables as derived from local temperature change with elevation. Except as noted, actual temperature measured gradients have been converted to °C/100M directly from temperature difference values (°F) per difference between sensor height levels.

Tables 25, 26 and 27 show the summary frequency distributions for the 10 meter level of wind direction and stability categories for the 1979-1980 data collection period. The tables show the annual, summer season and winter season summaries respectively.

IP2
FSAR UPDATE

TABLE 25
ANNUAL SUMMARY OF WIND DIRECTION
PERCENT FREQUENCY DISTRIBUTION AS A FUNCTION
OF STABILITY - 10M LEVEL
(JANUARY 1, 1979 - DECEMBER 31, 1980)

Wind Direction	Stability Class						
	A	B	C	D	E	F	G
N	1.28	0.36	0.48	3.39	2.67	0.50	0.09
NNE	1.76	0.40	0.46	3.15	3.33	0.80	0.17
NE	0.63	0.35	0.58	4.22	4.66	2.12	0.40
ENE	0.06	0.07	0.17	1.59	2.61	1.84	0.43
E	0.01	0.03	0.03	0.64	1.49	0.59	0.11
ESE	0.01	0.01	0.01	0.27	0.73	0.21	0.04
SE	0.03	0.01	0.02	0.23	0.67	0.26	0.02
SSE	0.09	0.03	0.04	0.45	1.04	0.31	0.05
S	2.04	0.25	0.29	1.74	3.39	0.76	0.11
SSW	2.58	0.51	0.38	2.14	5.04	0.72	0.05
SW	1.16	0.33	0.35	1.89	3.03	0.51	0.03
WSW	0.49	0.17	0.16	0.96	1.44	0.39	0.02
W	0.56	0.22	0.17	1.40	1.64	0.43	0.06
WNW	0.47	0.15	0.26	1.64	1.49	0.21	0.03
NW	0.70	0.31	0.32	2.36	1.85	0.10	0.01
NNW	0.80	0.40	0.49	3.26	1.60	0.17	0.04
CALM	0.00	0.00	0.00	0.00	0.00	0.00	0.00
MISSING	0.12	0.05	0.03	0.21	0.51	0.15	0.02
TOTAL %	12.80	3.66	4.23	29.56	37.17	10.08	1.69
NO. OF HOURS	2244	641	742	5183	6519	1768	297

IP2
FSAR UPDATE

TABLE 26
SUMMARY OF WIND DIRECTION PERCENT FREQUENCY
DISTRIBUTION AS A FUNCTION OF STABILITY
SUMMER SEASON - 10M LEVEL
(MAY 1, 1979, 80 - OCTOBER 31, 1979, 80)

Wind Direction	Stability Class						
	A	B	C	D	E	F	G
N	1.68	0.26	0.37	1.25	2.06	0.57	0.07
NNE	2.65	0.42	0.43	2.90	2.41	1.01	0.18
NE	0.58	0.31	0.46	3.46	4.44	3.17	0.35
ENE	0.11	0.10	0.24	1.38	2.66	2.62	0.39
E	0.02	0.07	0.01	0.57	1.57	0.61	0.05
ESE	0.01	0.01	0.00	0.31	1.01	0.36	0.06
SE	0.05	0.02	0.01	0.17	0.84	0.40	0.02
SSE	0.15	0.06	0.05	0.50	1.07	0.40	0.08
S	3.32	0.36	0.43	2.47	3.58	0.85	0.05
SSW	4.10	0.75	0.59	2.93	5.70	0.85	0.01
SW	1.84	0.49	0.48	2.23	3.03	0.51	0.05
WSW	0.87	0.20	0.18	0.94	1.05	0.34	0.00
W	0.88	0.28	0.19	1.38	1.42	0.34	0.07
WNW	0.80	0.09	0.25	0.94	1.03	0.15	0.05
NW	1.05	0.19	0.17	0.84	0.63	0.10	0.02
NNW	0.78	0.19	0.24	0.97	0.74	0.20	0.02
CALM	0.00	0.00	0.00	0.00	0.00	0.00	0.00
MISSING	0.22	0.06	0.01	0.31	0.68	0.22	0.03
TOTAL %	19.11	3.86	4.11	23.54	33.92	12.69	1.48
NO. OF HOURS	1687	341	363	2078	2994	1120	131

IP2
FSAR UPDATE

TABLE 27
SUMMARY OF WIND DIRECTION PERCENT FREQUENCY
DISTRIBUTION AS A FUNCTION OF STABILITY
WINTER SEASON - 10M LEVEL
(NOVEMBER 1, 1979, 80 - APRIL 30, 1979, 80)

Wind Direction	Stability Class						
	A	B	C	D	E	F	G
N	0.87	0.46	0.60	5.56	3.28	0.44	0.11
NNE	0.85	0.38	0.49	3.41	4.26	0.59	0.16
NE	0.86	0.40	0.69	4.99	4.88	1.06	0.45
ENE	0.01	0.05	0.10	1.79	2.56	1.06	0.48
E	0.00	0.00	0.06	0.72	1.40	0.56	0.18
ESE	0.00	0.01	0.01	0.23	0.45	0.06	0.02
SE	0.02	0.00	0.02	0.29	0.49	0.11	0.01
SSE	0.02	0.01	0.03	0.40	1.01	0.23	0.02
S	0.75	0.13	0.14	1.01	3.19	0.68	0.17
SSW	1.04	0.28	0.17	1.34	4.37	0.59	0.08
SW	0.48	0.16	0.22	1.55	3.03	0.51	0.02
WSW	0.10	0.13	0.14	0.99	1.84	0.45	0.03
W	0.24	0.15	0.14	1.42	1.86	0.52	0.06
WNW	0.13	0.22	0.28	2.34	1.95	0.28	0.02
NW	0.34	0.42	0.47	3.90	3.09	0.10	0.00
NNW	0.83	0.62	0.75	5.58	2.47	0.14	0.06
CALM	0.00	0.00	0.00	0.00	0.00	0.00	0.00
MISSING	0.02	0.03	0.05	0.11	0.33	0.09	0.01
TOTAL %	6.39	3.44	4.35	35.65	40.47	7.44	1.91
NO. OF HOURS	557	300	379	3105	3525	648	161

IP2 FSAR UPDATE

There are distinctive seasonal biases that coincide with variations in wind direction occurrence frequencies. It will be seen that these biases are consistent with variations in stability and wind speed on diurnal basis.

3.2.4.5.2 Frequency of Occurrence of Stability Categories

Table 28 shows a summary of historical comparison of percent occurrence of stability categories between the various reporting periods for the IP3 Tower and of the 122M Tower (IP4) for 1973/74. (Based on concurrent wind speed and temperature gradients). The former gradients were based on temperature differences from the 30M and 2M levels while the latter were based on differential measurements between the 60M and 10M levels.

On an annual basis there is generally good agreement between the results for the 122M Tower and the IP3 Tower composite year with temperature correction (FSAR 3, Supplement 13, 16).

The variation in percentages at the stability extreme A and G are most probably related to the lower gradient base level of measurement on the IP3 Tower - 2 meters. One would expect higher or lower temperatures closer to the ground with less accuracy in the thermal adjustment factor in these extreme ranges.

Table 29 shows a similar comparison for the 122 Meter Meteorological Tower for the 1973-1974 data collection period and the 1979-80 data collection period. These results are based on current wind speed data for the tower levels as noted. The 122M is shown based on two gradient differences: 122-10M and 122-60M. The percent occurrences of stability categories are sharply defined functions of season and, for the upper level, the vertical defined functions of season and, for the upper level, the vertical temperature gradient. This is apparent in both data sets.

There are seasonal differences in the two data sets particularly in the A and G stability category extremes at the 122M level, however, is noted that the percent occurrences in the 1973-1974 data set are based on only one or less than ten observations where these percentage differentials are most extreme. Where more data points are available in each stability category as for the lower gradient level (61-10M), there is generally good agreement.

IP2
FSAR UPDATE

TABLE 28
HISTORICAL COMPARISONS OF
PERCENT OCCURRENCE OF STABILITY

Temperature Gradient (M)	Stability Class							No. of Observ.
	A	B	C	D	E	F	G	
<u>Summer (1974)</u>								
61-10	21.44	5.46	4.37	27.92	30.21	9.28	1.31	2747
1973 (IP3)*	25.52	2.62	3.64	17.38	26.81	13.39	10.63	2935
<u>Winter (1973/74)</u>								
61-10	4.00	1.92	2.13	23.93	53.24	12.53	2.25	4797
1973 (IP3)*	21.49	3.52	3.74	23.29	23.76	14.24	9.96	4229
<u>Annual (1973/74)</u>								
61-10	10.35	3.21	2.94	25.38	44.86	11.35	1.91	7544
1970/72 (IP3) ¹	6.42	2.55	2.23	31.19	38.75	11.25	3.16	8366
1970 (IP3)*	21.68	2.20	3.39	33.35	24.75	9.01	5.62	NA
1971 (IP3)*	19.17	2.75	2.97	22.79	30.87	11.69	9.75	NA
1970/72 (IP3) ^{1*}	15.52	1.74	2.82	28.38	25.42	12.68	9.03	8366
1973 (IP3)**	23.14	3.16	3.70	20.87	25.02	13.89	10.23	NA

* Concurrent basis

¹ Composite year with temperature correction - concurrent basis (FSAR 3)

^{1*} Composite year concurrent basis (FSAR 3)

** March-December only concurrent basis

NA Not Available

NOTE: Gradient for IP3 Tower: 30-2 M

IP2
FSAR UPDATE

TABLE 29
COMPARISON OF PERCENT OCCURRENCE OF STABILITY
ON 122 METER TOWER

Date	Wind Freq LVL (M)	Stability Class							No. of Observ	Temperature Gradient(M)
		A	B	C	D	E	F	G		
<u>Summer</u>										
1974	10	21.44	5.47	4.37	27.92	30.21	9.28	1.31	2747	61 - 10
1979/80	10	19.34	3.93	4.22	23.96	34.35	12.73	1.48	8557	60 - 10
1974	122	0.51	0.66	2.15	47.40	41.54	7.72	0.04*	2747	122 - 10
1979/80	122	4.54	5.50	5.81	42.84	34.95	6.23	0.14**	7838	122 - 10
1974	122	0.04*	0.04*	0.11**	20.13	74.01	5.42	0.25**	2747	122 - 61
1979/80	122	0.17**	0.42	1.49	68.09	26.72	2.82	0.29	7838	122 - 60
<u>Winter</u>										
1973/74	10	4.00	1.92	2.13	23.93	53.24	12.53	2.25	4797	61 - 10
1979/80	10	6.44	3.47	4.37	35.79	40.55	7.46	1.92	8648	60 - 10
1973/74	122	3.17	1.70	1.63	41.46	48.86	3.09	0.08**	4797	122 - 10
1979/80	122	0.59	1.18	2.78	56.07	34.75	4.29	0.31	8594	122 - 10
1973/74	122	0.02*	0.31	1.19	41.94	49.59	6.82	0.13**	4797	122 - 61
1979/80	122	0.28	0.14	0.37	71.89	25.35	1.84	0.13	8594	122 - 60
<u>Annual</u>										
1973/74	10	10.35	3.21	2.94	25.38	44.86	11.35	1.91	7544	61 - 10
1979/80	10	12.86	3.70	4.30	29.90	37.47	10.08	1.70	17205	60 - 10
1973/74	122	2.63	1.33	1.82	43.62	46.20	4.77	0.07	7544	122 - 10
1979/80	122	2.48	3.24	4.23	49.76	34.84	5.22	0.23	16432	122 - 10
1973/74	122	0.03	0.08	0.80	34.00	58.48	6.31	0.17	7544	122 - 61
1979/80	122	0.23	0.27	0.91	70.08	26.00	2.31	0.21	16432	122 - 60

It may be inferred that, except as stated for the reasons noted, the percent frequency of stability classes with the existing tower system is representative and consistent with data referenced in FSAR 2.

* Single observations
** Less than ten observations

IP2
FSAR UPDATE

3.2.4.5.3 Average Wind Speed and Diurnal Variation as a Function of Stability Categories

Tables 30, 31, and 32 show the average wind speed and number of observations as functions of time of day and stability category for the summer and winter seasons of the combined 1979 and 1980 data collection period.

The results are derived from valid wind speeds measured at 10M relative to the temperature difference 60 - 10M and 122M wind speeds based on the temperature difference between 122-10M and 122-60M. The latter gradient was generated by subtraction of gradient levels:

$$(122-60) = (122-10) - (60-10)$$

These tables indicate a distinctive diurnal pattern to the stability. During the summer season at the 10M level for all practical purposes G stability does not occur between 0700 to 1900 EST and F stability does not occur between 0900 and 1400. During the nocturnal hours between 1900 to 0600, for all practical purposes A, B, and C stability categories do not appear. Stability Category A appears from 0700 to 1800 EST and is the dominant gradient between 0900 and 1600 EST. Out of 2,855 observations during this time interval, the percent frequency of occurrences were 52.9 for A, 8.1 for B, 8.4 for C, 24.2 for D, 6.1 for E, 0.2 for F, and 0.04 for G.

In the winter season at 10M, the A, B, and C stability categories do not appear during the nocturnal hours from 1900 to 0600 (with random singular exceptions). D is the dominant day time stability category and E is the dominant nighttime category.

Somewhat similar patterns are found with the upper level gradients based on the 122-10M and 122-60M temperature gradients. Between these latter two gradients

TABLE 30
Diurnal Variation of Stability Class and Wind Speed
(concurrent data)

TABLE 31
Diurnal Variation of Stability Class and Wind Speed
(concurrent data)

TABLE 32
Diurnal Variation of Stability Class and Wind Speed
(concurrent data)

IP2
FSAR UPDATE

TABLE 33
COMPARISONS OF AVERAGE WIND SPEEDS (MPH)
AS A FUNCTION OF STABILITY

Year/ Season	Anemom LVL	Stability Class							Temperature Gradient (M)
		A	B	C	D	E	F	G	
<u>Summer</u>									
1974	10M	4.2	4.4	4.0	3.8	2.7	2.3	2.6	60 - 10
1979/80	10M	4.0	3.6	3.5	3.7	2.7	2.1	2.2	60 - 10
1974	122M	4.3**	14.3	12.3	9.5	7.7	4.5	4.5*	122 - 10
1979/80	122M	11.2	10.4	9.8	10.0	7.6	4.8	4.3**	122 - 10
1974	122M	3.5*	49.0*	3.8**	10.6	8.2	4.4	2.6**	122 - 60
1979/80	122M	9.3**	12.6	12.1	10.0	6.4	4.3	4.0	122 - 60
<u>Winter</u>									
1973/74	10M	4.8	5.2	4.8	6.1	5.0	2.4	2.3	60 - 10
1979/80	10M	5.9	6.4	6.0	5.9	4.0	2.2	2.8	60 - 10
1973/74	122M	15.8	11.5	10.1	13.5	9.0	5.7	3.6**	122 - 10
1979/80	122M	13.9	12.4	13.9	12.9	8.6	5.6	8.6	122 - 10
1973/74	122M	16.0*	15.0	13.9	13.3	9.7	6.0	4.7**	122 - 60
1979/80	122M	19.9	21.0	20.4	12.3	7.8	7.2	6.3**	122 - 60

for the same data base the number of occurrences of A, B, and C stability categories in both summer and winter seasons are substantially reduced and become almost random when based on the 122-60M gradient. The obvious implication is that temperature gradient extremes are controlled by the surface level. This is consistent with Kaplan, et. al., 1974.

At the upper levels, for the summer season, F stability has a distinct diurnal function. It rarely occurs during the daytime from 0800 to 2000 EST. The distribution of G stability during the summer season, while a diurnal function, is clearly biased to the early morning hours. It occurs more frequently with relation to the 122-60M gradient than the 122-10M gradient. These factors are consistent with a nocturnal cool air surface drainage flow. This routine drainage flow does not exist during the winter season, and the occurrence frequencies, while still diurnal, are clearly related to the local surface air temperatures.

It is noted that during the winter seasons, drainage flow patterns are not routine occurrences. They can occur, however, during periods of weak pressure gradients. They are dependent on the horizontal and vertical temperature gradients that develop between the land (snow covered or bare ground) as well as the Hudson River (free water or ice bound).

The average wind speeds as a function of stability category are shown in Table 33 for the 1973-1974 data collection period and the 1979-1980 data period. As noted, there are some apparent anomalies with respect to the 122 meter level wind speeds. These are probably induced by the few data points available in 1973-1974 rather than a reality. Where the

* Single observations

** Less than 15 observations

IP2
FSAR UPDATE

total number of occurrences were in a more reliable range, at the 10 meter and the 122 meter levels, there was good agreement between average wind speeds.

Based on these data, it is concluded that within the range of normal climatological variations, there are no significant changes in the local meteorological parameters on a seasonal and annual basis. The existing meteorological data are consistent with data referenced in FSAR 2.

4.0 SUMMARY

4.1 METEOROROLOGY

4.1.1 General

The meteorology of the Indian Point site and its environs has been thoroughly studied over the span of years. For the past nine years the source of on-site meteorology has been the 122 Meter Meteorological Tower that became fully operative as of October 1, 1973. This tower is located at latitude: 41° 15' 55" N and longitude 73° 57' 08" W (N38 + 31.453 and E22 + 49.473 on the Indian Point Grid).

Meteorological data from the 122 Meter Tower have, in previous studies and in this report, have been compared, in so far as possible, to those meteorological data, which were the data base for the FSAR 2 Report.

4.1.2 122 Meter Meteorological Tower System

The 122 Meter Tower and support systems as presently comprised, maintained, and operated are in compliance with the meteorological measurement programs included in Regulatory Guides 1.23 and 1.97 and the criteria set forth in NUREG-0654, -0696, and -0737.

The system is outlined in Figure 4. It consists of an instrumented 122 Meter Tower. The critical sensors are for winds at the 10, 60, and 122 meter levels; ambient temperature and dew point at the 10 meter level and temperature difference between the 60-10 meter and 122-10 meter levels. In addition, a precipitation gage is located within the tower complex. All sensor signals are carried to a trailer, which houses:

Signal Conditioners
Analog Recorders
Data Acquisition System - Magnetic Tape
Terminal Printer
LED Satellite Displays for Control Rooms 2 and 3
Telephone Modems
Dedicated Telephone Lines
Air Conditioning Systems

All systems are operated on primary AC voltage. A backup diesel generator within the complex provides for the automatic transfer of power if the primary source is cut off.

Appropriate meteorological data are transmitted from the Meteorological Trailer to:

Reactor Control Rooms 2 (CON-EDISON) and 3 (PASNY)

IP2
FSAR UPDATE

MIDAS and ARAC Computers

The Emergency Control Center in addition to the computer systems and interrogation systems receives wind data from backup wind sensors.

The status of the backup wind system and the MIDAS computer may be assessed by remote telephone interrogation.

4.1.3 Local Meteorological Characteristics

All earlier studies and the data evaluated and included in this report indicates that the most important characteristic of the Indian Point area is the prevalence of winds from the north and south sectors. These winds are induced by meso-scale factors: terrain channeling at all times and drainage flow and land-sea circulations during periods of weak synoptic-cyclonic scale pressure gradient field.

At all wind levels there are distinctive diurnal variation patterns to local winds as well as to the local winds in addition to the local atmospheric stability as determined by vertical temperature gradients related to Pasquill stability categories. Unstable A, B, and C categories are dominant daytime occurrences. Stable F and G categories are nocturnal occurrences.

Because of the dominance of meso-scale factors in the Indian Point and lower Hudson Avenue Valley environs, persistent straight line flow of air from Indian Point is impossible. Paths of movement of air parcels are best generated by the use of local data on a real time basis. Recirculation of air parcels within a time frame of eight consecutive hours is a likely event. Within ten miles of Indian Point there are three zones, which indicated the probability of convergence and divergence of local surface air streams:

Peekskill Bay
Haverstraw Bay
Tappan Zee

4.1.4 Conclusion

From the evaluation of previous studies and the recent data years January 1, 1979 - December 31, 1980, it has been concluded that the meteorological data being collected at the 122 Meter Meteorological Tower are representative of the Indian Point site and are consistent with the original and expanded meteorological data basis of FSAR for Unit No. 2. All deviations of data at any given time (not otherwise specifically assigned to measurement techniques, methodologies, and, evaluation procedural changes to comply with existing Regulatory Guides) can be assigned to normal regional climatological variations in any given year on, at least, the synoptic-cyclonic meteorological scale.

5.0 REFERENCES

- 1) Halitsky, James, J. Laznow and D. Leahey, (1970): Wind Observations at Indian Point, Montrose and Bowline Point, 31 August 1968 to 30 June 1969. New York University, School of Engineering and Science, Department of Meteorology and Oceanography, G.S.L. Technical Report No. TR-70-3, February, 1970.
- 2) Halitsky, James, E. J. Kaplin and J. Laznow (1971): Wind Observations at Indian Point, 26 November 1969 to October 1970. New York University, School of

IP2
FSAR UPDATE

Engineering and Science, Department of Meteorology and Oceanography, G.S.L. Technical Report No. TR 71-3, May, 1971.

- 3) Kaplin, Edward J. and J. Laznow (1972): Meteorological Observations at Indian Point, Trap Rock, Montrose Point and Cape Charles, 1 January 1970 to 31 December 1971. New York University, School of Engineering and Science, Department of Meteorology and Oceanography, G.S.L. Technical Report No. TR-73-1, December, 1972.
- 4) Kaplin, Edward J., J. Laznow and M. M. Wurmbrand (1972): Selection of Air Monitoring Locations, Calculations of Dispersion Patterns for Diffusion Overlays, and Recommendations for a Meteorological Program to Satisfy A.E.C. Safety Guide 23 at the Indian Point Complex. New York University, School of Engineering and Science, Department of Meteorology and Oceanography, G.S.L. Technical Report No. TR-72-3, July, 1972.
- 5) Kaplin, Edward J. and C. E. Kitson (1974): Final Report - Meteorological Services and Data Evaluation Indian Point 100 Foot Tower. York Research Corporation Report NO. Y-8127, September, 1974.
- 6) United States Atomic Energy Commission Safety Guide 23 - Onsite Meteorological Programs, February 17, 1972.
- 7) Kaplin, Edward J., M. Kozenko and J. Kirschner (1974): Report No. 1, Meteorological, Ambient Salt Studies and Upper Air Studies at Indian Point, Buchanan, NY, York Research Corporation Report No. Y-8162/8166, January, 1974.
- 8) Kaplin, Edward J., C. E. Kitson, and M. Kozenko (1974): Final Report: Meteorological, Upper Air and Ambient Salt Studies, York Research Corporation Report Nos. Y-8162 and Y-8166-2, October, 1974. (With Appendices A-N, I and II)
- 9) U.S. Nuclear Regulatory Commission (1980): NUREG-0654 (FEMA-FEP-1), Criteria for Preparation and Evaluation of Radiological Emergency Response Plans and Preparedness in Support of Nuclear Power Plants: Appendix 2, Meteorological Criteria for Emergency Preparedness at Operating Nuclear Power Plants, January, 1980.
- 10) U.S. Nuclear Regulatory Commission (1980): Proposal Revision 1 to Regulatory Guide 1.23 - Meteorological Programs in Support of Nuclear Power Plants, September, 1980.
- 11) Kaplin, Edward J. and B. Wuebber (1979): Final Report, Surface Air Trajectory Analyses, York Services Corporation Report No. 1-1025, December, 1979.
- 12) Kaplin, Edward J. (1979): Executive Summary, Final Report, Surface Air Trajectory Analysis, York Services Corporation Report No. 1-1025-1, December, 1979.
- 13) Kaplin, Edward J. and B. Wuebber (1981): Final Report Indian Point Trajectory II Study, York Services Corporation Report No. 01-4013, July, 1981.
- 14) FSAR: Final Facility Description and Safety Analysis Report, Consolidated Edison Company of New York, Inc., Nuclear Generating Station No. 2.

IP2
FSAR UPDATE

- 15) FSAR: Final Facility Description and Safety Analysis Report, Consolidated Edison Company of New York, Inc., Nuclear Generating Station No. 3.

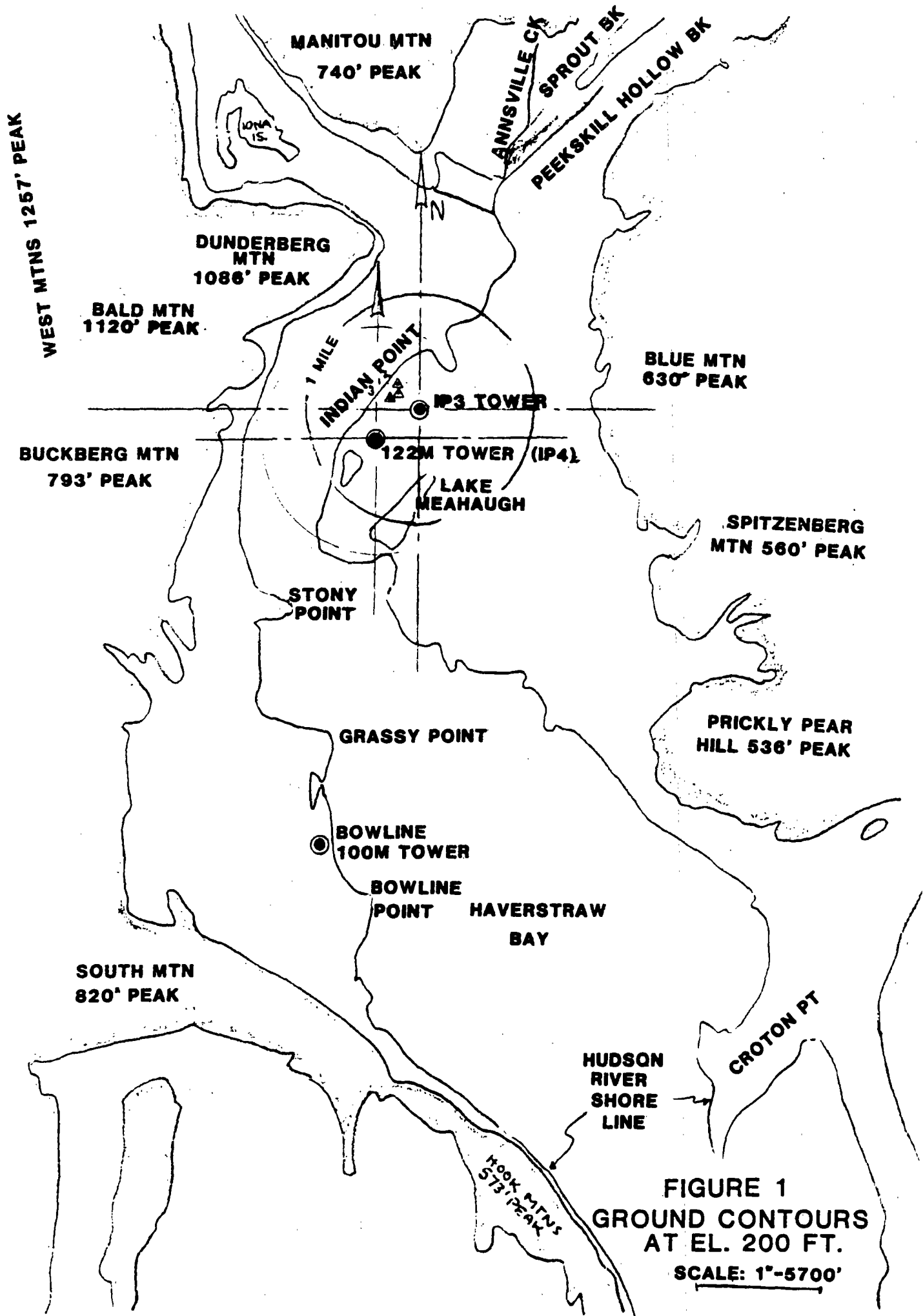


FIGURE 1
GROUND CONTOURS
AT EL. 200 FT.
SCALE: 1"-5700'

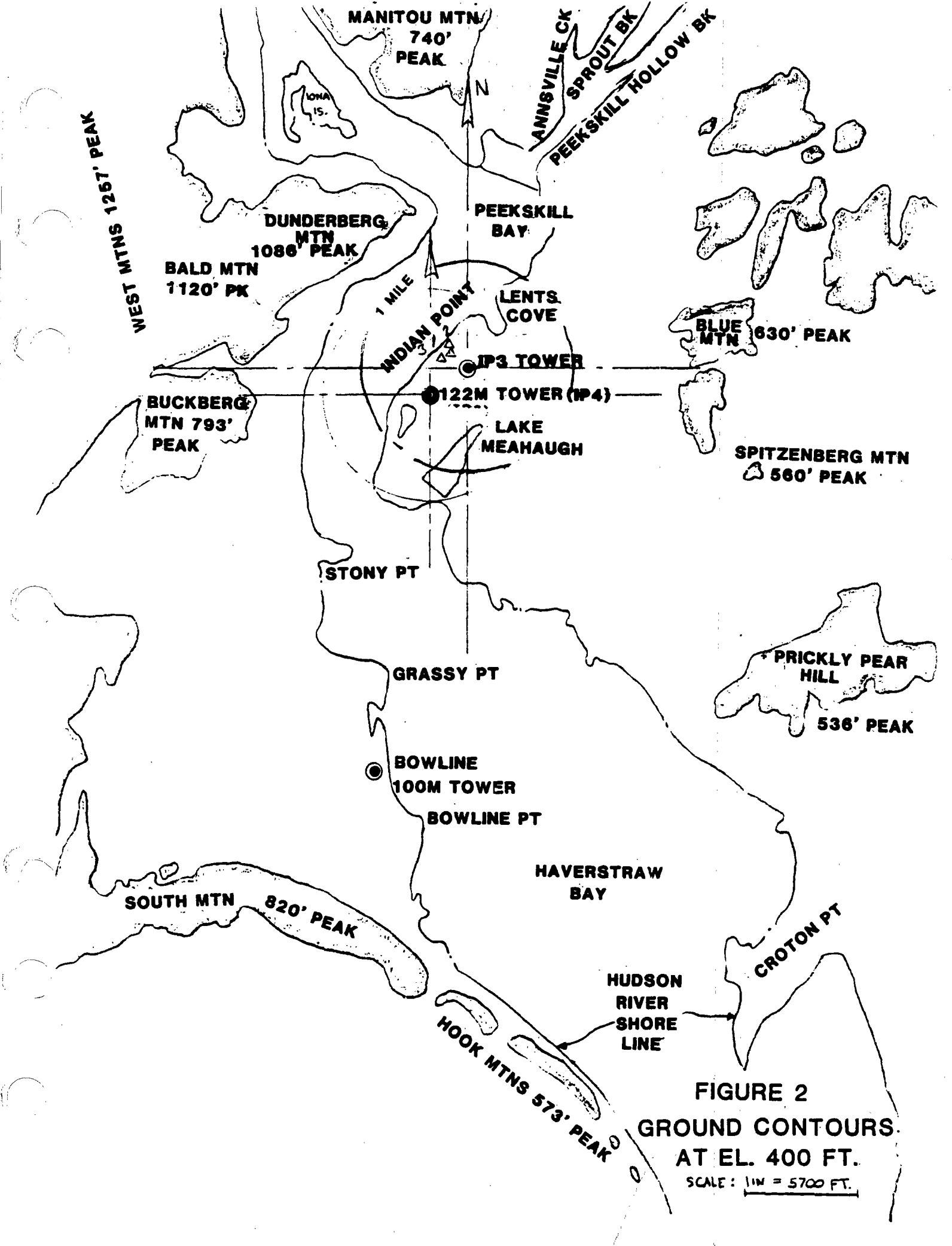


FIGURE 2
GROUND CONTOURS
AT EL. 400 FT.
 SCALE: 1" = 5700 FT.

FIGURE 4

WATER COURSES IN THE INDIAN POINT REGION

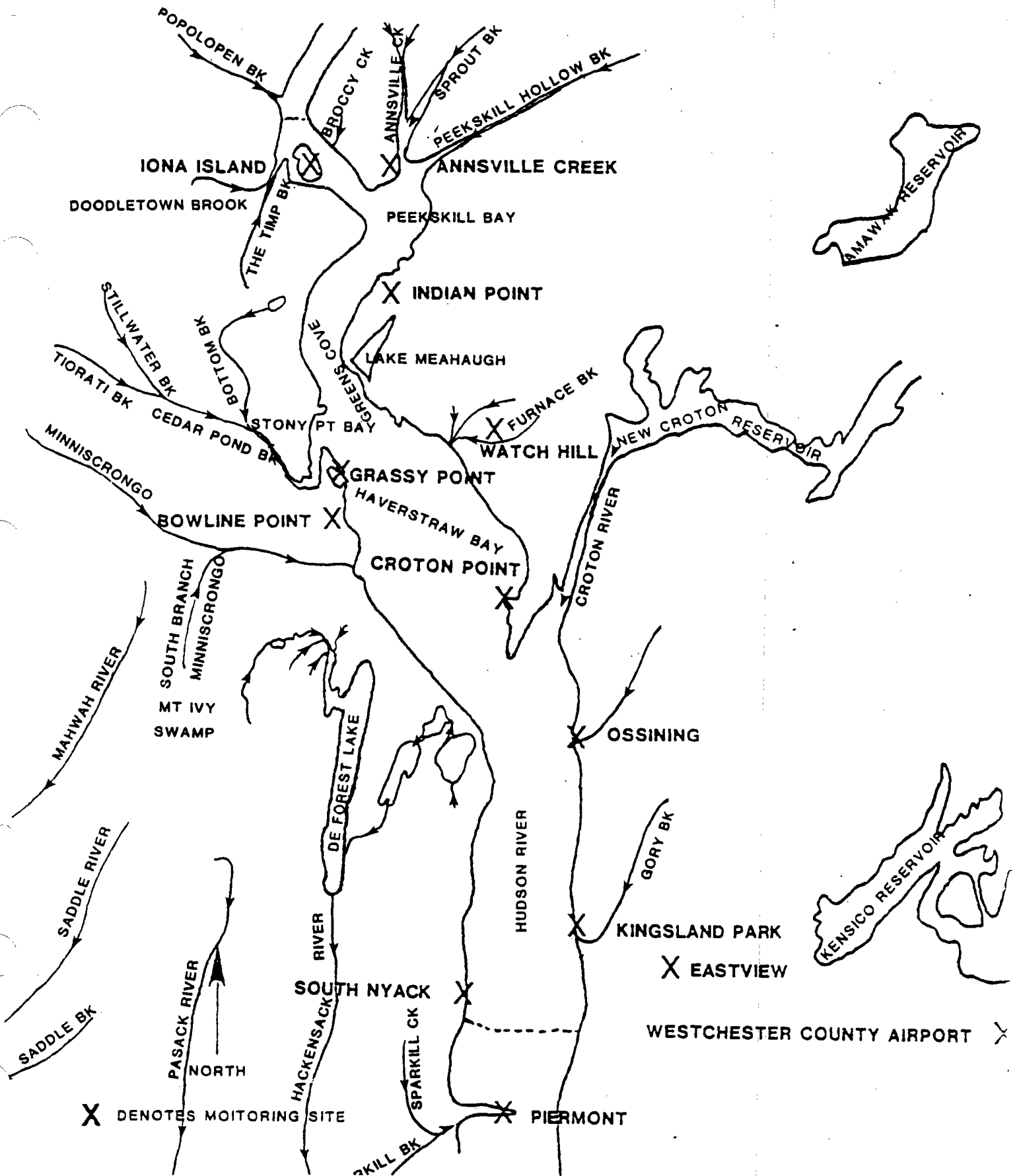


FIGURE 5

EXISTING AND HISTORICAL METEOROLOGICAL
TOWERS AT INDIAN POINT

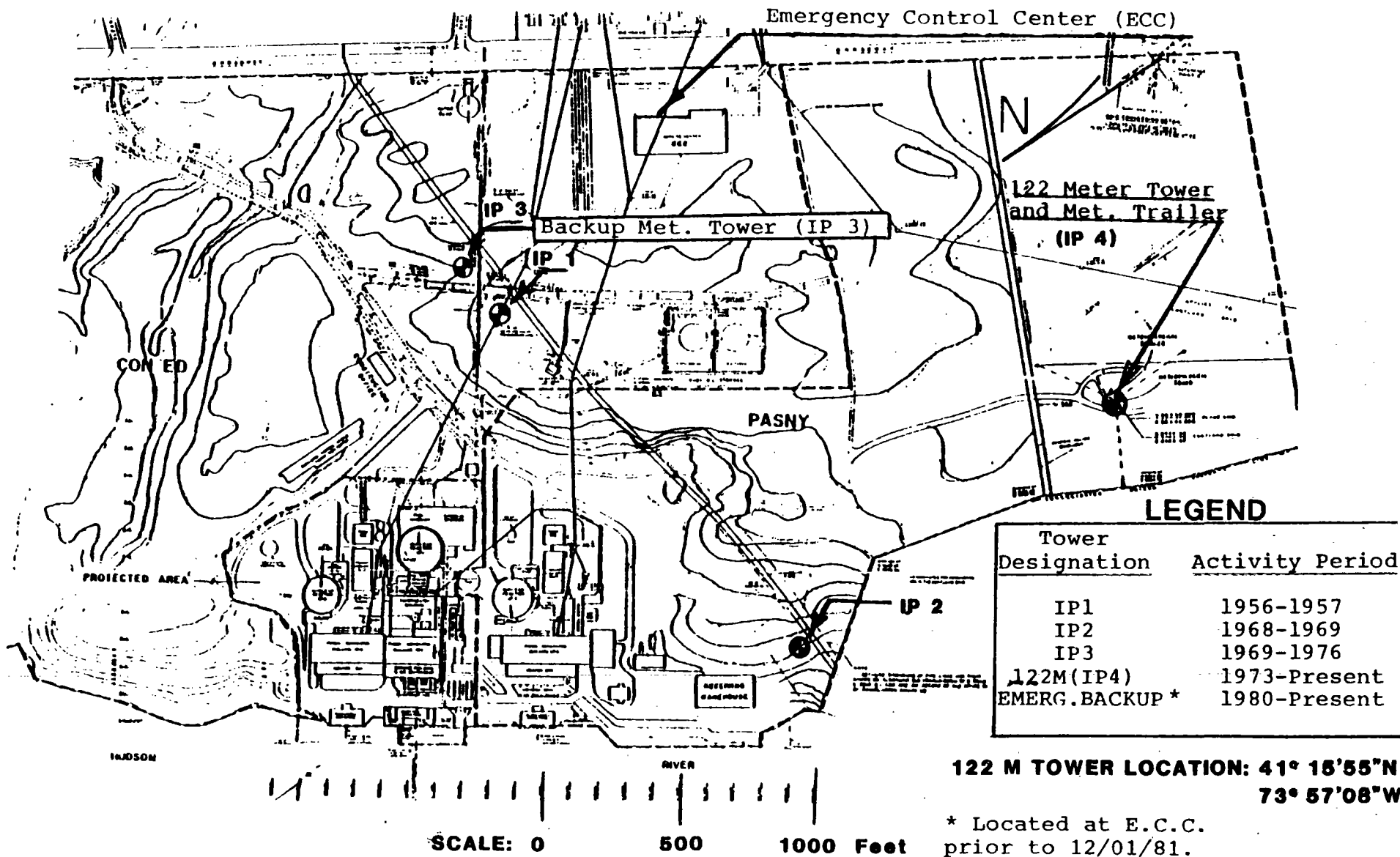
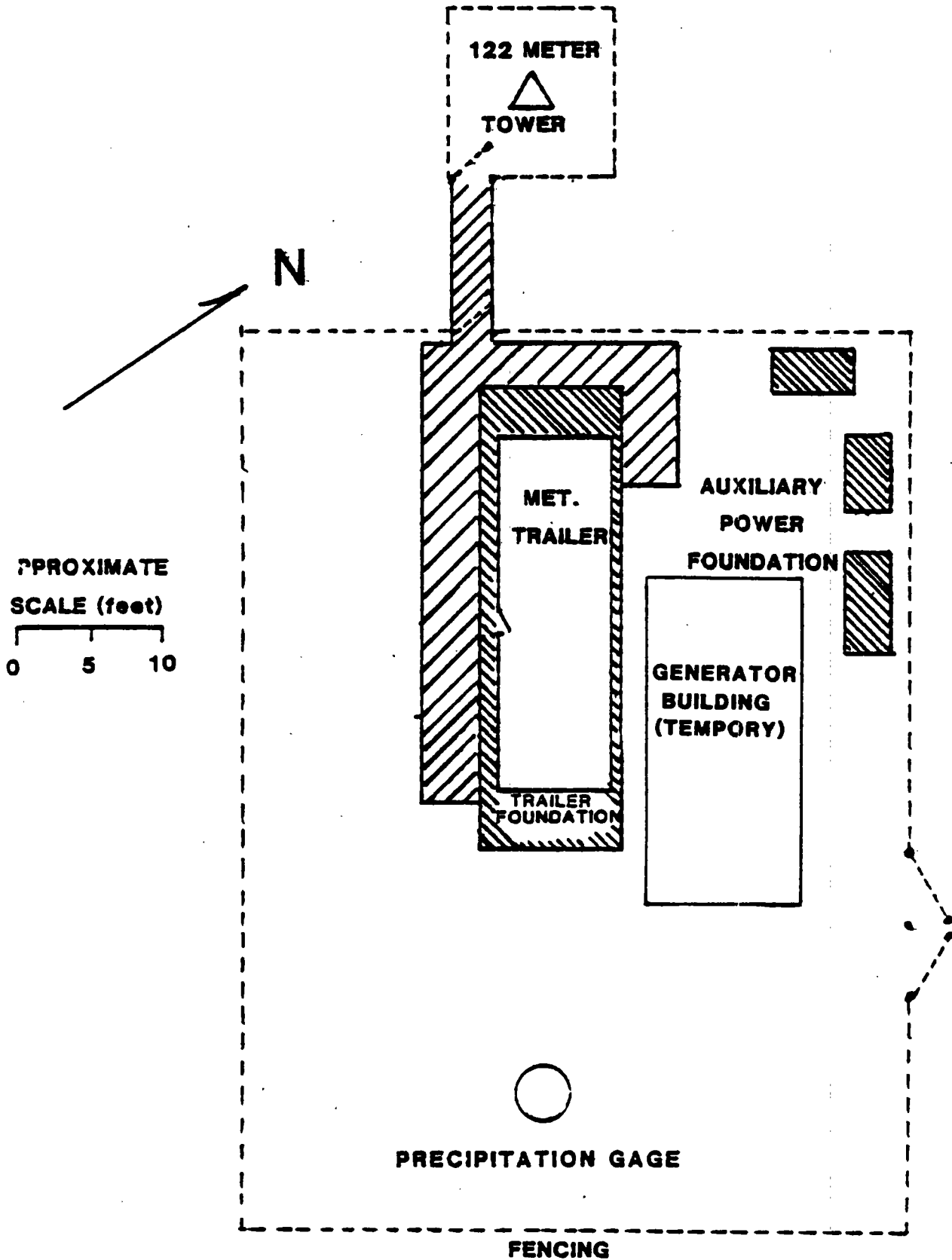


FIGURE 6

INDIAN POINT METEOROLOGICAL SITE



**FIGURE 7
TOWER CONFIGURATION**

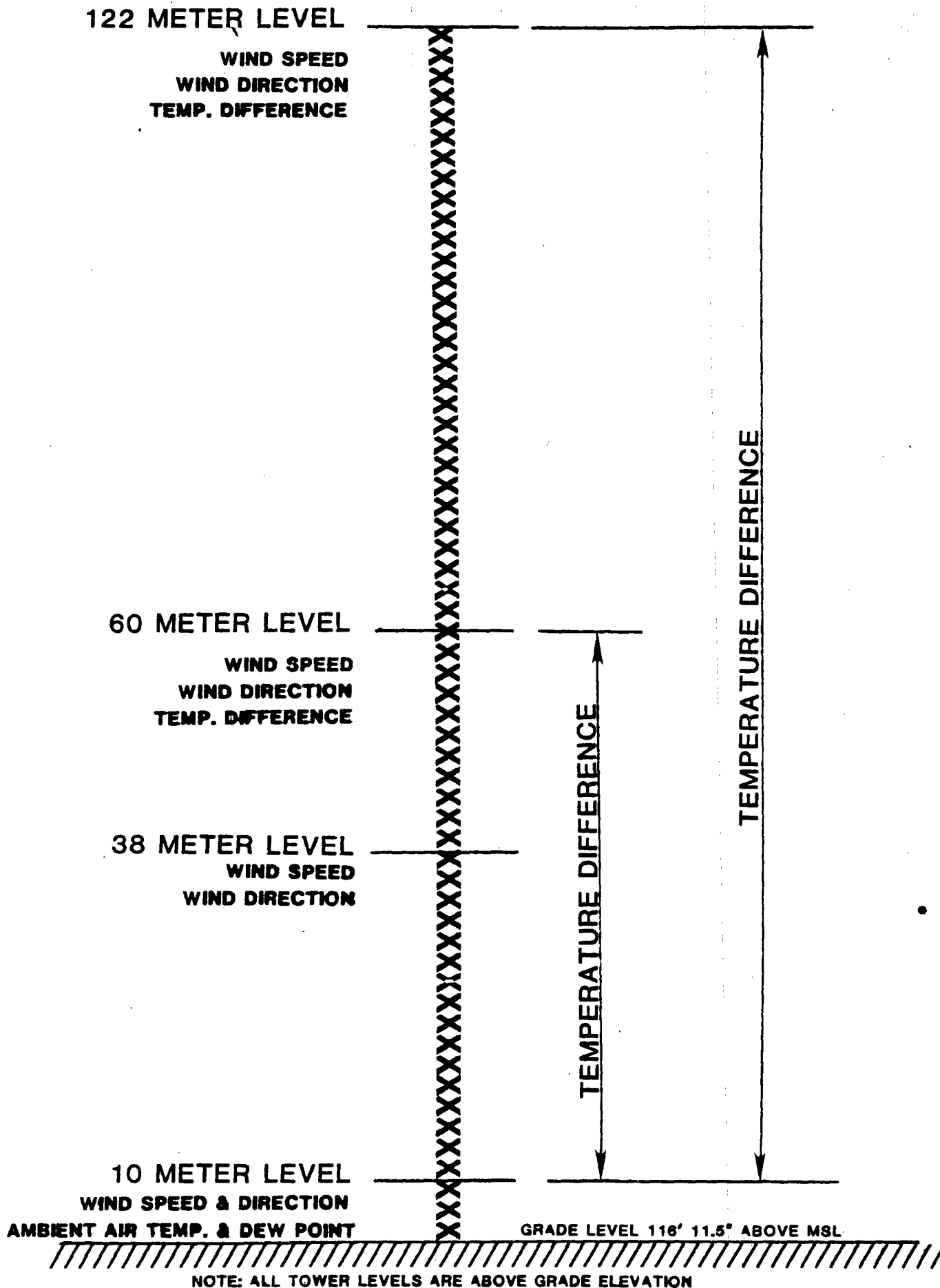
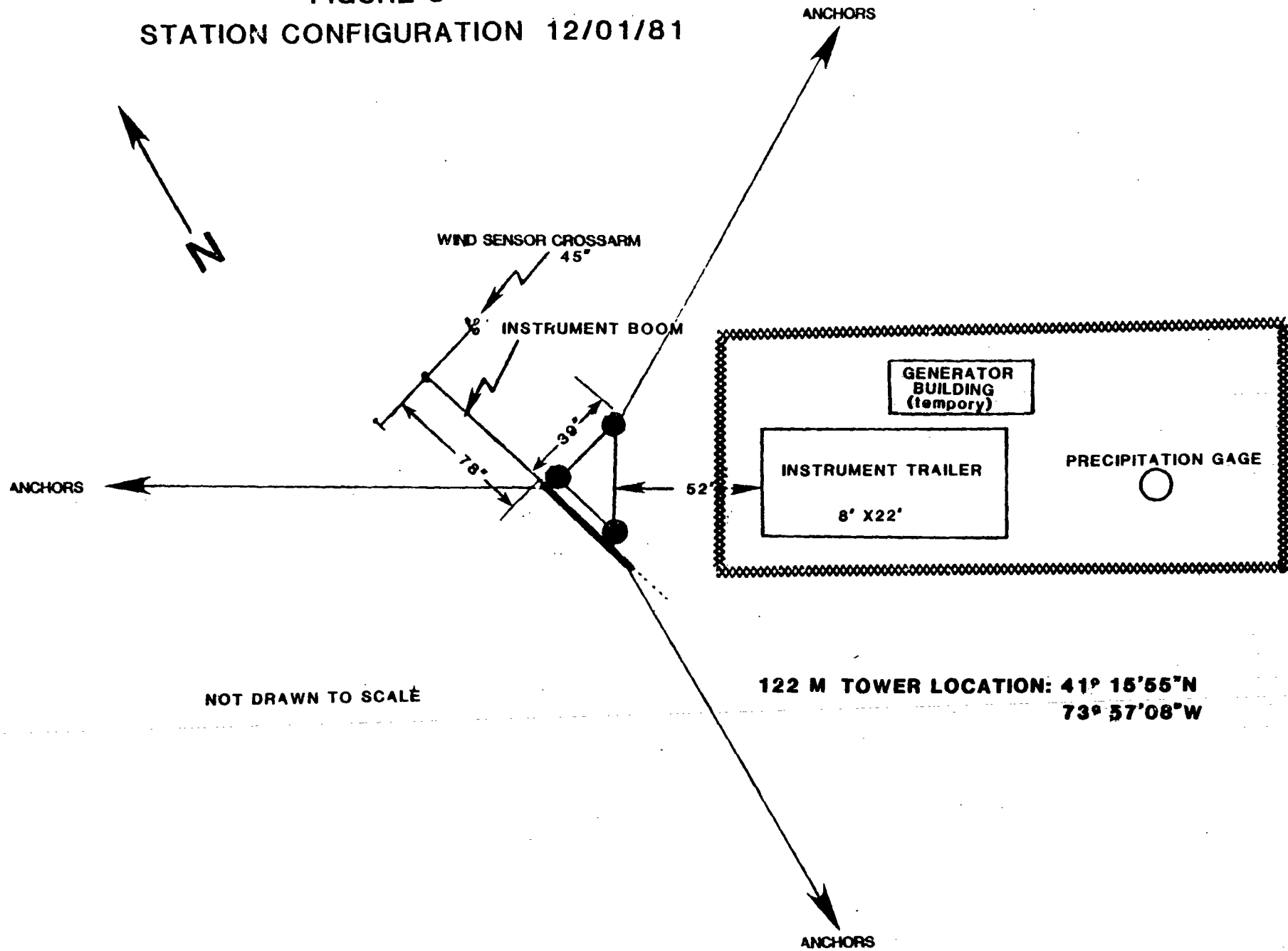


FIGURE 8
STATION CONFIGURATION 12/01/81



NOT DRAWN TO SCALE

FIGURE 9
INDIAN POINT-METEOROLOGICAL SUPPORT SYSTEMS

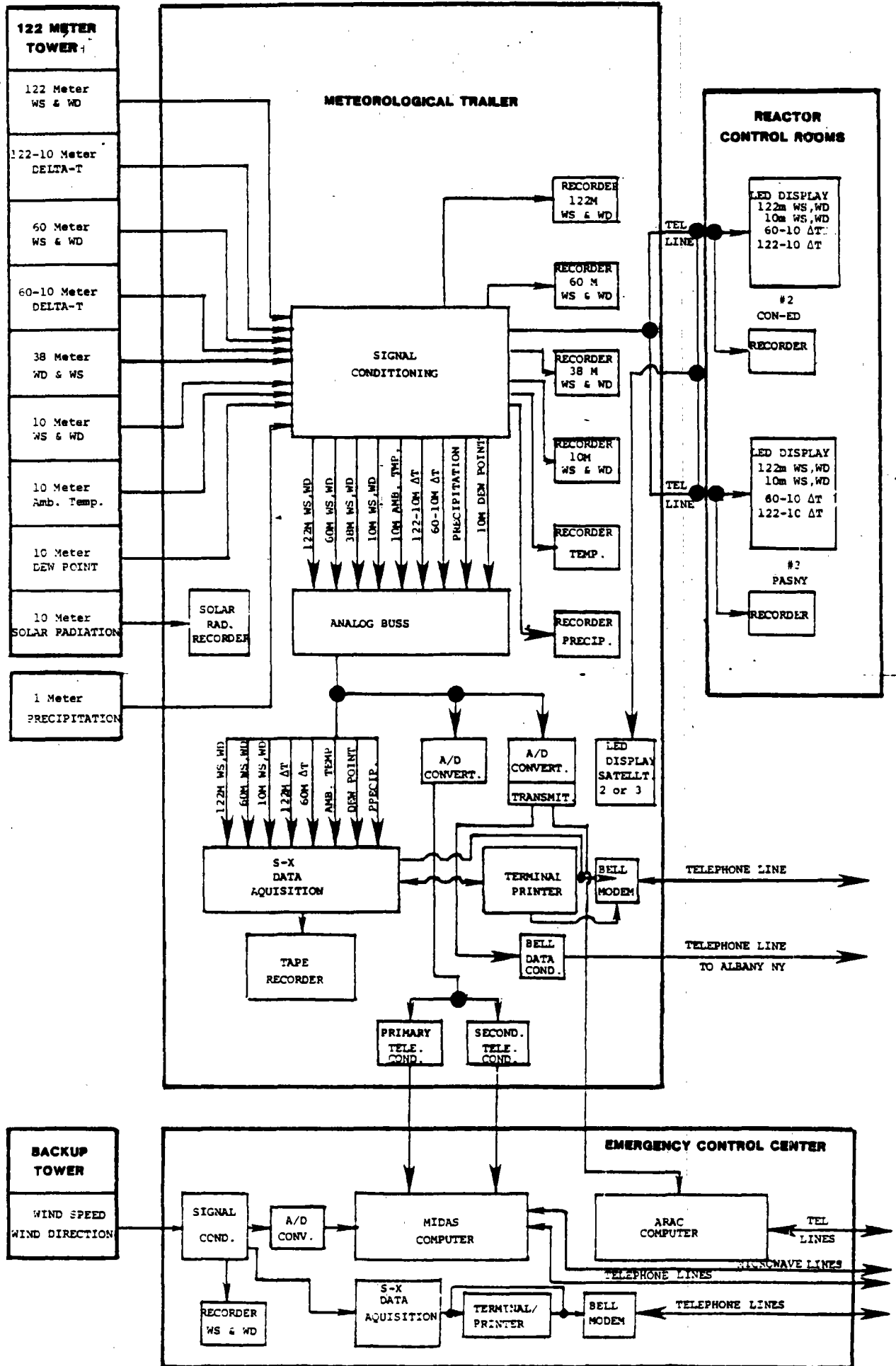


FIGURE 10A
TWO STATION WIND CORRELATION

DATA PERIOD
OCTOBER 1973

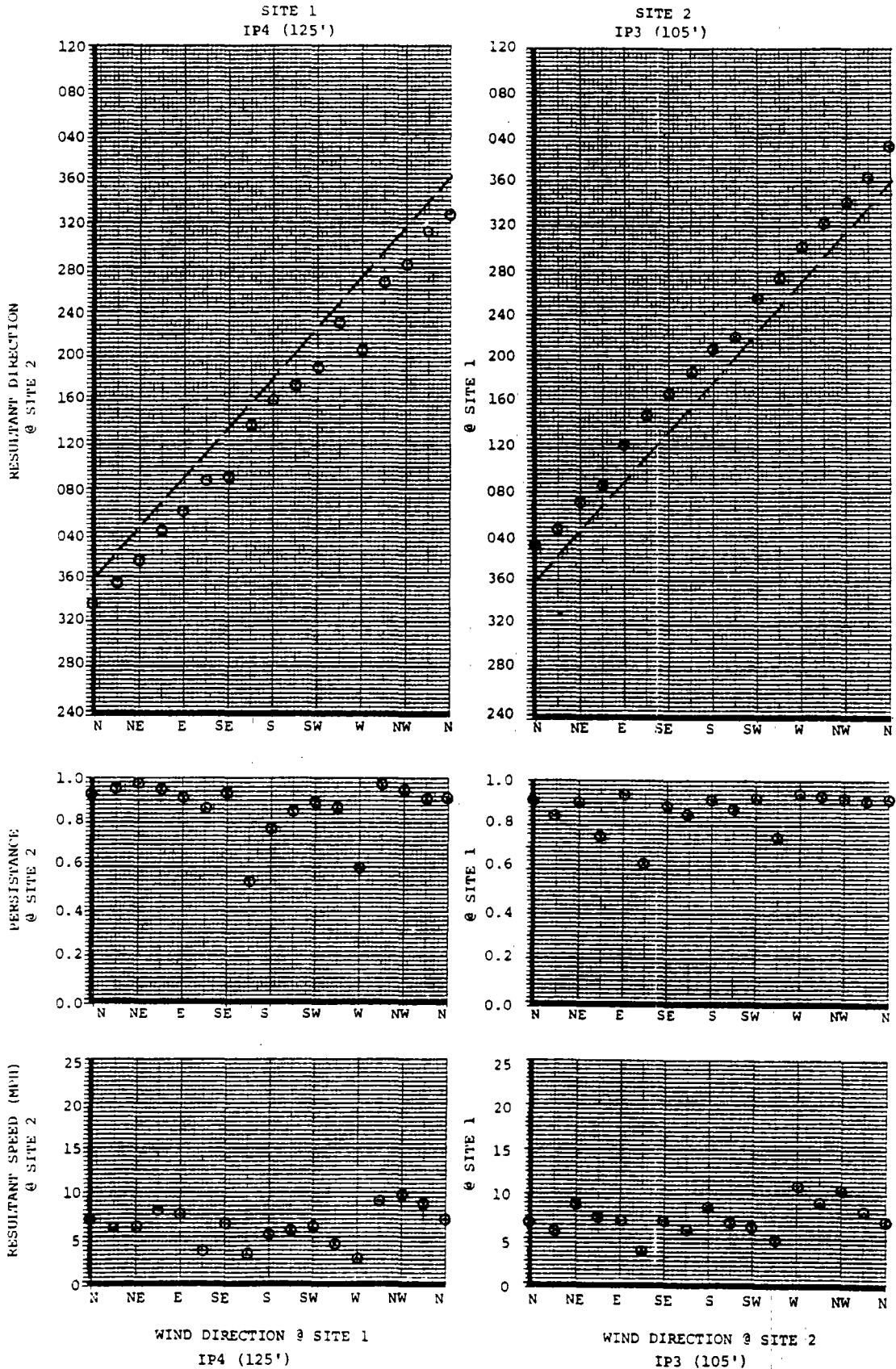


FIGURE 10B

TWO STATION WIND CORRELATION

DATA PERIOD
DECEMBER 1973

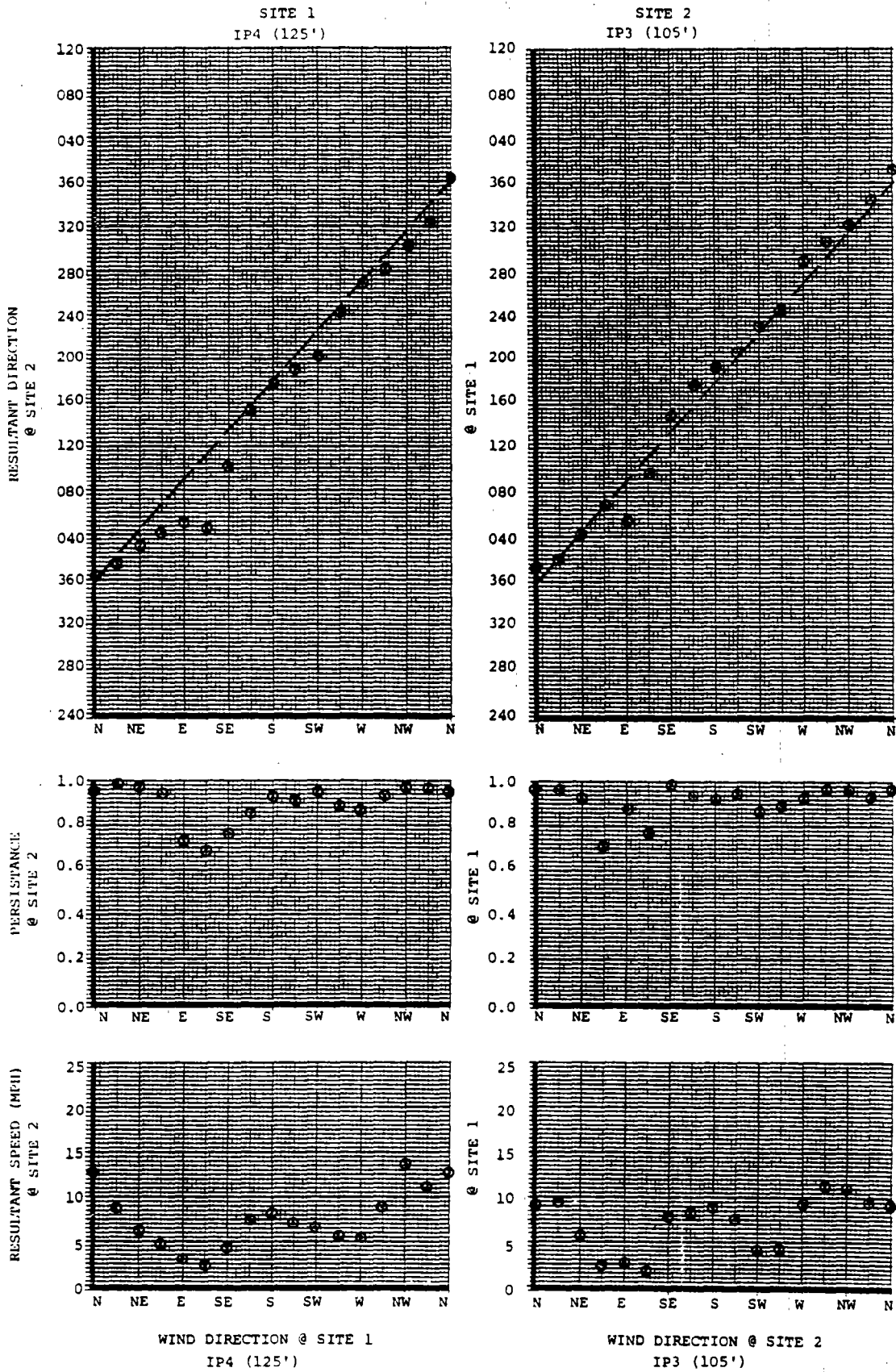


FIGURE 11
 POSITION OF ONE MILE GRID
 IN RELATION TO
 TOPOGRAPHIC FEATURES

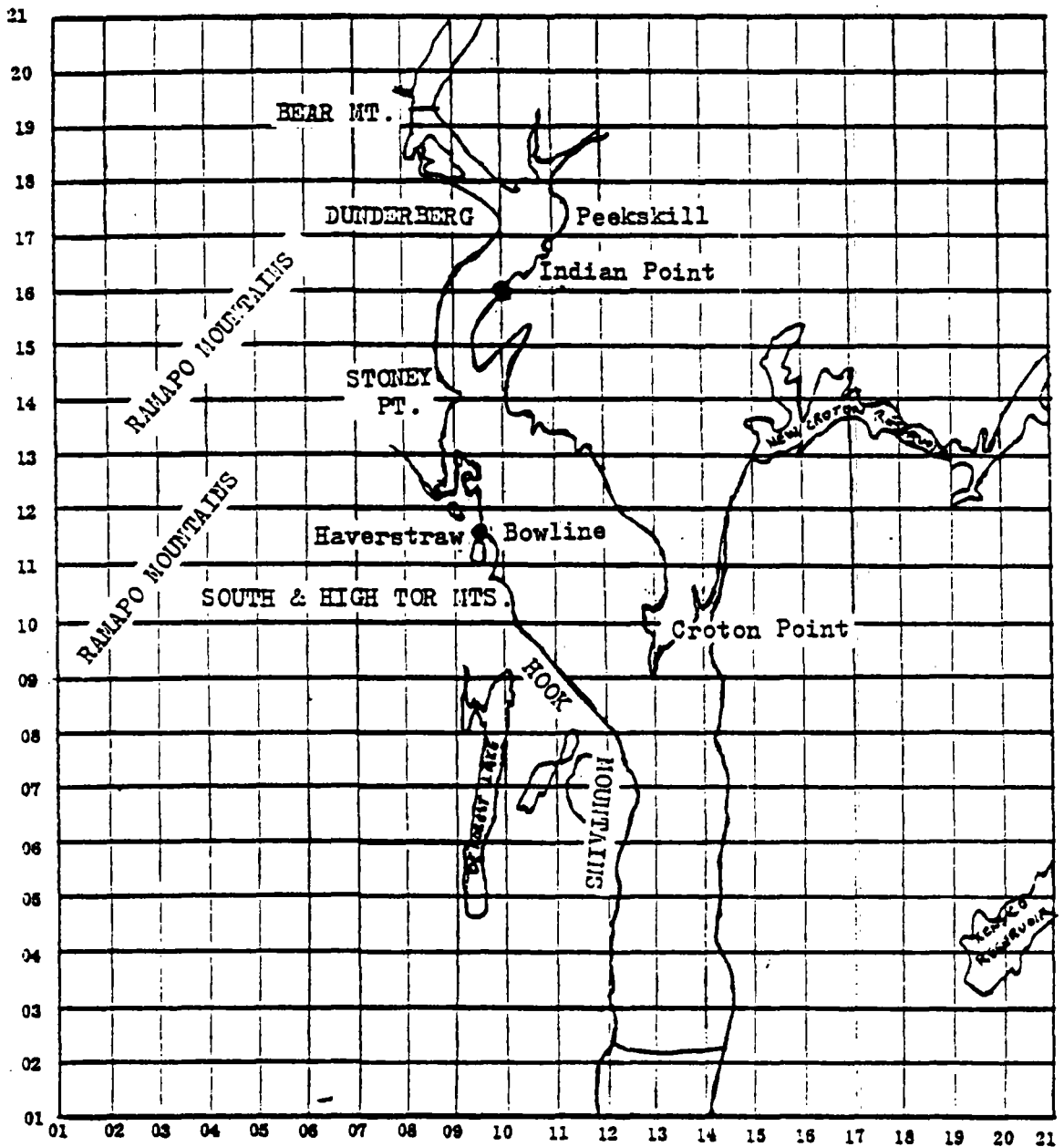


FIGURE 12
 POSITION OF WIND FILES ON GRID
 1: INDIAN POINT 2: BOWLINE POINT
 PATTERN 1

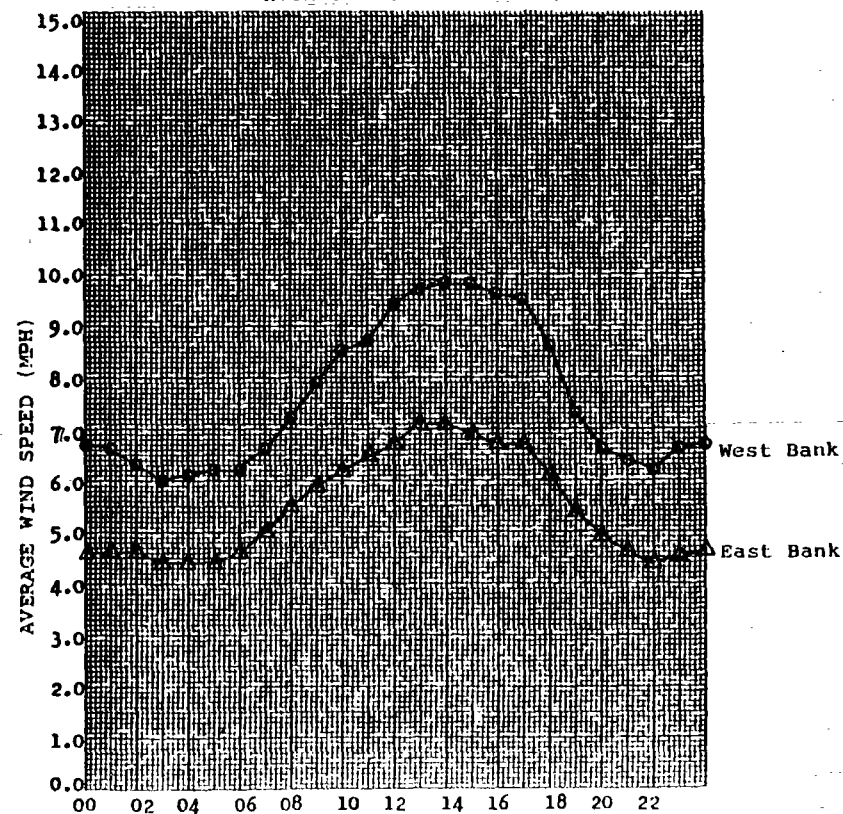
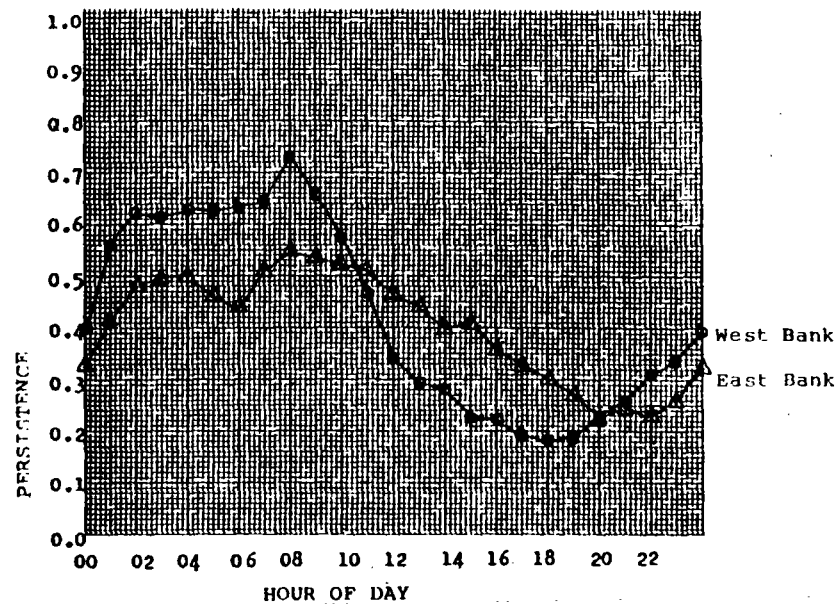
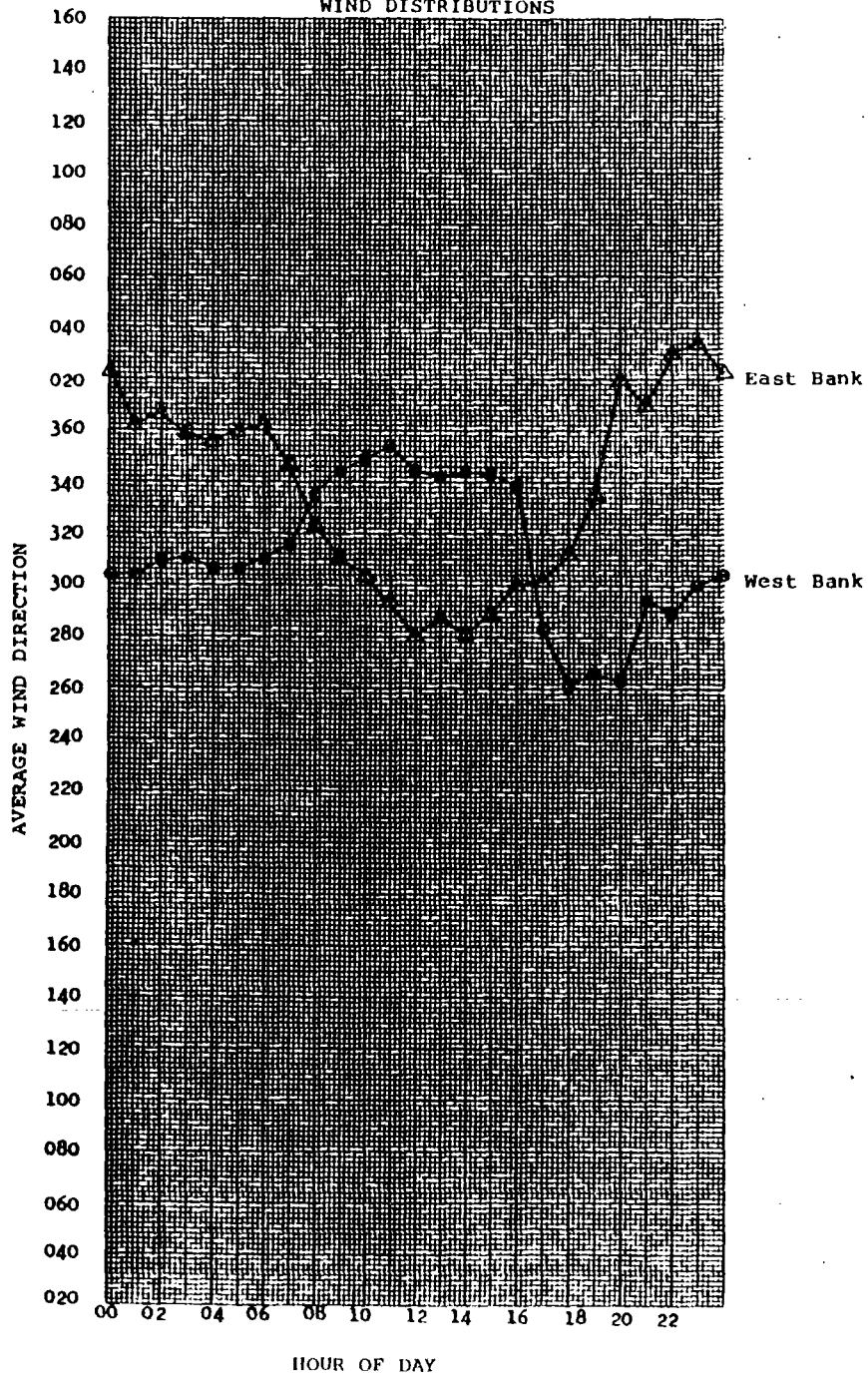
	1	2	3	4	5	6	7	8	9	10	11	12	13	14	15	16	17	18	19	20	21
21	1	1	1	1	1	1	1	1	1	1	1	1	1	1	1	1	1	1	1	1	1
20	1	1	1	1	1	1	1	1	1	1	1	1	1	1	1	1	1	1	1	1	1
19	1	1	1	1	1	1	1	1	1	1	1	1	1	1	1	1	1	1	1	1	1
18	1	1	1	1	1	1	1	1	1	1	1	1	1	1	1	1	1	1	1	1	1
17	1	1	1	1	1	1	1	1	1	1	1	1	1	1	1	1	1	1	1	1	1
16	1	1	1	1	1	1	1	1	1	1	1	1	1	1	1	1	1	1	1	1	1
15	1	1	1	1	1	1	1	1	1	1	1	1	1	1	1	1	1	1	1	1	1
14	1	1	1	1	1	1	1	1	1	1	1	1	1	1	1	1	1	1	1	1	1
13	2	2	2	2	2	2	2	2	2	2	2	1	1	1	1	1	1	1	1	1	1
12	2	2	2	2	2	2	2	2	2	2	2	2	1	1	1	1	1	1	1	1	1
11	2	2	2	2	2	2	2	2	2	2	2	2	2	2	1	1	1	1	1	1	1
10	2	2	2	2	2	2	2	2	2	2	2	2	2	2	2	2	2	2	2	2	2
9	2	2	2	2	2	2	2	2	2	2	2	2	2	2	2	2	2	2	2	2	2
8	2	2	2	2	2	2	2	2	2	2	2	2	2	2	2	2	2	2	2	2	2
7	2	2	2	2	2	2	2	2	2	2	2	2	2	2	2	2	2	2	2	2	2
6	2	2	2	2	2	2	2	2	2	2	2	2	2	2	2	2	2	2	2	2	2
5	2	2	2	2	2	2	2	2	2	2	2	2	2	2	2	2	2	2	2	2	2
4	2	2	2	2	2	2	2	2	2	2	2	2	2	2	2	2	2	2	2	2	2
3	2	2	2	2	2	2	2	2	2	2	2	2	2	2	2	2	2	2	2	2	2
2	2	2	2	2	2	2	2	2	2	2	2	2	2	2	2	2	2	2	2	2	2
1	2	2	2	2	2	2	2	2	2	2	2	2	2	2	2	2	2	2	2	2	2

PATTERN 2

	1	2	3	4	5	6	7	8	9	10	11	12	13	14	15	16	17	18	19	20	21
21	1	1	1	1	1	1	1	1	1	1	1	1	1	1	1	1	1	1	1	1	1
20	1	1	1	1	1	1	1	1	1	1	1	1	1	1	1	1	1	1	1	1	1
19	1	1	1	1	1	1	1	1	1	1	1	1	1	1	1	1	1	1	1	1	1
18	1	1	1	1	1	1	1	1	1	1	1	1	1	1	1	1	1	1	1	1	1
17	1	1	1	1	1	1	1	1	1	1	1	1	1	1	1	1	1	1	1	1	1
16	1	1	1	1	1	1	1	1	1	1	1	1	1	1	1	1	1	1	1	1	1
15	1	1	1	1	1	1	1	1	1	1	1	1	1	1	1	1	1	1	1	1	1
14	2	2	2	2	2	2	2	2	2	2	1	1	1	1	1	1	1	1	1	1	1
13	2	2	2	2	2	2	2	2	2	2	2	1	1	1	1	1	1	1	1	1	1
12	2	2	2	2	2	2	2	2	2	2	2	2	1	1	1	1	1	1	1	1	1
11	2	2	2	2	2	2	2	2	2	2	2	2	2	1	1	1	1	1	1	1	1
10	2	2	2	2	2	2	2	2	2	2	2	2	2	2	2	2	2	2	2	2	2
9	2	2	2	2	2	2	2	2	2	2	2	2	2	2	2	2	2	2	2	2	2
8	2	2	2	2	2	2	2	2	2	2	2	2	2	2	2	2	2	2	2	2	2
7	2	2	2	2	2	2	2	2	2	2	2	2	2	2	2	2	2	2	2	2	2
6	2	2	2	2	2	2	2	2	2	2	2	2	2	2	2	2	2	2	2	2	2
5	2	2	2	2	2	2	2	2	2	2	2	2	2	2	2	2	2	2	2	2	2
4	2	2	2	2	2	2	2	2	2	2	2	2	2	2	2	2	2	2	2	2	2
3	2	2	2	2	2	2	2	2	2	2	2	2	2	2	2	2	2	2	2	2	2
2	2	2	2	2	2	2	2	2	2	2	2	2	2	2	2	2	2	2	2	2	2
1	2	2	2	2	2	2	2	2	2	2	2	2	2	2	2	2	2	2	2	2	2

FIGURE 13

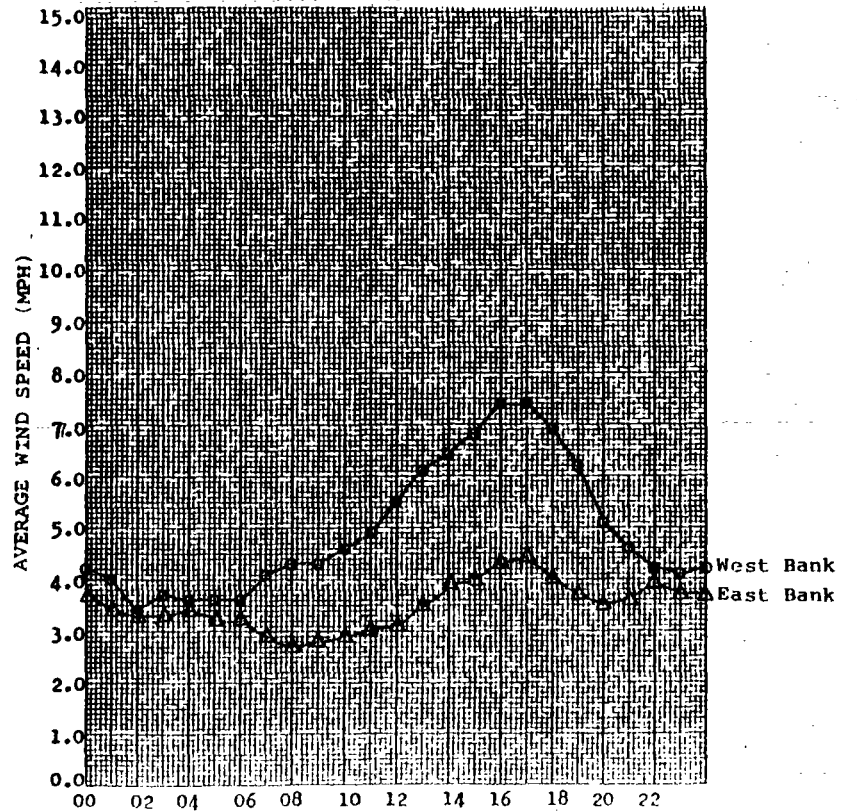
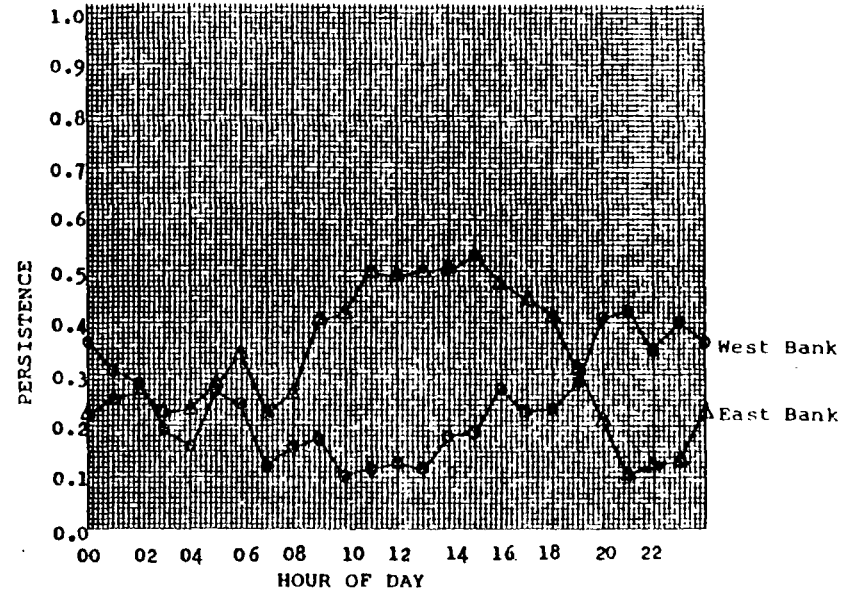
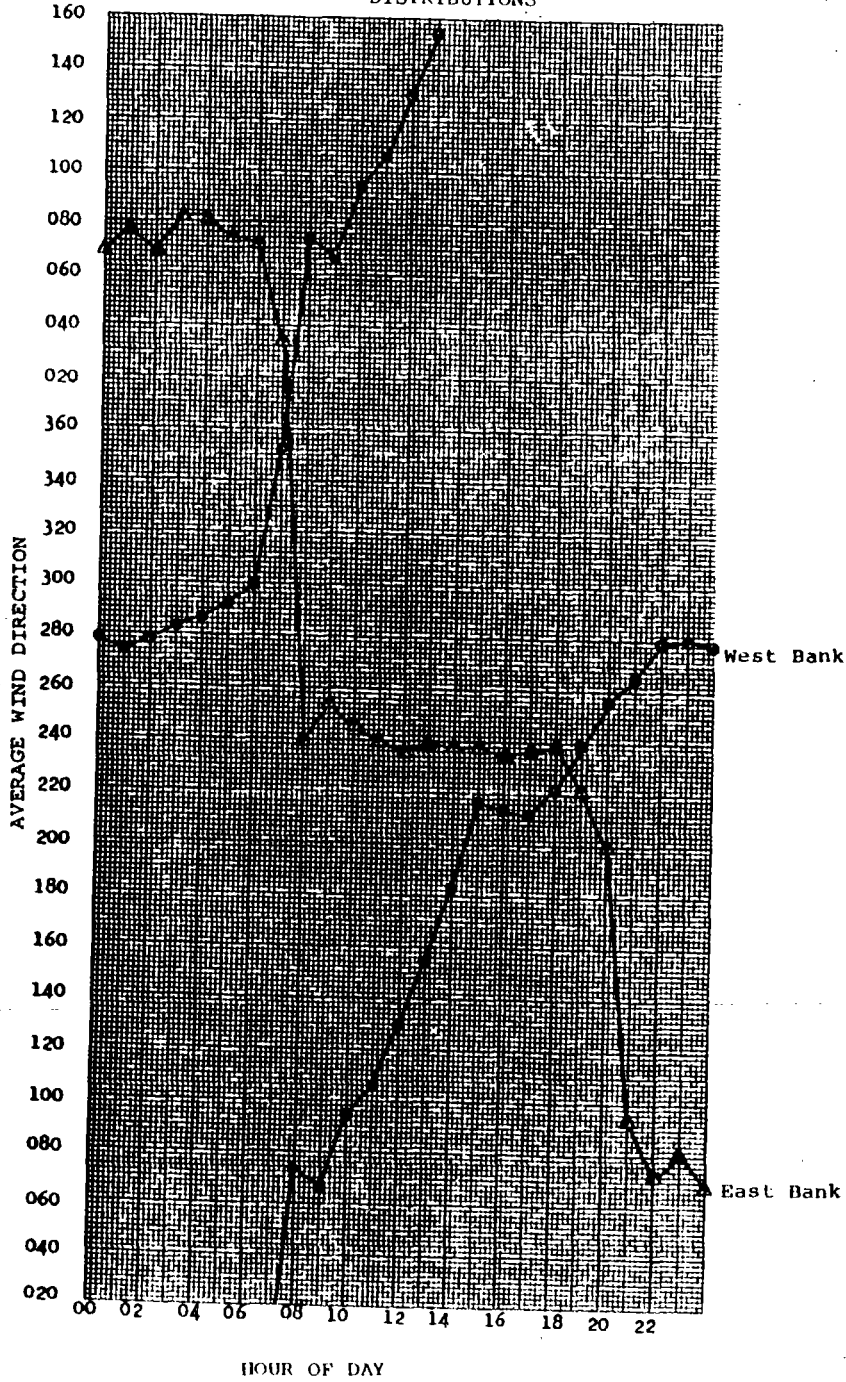
AVERAGE MARCH, 1980 EAST AND WEST BANK DIURNAL WIND DISTRIBUTIONS



OAG10000215_0239

FIGURE 14

AVERAGE JUNE, 1980 EAST AND WEST BANK DIURNAL WIND DISTRIBUTIONS



OAGI0000215_0240

FIGURE 15

AVERAGE DECEMBER, 1980 EAST AND WEST BANK DIURNAL WIND DISTRIBUTIONS

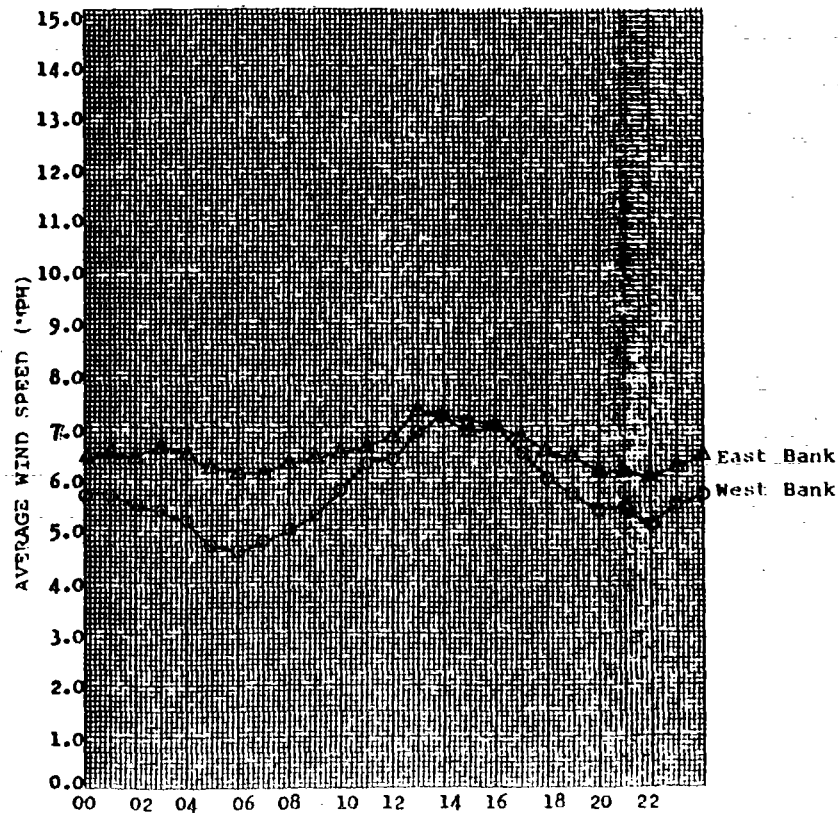
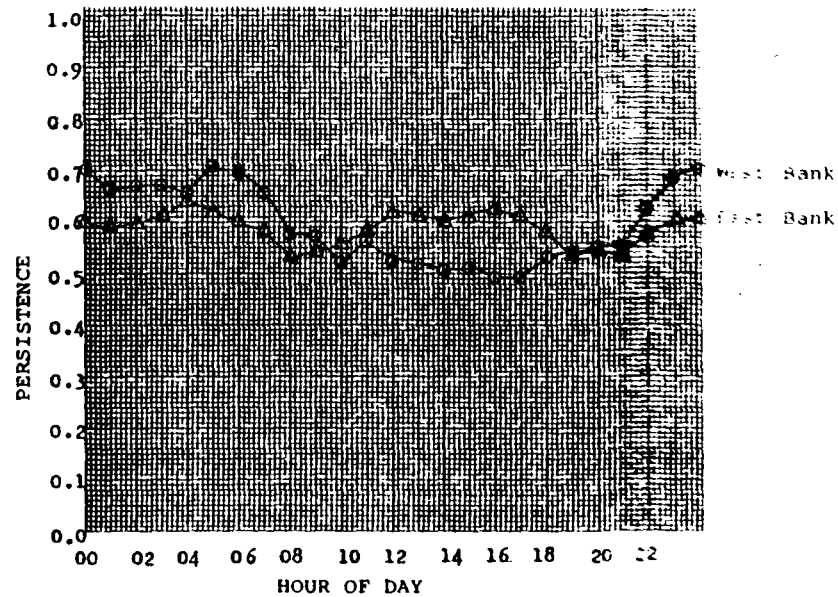
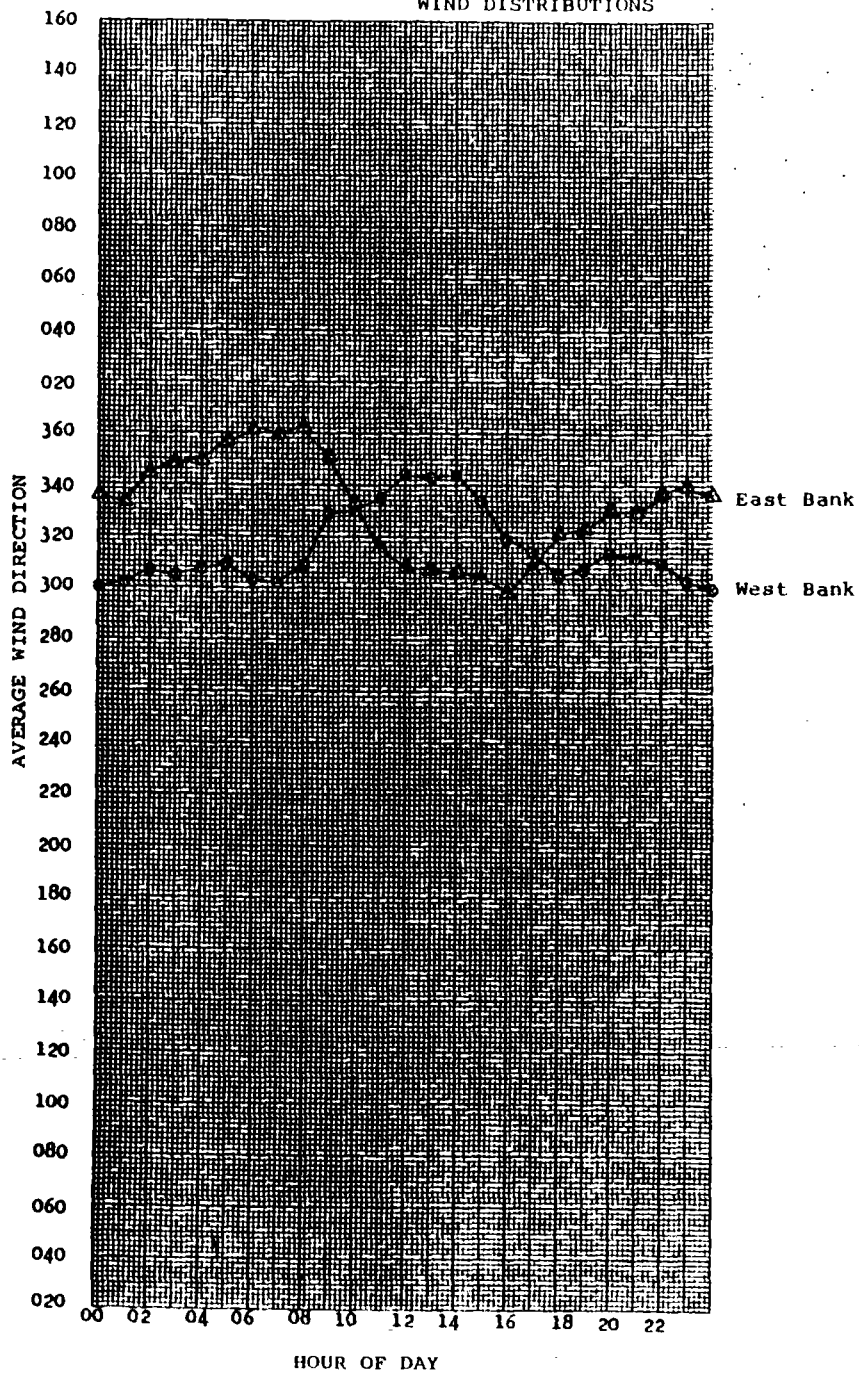
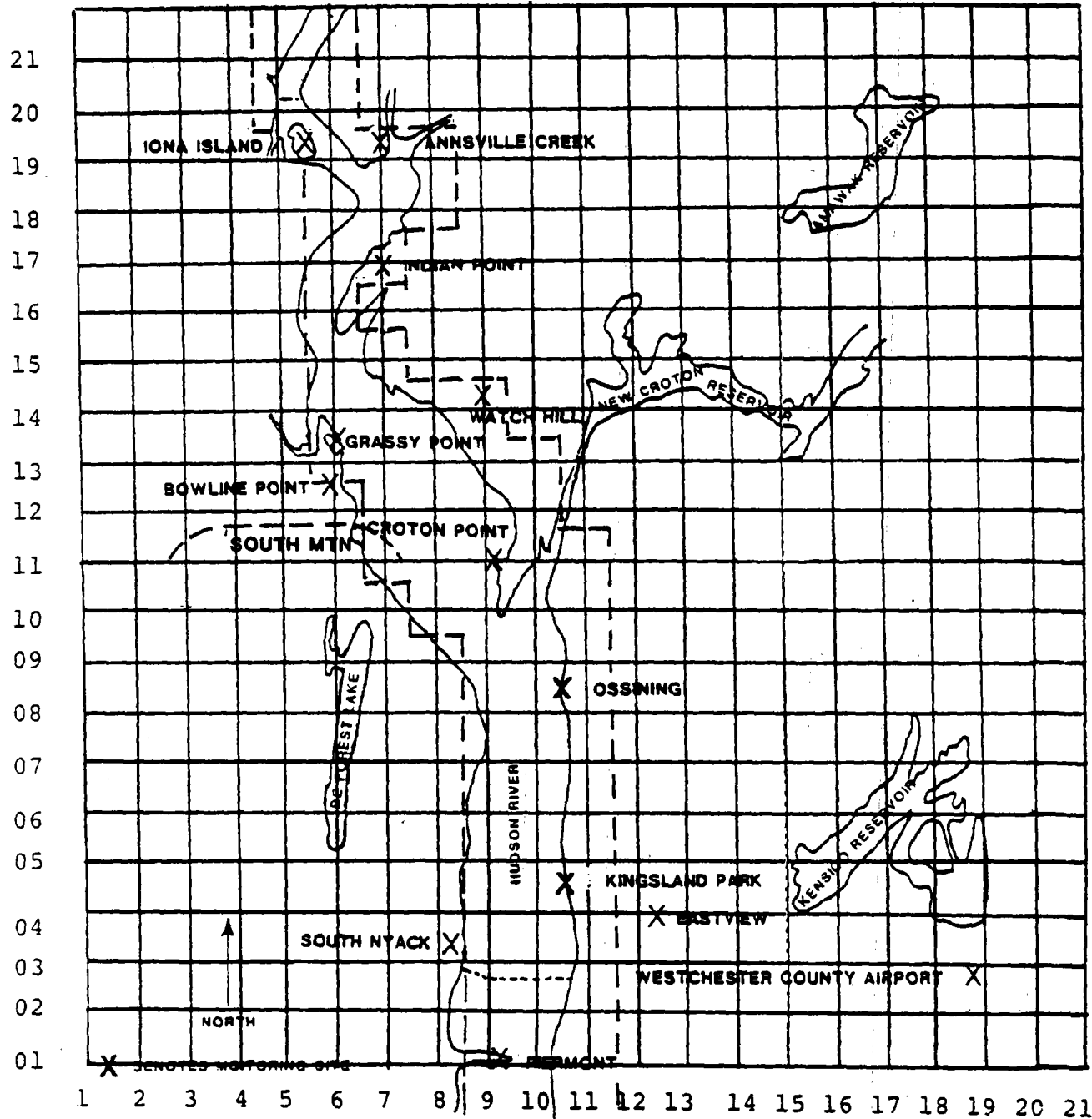


FIGURE 16

LOCATIONS OF MONITORING SITES IN RELATION TO ONE MILE GRID



Idealized
River Valley

FIGURE 17
 COMPARISON OF 10M LEVEL DIURNAL WIND DISTRIBUTIONS

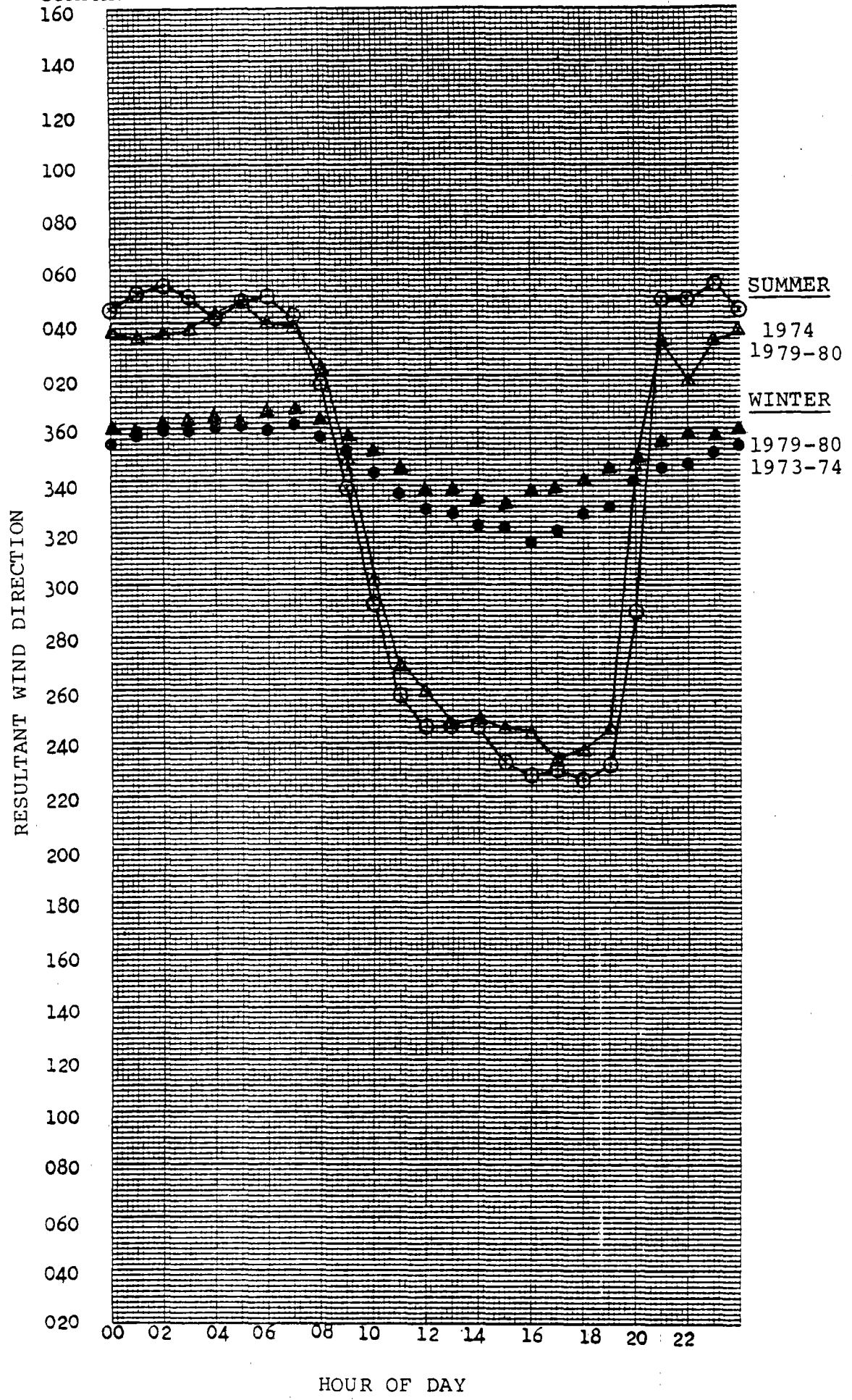


FIGURE 18
 COMPARISON OF 122M LEVEL DIURNAL AND WIND DISTRIBUTION

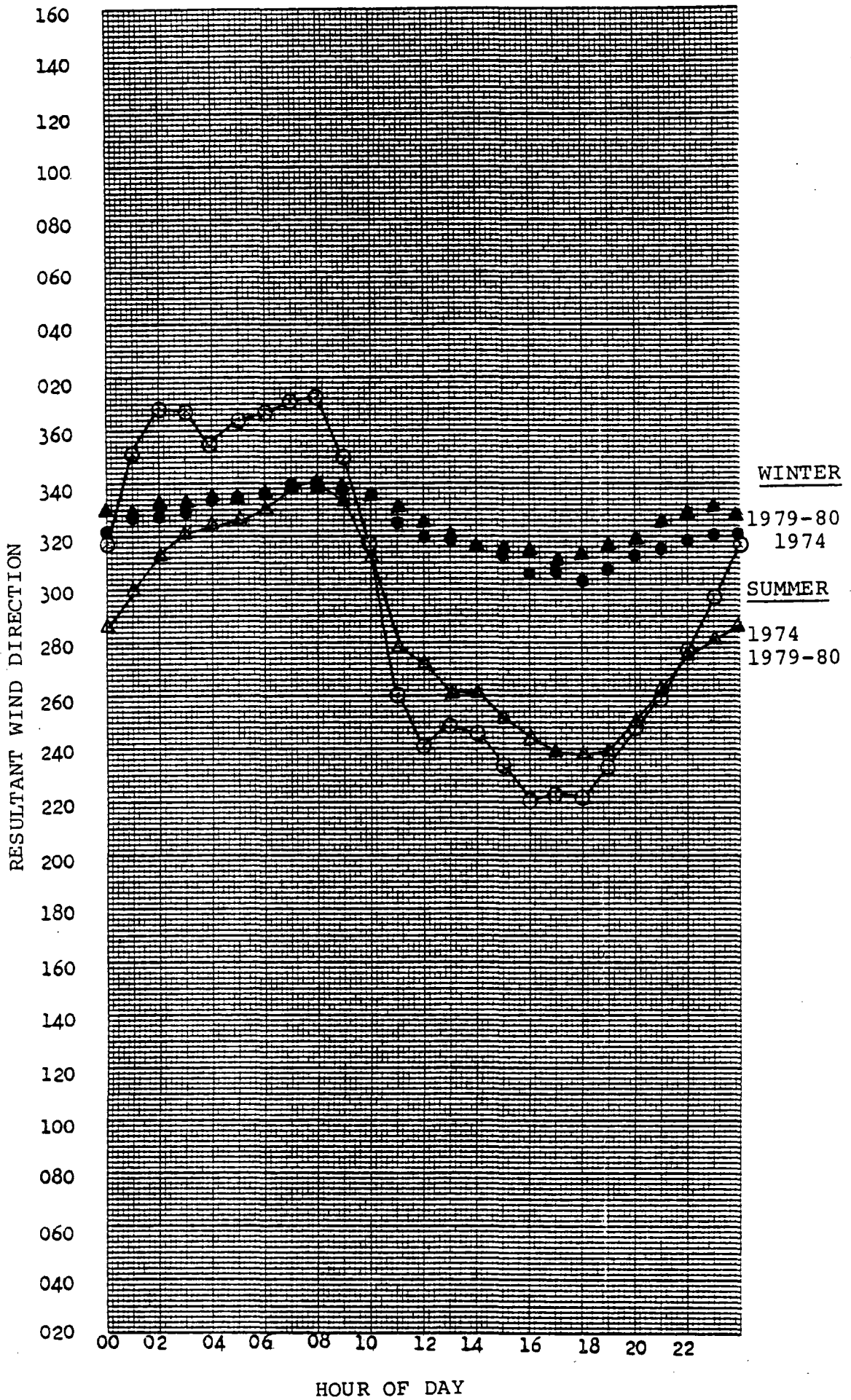


FIGURE 19

DIURNAL DISTRIBUTION OF WIND SPEEDS

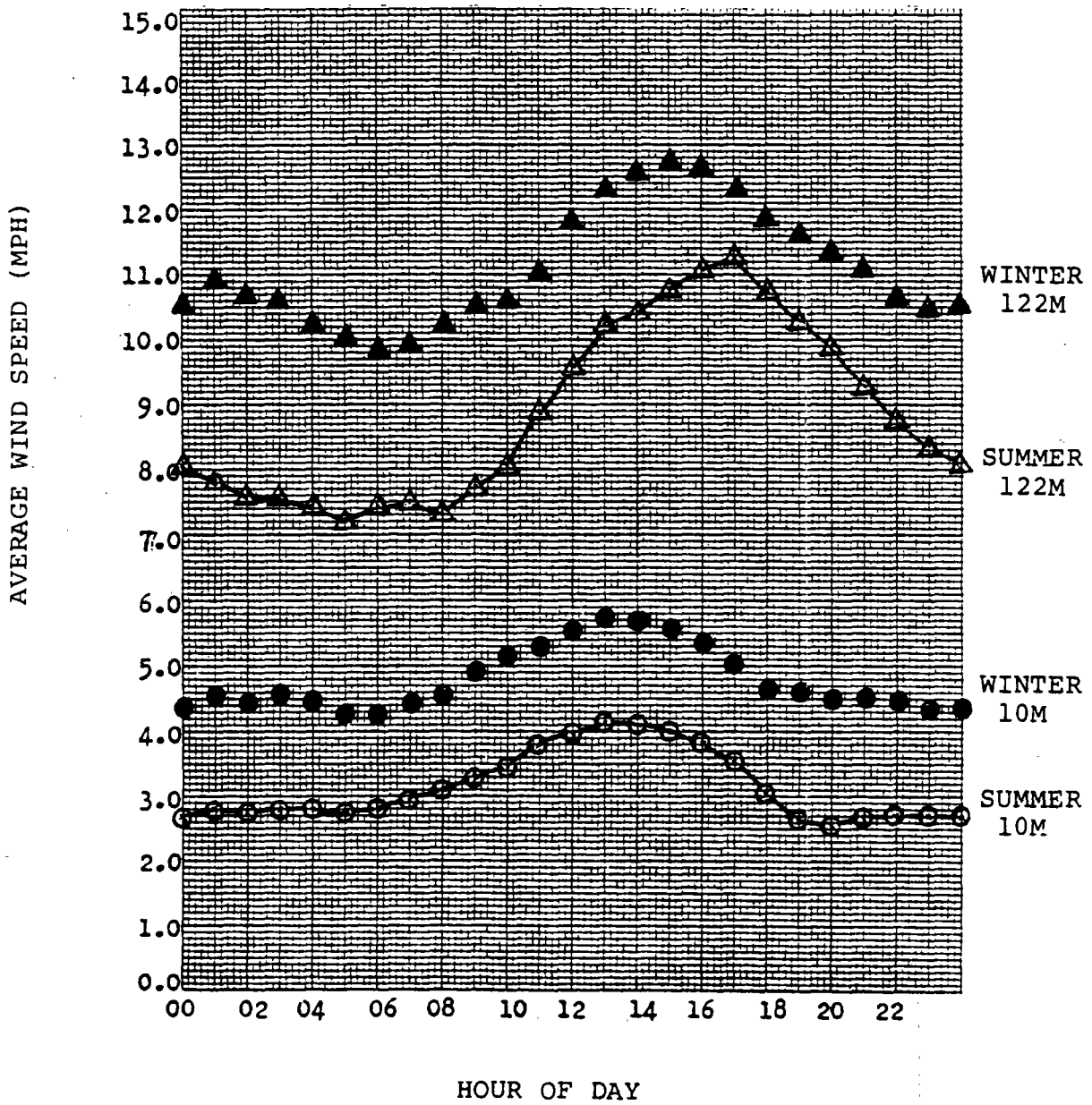
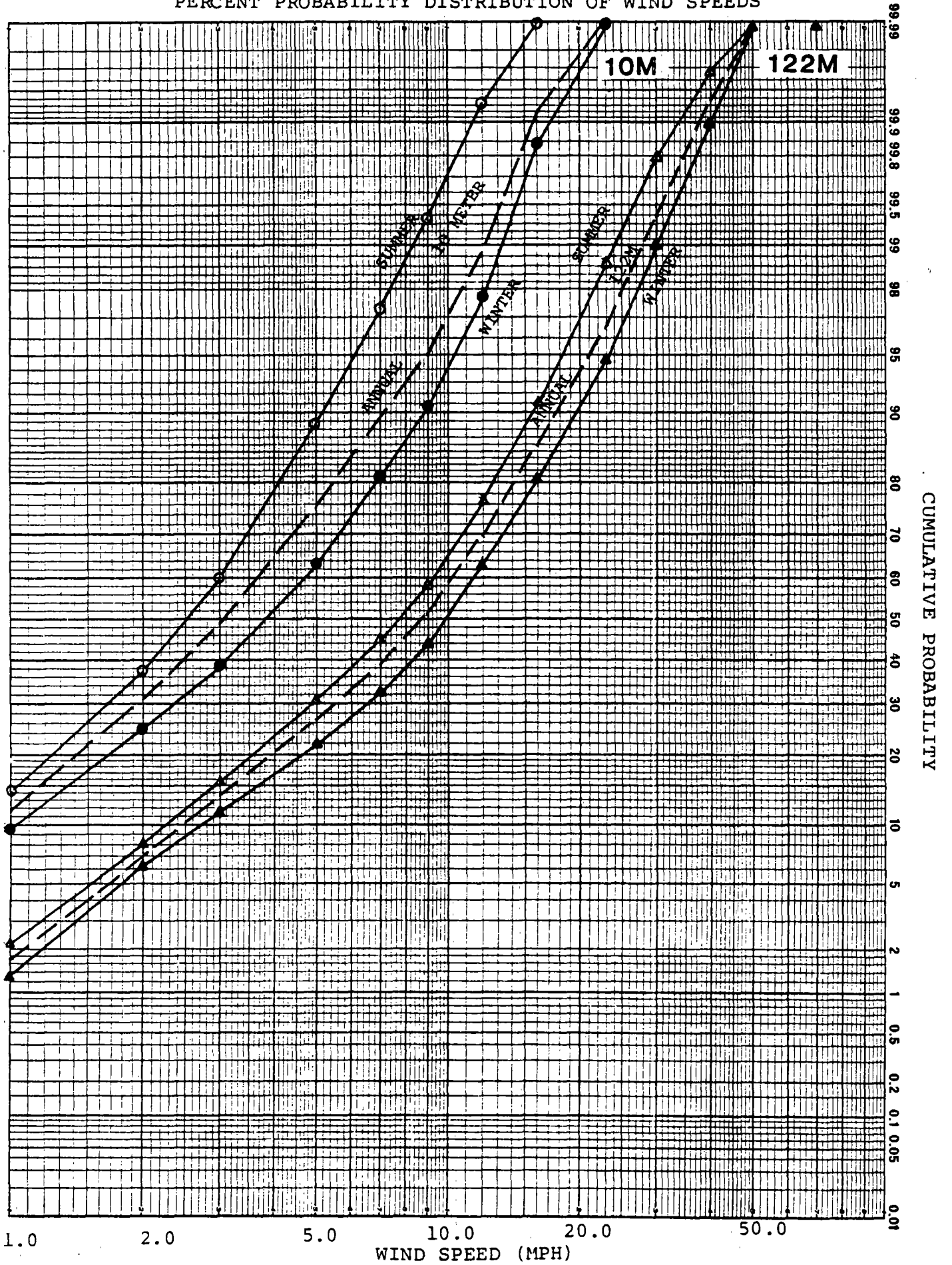
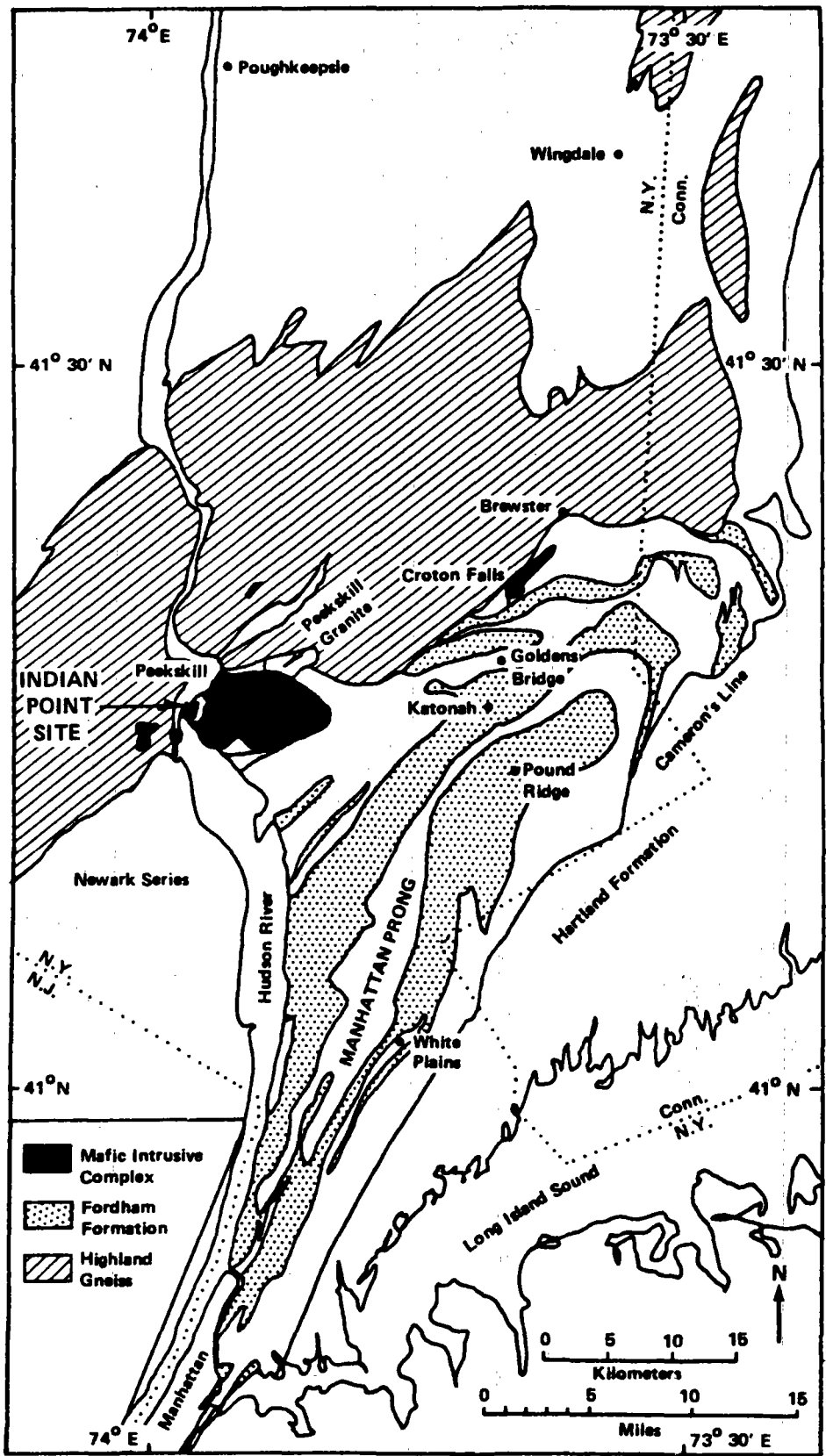


FIGURE 20

PERCENT PROBABILITY DISTRIBUTION OF WIND SPEEDS





GEOLOGIC MAP, SOUTHEASTERN NEW YORK
(AFTER BROCK & MOSE, 1979)

FIGURE 1

IP2
FSAR UPDATE

NOTE: This information is classified as Historical Information

APPENDIX 2B

INDIAN POINT FSAR
UPDATE

REVISED

Prepared for:

Consolidated Edison Company, Inc.
of New York
4 Irving Place
New York, NY 10003

Submitted by:

WOODWARD-CYCLE CONSULTANTS
201 Willowbrook Boulevard
Wayne, New Jersey 07470

16 April 1982

IP2
FSAR UPDATE

TABLE OF CONTENTS

	Page No.
INTRODUCTION	
Physiography	2.7A-1
General Geology and Tectonics	2.7A-2
Geology of the Hudson Highlands	2.7A-3
Geology of the Manhattan Prong	2.7A-4
The Geology of the Newark Basin	2.7A-7
History of Brittle Deformation	2.7A-8
Recent Seismicity	2.7A-12
CONCLUSION	2.7A-15
REFERENCES	R-1
GLOSSARY	G-1
TABLES	
Table 1 - Geologic Time Scale	
Table 2 - Stratigraphic Correlation Chart	
Table 3 - Geologic History in the Croton Falls Area	
FIGURES	
Figure 1 - Location Map	
Figure 2 - Seismotectonic Map	

IP2
FSAR UPDATE

INDIAN POINT FSAR
UPDATE

INTRODUCTION

This report is intended as an update and synthesis of previous geologic reports on the area surrounding Con-Edison's Indian Point nuclear facilities. The report reflects current thinking on the geology, structure, tectonic history, neotectonics and recent seismicity in the region. Main sources of information include Ratcliffe's (1976) final report on the Ramapo fault system, the Dames and Moore Geotechnical Investigation of the Ramapo Fault (1977), and the recent literature on the subject of the geology of the Manhattan and Reading Prongs.

Con Edison's Indian Point power plants are located in Buchanan, New York, on the east bank of the Hudson River. The site is situated in the central portion of the Peekskill Quadrangle.

Physiography

The rocks in the vicinity of the Indian Point generating stations belong to three geologic provinces, the Hudson Highlands, the Manhattan Prong and the Newark Basin (Figure 1). Rocks that outcrop within the provinces range in age from Precambrian through Triassic (Jurassic?).

The landscape consists of northeast trending ridges and rather broad swampy valleys. Ridges are supported by bedrock and tend to follow prominent generally northeast, structural trends. Valley walls tend to be steep, the result of modification by Pleistocene glaciation. Elevations in the area reach a maximum of 1000 feet, and range from 50 to 300 feet above sea level in low lying areas.

General Geology and Tectonics

The eastern third of the North American continent has been the site of episodic tectonism since Precambrian time (see Table1). Paleozoic aged tectonism has molded a broad geologically varying zone known as the Appalachian orogen. The core of the orogen is marked by intrusive rocks modified by ductile and brittle deformation and regional metamorphism. The Indian Point site lies within the Manhattan Prong of the Appalachian Mountains.

The earliest recognized event in the area occurred in Precambrian time, and is known as the Grenville Orogeny. The Grenville orogeny, dated at 1.1 b.y., produced brittle and ductile deformation accompanied by regional granulite facies metamorphism and intrusive activity. The deformation and metamorphism affected the rocks of the Reading Prong and the Precambrian rocks of the Manhattan Prong. The Grenville events are not tectonically or temporarily related to the development of the Appalachian Orogen, which began in the latest Precambrian.

The earliest tectonic activity in the Appalachian Orogen probably involved latest Precambrian continental rifting and associated intrusive activity. The opening of the Proto-Atlantic Ocean (Iapetus) set the stage for the development of the Appalachian geosyncline. The geosyncline received sediments from earliest Precambrian through the mid-Ordovician time. The Taconic orogeny occurred in Mid-Ordovician time, and resulted in extensive thrust faulting, folding, metamorphism and intrusion in the northern Appalachians. The Taconic orogeny, generally interpreted as a continent-island arc collision was very intense in

IP2
FSAR UPDATE

the Manhattan Prong region, and produced most of the structure evident in the current map pattern.

The Acadian orogeny (Devonian), possibly a continent-continent collision, was the next pulse of orogenic activity. The Acadian orogeny caused considerable deformation, metamorphism and intrusion in New England, but was not as intense as the Taconic orogeny in the Manhattan Prong.

The rocks of the Hudson Highlands (see Figure 1), an extension of the Reading Prong in New York State, consist of Precambrian gneisses and granites of Grenville (1.1 b.y.) age. The Manhattan Prong is underlain by Precambrian basement. An unconformity separates Cambro-Ordovician aged metasedimentary rocks from Precambrian rocks. The Newark Basin is filled with Triassic (Jurassic?) arkosic sediments diabase intrusives and basaltic flows.

Geology of the Hudson Highlands

The Hudson Highlands outcrop in a northeast (040°) trending belt, approximately 10-miles wide, north, northwest and west of the Indian Point site (Figure 1). Four major rock types are present in the vicinity of Dunderburg Mountain, across the Hudson River from Indian Point. They are quartzo-feldspathic ± calc-silicate hornblende gneiss; migmatitic quartzo-feldspathic biotite ± garnet gneiss; calc-silicate bearing quartzite; and gneissic hornblende granite. Granite probably intruded the gneisses during Precambrian time.

Heleneck and Mose (1978) mapping in Highlands rocks near Lake Carmel, New York, recognize a mappable sequence of five rock units consisting of, gray migmatitic quartzo-feldspathic gneiss; amphibolite hornblende gneiss; leuco-granite gneiss and amphibolite; layered quartzo-feldspathic gneiss; and interlayered feldspathic quartzite and amphibolite. Highland rocks represent a sequence of Precambrian aged mio- and eugeosynclinal deposits, that have undergone a complex sequence of metamorphism and deformation. The rocks typically yield Rb/Sr ages of 1.1 billion years, the time of Grenville regional metamorphism. Mineralogic and textural evidence indicates that the rocks were metamorphosed to granulite facies, and multiply deformed during the Grenville orogeny. Recrystallization from granulite to amphibolite facies in Highland rocks near Lake Carmel accompanied folding during the Taconic orogeny (mid-Ordovician). Evidence of Taconic recrystallization in other areas of the Highlands remains equivocal. The Highlands are separated from the rocks of the Manhattan Prong and the Newark Basin by a complex fault system known as the Ramapo Fault Zone.

Geology of the Manhattan Prong

The Manhattan Prong is a sequence of highly deformed metamorphic rocks, trending north-northeast, from New York City through Westchester County and western Fairfield County, Connecticut. The prong is bounded on the east by Cameron's Line, a complicated structure possibly representing a suture between two crustal blocks. On the west, the prong is bounded by the Newark Basin border fault and the Hudson River.

The stratigraphy of the Manhattan Prong has long been the subject of controversy and frequent revision, however, most recent workers recognize five formations within the prong. In order of decreasing age they are the Fordham Gneiss, the Yonkers-Pound Ridge Granite, the Lowerre Quartzite, the Inwood Marble and the Manhattan Schist (see Table 2). The Fordham and Yonkers formations are Precambrian in age, and are separated from the Cambro-Ordovician aged Lowerre, Inwood and Manhattan formations by an angular

IP2
FSAR UPDATE

unconformity. The relative ages of the Fordham and Yonkers formations are not known with absolute certainty. The Fordham is generally considered at least Grenville in age, and the Yonkers latest Precambrian.

Hall's (1968) detailed subdivision of the rocks of the Manhattan Prong near White Plains, New York, served as a basis for more recent workers. Correlations of the White Plains stratigraphy to other parts of the prong are tenuous due to the complex structural and metamorphic history of the area. Difficulties in correlation are compounded by the possibility of changes in original sedimentary facies.

The Fordham was divided into five members by Hall. They are:

Fordham A - Brown weathering garnet biotite quartzo-feldspathic gneiss.

Fordham B - Gray garnet biotite quartz feldspar gneiss interlayered with amphibolite.

Fordham C - Gray biotite hornblende quartzo-feldspathic gneiss with some amphibolite.

Fordham D - Rusty weathering sillimanite-garnet biotite quartzo-feldspathic gneiss.

Fordham E - Siliceous biotite-quartz plagioclase gneiss.

Most of the Fordham rocks probably represent metamorphosed eugeosynclinal deposits, interbedded with mafic volcanics. The Fordham formation was deformed and metamorphosed to granulite facies during the Grenville orogeny. Mineralogic and structural evidence indicates that the Fordham was recrystallized and deformed during Paleozoic orogenesis.

The Yonkers Granite is thought to represent a metamorphosed rhyolite, emplaced during the opening of the Proto-Atlantic in late Precambrian time.

The assignment of formation status to the Lowerre, has been the subject of debate for nearly 100 years. It was first named and described by Merrill in 1896, but many workers in the 20th century preferred to consider the Lowerre as part of the Fordham. In addition, the unconformity between the Cambro-Ordovician rocks and the Fordham, has not been recognized by all workers in the prong. The Lowerre is a relatively thin (40-ft. thickness), discontinuous unit representing an arkosic sandstone. The discontinuity of the unit is probably the result of deposition on an irregular Precambrian aged erosional surface. The Lowerre consists of quartz, with considerable amounts of potassium feldspar and minor biotite. The Lowerre is always observed in the same stratigraphic position, at the base of the Cambro-Ordovician aged cover rocks, overlying and truncating various members of the Fordham.

The Inwood Marble, consisting of dolomite and calcite marble interlayered with calc-silicate schists, overlies the Lowerre. Hall has divided the Inwood into five members, that lens in and out. In map pattern, the Inwood does not appear to be continuous, the result of tectonic thinning of fairly ductile marble during deformation. The Inwood represents deposition on a carbonate bank, widespread in the Appalachian orogen during the late Cambrian and early Ordovician.

IP2
FSAR UPDATE

In the White Plains area, Hall recognizes three mappable members of the Manhattan, 'A', 'B', and 'C' (see Table 2). Manhattan 'A' (basal Manhattan) is a fissile sillimanite garnet biotite schist, interlayered with marble and calc-silicate schist. The Manhattan 'A' may be a transitional facies between carbonate and clastic sedimentation. It is recognized by Ratcliffe (1976) near the Cortlandt complex, and by Brock (1977) north of White Plains. Manhattan 'B' is a discontinuous amphibolite and Manhattan 'C' is a brown weathering, garnet muscovite biotite schistose gneiss. The Manhattan Formation was originally deposited in a miogeosyncline, and represents pelites, mafic volcanics and greywackes. The Manhattan Prong was metamorphosed, deformed and intruded during two major orogenic episodes, the Taconic (late Ordovician) and the Acadian (Devonian). A late Acadian metamorphic and deformational event can be recognized in some locations within the prong (Brock and Mose 1979). Mose and Hall (1979) infer a mid-Ordovician unconformity within the New York City group based on structural and isotopic evidence.

Brock (1977) has worked out a detailed sequence of events for the Manhattan Prong near Croton Falls, New York (see Table 3). The rocks of the prong were metamorphosed to K-feldspar sillimanite grade (upper amphibolite facies) at the peak of the Taconic orogeny. At this time the rocks underwent intense deformation, reflecting the effects of four distinct fold events during the orogeny. Taconic aged recrystallization affected the Precambrian rocks of the Manhattan Prong, destroying most Grenville aged metamorphic and structural features. Granulite facies mineralogy and textures survive as relicts within the Fordham, but are not present in the Cambro-Ordovician rocks, supporting the inferred unconformity between Fordham and younger rocks.

During Silurian time, deformation eased, but the prong was intruded by the Croton Falls and Cortlandt mafic complexes. The Acadian orogeny (Devonian) produced another set of folds (F_5), metamorphism of kyanite-staurolite (mid-amphibolite facies) grade, and the intrusion of the Peekskill Granite. The "final" Paleozoic metamorphic and deformational event occurred late in the Acadian Orogeny or during the Mississippian, causing local retrograde metamorphism (muscovite grade) and folding (F_6) (Brock, 1977). The "final" orogenic event is seen locally as tight isoclinal folds. Late metamorphism is evidenced by recrystallization on undeformed joint faces.

The ductile deformation occurred coevally with brittle deformation along the border fault and within the Manhattan Prong. The relationship of Precambrian, Paleozoic and post Paleozoic aged faulting will be discussed in a following section.

One of the significant problems involving rocks of the Manhattan Prong is correlation on a regional scale (see Table 2). The Fordham Formation is often correlated with the Precambrian Highlands gneisses. Some workers have tried tracing the Highlands across the boundary fault, comparing structure and metamorphic details with Fordham rocks. Correlation is tenuous since the Grenville age yielded by the Highlands and Fordham rocks, is a metamorphic age, not a time of deposition. Correlation of the rest of the New York City Group with rocks of the surrounding region is based on similarities in lithology, structural position, radiometric age determinations and fossil evidence. The Lowerre is considered the metamorphosed equivalent of the Poughquag Sandstone. The Inwood is correlated with the Wappinger Limestone Group, and the Manhattan with the Annsville Phyllite and Hudson River Shale. Metamorphism increases from chlorite grade near the Hudson River, to K-feldspar-sillimanite grade near the Connecticut border.

The Geology of the Newark Basin

IP2
FSAR UPDATE

The third geologic province in the area is the Newark-Gettysburg Basin. The basin extends 140-miles from York County, Pennsylvania, to Rockland County, New York (Figure 1). The basin, a down dropped crustal block, formed during Mesozoic time. Deposition was continuous from the late triassic through the upper Jurassic (Dames and Moore, 1977). Intrusion of the Palisades sill apparently occurred during deposition of sediments in latest Triassic-earliest Jurassic. The extrusion of the Watchung basalt flows followed later in the Jurassic. Rocks of the Newark series are in contact with the crystalline rocks of both the Manhattan and Reading Prongs, but the nature of the contact varies. At the northeastern edge of the basin, Triassic sediments unconformably lie over the Highland rocks, while the northeastern edge of the basin is in fault with the rocks of the Highlands.

The Newark Group is divided into four formations, the Hammer Creek Conglomerate, the Stockton Arkose, the Lockatong Argillite, and the Brunswick Shale and Sandstone. Deposits of conglomerate and sedimentary breccia lie at the edges of the basin, reflecting proximity to the uplifted Precambrian and Paleozoic rocks that are the sources of the Triassic aged sediments.

The boundary fault between the Newark series and older crystalline rocks is the Ramapo fault. Movement along the fault and subsidence of the basin, concurrent with sedimentation, produced the half-graben configuration of the basin. The rocks within the basin are not greatly deformed, displaying broad open folds of uncertain origin, gentle dips of strata, and minor faults with small offsets.

History of Brittle Deformation

A series of north-northeast trending faults pass through the area surrounding the Indian Point sites. The faults, some of which have been episodically active since the Precambrian time are collectively known as the Ramapo fault system. The system is composed of a number of parallel to sub-parallel branches and draws its name from the Ramapo fault, the boundary between the Reading Prong and the Newark Basin.

Ratcliffe (1976) mapped the faults in the vicinity of the Indian Point site, and interpreted a chronologic sequence of fault movements. Ratcliffe classified faults utilizing radiometric ages, cross-cutting lithologic relationships, and textural evidence. Dames and Moore (1977) utilize Ratcliffe's conclusions, and present evidence for timing fault movements based on geothermometry of fluid inclusions in calcite. More recently, Nelson (1980) and others have examined the stratigraphy and pollen remains in swamps and sag ponds along the Ramapo, seeking evidence of Post-Pleistocene faulting in the area. In addition, Aggarwal and Sykes (1978), Yang and Aggarwal (1981) Dames and Moore (1977), and Woodward-Cyldle Consultants (Quarterly Reports, Jan 1977 - Jan 1982) have studied the recent seismicity in the region, solving for magnitude and location of earthquake epicenters.

The earliest documented movement along the Ramapo fault system is Grenville age (Ratcliffe 1976). Textural evidence seen in the Canopus Pluton indicates that movement along the Canopus Hollow fault (north of Peekskill) was synchronous with emplacement of the pluton. Flow structures and mylonitization displayed within the pluton indicate crystallization during shearing. Drag folds and the overall shape of the pluton suggest right lateral strike-slip motion. The Canopus Pluton, a diorite-monzontie, has been radiometrically dated at 1150 m.y. (Rb/Sr), thus providing a minimum age for movement along the fault.

The Lake Peekskill fault is defined by a shear zone in the Precambrian gneisses that has not affected the Annsville Phyllite (Ordovician). The fact that the Annsville has not been

IP2
FSAR UPDATE

deformed, places a limit on the last motion along the fault. Ratcliffe (1976) states that both the Canopus Hollow and Lake Peekskill faults were not reactivated during Paleozoic time, however, in a more recent article (Ratcliffe 1980) he suggests that movement as recent as Triassic has taken place within the Canopus Fault Zone.

Dames and Moore (1977) disagree with Ratcliffe's 1976 opinion, citing as evidence a sheared inlier of Poughquag Quartzite near Canopus Lake. The shear zone is considered by Dames and Moore to reflect thrust faulting along a northeast trending fault, sub-parallel to the Canopus Hollow fault. This implies post-Precambrian reactivation along the Canopus Hollow Fault. An additional strike-slip shear zone was mapped by Dames and Moore in Highland rocks, near the southwest corner of Canopus Lake, along the strike of the Canopus Hollow fault. This shear is considered additional evidence for reactivation of the Canopus Hollow fault in Paleozoic time. It is important to note that local activity occurring along part of a fault does not require movement along the entire length of a fault. Furthermore, the shear zone that displaces the Poughquag is not necessarily an extension of the Canopus shear zone, and may in fact be related to Paleozoic aged folding. Thus, Paleozoic aged movement along the Canopus Hollow fault is not required in the vicinity of Indian Point.

A number of faults of Paleozoic age separate the Manhattan Prong from the Hudson Highlands. Most prominent are the Thiells fault, the Annsville fault, the Peekskill fault and the Croton Falls fault. The Peekskill and Croton Falls faults outcrop on the east bank of the Hudson River, and generally trend east-west. The Thiells fault, outcropping on the west bank of the Hudson, and the Annsville fault on the east bank trend northeast. The Ramapo fault extends northeast from Peapack, New Jersey separating the Newark Basin from the Reading Prong. At Ladentown, it splays into two branches, trending 020° and 060°, respectively. The 060° branch connects with the Thiells fault, and the more northerly trending branch extends into the Highlands, through Tomkins Cove, New York.

The Peekskill, Croton Falls, Thiells and Annsville faults are primarily Paleozoic in age. The faults are marked by mylonite and ultra-mylonite, displaying retrograde chlorite grade, green schist facies mineral assemblages. Movement along the faults is generally right-lateral-strike-slip. Mid-Ordovician minimum ages of movement are inferred from cross-cutting relationships with dikes related to the Rosetown Pluton (mid-Ordovician), and radiometric ages of undeformed biotites from within shear zones (Ratcliffe, 1976). A lower Devonian K-Ar age of 396 m.y. places the most recent probable movement along the Roa Hook branch of the fault squarely within the Acadian orogeny. Similar data is available for the Thiells fault.

Younger faults can be distinguished from Paleozoic aged and older faults (Ratcliffe, 1980) by their different mineralization, and cataclastic textures. Younger faults are characterized by open work breccias, clay gouge, platy fracture and deeply incised fault scarps. Older faults display healed breccia, semi-ductile mylonite shear zones, and higher temperature minerals that reflect the general pattern of Paleozoic aged regional metamorphism.

Reactivation and development of new faults occurred during Mesozoic time (Ratcliffe, 1980). Deep seated zones of weakness in crystalline basement were utilized in the development of the Triassic basin, particularly the Ramapo-Cheesecote and Mott Farm Road faults (Ratcliffe, 1976). Structural evidence indicates that normal faulting was dominant during mesozoic time, with the latest activity along the Mott Farm Road branch of the Ramapo, dated at 163 m.y. by K-Ar methods (Ratcliffe, 1976). Late north-south vertical strike-slip faults with both left-lateral and right-lateral movements are present in the vicinity of Indian Point. The relationship of these faults to the Ramapo is uncertain, although the faults are probably Mesozoic in age (Ratcliffe, 1976; Dames & Moore, 1977).

IP2
FSAR UPDATE

Detailed work (Ratcliffe, 1976) shows that north-south faults at Tomkins Cove across the river from Indian Point are the youngest in the area. Mineralogy and textures found in the young, Tomkins Cove faults bear a strong resemblance to faults that have been radiometrically dated as Mesozoic. In addition, the time of last movement along the faults is constrained by the lack of fault related deformation in overlying Pleistocene sediments (Ratcliffe, 1976, 1980; Dames and Moore, 1977). A group of faults located at the Indian Point site was mapped in detail by Dames and Moore (1977). Displacement along the faults is not significant, no more than a few feet. The faults are filled with undeformed euhedral calcite crystals, many of which contain fluid inclusions. Temperature equilibrium studies on the fluid inclusions indicate average formation temperatures of 160°C. Dames and Moore (1978), infer a depth of formation, by applying the geologically conservative geothermal gradient of 50°C/km. This yields a temperature of 150°C at 3 km.

The amount of time necessary to expose rocks that form at a depth of 3 km is a function of denudation rates. A minimum of 45 m.y. is required to remove 3 km of material, if the rather rapid denudation rate of 15,000 yrs/meter is applied (Dames and Moore, 1978). This calculation sets another constraint on the possible minimum age of last movement on the faults. The growth of calcite in the fault zones has been attributed to circulating hydrothermal fluids related to Mesozoic igneous activity (Dames and Moore, 1978), suggesting a time of last movement in the Mesozoic.

Radiometric age determination of undeformed minerals that have grown within fault zones (Ratcliffe, 1976) and the lack of fault related deformation of Pleistocene deposits and surface features (Dames and Moore, 1977); Ratcliffe 1976, 1980), provide the best evidence that the faults in the Indian Point area have not moved in the last two million years. Data from recent drill cores that intercepted the Ramapo fault plane, show that the dip of the structure is highly variable. The cores, taken at four locations along the fault, indicate that the dip is consistently to the southeast, ranging from 45° through 70° (Ratcliffe, 1980). Textural evidence observed in the cores, indicate that the dominant latest motion in the fault has been right oblique normal faulting (Ratcliffe, 1980).

Recent Seismicity

In the last twenty years, the catalogue of instrumentally recorded seismic events in the northeast has grown tremendously. Locally, this is the result of a dense network of seismic stations, situated in the area around Indian Point, that has been operated since 1975. Data collection by regional seismic stations has continued in the same area since 1970 with a reported detection threshold of about magnitude 2 mb (Lg). Seismic networks have provided a basis for accurately determining the location, magnitude, and in some case focal mechanism solution for many small magnitude seismic events in the area of the power plant and the Ramapo fault zone. This recent seismicity is not markedly dissimilar from the historical seismicity reported for the region. The composite data set does not define or suggest a structural association of earthquakes, however, a regional overview does suggest a higher level of activity in the northern New Jersey, southeastern New York area than that of the surrounding areas.

A number of hypotheses have been proposed to explain the observed pattern of seismicity. Current seismicity in the northeastern United States has been attributed to: a proposed stress system in which the maximum compressive stress trends to the northwest (Yang and Aggarwal, 1981); proximity to relatively young igneous bodies (McKeown, 1978); the response of the crust to glacial unloading (Stein and others, 1979); and, in the immediate region about the site, proposed reactivation of pre-existing fault zones based on a spatial

IP2
FSAR UPDATE

correlation with surface traces of faults exposed within the region (Aggarwal and Sykes, 1978).

Earthquakes occurring near Indian Point have been characterized as shallow focus (<10 km) and low magnitude (1.0-3.0) (Aggarwal and Sykes, 1978). Focal mechanism solutions reported for earthquakes near the Ramapo fault or the margins of the Triassic basin indicate thrust movement on faults that parallel the dominant structural grain in the exposed bedrock (Figure 2) (Aggarwal and Sykes, 1978; Yang and Aggarwal, 1981). The stress field required for this interpretation, must be compressional and oriented to the northwest (Yang and Aggarwal, 1981). Whereas some of the seismic activity in southern New York may be related to northeast trending structures, a number of other trends, transversely oriented with respect to the dominant structures are present (Ratcliffe, 1976; Pomeroy et al, 1976; Blackford and Statton, 1978; Quarterly Report for the Indian Point Seismic Monitoring Network, November 1979 through January 1980) (see Figure 2). Thompson and Bebel (1979) describe northeast and northwest trends of epicenters in the coastal plain area of New Jersey, Delaware and Pennsylvania.

Many studies have attempted to quantify the stress regimes operating in the vicinity of the Ramapo fault. Dames and Moore (1977) determined the near surface stress by in-site measurements. While these results are variable, a fairly consistent northeast to eastwest trend for the horizontal component of compression was determined. This stress direction is transverse to that suggested by others (Aggarwal & Sykes, 1978) who base their interpretations on reported focal mechanism solutions. It is, however, in general agreement with regional stresses inferred from measurements and observations made throughout the northeastern United States (Sbar and Sykes, 1973).

An examination of the distribution of earthquakes in the vicinity of Indian Point indicates that not all earthquakes in the region can be attributed to northeast trending faults. A sequence of earthquakes occurred near Annsville, New York, from 17 January to 23 January 1980. A composite focal mechanism solution was constructed using data recorded by the Indian Point Seismic Monitoring Network. The solution indicates thrust faulting along one of two possible planes, oriented N2°W 29°E or N16°W 62°W (Quarterly Report for the Indian Point Seismic Monitoring Network, November 1979 - January 1980). This trend is obliquely oriented to the dominant structural fabric in the region, and requires a compressive stress field oriented east-west to northeast-southwest.

Low level microseismicity existing in the region is evidence that crustal adjustments are continuing in response to regional stresses. No evidence exists at the surface or in drill cores of the fault zones (in particular the Ramapo fault zone), that suggest any contemporary movement along faults exposed at the surface since the major period of activity during Mesozoic time. In fact geologic data obtained from cores of the Ramapo fault zone (Ratcliffe, 1980) show evidence of normal faulting as the last movement, which is consistent with the Mesozoic faulting regime and inconsistent with the thrust mechanism proposed by Aggarwal and Sykes (1978). To date, no satisfactory stress regime has been proposed that adequately accommodates the observed pattern of low level seismicity, regional stress measurement data and those stresses inferred from recently reported focal mechanism solutions.

CONCLUSION

Low level microseismicity in the region is evidence that crustal adjustments are continuing in response to regional stresses. Detailed field investigations (e.g., Ratcliffe, 1976, 1980; Dames and Moore, 1977) have been conducted in the immediate vicinity of Indian Point,

IP2
FSAR UPDATE

and along the major faults in the region. To date, no evidence has been found in the rocks exposed at the surface or sediments overlying fault traces or in cores obtained in the vicinity of Indian Point, that might support a conclusion that displacement has occurred along major fault systems within the New York Highlands, the Ramapo or its associated branches during Quaternary time (the last 1.5 m.y.). In the vicinity of Indian Point, evidence that no displacement has occurred in the last 65 m.y. (since the Mesozoic) along specific major structures has been observed.

IP2
FSAR UPDATE

- Aggarwal, Y.P., and Sykes, L.R., 1978, Earthquakes, faults and nuclear power plants in southern New York and northern New Jersey: *Science*, v. 200, p. 425-429.
- American Geological Institute, 1977, Glossary of Geology, Gary, M., McAfee, R. Jr., and Wolf, C.L. eds., Am. Geol. Inst., Falls Church, Va., 805 p.
- Blackford, M., and Statton, C. T., 1978, The Annsville, New York earthquake of September 2, 1977. Presented at the seventy-third annual meeting of the Seismological Society of America.
- Brock, P.W.G., Structural and age relationships within the New York City Group in southeastern New York, Unpublished Grant Proposal.
- Brock, P.W.G., and Mose, D.G., 1979, Taconic and younger deformation and metamorphism in the Croton Falls area, southeastern New York: *Bull. Geol. Soc. Am.*, Pt. II, v. 90, p. 1158-1195.
- Dames & Moore, 1977, Geotechnical investigation of the Ramapo Fault System in the region of the Indian Point Generating Station.
- Hall, L.M., 1968, Times of origin and deformation of bedrock in the Manhattan Prong, in: Zen, White, Hadley and Thompson, eds., Studies of Appalachian Geology, Northern and Maritime, Interscience Publishers, New York, p. 117-128.
- Heleneck, H.L. and Mose, D.G., 1978, Geology and geochronology of Precambrian rocks in the Lake Carmel region, Hudson Highlands, New York: *Geol. Soc. Am.*, Abstracts with Programs, v. 10, no. 2, p. 47.
- Heleneck, H.L. and Mose D.G., 1976, Structure, petrology and geochronology of the Precambrian rocks in the Central Hudson Highlands; in: Johnson, J.H., ed., Guidebook to Field Excursions, 48th Annual Meeting of the New York State Geological Association: New York, Vassar College, p. B1 1-27.
- Mc Keown, F.H., 1978, Hypothesis: Many earthquakes in the central and southeastern United States are casually related to mafic intrusive bodies: *Jour. Res. U.S. Geol. Surv.*, v. 6, p. 41-50.
- Merrill, F.J., 1896, The geology of the crystalline rocks of southeastern New York: New York State Museum. Ann. Rpt. No. 50, Appendix A., p. 21-31
- Mose, D.G. and Hall, L.M., 1979, Rb-Sr whole-rock age determination of Member C of the Manhattan Schist and its bearing on allochthony in the Manhattan Prong, southeastern New York: *Geol. Soc. Am.*, Abstracts with Programs, V. 11, no. 1, p. 46.
- Nelson, S., 1980, Determination of Holocene fault movement along the Ramapo Fault in southeastern New York using pollen stratigraphy: *Geol. Soc. Am.*, Abstracts with Programs, v. 12, no. 2, p. 75.
- Pomeroy, P.W., Simpson, D.W., and Sbar, M.L., 1976, Earthquakes triggered by surface quarrying-the Wappingers Falls, New York sequence of June, 1974: *Bull. Seis. Soc. Am.* V. 66, p. 685-700.

IP2
FSAR UPDATE

Ratcliffe, N.M., 1976, Final Report on major fault systems in the vicinity of Tomkins Cove-Buchanan, New York: Report for Consolidated Edison Company, Inc. of New York, 157 p.

Ratcliffe, N.M., 1980, Brittle faults (Ramapo Fault) and phyllonitic ductile shear zones in the basement rocks of the Ramapo seismic zone, New York and New Jersey, and their relationship to current seismicity, *in*: Manspeizer, W., ed., Field Studies of New Jersey Geology and Guide to Field Trips, 52nd Annual Meeting of the New York State Geological Association, Newark, N.J., Rutgers University, p. 278-312.

Robinson, P., and Hall, L.M., 1979, Tectonic synthesis of southern New England *in*: The Caledonides in the USA, I.G.C.P., 1979. Blacksburg, Va.

Sbar, M.L., and Sykes, L.R., 1973, Contemporary compressive stress and seismicity in eastern North America: An example of intra-plate tectonics: Bull. Geol. Soc. Am., v. 84, p. 1861-1882.

Stein, S., Sleep, S., Geller, R.J., Wang, S-C, and Krueger, G.C., 1979, Earthquakes along the passive margin of eastern Canada: Geophys. Res. Letts. v.6, p. 537-540.

Thompson, A.M., and Bebel, D.J., 1980, Modern seismicity in the middle Atlantic Seaboard Region, and some neotectonic Implications: Geol. Soc. Am., Abstracts with Programs, v. 12, no. 2, p. 55.

Woodward-Clyde Consultants, Quarterly Reports for the Indian Point Seismic Monitoring Network, Jan., 1977-Jan., 1982.

Yang, J-P, and Aggarwal, Y.P., 1981, Seismotectonics of northeastern United States and adjacent Canada. Jour. Geophys. Res., v. 86, p. 4981-4998.

In addition, the following reports were used as background information:

Fluhr, T.W., 1965, Memorandum on geologic features of Indian Point Nuclear Power Plant site: for Consolidated Edison Company of New York, Inc., 9 p.

Paige, S., 1955, A geologic report on the Indian Point Power House Site of the Consolidated Edison Company, Inc., New York.

GLOSSARY

amphibole - A complex chain silicate mineral rich in iron and magnesium.

amphibolite - A metamorphic rock whose main components are amphibole and plagioclase feldspar

amphibolite facies - Rocks formed at moderate temperature and pressure conditions during regional metamorphism.

angular unconformity - An unconformity recognizable by the deposition of sediments over deformed rocks.

argillite - A compact mudstone, generally not laminated and not fissile.

arkose - A feldspar rich, generally coarse grained, sandstone derived from continental rocks.

breccia - A generally coarse grained rock composed of angular or broken fragments of rock, which may be formed tectonically in a fault zone, or by sedimentary processes.

brittle deformation - A term used to describe faulting and fracturing of rocks.

calc-silicate - A descriptive term applied to minerals or rocks consisting of calcium bearing silicates, such as diopside.

chlorite - A green iron-magnesium rich platy mineral.

chlorite grade metamorphism - Low-grade regional metamorphism indicated by the first appearance of chlorite in rocks of appropriate composition.

dike - An igneous intrusion that cuts across planar features of a rock.

disconformity - A break in the time-stratigraphic record separating two sequences of rock, both of which are bedded parallel to the unconformity.

ductile deformation - Occurs where rocks fold or flow when subjected to a stress field.

eugeosyncline - A geosyncline or basin in which vulcanism is associated with clastic sedimentation.

euohedral - A crystal bounded by well developed crystal faces.

facies - A set of conditions that specify the environment of formation of rocks (metamorphic or sedimentary).

geosyncline - A long linear basin, characterized by subsidence coincidental with sedimentation.

geothermal gradient - The relationship of temperature to depth (pressure) in the earth's crust.

gneiss - A metamorphic rock formed by regional metamorphism, generally high grade.

IP2
FSAR UPDATE

granulite facies - Rocks formed at very high temperatures and pressures during regional metamorphism.

intrusion - The emplacement of an igneous body in a pre-existing rock.

isocinal folds - A fold in which the limbs are parallel.

mafic - A term used to describe dark rocks or minerals containing large amounts of magnesium or iron.

marble - A metamorphic rock consisting primarily of calcite or dolomite.

metamorphic grade - Rocks of any composition that have been metamorphosed under a specific range of temperature and pressure conditions.

metasediment - A metamorphosed sedimentary rock.

migmatite - A mixed rock composed of metamorphic material containing segregation of igneous material formed by injection or in-situ partial melting.

miogeosyncline - A geosyncline lacking volcanic deposits, commonly located adjacent to continental margins.

neotectonics - Post-Miocene structural history of the earth's crust.

orogen - A region that has been subjected to orogeny.

orogeny - The development of structures, metamorphism and igneous activity relating to mountain building.

pelite - A sedimentary or metamorphic rock rich in aluminum.

quartzite - A metamorphic or sedimentary rock consisting mainly of quartz.

retrograde metamorphism - Recrystallization of metamorphic rocks at conditions that are lower grade than those at which the rock was originally metamorphosed.

schist - A well foliated metamorphic rock that easily separates into flakes or slabs due to an abundance of platy minerals.

sedimentary facies - An restricted area within a litho-stratigraphic unit representing a particular depositional environment.

sill - An igneous intrusion that parallels the layering of the country rock.

tectonic - Pertaining to the forces that cause crustal deformation.

throw - The vertical component of fault motion.

unconformity - A primary feature representing erosion or non-deposition, resulting in a break in the stratigraphic sequence.

**TABLE 1
GEOLOGICAL TIME SCALE**

**TABLE 2
PROPOSED CORRELATION OF THE STRATIGRAPHIC SUBDIVISIONS IN THE
MANHATTAN PRONG WITH ROCKS IN ADJACENT AREAS**

**TABLE 3
GEOLOGIC HISTORY IN THE CROTON FALLS AREA
(after Brock & Mose, 1979)**

FIGURES

Figure No.	Title
Figure 1	Geological Map, Southeastern New York (after Brock & Mose, 1979)
Figure 2	Seismicity of Southeastern New York and New Jersey (after Dames & Moore, 1977)



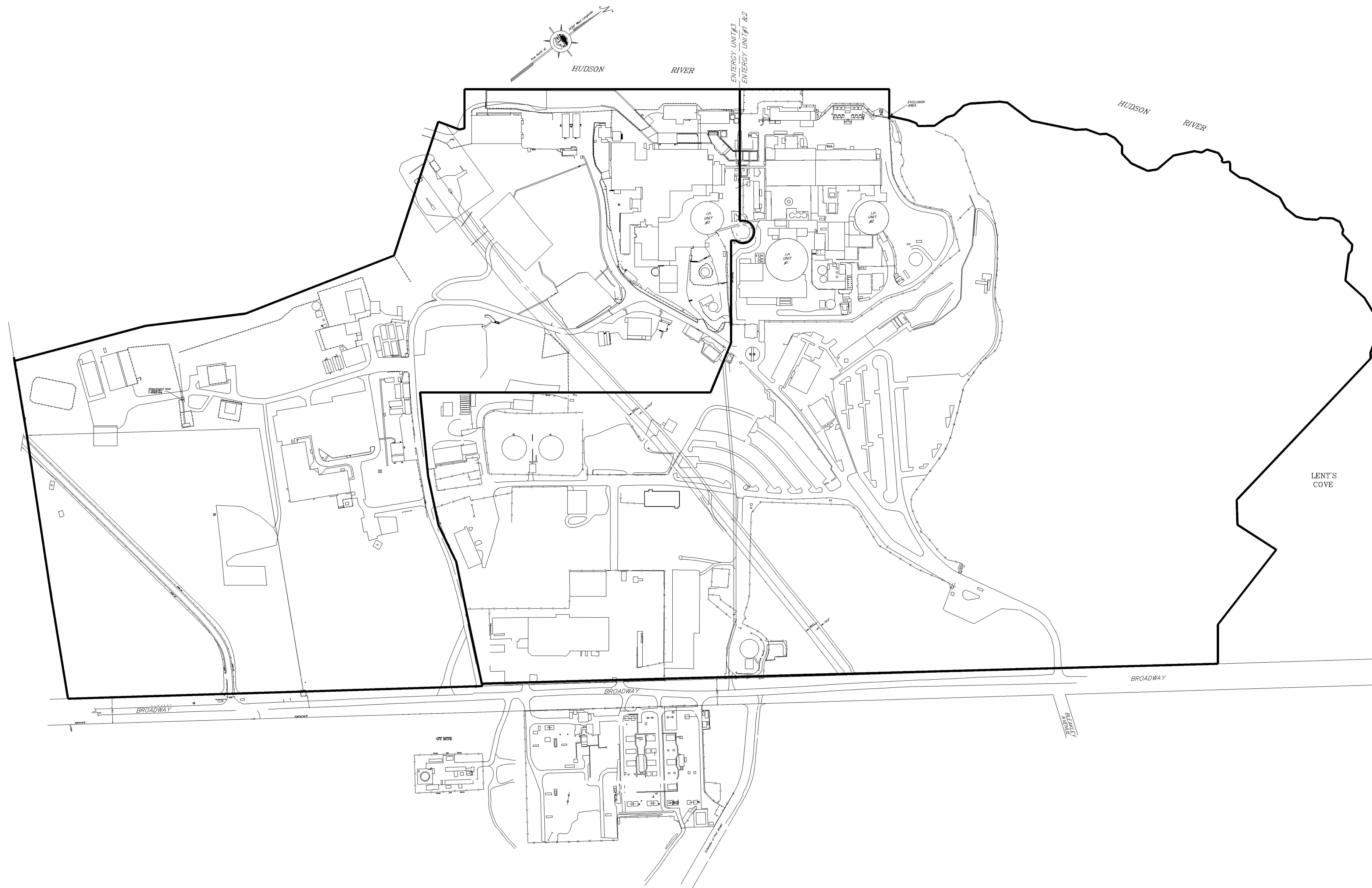
INDIAN POINT UNIT No. 2

UFSAR FIGURE 2.2-1

AERIAL PHOTO OF INDIAN POINT SITE
AND SURROUNDING AREA

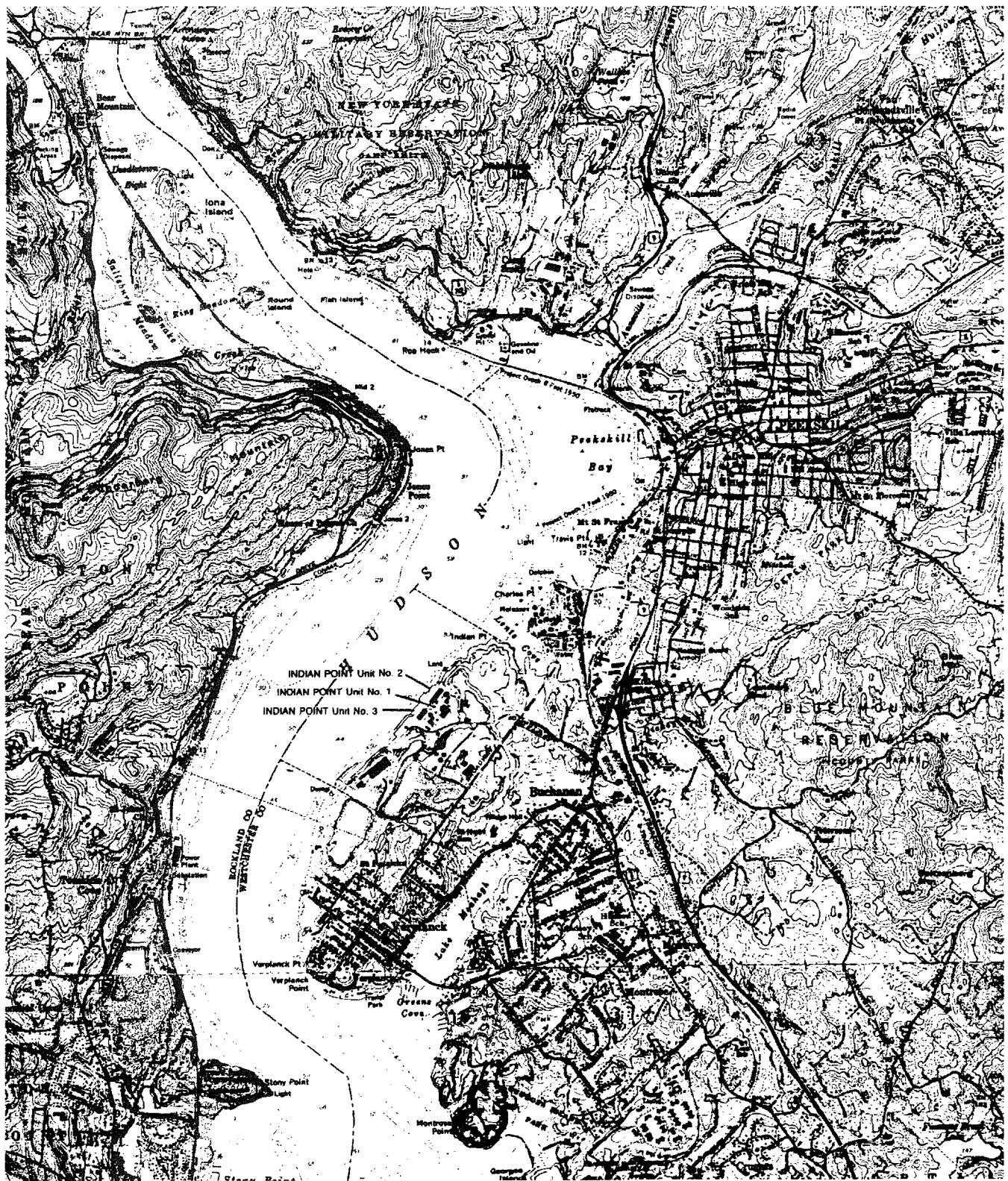
MIC. No. 1999MC3572

REV. No. 17A



NOT TO SCALE

INDIAN POINT UNIT No. 2	
UFSAR FIGURE 2.2-2	
INDIAN POINT BUILDING IDENTIFICATION	
MIC. No. 1999MC3573	REV. No. 17B



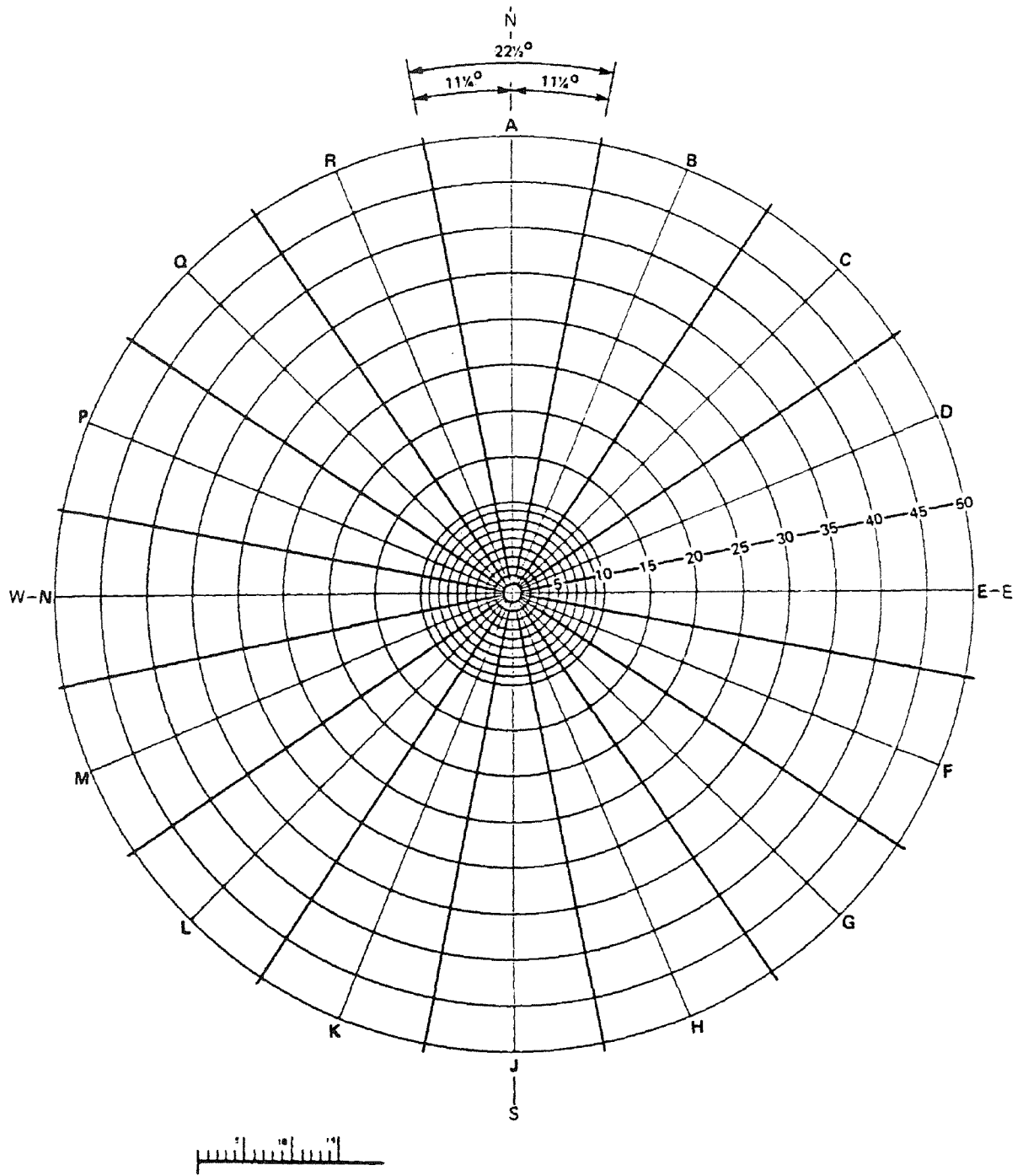
INDIAN POINT UNIT No. 2

UFSAR FIGURE 2.3-1

TOPOGRAPHICAL MAP OF INDIAN POINT
AND SURROUNDING AREA

MIC. No. 1999MC3574

REV. No. 17A



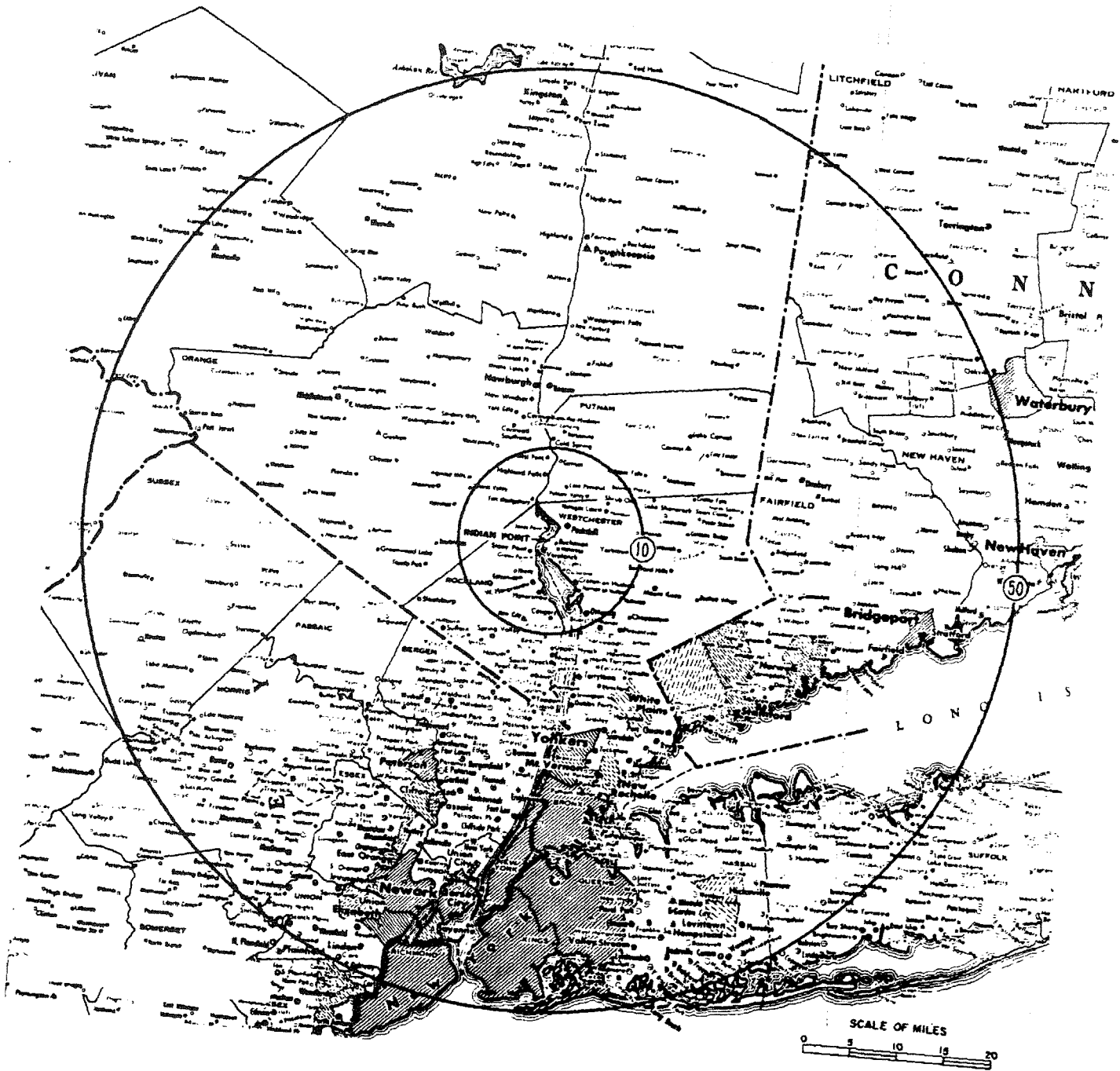
INDIAN POINT UNIT No. 2

UFSAR FIGURE 2.4-1

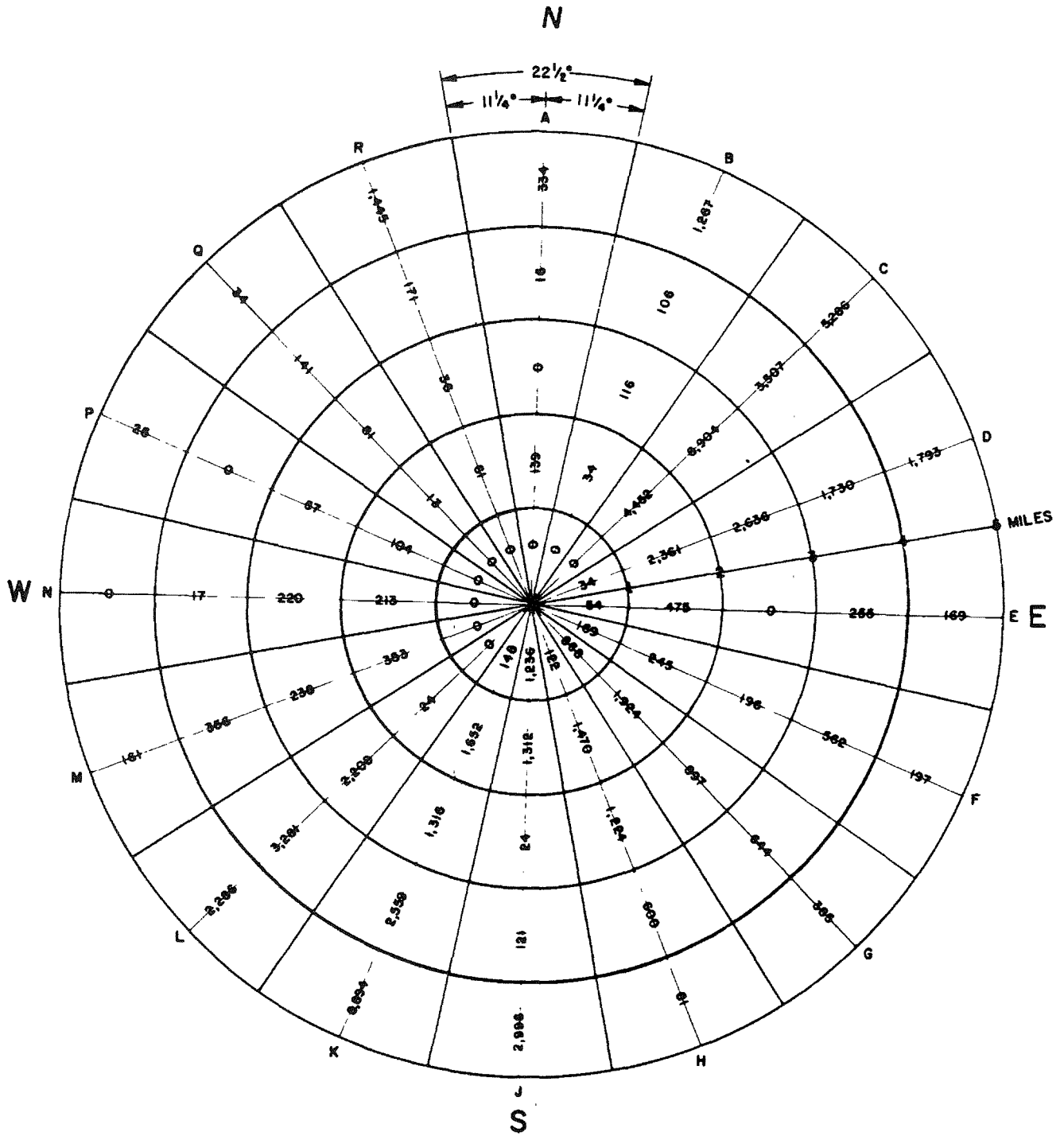
SCHEMATIC SECTOR/ZONE DIAGRAM

MIC. No. 1999MC3575

REV. No. 17A

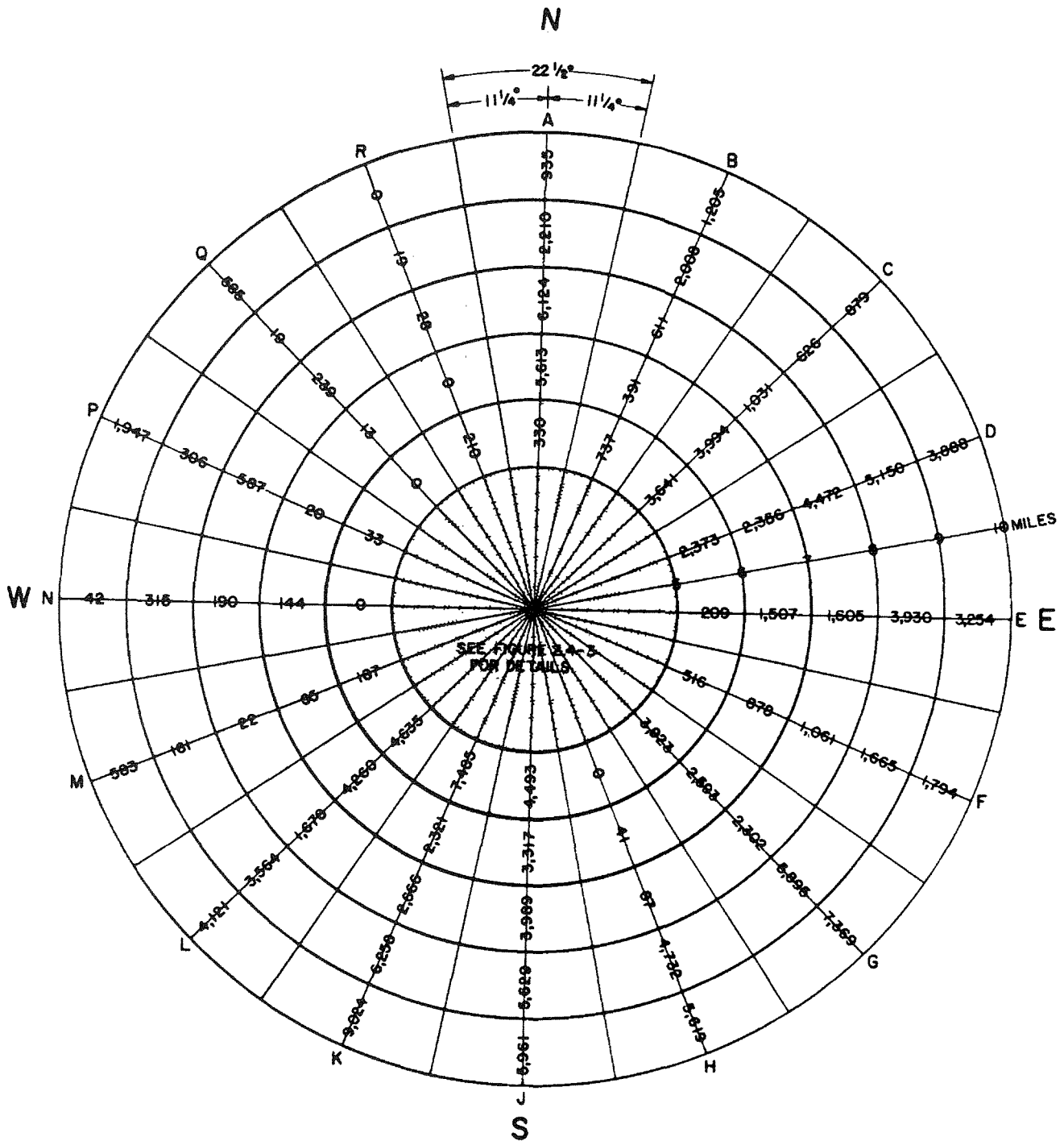


INDIAN POINT UNIT No. 2	
UFSAR FIGURE 2.4-2	
INDIAN POINT STATION TEN AND FIFTY MILE RADIUS MAP	
MIC. No. 1999MC3576	REV. No. 17A



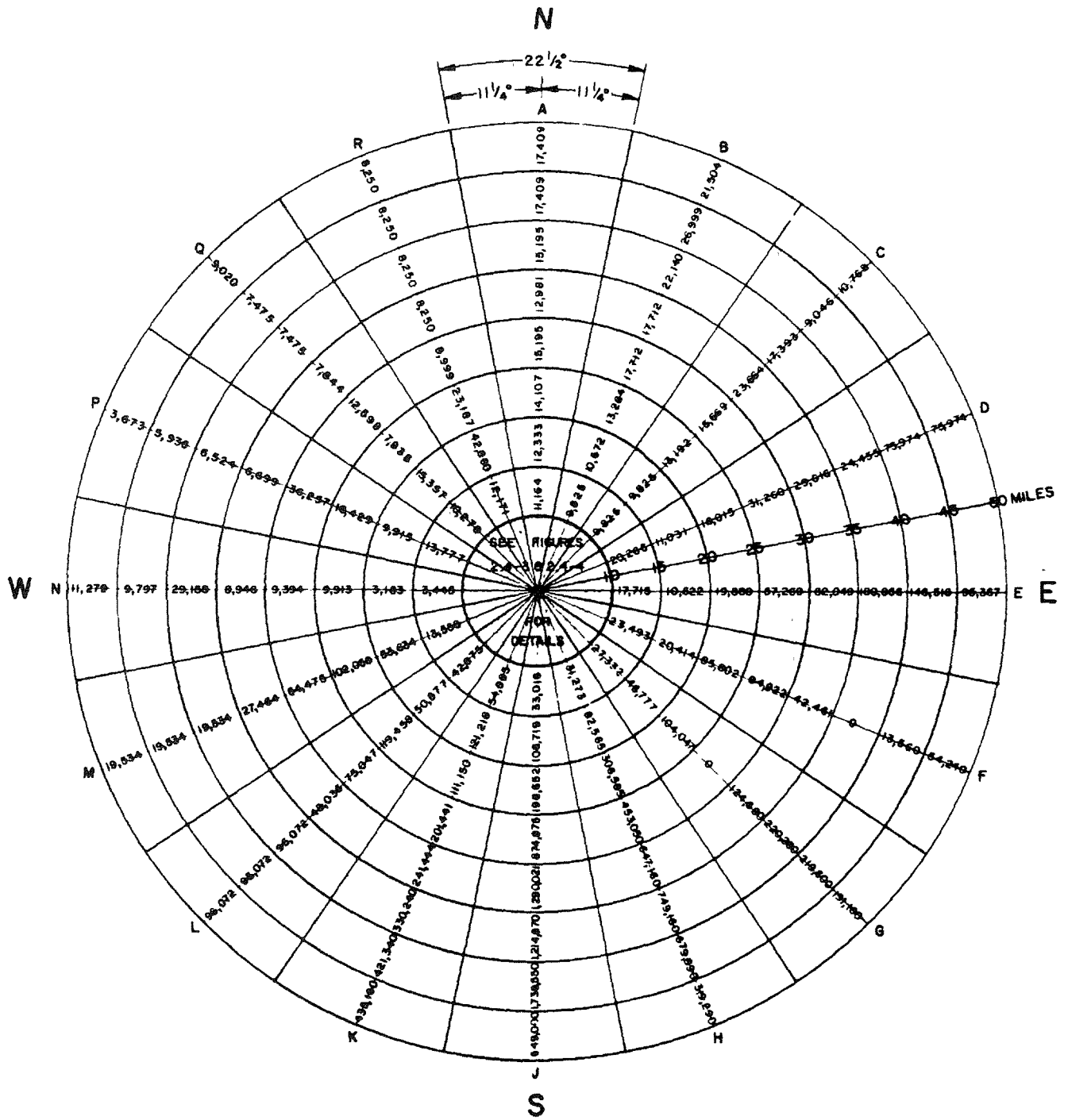
1980 PROJECTED POPULATIONS

INDIAN POINT UNIT No. 2	
UFSAR FIGURE 2.4-3	
FIVE MILE SECTOR/ZONE DIAGRAM	
MIC. No. 1999MC3577	REV. No. 17A



1980 PROJECTED POPULATIONS

INDIAN POINT UNIT No. 2	
UFSAR FIGURE 2.4-4	
TEN MILE SECTOR/ZONE DIAGRAM	
MIC. No. 1999MC3578	REV. No. 17A



1980 PROJECTED POPULATIONS

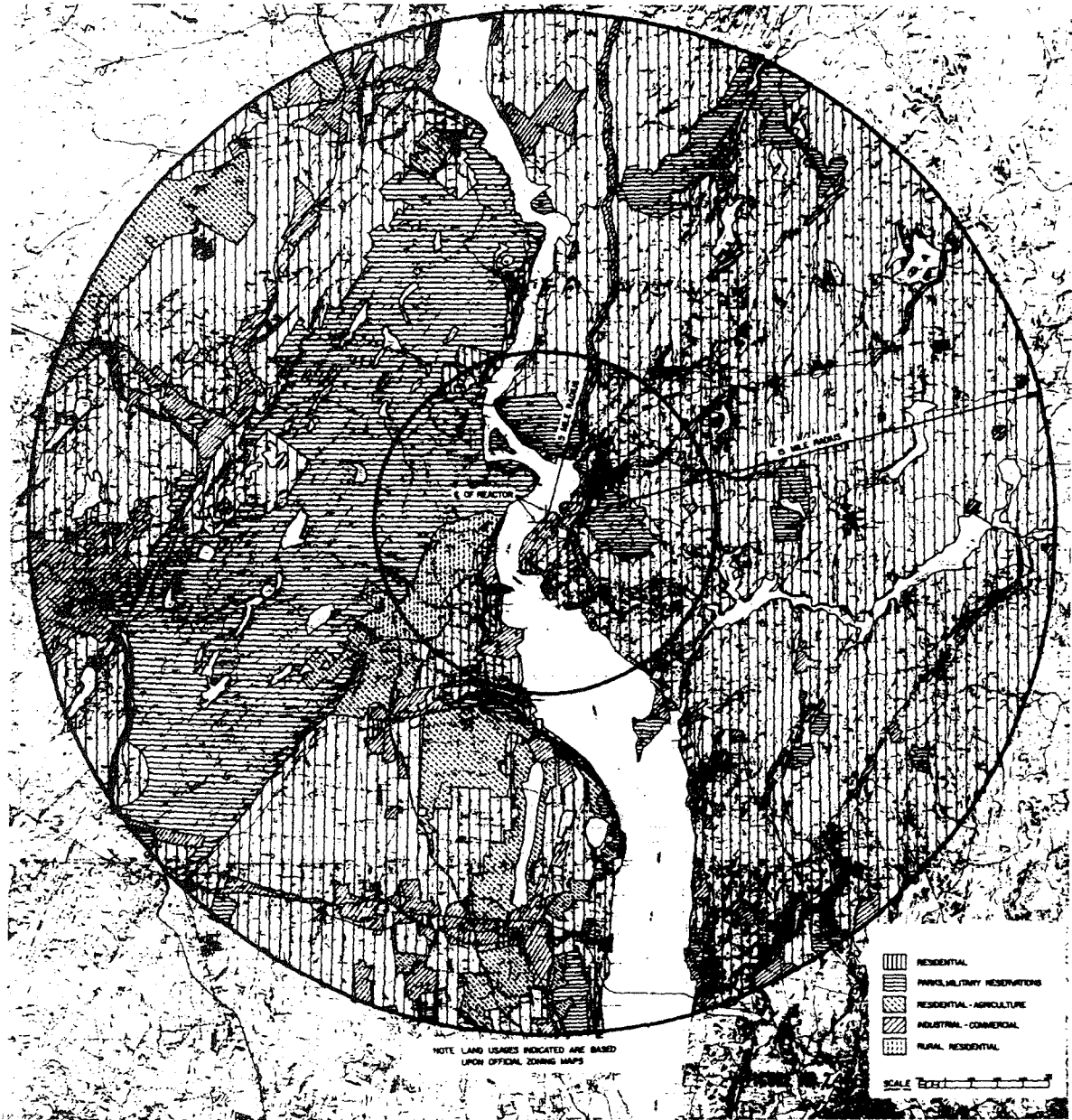
INDIAN POINT UNIT No. 2

UFSAR FIGURE 2.4-5

FIFTY MILE SECTOR/ZONE DIAGRAM

MIC. No. 1999MC3579

REV. No. 17A



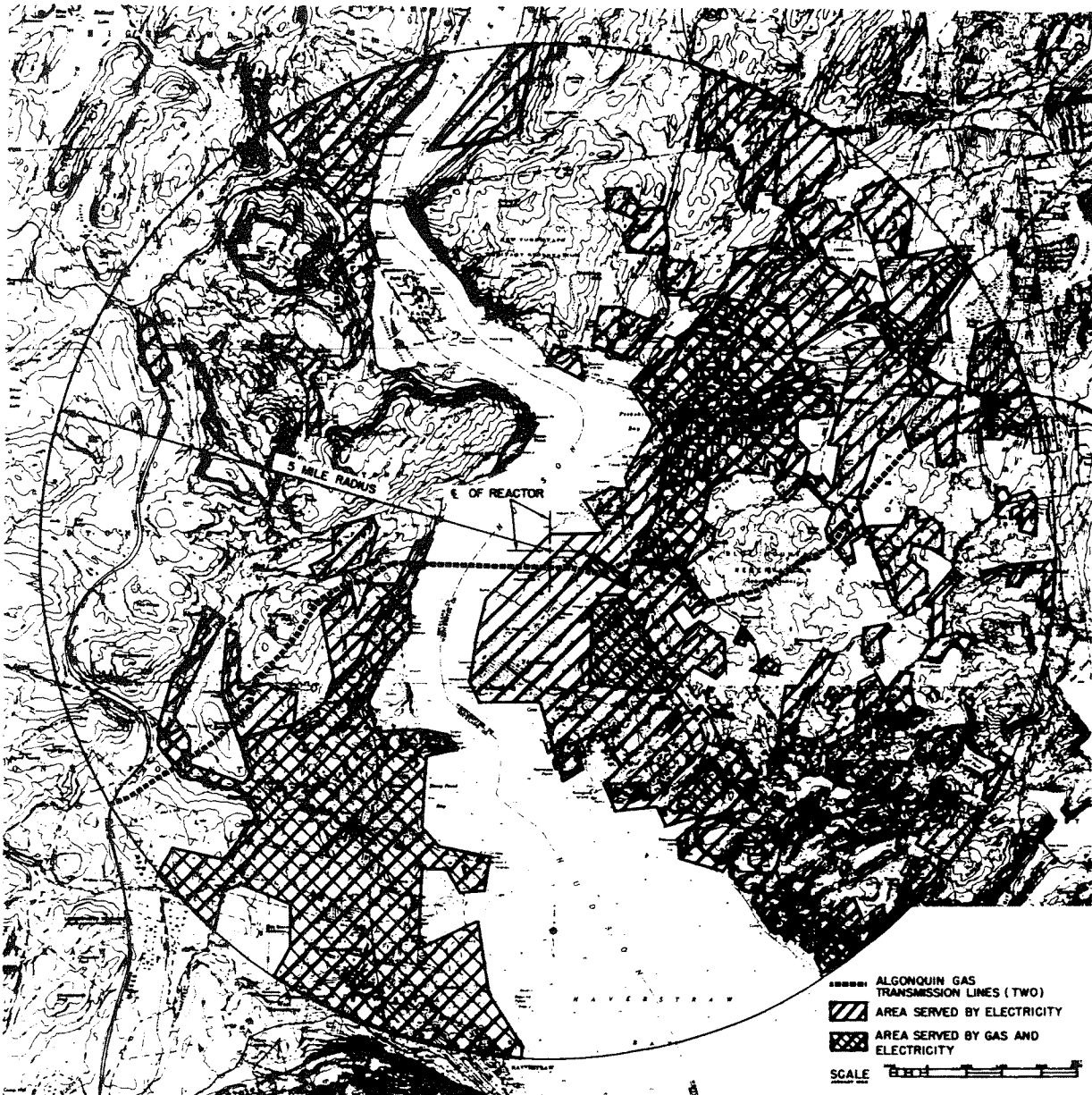
INDIAN POINT UNIT No. 2

UFSAR FIGURE 2.4-6

MAP AND DESCRIPTION
SHOWING LAND USAGE

MIC. No. 1999MC3580

REV. No. 17A



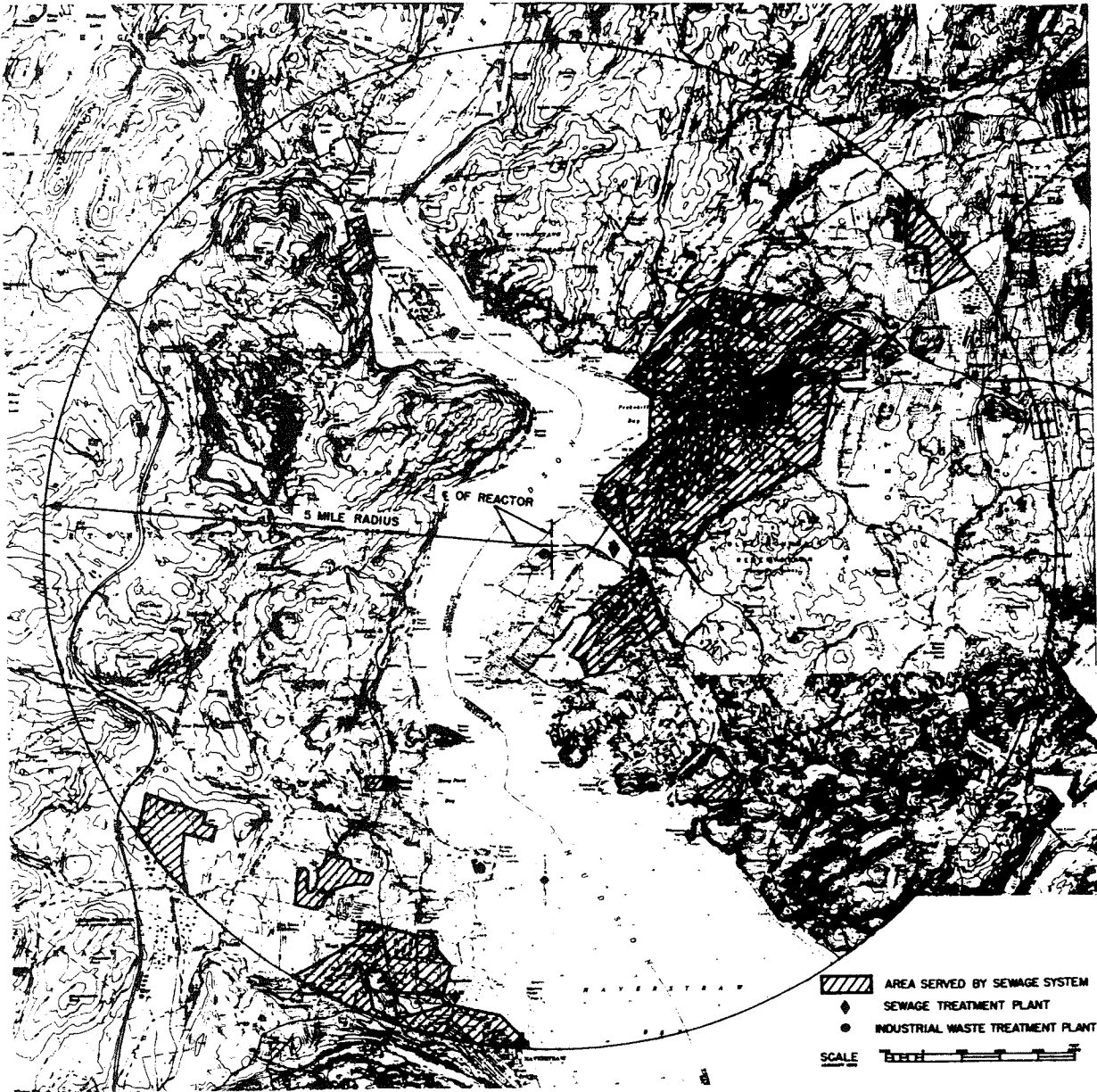
INDIAN POINT UNIT No. 2

UFSAR FIGURE 2.4-7

MAP AND DESCRIPTION OF THE AREA
SHOWING PUBLIC UTILITIES

MIC. No. 1999MC3581

REV. No. 17A



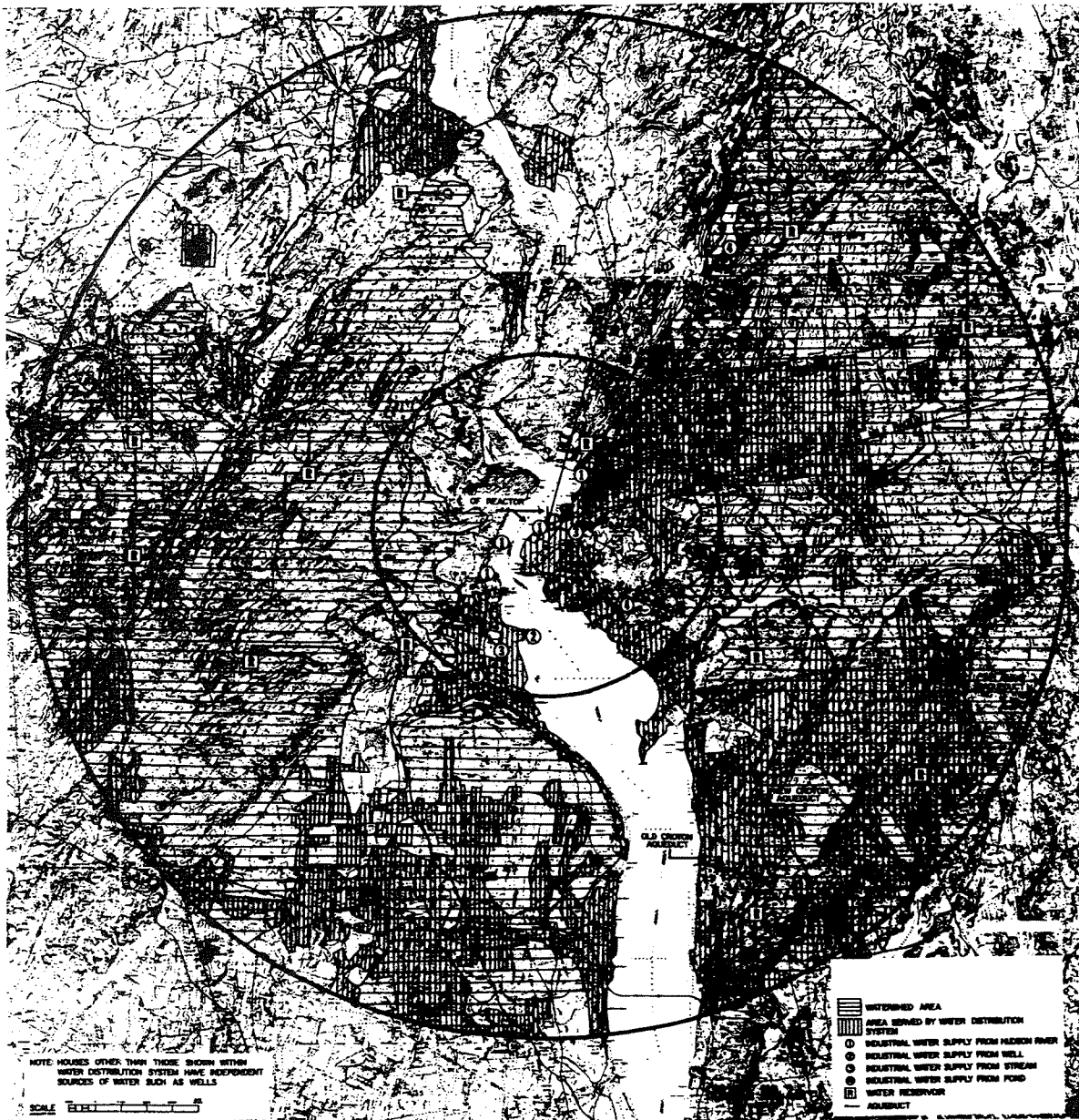
INDIAN POINT UNIT No. 2

UFSAR FIGURE 2.4-8

MAP AND DESCRIPTION OF THE AREA
SHOWING SEWAGE SYSTEMS

MIC. No. 1999MC3582

REV. No. 17A



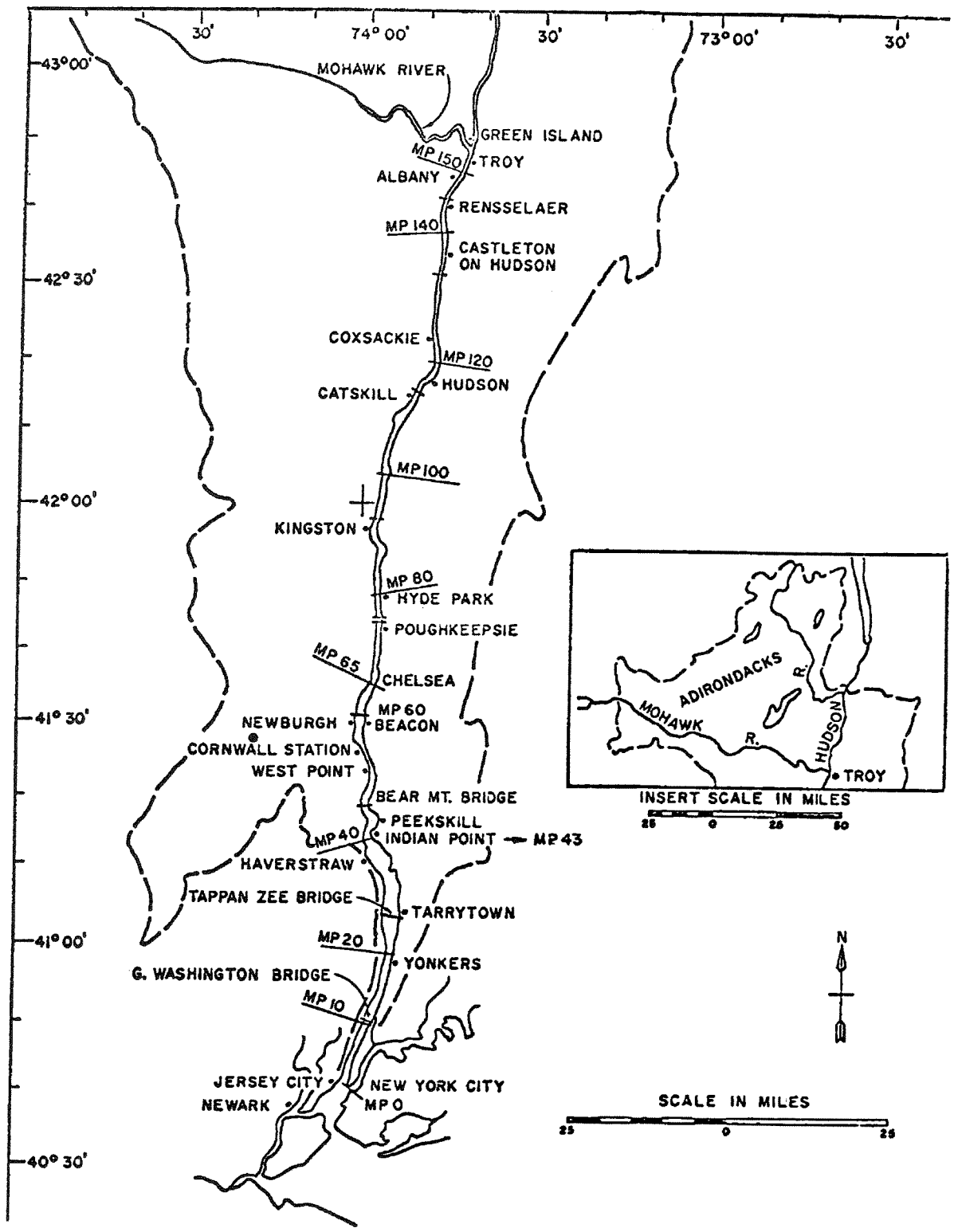
INDIAN POINT UNIT No. 2

UFSAR FIGURE 2.5-1

MAP & DESCRIPTION SHOWING LOCATION OF SOURCES OF POTABLE & INDUSTRIAL WATER SUPPLIES & WATERSHED AREAS

MIC. No. 2001MB1189

REV. No. 17A

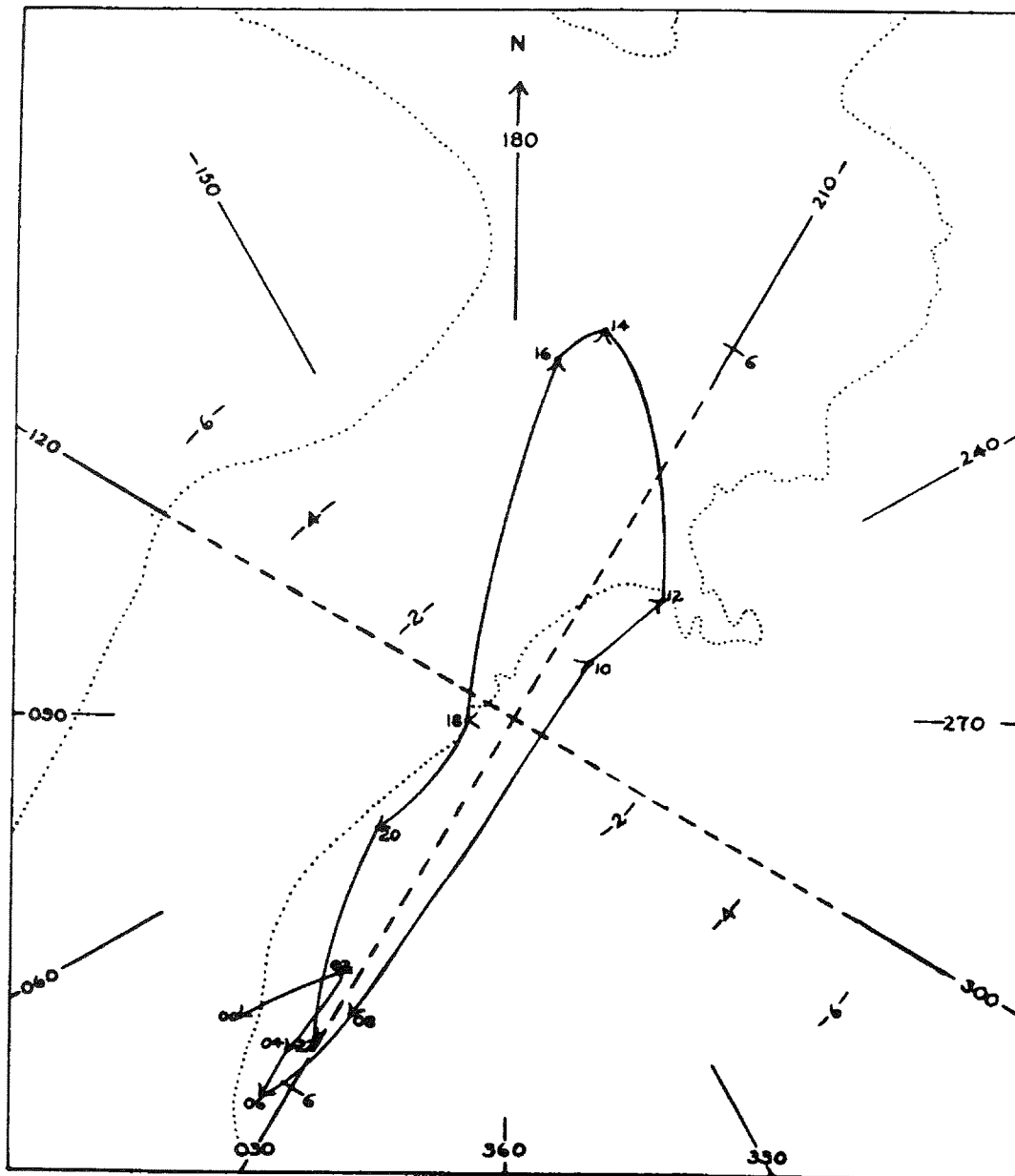


INDIAN POINT UNIT No. 2

UFSAR FIGURE 2.5-2

HUDSON RIVER DRAINAGE BASIN

MIC. No. 2001MB1190 | REV. No. 17A



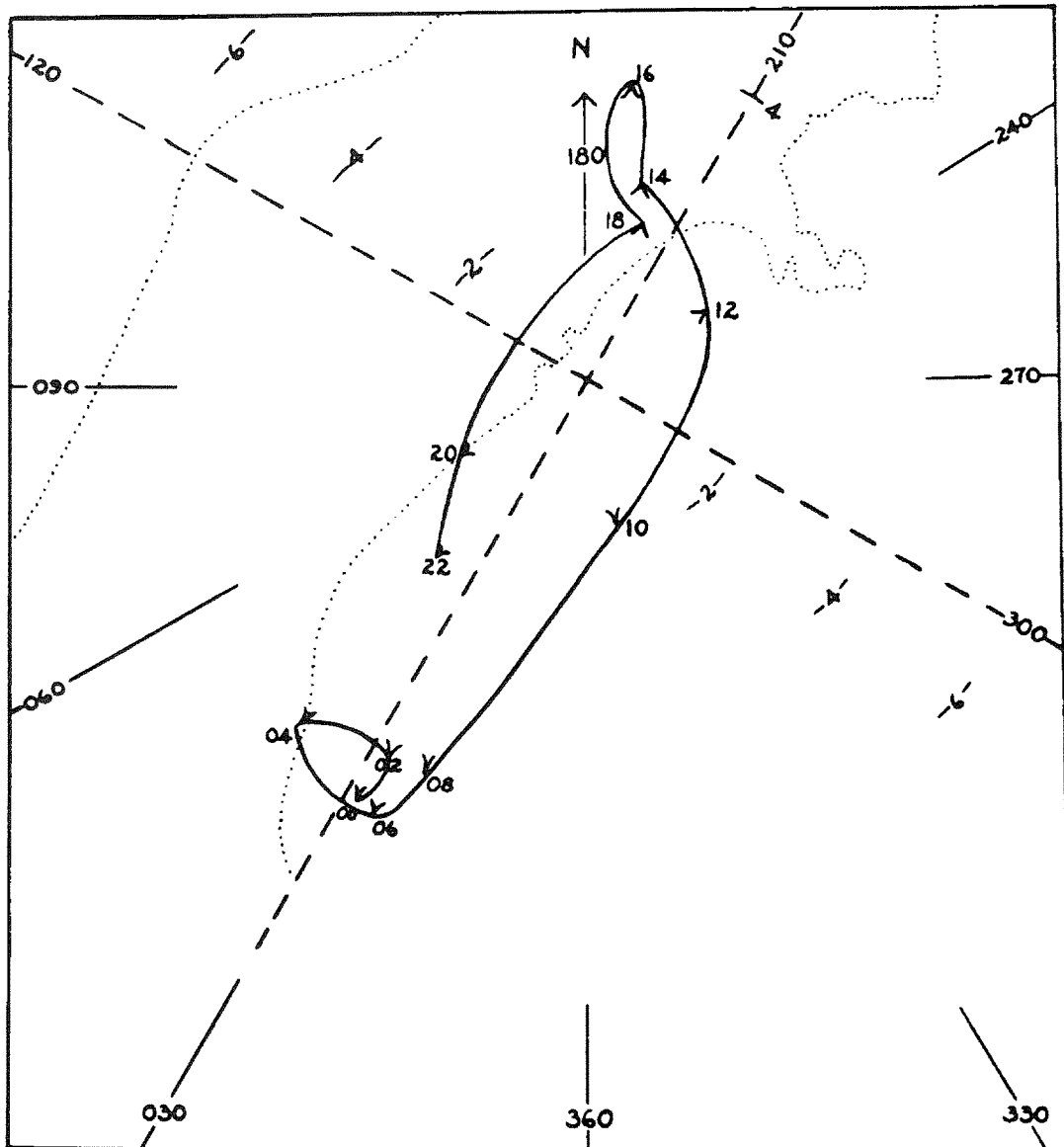
September - October, 1955
70 Ft Above River

INDIAN POINT UNIT No. 2

UFSAR FIGURE 2.6-1
DIURNAL VARIATION OF MEAN VECTOR
WIND FOR VIRTUALLY ZERO PRESSURE
GRADIENT CONDITIONS

MIC. No. 2001MB1191

REV. No. 17A



Geostrophic Winds Less Than 16 MPH
 September - October, 1955
 70 Ft Above River

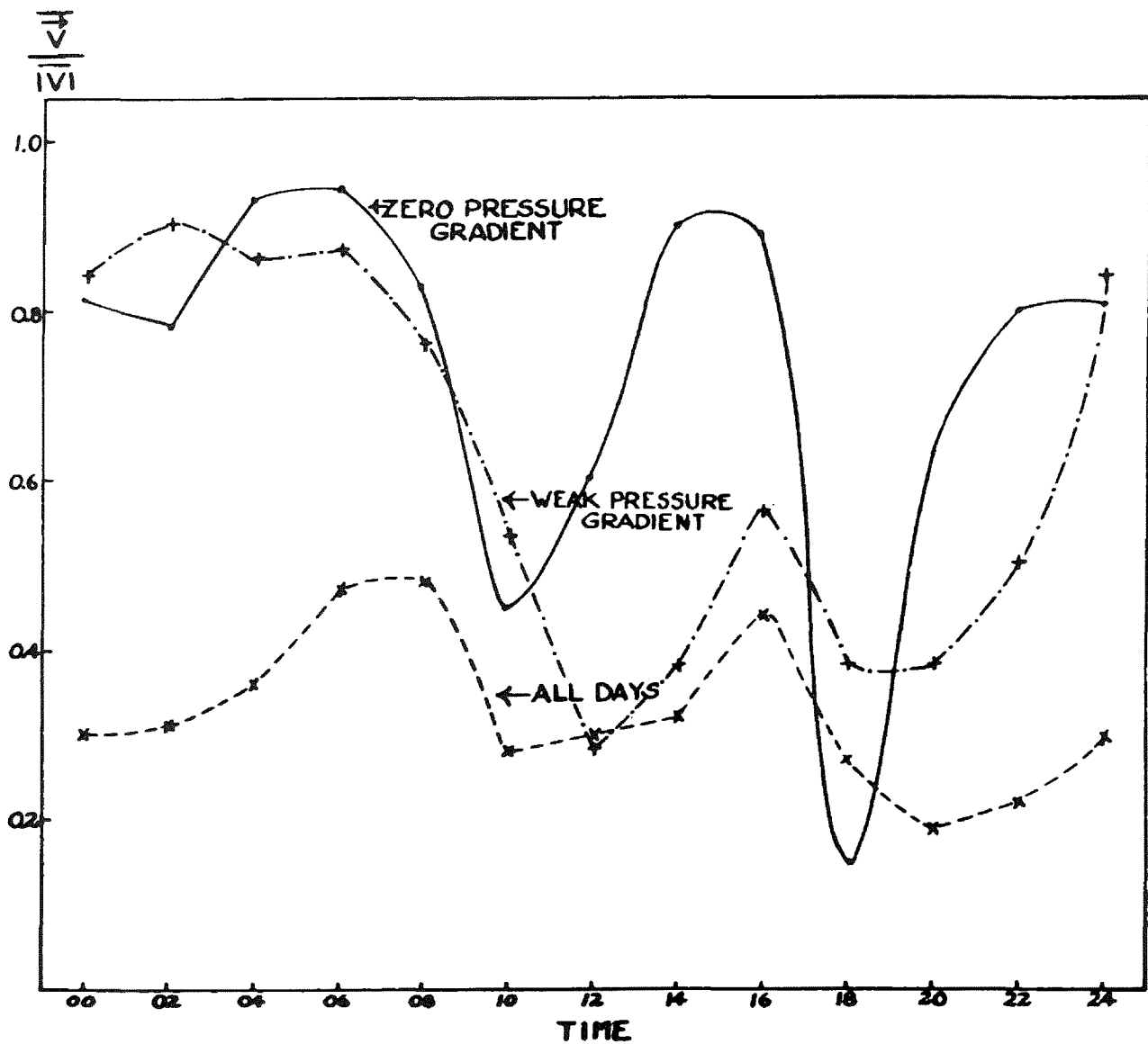
INDIAN POINT UNIT No. 2

UFSAR FIGURE 2.6-2

DIURNAL VARIATION OF MEAN VECTOR WIND
 FOR 24 HOUR PERIODS OF WEAK PRESSURE
 GRADIENT CONDITIONS

MIC. No. 2001MB1193

REV. No. 17A



INDIAN POINT UNIT No. 2

UFSAR FIGURE 2.6-3

STEADINESS OF WIND AS A FUNCTION OF
TIME OF DAY FOR INDICATED PRESSURE
GRADIENT CONDITIONS

MIC. No. 2001MB1194

REV. No. 17A

GEOLOGIC HISTORY IN THE CROTON FALLS AREA
(AFTER BROCK & MOSE, 1979)

ACADIAN	(F ₆ = tight to isoclinal fold; deformation of Goldens Bridge granite) (Goldens Bridge granite) Joints with muscovite and tourmaline ? open folds	
	F ₅ = folded isograd. S ₅ : retrograde muscovite schistosity; associated retrograde kyanite and staurolite; locally associated shearing and faulting. (Croton Falls granites intruded 387 ± 37 m.y. ago) (Croton Falls ultramafic complex; includes xenoliths of refolded schists; could be synchronous with F ₃ folding). ? Open folds	
	Quartz ± garnet ± sillimanite, and quartz plus two feldspar + garnet + sillimanite segregations. F ₄ = locally developed reclined close folds and chevron folds. Faint S ₄ : realigned biotite and sillimanite in F ₃ segregations and host rocks. Sillimanite K-feldspar facies. F ₃ = very common near-isoclinal folds; refolds S ₁ schistosity and F ₂ flasers. Variable S ₃ : slight re-alignment of sillimanite and biotite. Quartz-K-feldspar - sillimanite segregations. Sillimanite-K-feldspar facies. F ₂ = isoclinal to near-isoclinal intrafolial folds. Strong cataclastic S ₂ : flasers of quartz-feldspar segregations and plagioclase, smeared garnets, partial realignment of biotite and sillimanite. Quartz plagioclase segregations. F ₁ = a few isoclinal folds. Strong S ₁ : alignment of biotite, sillimanite, and quartz ± plagioclase segregations. Porphyroblastic garnets ± plagioclase.	
TACONIC	Manhattan Schist deposition Inwood Marble deposition Lowerre Quartzite deposition unconformity (Intrusion of Yonkers and Pound Ridge granite gneisses at 575-600 m.y.)	
	GRENVILLE	Fordham Gneiss (Hudson Highlands gneiss and related rocks metamorphosed at 0.9-1.2 b.y. and still contain granulite facies relicts.)

Note: All features or events except those in parenthesis are demonstrable in one roadcut about 1 km south of the Croton Falls Complex on Route 684.

TABLE 3

CLIENT: CUN EDISON CO. OF N.Y.
 LOCATION: INDIAN POINT (10M)

TABLE 30

DIURNAL VARIATION OF STABILITY CLASS AND WIND SPEED
 (CONCURRENT DATA)

MAY 1, 1980 - OCT 31, 1980

SUMMER

PASQUILL STABILITY CATEGORY

HOOR	A	B	C	D	E	F	G
MEAN SPEED (MPH)/NUMBER OF OBSERVATIONS							
100	5.0 / 2	0.0 / 0	0.0 / 0	4.1 / 49	2.7 / 197	2.2 / 94	2.4 / 15
200	0.0 / 0	0.0 / 0	0.0 / 0	4.0 / 62	2.7 / 186	2.2 / 98	2.2 / 11
300	0.0 / 0	0.0 / 0	0.0 / 0	4.0 / 73	2.7 / 175	2.1 / 97	2.5 / 12
400	0.0 / 0	0.0 / 0	0.0 / 0	4.1 / 62	2.6 / 187	2.5 / 97	2.1 / 12
500	0.0 / 0	0.0 / 0	0.0 / 0	3.7 / 62	2.6 / 195	2.3 / 89	3.2 / 8
600	0.0 / 0	0.0 / 0	4.0 / 2	3.4 / 123	2.5 / 100	2.2 / 43	3.4 / 5
700	2.7 / 13	3.2 / 28	3.3 / 29	3.2 / 157	2.5 / 107	2.1 / 18	1.0 / 1
800	3.5 / 68	3.2 / 43	3.2 / 44	3.1 / 152	2.2 / 46	4.7 / 3	0.0 / 0
900	3.6 / 142	3.5 / 42	3.2 / 41	2.9 / 105	3.4 / 27	0.0 / 0	0.0 / 0
1000	3.8 / 197	3.4 / 35	2.9 / 32	3.1 / 75	3.1 / 17	0.0 / 0	0.0 / 0
1100	4.0 / 233	3.2 / 17	3.7 / 28	3.5 / 64	3.0 / 18	0.0 / 0	0.0 / 0
1200	4.1 / 238	3.5 / 23	3.6 / 24	3.7 / 57	3.8 / 16	0.0 / 0	0.0 / 0
1300	4.3 / 226	3.7 / 29	3.8 / 23	3.8 / 62	4.8 / 16	3.5 / 1	0.0 / 0
1400	4.3 / 204	4.3 / 24	3.9 / 23	3.8 / 87	3.7 / 19	2.5 / 1	0.0 / 0
1500	4.1 / 159	4.4 / 32	3.8 / 35	3.9 / 100	3.7 / 28	4.8 / 2	4.0 / 1
1600	4.0 / 111	3.7 / 29	4.4 / 34	3.8 / 142	3.2 / 36	3.0 / 2	0.0 / 0
1700	3.7 / 55	3.6 / 26	3.6 / 26	3.9 / 154	3.0 / 88	2.5 / 8	0.0 / 0
1800	2.8 / 5	3.6 / 7	3.2 / 19	3.7 / 146	2.7 / 158	1.2 / 22	0.0 / 0
1900	0.0 / 0	0.0 / 0	0.0 / 0	3.8 / 75	2.5 / 227	1.7 / 55	1.0 / 1
2000	1.5 / 1	0.0 / 0	0.0 / 0	4.3 / 45	2.6 / 226	1.7 / 79	1.5 / 6
2100	0.0 / 0	0.0 / 0	0.0 / 0	4.3 / 42	2.7 / 216	2.1 / 92	1.9 / 7
2200	6.3 / 1	2.0 / 1	0.0 / 0	4.4 / 47	2.7 / 208	1.8 / 84	2.1 / 18
2300	0.0 / 0	0.0 / 0	0.0 / 0	4.0 / 55	2.9 / 182	1.9 / 106	1.7 / 14
2400	0.0 / 0	0.0 / 0	2.5 / 1	3.9 / 55	2.7 / 188	2.1 / 98	2.4 / 16
TOTAL	4.0 / 1655	3.6 / 336	3.5 / 361	3.7 / 2050	2.7 / 2939	2.1 / 1089	2.2 / 127

NOV 1, 1980 - APR 30, 1980

WINTER

PASQUILL STABILITY CATEGORY

HOOR	A	B	C	D	E	F	G
MEAN SPEED (MPH)/NUMBER OF OBSERVATIONS							
100	10.0 / 1	0.0 / 0	21.0 / 1	6.1 / 112	4.1 / 187	2.1 / 47	2.8 / 12
200	11.5 / 1	0.0 / 0	0.0 / 0	6.5 / 111	3.9 / 191	2.0 / 44	3.0 / 14
300	0.0 / 0	0.0 / 0	0.0 / 0	6.6 / 109	4.0 / 191	2.0 / 48	2.8 / 13
400	2.0 / 1	0.0 / 0	7.5 / 2	6.6 / 107	3.9 / 194	1.9 / 40	2.7 / 16
500	3.0 / 2	0.0 / 0	8.0 / 1	6.4 / 108	3.7 / 194	2.4 / 44	2.4 / 11
600	2.8 / 2	0.0 / 0	0.0 / 0	6.2 / 115	3.6 / 190	2.3 / 35	3.0 / 11
700	0.0 / 0	0.0 / 0	6.0 / 5	6.2 / 134	3.6 / 183	2.5 / 33	2.6 / 7
800	6.3 / 5	6.2 / 10	4.5 / 14	5.5 / 158	3.7 / 152	2.0 / 18	2.7 / 5
900	5.5 / 21	5.7 / 25	6.2 / 38	5.3 / 181	3.4 / 89	2.8 / 6	2.0 / 2
1000	5.8 / 62	7.0 / 35	5.4 / 56	5.1 / 141	3.6 / 61	4.2 / 3	2.0 / 2
1100	5.8 / 74	6.3 / 47	5.2 / 38	5.3 / 128	3.7 / 48	3.3 / 3	4.0 / 2
1200	6.0 / 115	6.2 / 37	6.1 / 47	5.2 / 116	4.1 / 39	5.1 / 6	5.0 / 1
1300	6.1 / 97	7.0 / 56	6.0 / 46	5.5 / 108	4.0 / 48	3.3 / 4	5.0 / 2
1400	5.9 / 82	6.6 / 44	6.2 / 57	5.7 / 114	4.2 / 59	4.0 / 3	6.5 / 2
1500	5.6 / 43	5.8 / 31	6.6 / 42	5.9 / 176	4.1 / 62	2.9 / 5	6.5 / 1
1600	5.2 / 20	5.6 / 12	5.3 / 15	5.8 / 222	4.3 / 81	2.8 / 6	3.5 / 3
1700	5.1 / 8	3.7 / 2	6.9 / 10	5.9 / 173	4.2 / 150	2.2 / 14	2.3 / 2
1800	0.0 / 0	0.0 / 0	11.0 / 1	6.1 / 135	4.0 / 198	2.0 / 18	2.1 / 7
1900	0.0 / 0	0.0 / 0	0.0 / 0	6.3 / 106	4.3 / 210	2.1 / 41	3.6 / 4
2000	4.5 / 2	0.0 / 0	0.0 / 0	6.3 / 105	4.2 / 207	1.9 / 40	1.9 / 6
2100	0.0 / 0	4.5 / 1	0.0 / 0	6.0 / 111	4.2 / 197	2.1 / 43	2.5 / 8
2200	0.0 / 0	0.0 / 0	6.0 / 1	6.0 / 102	4.3 / 197	2.1 / 45	2.6 / 14
2300	0.0 / 0	0.0 / 0	8.0 / 1	6.1 / 109	4.0 / 191	2.0 / 46	2.5 / 12
2400	12.0 / 1	0.0 / 0	10.3 / 3	6.0 / 114	4.0 / 180	1.8 / 53	2.8 / 9
TOTAL	5.9 / 557	6.4 / 300	6.0 / 378	5.9 / 3095	4.0 / 3507	2.2 / 645	2.8 / 166

CLIENT: CON EDISON CO. OF N.Y.
 LOCATION: INDIAN POINT (122M)

TABLE 31

DIURNAL VARIATION OF STABILITY CLASS AND WIND SPEED
 (CONCURRENT DATA)

MAY 1, 79, 80 - OCT 31, 79, 80

SUMMER

PASQUILL STABILITY CATEGORY

HOOR	A	B	C	D	E	F	G
	MEAN SPEED (MPH)/NUMBER OF OBSERVATIONS						
100	0.0 / 0	0.0 / 0	0.0 / 0	11.8 / 86	6.8 / 190	4.4 / 48	5.3 / 2
200	0.0 / 0	0.0 / 0	0.0 / 0	10.9 / 93	6.8 / 176	4.2 / 56	0.0 / 0
300	0.0 / 0	0.0 / 0	0.0 / 0	10.8 / 96	6.5 / 177	4.5 / 51	3.0 / 1
400	0.0 / 0	0.0 / 0	0.0 / 0	10.9 / 93	6.3 / 182	4.7 / 49	3.5 / 2
500	0.0 / 0	0.0 / 0	0.0 / 0	11.0 / 92	6.0 / 188	4.0 / 40	4.0 / 3
600	0.0 / 0	0.0 / 0	0.0 / 0	10.4 / 123	5.0 / 174	4.5 / 26	4.0 / 1
700	0.0 / 0	9.3 / 4	8.9 / 5	8.7 / 194	5.2 / 114	3.7 / 8	0.0 / 0
800	11.3 / 6	10.6 / 9	8.0 / 23	7.2 / 235	5.3 / 53	2.0 / 1	0.0 / 0
900	11.7 / 13	9.4 / 27	7.6 / 47	7.2 / 211	7.0 / 31	0.0 / 0	0.0 / 0
1000	10.8 / 32	9.0 / 63	9.6 / 52	6.7 / 167	7.0 / 18	0.0 / 0	0.0 / 0
1100	11.0 / 59	9.9 / 58	9.0 / 49	7.7 / 149	6.8 / 17	0.0 / 0	0.0 / 0
1200	10.7 / 78	9.7 / 51	9.4 / 60	9.1 / 128	10.8 / 11	12.0 / 1	0.0 / 0
1300	11.1 / 59	10.2 / 65	10.4 / 50	9.9 / 148	11.0 / 14	0.0 / 0	0.0 / 0
1400	11.6 / 55	11.1 / 68	10.7 / 46	9.7 / 147	12.0 / 14	0.0 / 0	0.0 / 0
1500	11.4 / 36	12.5 / 47	10.8 / 51	10.5 / 179	10.7 / 14	10.0 / 1	0.0 / 0
1600	13.3 / 14	11.9 / 28	11.1 / 45	11.0 / 210	10.7 / 26	0.0 / 0	0.0 / 0
1700	10.3 / 2	12.3 / 10	11.7 / 23	11.3 / 245	11.0 / 42	14.0 / 2	0.0 / 0
1800	0.0 / 0	15.0 / 1	10.7 / 3	11.3 / 198	10.1 / 122	6.0 / 1	0.0 / 0
1900	0.0 / 0	0.0 / 0	0.0 / 0	11.7 / 118	7.7 / 199	4.9 / 7	0.0 / 0
2000	0.0 / 0	0.0 / 0	0.0 / 0	12.3 / 86	9.5 / 217	5.5 / 21	0.0 / 0
2100	0.0 / 0	0.0 / 0	0.0 / 0	12.5 / 88	6.8 / 205	4.8 / 34	0.0 / 0
2200	0.0 / 0	0.0 / 0	0.0 / 0	12.2 / 100	7.8 / 183	5.4 / 43	3.5 / 1
2300	0.0 / 0	0.0 / 0	8.0 / 1	11.6 / 89	7.7 / 187	5.5 / 49	0.0 / 0
2400	0.0 / 0	0.0 / 0	0.0 / 0	11.4 / 91	7.2 / 185	5.0 / 50	7.0 / 1
TOTAL	11.2 / 356	10.4 / 431	9.8 / 455	10.0 / 3358	7.6 / 2739	4.8 / 468	4.3 / 11

NOV 1, 79, 80 - APR 30, 79, 80

WINTER

PASQUILL STABILITY CATEGORY

HOOR	A	B	C	D	E	F	G
	MEAN SPEED (MPH)/NUMBER OF OBSERVATIONS						
100	0.0 / 0	0.0 / 0	0.0 / 0	13.9 / 172	8.6 / 155	4.1 / 25	10.4 / 4
200	0.0 / 0	0.0 / 0	0.0 / 0	13.5 / 174	6.5 / 148	5.3 / 32	8.0 / 3
300	0.0 / 0	0.0 / 0	0.0 / 0	13.7 / 164	6.6 / 160	4.9 / 30	8.3 / 3
400	0.0 / 0	0.0 / 0	0.0 / 0	13.2 / 167	6.4 / 155	4.4 / 33	10.8 / 2
500	0.0 / 0	0.0 / 0	0.0 / 0	13.4 / 163	7.8 / 163	4.1 / 28	10.0 / 2
600	0.0 / 0	0.0 / 0	0.0 / 0	13.4 / 164	7.0 / 164	4.9 / 24	6.9 / 4
700	0.0 / 0	0.0 / 0	0.0 / 0	13.5 / 167	6.9 / 166	5.1 / 21	4.0 / 1
800	0.0 / 0	0.0 / 0	14.5 / 4	12.7 / 195	7.3 / 161	3.8 / 15	0.0 / 0
900	0.0 / 0	10.7 / 5	13.0 / 12	12.0 / 241	6.5 / 93	7.9 / 6	0.0 / 0
1000	14.0 / 1	14.3 / 7	11.2 / 25	11.3 / 260	7.1 / 62	6.8 / 3	0.0 / 0
1100	11.7 / 8	10.8 / 19	13.4 / 32	11.6 / 243	7.4 / 57	8.5 / 2	0.0 / 0
1200	14.2 / 15	13.4 / 24	13.7 / 45	11.8 / 220	5.3 / 54	10.0 / 3	0.0 / 0
1300	15.5 / 12	12.6 / 24	14.1 / 44	12.2 / 227	10.3 / 52	8.0 / 1	7.0 / 1
1400	15.0 / 4	12.9 / 14	15.7 / 41	12.4 / 241	10.0 / 55	21.0 / 1	12.0 / 1
1500	13.0 / 2	10.6 / 5	13.6 / 26	13.2 / 270	10.3 / 56	13.0 / 2	0.0 / 0
1600	12.8 / 3	11.3 / 2	15.6 / 8	13.1 / 278	10.4 / 65	10.3 / 4	0.0 / 0
1700	0.0 / 0	0.0 / 0	20.5 / 3	13.2 / 239	10.5 / 112	8.4 / 5	0.0 / 0
1800	0.0 / 0	0.0 / 0	0.0 / 0	13.7 / 201	9.5 / 146	10.5 / 10	17.0 / 1
1900	0.0 / 0	0.0 / 0	0.0 / 0	13.6 / 172	9.8 / 178	10.4 / 10	0.0 / 0
2000	7.5 / 1	0.0 / 0	0.0 / 0	13.6 / 175	9.6 / 167	6.7 / 16	0.0 / 0
2100	0.0 / 0	0.0 / 0	0.0 / 0	13.2 / 174	9.5 / 162	6.0 / 22	0.0 / 0
2200	0.0 / 0	13.0 / 1	0.0 / 0	12.9 / 168	9.1 / 161	5.6 / 25	4.5 / 1
2300	8.0 / 1	16.0 / 1	0.0 / 0	13.1 / 168	6.5 / 160	5.3 / 25	2.0 / 1
2400	0.0 / 0	0.0 / 0	0.0 / 0	13.1 / 176	6.5 / 152	4.8 / 26	8.6 / 3
TOTAL	13.9 / 51	12.4 / 102	13.9 / 240	12.9 / 4819	6.6 / 2986	5.6 / 369	8.6 / 27

CLIENT: CON EDISON CO. OF N.Y.
 LOCATION: INDIAN POINT (DELTA-E 122M-60M)

TABLE 32
 DIURNAL VARIATION OF STABILITY CLASS AND WIND SPEED
 (CONCURRENT DATA)

MAY 1, 1980 - OCT 31, 1980

SUMMER

HOUR	PASQUILL STABILITY CATEGORY						
	A	B	C	D	E	F	G
MEAN SPEED (MPH)/NUMBER OF OBSERVATIONS							
100	0.0 / 0	0.0 / 0	15.0 / 1	9.8 / 166	5.6 / 138	5.6 / 19	1.6 / 2
200	0.0 / 0	0.0 / 0	15.3 / 2	9.9 / 161	5.2 / 137	4.2 / 23	2.0 / 2
300	0.0 / 0	0.0 / 0	17.5 / 1	9.5 / 171	5.3 / 126	4.3 / 24	2.3 / 3
400	0.0 / 0	0.0 / 0	18.0 / 1	9.2 / 169	5.0 / 135	3.6 / 19	4.3 / 2
500	0.0 / 0	0.0 / 0	0.0 / 0	9.3 / 167	5.1 / 132	3.3 / 19	4.9 / 5
600	0.0 / 0	0.0 / 0	14.3 / 3	9.5 / 166	5.1 / 122	4.0 / 28	4.6 / 5
700	5.5 / 1	2.0 / 1	10.0 / 3	9.0 / 202	4.6 / 105	2.8 / 12	3.0 / 1
800	13.3 / 3	0.0 / 0	12.8 / 5	7.7 / 260	4.0 / 52	2.7 / 1	0.0 / 0
900	7.0 / 1	15.3 / 2	9.0 / 6	8.0 / 267	5.3 / 52	3.0 / 1	0.0 / 0
1000	0.0 / 0	0.0 / 0	11.7 / 12	8.5 / 277	4.0 / 43	0.0 / 0	0.0 / 0
1100	0.0 / 0	14.5 / 2	11.7 / 3	9.5 / 271	5.2 / 50	0.0 / 0	0.0 / 0
1200	0.0 / 0	14.0 / 2	11.7 / 9	10.0 / 281	6.4 / 35	4.5 / 1	12.0 / 1
1300	13.0 / 1	11.5 / 3	9.6 / 4	10.7 / 282	7.7 / 38	0.0 / 0	0.0 / 0
1400	0.0 / 0	13.3 / 6	11.9 / 20	10.9 / 265	7.3 / 39	0.0 / 0	0.0 / 0
1500	5.5 / 2	13.0 / 9	11.4 / 25	11.1 / 254	9.1 / 38	0.0 / 0	0.0 / 0
1600	0.0 / 0	9.9 / 4	13.3 / 12	11.3 / 271	9.0 / 38	0.0 / 0	0.0 / 0
1700	9.0 / 1	10.0 / 1	12.8 / 5	11.5 / 282	10.3 / 33	10.5 / 2	0.0 / 0
1800	5.0 / 1	15.0 / 1	0.0 / 0	11.2 / 259	9.0 / 64	0.0 / 0	0.0 / 0
1900	12.0 / 1	0.0 / 0	0.0 / 0	10.8 / 228	9.2 / 94	2.0 / 1	0.0 / 0
2000	0.0 / 0	0.0 / 0	0.0 / 0	10.9 / 196	8.0 / 122	6.9 / 6	0.0 / 0
2100	4.0 / 1	26.0 / 1	0.0 / 0	10.9 / 194	7.3 / 120	4.1 / 11	0.0 / 0
2200	13.0 / 1	0.0 / 0	23.0 / 1	10.1 / 193	7.0 / 117	5.7 / 13	3.5 / 2
2300	0.0 / 0	4.5 / 1	13.0 / 2	10.1 / 173	6.0 / 136	4.4 / 14	0.0 / 0
2400	0.0 / 0	0.0 / 0	15.5 / 2	9.8 / 176	6.2 / 128	4.3 / 21	0.0 / 0
TOTAL	9.3 / 13	12.6 / 33	12.1 / 117	10.0 / 5337	6.4 / 2094	4.3 / 221	4.0 / 23

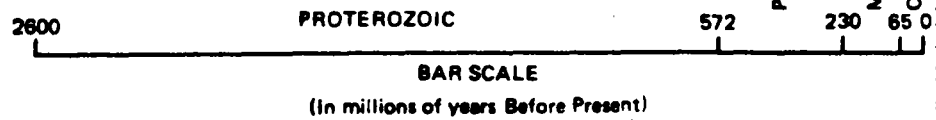
NOV 1, 1980 - APR 30, 1980

WINTER

HOUR	PASQUILL STABILITY CATEGORY						
	A	B	C	D	E	F	G
MEAN SPEED (MPH)/NUMBER OF OBSERVATIONS							
100	5.0 / 1	0.0 / 0	0.0 / 0	12.4 / 244	7.3 / 97	10.0 / 13	4.0 / 1
200	0.0 / 0	0.0 / 0	3.0 / 1	12.3 / 235	7.4 / 108	8.8 / 11	4.0 / 2
300	0.0 / 0	0.0 / 0	0.0 / 0	12.7 / 230	7.0 / 114	6.8 / 11	2.5 / 2
400	0.0 / 0	0.0 / 0	0.0 / 0	12.4 / 228	6.8 / 116	4.5 / 12	1.5 / 1
500	7.0 / 1	0.0 / 0	0.0 / 0	12.2 / 236	5.9 / 105	5.4 / 14	0.0 / 0
600	9.0 / 0	8.0 / 1	11.0 / 1	11.7 / 235	6.2 / 105	5.5 / 12	4.0 / 2
700	0.0 / 0	0.0 / 0	0.0 / 0	12.1 / 225	6.2 / 117	4.8 / 13	0.0 / 0
800	10.0 / 1	0.0 / 0	19.5 / 2	12.5 / 224	6.3 / 118	3.7 / 10	0.0 / 0
900	8.5 / 1	5.0 / 1	33.0 / 1	12.2 / 258	6.0 / 91	4.7 / 5	0.0 / 0
1000	0.0 / 0	30.0 / 1	11.5 / 2	11.6 / 283	6.7 / 69	2.5 / 3	0.0 / 0
1100	12.0 / 1	11.5 / 1	31.5 / 2	11.8 / 292	7.4 / 61	3.6 / 4	0.0 / 0
1200	10.5 / 2	0.0 / 0	27.7 / 3	12.3 / 296	6.6 / 59	15.0 / 1	0.0 / 0
1300	14.0 / 4	30.0 / 1	23.8 / 5	12.5 / 299	9.7 / 51	6.0 / 1	0.0 / 0
1400	11.0 / 2	30.6 / 2	19.0 / 1	12.8 / 298	10.4 / 55	10.2 / 3	0.0 / 0
1500	4.3 / 3	26.5 / 2	21.1 / 7	13.0 / 290	10.0 / 56	9.5 / 2	18.0 / 1
1600	4.0 / 1	0.0 / 0	35.0 / 1	13.1 / 294	10.4 / 61	8.8 / 3	0.0 / 0
1700	4.5 / 1	0.0 / 0	22.0 / 1	12.7 / 285	10.8 / 72	0.0 / 0	0.0 / 0
1800	0.0 / 0	0.0 / 0	6.0 / 1	12.5 / 269	10.0 / 84	11.5 / 6	0.0 / 0
1900	0.0 / 0	0.0 / 0	0.0 / 0	12.3 / 262	9.7 / 97	31.0 / 1	0.0 / 0
2000	0.0 / 0	26.0 / 1	10.0 / 1	12.3 / 253	8.7 / 99	17.6 / 5	0.0 / 0
2100	13.0 / 1	0.0 / 0	12.5 / 1	12.3 / 240	8.6 / 110	9.5 / 6	0.0 / 0
2200	8.5 / 2	11.0 / 1	8.0 / 1	11.9 / 234	6.1 / 108	7.5 / 5	0.0 / 0
2300	12.0 / 2	0.0 / 0	13.0 / 1	12.1 / 234	7.0 / 115	9.9 / 4	0.0 / 0
2400	4.0 / 1	16.0 / 1	0.0 / 0	12.2 / 229	7.6 / 111	5.5 / 13	12.3 / 2
TOTAL	9.9 / 24	21.0 / 12	20.4 / 32	12.3 / 6178	7.8 / 2179	7.2 / 156	6.3 / 11

GEOLOGIC TIME SCALE

ABSOLUTE AGE (In millions of years Before Present)	ERA	PERIOD	EPOCH	SIGNIFICANT EVENTS		
— 0.01 —	CENOZOIC	QUATERNARY		HOLOCENE (RECENT)	WISCONSINAN GLACIATION	
— 1.8 —				PLEISTOCENE		
— 22.5 —		TERTIARY	NEOGENE			PLIOCENE
						MIOCENE
			PALEOGENE			OLIGOCENE
						EOCENE
						PALEOCENE
— 65 —	MESOZOIC	CRETACEOUS		OPENING OF ATLANTIC BREAK UP OF PANGEA		
JURASSIC						
TRIASSIC						
— 141 —	PALEOZOIC	PERMIAN		ALLEGHENIAN OROGENY		
— 195 —		Carboniferous			PENNSYLVANIAN	
— 230 —				MISSISSIPPIAN		
— 280 —		DEVONIAN		ACADIAN OROGENY		
— 345 —		SILURIAN		TACONIC OROGENY		
— 395 —		ORDOVICIAN				
— 435 —		CAMBRIAN				
— 502 —		PROTEROZOIC	HADRYNIAN		OPENING OF IAPETUS GRENVILLIAN OROGENY	
— 572 —			HELIKIAN			
— 1000 —			APHEBIAN			
— 1800 —	PRECAMBRIAN	ARCHEAN				
— 2600 —						
— 4500 —						



(After: F.W.B. van Eysinga, 1978)

TABLE 1

LOCATION AGE	MANHATTAN PRONG THIS REPORT	DUTCHESS COUNTY, NEW YORK FISHER, (1962a, 1962b) KNOPF, (1962)	WESTERN MASSACHUSETTS AND CONNECTICUT ZEN AND HARTSHORN, (1966) ZEN, (1967)	WESTERN VERMONT DOLL AND OTHERS, (1961) ZEN, (1961)				
MIDDLE ORDOVICIAN	MANHATTAN SCHIST	C-MEMBER	WALLOOMSAC FORMATION	WALLOOMSAC FORMATION	IRA FORMATION			
		B-MEMBER				BALMVILLE LIMESTONE	INTERBEDDED LIMESTONE AND SCHIST	WHIPPLE MARBLE MEMBER
		A-MEMBER INTERBEDDED MARBLE AND SCHIST						
EARLY ORDOVICIAN	MARBLE	E-MEMBER	STOCKBRIDGE GROUP & WAPPINGERS GROUP	STOCKBRIDGE FORMATION	CHIPMAN FORMATION BASCOM FORMATION			
		D-MEMBER				COPAKE LIMESTONE ROCHDALE LIMESTONE	UNIT-G	CUTTING DOLOMITE
						MALCYON LAKE	UNIT-F UNIT-E UNIT-D	SHELBURNE FORMATION
CAMBRIAN	INWOOD	C-MEMBER	STOCKBRIDGE GROUP & WAPPINGERS GROUP	STOCKBRIDGE FORMATION	CLARENDON SPRINGS DOLOMITE DANBY FORMATION			
		B-MEMBER				BRIARCLIFF DOLOMITE	UNIT-C	
						PINE PLAINS FORMATION	UNIT-B	WINDOOSKI DOLOMITE MONKTON QUARTZITE
		A-MEMBER				STISSING DOLOMITE	UNIT-A	DUNHAM DOLOMITE
	LOWERRE QUARTZITE	POUGHQUAG QUARTZITE		CHESHIRE QUARTZITE DALTON FORMATION	CHESHIRE QUARTZITE DALTON FORMATION			
PRECAMBRIAN	FORDHAM GNEISS YONKERS GNEISS	GNEISS		BERKSHIRE MASSIF	MOUNT HOLLY COMPLEX			

PROPOSED CORRELATION OF THE STRATIGRAPHIC SUBDIVISIONS IN THE MANHATTAN PRONG
WITH ROCKS IN ADJACENT AREAS
(AFTER HALL, 1968)

IP2
FSAR UPDATE

CHAPTER 3
REACTOR

3.0 DESCRIPTION

The reactor core has a number of fuel regions with fuel assemblies arranged in a zone and/or checkered core pattern. The fuel rods are cold worked Zircaloy or ZIRLO™ tubes containing slightly enriched uranium-dioxide fuel.

The fuel assembly is a canless type with the basic assembly consisting of the rod cluster control guide thimbles attached to the grids and the top and bottom nozzles. The fuel rods are held by the spring clip grid in this assembly, which provides support for the fuel rods.

High parasitic (HIPAR) fuel was used for the initial fuel and reload fuel through Cycle 4. Low parasitic (LOPAR) fuel was loaded for Cycles 5 through 9, and optimized fuel assemblies (OFA) were loaded for Cycles 10, 11, and 12. For Cycles 13, 14 and 15, 15x15 VANTAGE+ fuel assemblies were loaded as the feed fuel. For Cycle 16, 15x15 Vantage + fuel assemblies with Performance + enhancements are loaded as feed fuel. For Cycle 17 and 18, 15x15 Upgraded fuel design assemblies have been loaded as feed fuel.

Rod cluster control assemblies and wet annular burnable absorber rods are inserted into the guide thimbles of the fuel assemblies. The absorber sections of the control rods are fabricated of silver-indium-cadmium alloy sealed in stainless steel tubes.

The control rod drive mechanisms for the full-length rod cluster control assemblies are of the magnetic latch type. The latches are controlled by three magnetic coils. They are so designed that upon a loss of power to the coils, the rod cluster control assembly is released and falls by gravity to shut down the reactor.

3.1 DESIGN BASES

3.1.1 Performance Objectives

The reactor thermal power analyzed is 3216 MWt (3230 MWt total NSSS power), which is the licensed power rating. Calculations and operating experience indicate that hot channel factors will be considerably less than those used for design purposes in this application.

The initial reactor core fuel loading and programming were designed to yield the first cycle average burnup of 16,100 MWd/metric ton uranium (MTU). Cycles 2 through 4 reload designs yielded an average cycle burnup of 10,000 MWd/metric ton uranium, and Cycles 5 through 10 yielded an average cycle burnup of 13,500 MWd/metric ton uranium. Cycles 11, 12, and 13 achieved burnups of 18,094 MWd/MTU, 20,674 MWd/MTU, and 21,650 MWd/MTU, all of which included coastdown operation. Cycle 14 achieved a cycle burnup of 18,970 MWd/MTU. Cycle 15 achieved a cycle burnup of 22,110 MWd/MTU. Cycle 16 achieved a cycle burnup of 23,950 MWd/MTU with a coastdown. Cycle 17 was designed to achieve a cycle burnup of 18,881 MWd/MTU. Cycle 18 is designed to achieve a cycle burnup of 25,077 MWd/MTU. The fuel rod cladding is designed to maintain its integrity for the anticipated core life. The effects of gas release, fuel dimensional changes, and corrosion-induced or irradiation-induced changes in the mechanical properties of cladding are considered in the design of the fuel assemblies.

IP2
FSAR UPDATE

Rod cluster control assemblies are employed to provide sufficient reactivity control to terminate any credible power transient prior to reaching the minimum departure from nucleate boiling ratio (DNBR). This is accomplished by ensuring sufficient cluster control worth to shut the reactor down by at least 1.3-percent throughout core life in the hot condition with the most reactive cluster control stuck in the fully withdrawn position. Redundant equipment is provided to add soluble poison to the reactor coolant in the form of boric acid to maintain shutdown margin when the reactor is cooled to ambient temperatures.

Experimental measurements from critical experiments or operating reactors, or both, are used to validate the methods employed in the design. During design, nuclear parameters have been calculated for every phase of operation of the first core and reload cycles and, where applicable, are compared with design limits to show that an adequate margin of safety exists.

In the thermal hydraulic design of the core, the maximum fuel and clad temperatures during normal reactor operation and at overpower conditions have been conservatively evaluated and found to be consistent with safe operating limitations.

3.1.2 Principal Design Criteria

3.1.2.1 Reactor Core Design

Criterion: The reactor core with its related controls and protection systems shall be designed to function throughout its design lifetime without exceeding acceptable fuel damage limits, which have been stipulated and justified. The core and related auxiliary system designs shall provide this integrity under all expected conditions of normal operation with appropriate margins for uncertainties and for specified transient situations, which can be anticipated. (GDC 6)

The reactor core, with its related control and protection system, is designed to function throughout its design lifetime without exceeding acceptable fuel damage limits. The core design, together with reliable process and decay heat removal systems, provides for this capability under all expected conditions of normal operation with appropriate margins for uncertainties and anticipated transient situations, including the effects of the loss of reactor coolant flow (Section 14.1.6), trip of the turbine generator (Section 14.1.8), loss of normal feedwater (Section 14.1.9), and loss of all offsite power (Section 14.1.12). The reactor protection system is designed to actuate a reactor trip for any anticipated combination of plant conditions, when necessary, to ensure a minimum departure from nucleate boiling (DNB) ratio equal to or greater than the applicable safety analysis limit DNBR.

The integrity of fuel cladding is ensured by preventing excessive fuel swelling, excessive fuel densification, excessive clad heating, excessive cladding stress and strain. This is achieved by designing the fuel rods so that the following conservative limits are not exceeded during normal operation or any anticipated transient condition (Condition II events):

1. Minimum DNB ratio equal to or greater than the safety analysis limit DNBR.
2. Fuel center temperature below 4700°F.
3. Internal gas pressure (limited to value below that which could cause the diameter-to-gap to increase due to outward clad creep during steady-state operation, and which could cause excessive DNB propagation to occur).

IP2
FSAR UPDATE

4. Clad stresses less than the Zircaloy or ZIRLO™ yield strength.
5. Clad strain less than 1-percent.

The ability of fuel designed and operated to these criteria to withstand postulated normal and abnormal service conditions is shown by analyses described in Chapter 14 to satisfy the demands of plant operation well within applicable regulatory limits.

The reactor coolant pumps provided for the plant are supplied with sufficient rotational inertia to maintain an adequate flow coastdown and prevent core damage in the event of a simultaneous loss of power to all pumps as discussed in section 14.1.6.1.

In the unlikely event of a turbine trip from full power without an immediate reactor trip, the subsequent reactor coolant temperature increase and volume surge to the pressurizer result in a high pressurizer pressure trip and thereby prevent fuel damage for this transient. A loss of external electrical load of 50-percent of full power or less is normally controlled by rod cluster insertion together with a controlled steam dump to the condenser to prevent a large temperature and pressure increase in the reactor coolant system and thus prevent a reactor trip. In this case, the overpower-temperature protection would guard against any combination of pressure, temperature, and power, which could result in a DNB ratio less than the applicable safety analysis limit DNBR during the transient.

In neither the turbine trip nor the loss-of-flow events do the changes in coolant conditions provoke a nuclear power excursion because of the large system thermal inertia and relatively small void fraction as discussed in UFSAR sections 14.1.8 and 14.1.6, respectively. Protection circuits actuated directly by the coolant conditions identified with core limits are therefore effective in preventing core damage.

3.1.2.2 Suppression of Power Oscillations

Criterion: The design of the reactor core with its related controls and protection systems shall ensure that power oscillations, the magnitude of which could cause damage in excess of acceptable fuel damage limits, are not possible or can be readily suppressed. (GDC 7)

The potential for possible spatial oscillations of power distribution for this core has been reviewed. It is concluded that low frequency xenon oscillations may occur in the axial dimension, and the control rods are provided to suppress these oscillations. The core is expected to be stable to xenon oscillations in the X-Y dimension. Ex-core instrumentation is provided to obtain necessary information concerning power distribution. This instrumentation is adequate to enable the operator to monitor and control xenon induced oscillations. (In-core instrumentation is used periodically to calibrate and verify the information provided by the ex-core instrumentation. The analysis, detection, and control of these oscillations is discussed in Reference 1.)

3.1.2.3 Redundancy of Reactivity Control

Criterion: Two independent reactivity control systems, preferably of different principles, shall be provided. (GDC 27)

IP2
FSAR UPDATE

Two independent reactivity control systems are provided, one involving rod cluster control assemblies and the other involving chemical shim.

3.1.2.4 Reactivity Hot Shutdown Capability

Criterion: The reactivity control systems provided shall be capable of making and holding the core subcritical from any hot standby or hot operating condition. (GDC 28)

The reactivity control systems provided are capable of making and holding the core subcritical from any hot standby or hot operating condition, including those resulting from power changes. The maximum excess reactivity expected for the core occurs for the cold, clean condition at the beginning-of-life of the initial core.

The rod cluster control assemblies are divided into control banks and shutdown banks. The control banks used in combination with chemical shim control provide control of the reactivity changes of the core throughout the life of the core during power operation. These banks of rod cluster control assemblies are used to compensate for short term reactivity changes at power that might be produced due to variations in reactor power level or in coolant temperature. The chemical shim control is used to compensate for the more slowly occurring changes in reactivity throughout core life such as those due to fuel depletion and fission product buildup.

3.1.2.5 Reactivity Shutdown Capability

Criterion: One of the reactivity control systems provided shall be capable of making the core subcritical under any anticipated operating condition including anticipated operational transients sufficiently fast to prevent exceeding acceptable fuel damage limits. Shutdown margin should assure subcriticality with the most reactive control rod fully withdrawn. (GDC 29)

The reactor core, together with the reactor control and protection system, is designed so that the minimum allowable DNBR is equal to or greater than the applicable safety analysis limit DNBR and there is no fuel melting during normal operation including anticipated transients.

The shutdown banks are provided to supplement the control banks of rod cluster control assemblies to make the reactor at least 1.3-percent subcritical ($k_{\text{eff}} = 0.987$) following trip from any credible operating condition assuming the most reactive rod cluster control assembly is in the fully withdrawn position.

Sufficient shutdown capability is also provided so that the minimum DNBR is equal to or greater than the applicable safety analysis limit DNBR, assuming the most reactive rod to be in the fully withdrawn position for the most severe anticipated cooldown transient associated with a single active failure, e.g., accidental opening of a steam bypass, or relief valve, or safety valve stuck open. This is achieved by the combination of control rods and automatic boric acid injection via the emergency core cooling system. The minimum design margin is 1.3-percent throughout core life, as discussed in UFSAR Section 14.2.5.2, assuming the maximum worth control rod is in the fully withdrawn position allowing 10-percent uncertainty in the control rod worth calculations.

Technical Specification 3.1.1 specifies the actual minimum required shutdown margin for core design.

Manually controlled boric acid addition is used to maintain the shutdown margin for the long-term conditions of xenon decay and plant cooldown. Redundant equipment is provided to guarantee the capability of adding boric acid to the reactor coolant system.

3.1.2.6 Reactivity Holddown Capability

Criterion: The reactivity control systems provided shall be capable of making the core subcritical under credible accident conditions with appropriate margins for contingencies and limiting any subsequent return to power such that there will be no undue risk to the health and safety of the public. (GDC 30)

Normal reactivity shutdown capability is provided by control rods following a trip signal, with boric acid injection used to compensate for the long-term xenon decay transient and for plant cooldown. As discussed in response to the previous criteria, the shutdown capability maintains the minimum DNBR above the limiting value and prevents exceeding core safety limits as a result of the cooldown associated with a safety valve stuck fully open.

Any time that the reactor is at power, the quantity of boric acid retained in the boric acid tanks and ready for injection always exceeds that quantity required for the normal cold shutdown. This quantity always exceeds the quantity of boric acid required to bring the reactor to hot shutdown and to compensate for subsequent xenon decay. Boric acid is pumped from the boric acid tanks by one of two boric acid transfer pumps to the suction of one of three charging pumps, which injects boric acid into the reactor coolant. Any charging pump and either boric acid transfer pump can be operated from diesel-generator power on loss of station power.

On the basis of the above, the injection of boric acid is shown to afford backup reactivity shutdown capability, diverse from rod cluster controls, which normally serve this function in the short-term situation. Shutdown for long-term and reduced temperature conditions can be accomplished with boric acid injection using redundant components, thus achieving the measure of reliability implied by the criterion.

Alternately, boric acid solution at lower concentration can be supplied from the refueling water storage tank. This solution can be transferred directly by the charging pumps or alternately by the safety injection pumps. The reduced boric acid concentration lengthens the time required to achieve equivalent shutdown.

3.1.2.7 Reactivity Control Systems Malfunction

Criterion: The reactor protection systems shall be capable of protecting against any single malfunction of the reactivity control system, such as unplanned continuous withdrawal (not ejection or dropout of a control rod, by limiting reactivity transients to avoid exceeding acceptable fuel damage limits. (GDC 31)

The reactor protection systems are capable of protecting against any single credible malfunction of the reactivity control system, by limiting reactivity transients to avoid exceeding acceptable fuel damage limits.

Reactor shutdown with rods is completely independent of the normal rod control functions since the trip breakers completely interrupt the power to the rod mechanisms regardless of existing control signals.

IP2
FSAR UPDATE

Details of the effects of continuous withdrawal of a control rod and continuous deboration are described in Section 14.1 and Section 9.2, respectively.

3.1.2.8 Maximum Reactivity Worth of Control Rods

Criterion: Limits, which include reasonable margin, shall be placed on the maximum reactivity worth of control rods or elements and on rates at which reactivity can be increased to ensure that the potential effects of a sudden or large change of reactivity cannot (a) rupture the reactor coolant pressure boundary or (b) disrupt the core, its support structures, or other vessel internals sufficiently to lose capability of cooling the core. (GDC 32)

Limits, which include considerable margin, are placed on the maximum reactivity worth of control rods or elements and on rates at which reactivity can be increased to ensure that the potential effects of a sudden or large change of reactivity cannot (a) rupture the reactor coolant pressure boundary or (b) disrupt the core, its support structures, or other vessel internals so as to lose capability to cool the core.

The reactor control system employs control rod clusters. A portion of these are designated shutdown rods and are fully withdrawn during power operation. The remaining rod clusters comprise the control groups, which are used to control load and reactor coolant temperature. The rod cluster drive mechanisms are wired into preselected groups, and are therefore prevented from being withdrawn in other than their respective groups. The rod drive mechanism is of the magnetic latch type and the coil actuation is sequenced to provide variable speed rod travel. The maximum reactivity insertion rate is analyzed in the detailed plant analysis assuming two of the highest worth groups to be accidentally withdrawn at maximum speed. This yields a reactivity insertion rate of the order of 70 pcm/sec, which is well within the capability of the overpower-overtemperature protection circuits to prevent core damage.

No single credible mechanical or electrical control system malfunction can cause a rod cluster to be withdrawn at a speed greater than 72 steps per min (approximately 45-in. per min) when the Rod Control System is operating in the MANUAL mode. Single credible electrical system failures can result in withdrawal speeds greater than 72 steps per min during automatic operation. The automatic rod withdrawal feature however, has been permanently defeated at IP2.

3.1.3 Safety Limits

The reactor is capable of meeting the performance objectives throughout core life under both operating and malfunction conditions without violating the integrity of the fuel elements. Thus the release of unacceptable amounts of fission products to the coolant is prevented.

The limiting conditions for operation established in the Technical Specifications specify the functional capacity of performance levels permitted to assure safe operation of the facility.

Design parameters, which are pertinent to safety limits are specified below for the nuclear, reactivity control, thermal and hydraulic, and mechanical aspects of the design.

IP2
FSAR UPDATE

3.1.3.1 Nuclear Limits

The nuclear axial peaking factor F_z , and the nuclear enthalpy rise hot channel factor $F^N_{\Delta_H}$ are limited in their combined relationship so as not to exceed the F_Q or DNBR limits.

Potential axial xenon oscillations are controlled with control rods to preclude adverse core conditions. The protection system ensures that the nuclear core limits are not exceeded.

For Cycles 13 and beyond, a cycle specific Core Operating Limits Report (COLR) is generated. Provided in the COLR is the cycle specific F_Q and F_{Δ_H} limits as well as the limiting $K(z)$ curve (normalized F_{q^*} Power versus core height axial envelope). Also, cycle specific rod insertion limits and axial flux difference band width (ΔI) limits are provided in the COLR. Utilization of the COLR provides maximized operational and/or design flexibility, while adherence to the limits of the COLR and plant Technical Specifications assures that DNB and overpower design limits are met. The expected values for the nuclear heat flux and nuclear enthalpy rise hot channel factors for the current cycle are provided in Table 3.2-1A.

3.1.3.2 Reactivity Control Limits

The control system and the operational procedures provide adequate control of the core reactivity and power distribution. The following control limits are met:

1. A minimum hot shutdown margin of 1.3% K_{eff} is available throughout core life assuming a 10-percent uncertainty in the control rod calculation.
2. This shutdown margin is maintained with the most reactive rod cluster control assembly in the fully withdrawn position.
3. The shutdown margin is maintained at ambient temperature by the use of soluble poison.

Technical Specification 3.1.1 specifies the actual minimum required shutdown margin for core design.

3.1.3.3 Thermal and Hydraulic Limits

The reactor core is designed to meet the following limiting thermal and hydraulic criteria:

1. The minimum allowable DNBR during normal operation, including anticipated transients, is equal to the applicable safety analysis limit DNBR.
2. Fuel temperature not to exceed 4700°F during any anticipated operating condition or anticipated malfunction.

To maintain fuel rod integrity and prevent fission product release, it is necessary to prevent clad overheating under all operating conditions. This is accomplished by preventing a departure from nucleate boiling (DNB), which would cause a large decrease in the heat transfer coefficient between the fuel rods and the reactor coolant, resulting in high clad temperatures.

IP2
FSAR UPDATE

The ratio of the heat flux causing DNB at a particular core location (as predicted by the WRB-1 correlation) to the existing heat flux at the same core location is the DNB ratio. A DNB ratio of 1.17 for the WRB-1 correlation corresponds to a 95-percent probability at a 95-percent confidence level that DNB does not occur. The DNB ratio for the W-3 correlation is 1.3 for pressure from 1000 to 2300 psia and 1.45 for pressure from 500 to 1000 psia.

3.1.3.4 Mechanical Limits

3.1.3.4.1 Reactor Internals

The reactor internal components are designed to withstand the stresses resulting from startup, steady state operation with any number of pumps running, and shutdown conditions. No damage to the reactor internals occurs as a result of loss of pumping power.

Lateral deflection and torsional rotation of the lower end of the core barrel is limited to prevent excessive movements resulting from seismic disturbances and thus prevent interference with rod cluster control assemblies. Core drop in the event of failure of the normal supports is limited so that the rod cluster control assemblies do not disengage from the fuel assembly guide thimbles.

The internals are further designed to maintain their functional integrity in the event of a major loss-of-coolant accident. The dynamic loading resulting from the pressure oscillations because of a loss-of-coolant accident does not cause sufficient deformation to prevent rod cluster control assembly insertion.

3.1.3.4.2 Fuel Assemblies

The fuel assemblies are designed to perform satisfactorily throughout their lifetime. The loads, stresses, and strains resulting from the combined effects of flow induced vibrations, earthquakes, reactor pressure, fission gas pressure, fuel growth, thermal strain, and differential expansion during both steady state and transient reactor operating conditions have been considered in the design of the fuel rods and fuel assemblies. The assemblies are also structurally designed to withstand handling and shipping loads prior to irradiation, and to maintain sufficient integrity at the completion of design burnup to permit safe removal from the core, subsequent handling during cooldown, shipment, and fuel reprocessing.

The fuel rods are supported at nine locations along their length within the fuel assemblies by grid assemblies, which are designed to maintain control of the lateral spacing between the rods through the design life of the assemblies. The magnitude of the support loads provided by the grids is established to minimize possible fretting without overstressing the cladding at the points of contact between the grids and fuel rods and without imposing restraints of sufficient magnitude to result in buckling or distortion of the rods. In addition, there are 3 Intermediate Flow Mixing (IFM) grids spaced along the fuel assembly and a protective grid (P-grid) on the bottom of the assembly. These grids do not provide any support function.

The fuel rod cladding is designed to withstand operating pressure loads without rupture and to maintain encapsulation of the fuel throughout the design life.

3.1.3.4.3 Rod Cluster Control Assemblies

The criteria used for the design of the cladding on the individual absorber rods in the rod cluster control assemblies are similar to those used for the fuel rod cladding. The cladding is designed to be free standing under all operating conditions and will maintain encapsulation of the absorber material throughout the absorber rod design life. Allowance for wear during operation is included for the rod cluster control assembly cladding thickness.

Adequate clearance is provided between the absorber rods and the guide thimbles, which position the rods within the fuel assemblies so that coolant flow along the length of the absorber rods is sufficient to remove the heat generated without overheating of the absorber cladding. The clearance is also sufficient to compensate for any misalignment between the absorber rods and guide thimbles and to prevent mechanical interference between the rods and guide thimbles under any operating conditions.

3.1.3.4.4 Control Rod Drive Assembly

Each control rod drive assembly is designed as a hermetically sealed unit to prevent leakage of reactor coolant. All pressure-containing components are designed to meet the requirements of the ASME Code, Section III, Nuclear Vessels for Class A vessels.

The control rod drive assemblies for the full length rods provide rod cluster control assembly insertion and withdrawal rates consistent with the required reactivity changes for reactor operational load changes. This rate is based on the worths of the various rod groups, which are established to limit power-peaking flux patterns to design values. The maximum reactivity addition rate is specified to limit the magnitude of a possible nuclear excursion resulting from a control system or operator malfunction. Also, the control rod drive assemblies for the full length rods provide a fast insertion rate during a "trip" of the rod cluster control assemblies, which results in a rapid shutdown of the reactor for conditions that cannot be handled by the reactor control system.

REFERENCES FOR SECTION 3.1

1. Westinghouse Proprietary, "Power Distribution Control in Westinghouse Pressurized Water Reactors," WCAP-7208, 1968.

3.2 REACTOR DESIGN

3.2.1 Nuclear Design And Evaluation

This section presents the nuclear characteristics of the core and an evaluation of the characteristics and design parameters, which are significant to design objectives. The capability of the reactor to achieve these objectives while performing safely under normal operational modes, including both transient and steady state, is demonstrated.

3.2.1.1 Nuclear Characteristics of the Design

A summary of the reactor nuclear design characteristics is presented in Table 3.2-1 for Cycle 1 and Table 3.2-1A for the current cycle. Some of the presented parameters will change from cycle to cycle depending on reload core designs.

3.2.1.1.1 Reactivity Control Aspects

Reactivity control is provided by neutron absorbing control rods and by a soluble chemical neutron absorber (boric acid) in the reactor coolant. The concentration of boric acid is varied as necessary during the life of the core to compensate for: (1) changes in reactivity, which occur with changes in temperature of the reactor coolant from cold shutdown to the hot operating, zero power conditions, (2) changes in reactivity associated with changes in the fission product poisons xenon and samarium, (3) reactivity losses associated with the depletion of fissile inventory and buildup of long-lived fission product poisons (other than xenon and samarium), and (4) changes in reactivity due to burnable poison burnup.

The control rods provide reactivity control for: (1) fast shutdown, (2) reactivity changes associated with changes in the average coolant temperature above hot zero power (core average coolant temperature is increased with power level), (3) reactivity associated with any void formation, and (4) reactivity changes associated with the power coefficient of reactivity.

3.2.1.1.1.1 Chemical Shim Control

Control to render the reactor sub-critical at temperatures below the operating range is provided by a chemical neutron absorber (boron). The boron concentration during refueling following Cycle 1 has been established as shown in Table 3.2-1, line 29. This concentration together with the control rods provides approximately 10-percent shutdown margin for these operations. The concentration is also sufficient to maintain the core shutdown without any rod cluster control rods during refueling. For cold shutdown, at the beginning of core life, a concentration (shown in Table 3.2-1, line 37) is sufficient for 1-percent shutdown with all but the highest worth rod inserted. The boron concentration (Table 3.2-1, line 29) for refueling is equivalent to less than 2-percent by weight boric acid (H_3BO_3) and is well within solubility limits at ambient temperature. This concentration is also maintained in the spent fuel pit since it is directly connected with the refueling canal during refueling operations.

The refueling boron concentration requirement for the current cycle is shown in Table 3.2-1A.

For example, the initial Cycle 1 full power boron concentration without equilibrium xenon and samarium was 1186 ppm. As the fission product poisons built up, the boron concentration was reduced to 890 ppm.

This initial boron concentration was that which permitted the withdrawal of the control banks to their operational limits. The Cycle 1 xenon-free, hot zero power shutdown ($k = 0.99$) with all but the highest worth rod inserted, could be maintained with the boron concentration of 677 ppm. This concentration is less than the full power operating value with equilibrium xenon.

3.2.1.1.1.2 Control Rod Requirements

Neutron-absorbing control rods provide reactivity control to compensate for more rapid variations in reactivity. The rods are divided into two categories according to their function. Some rods compensate for changes in reactivity due to variations in operating conditions of the reactor such as power or temperature. These rods comprise the control group of rods. The remaining rods, which provide shutdown reactivity, are termed shutdown rods. The total shutdown worth of all the rods is also specified to provide adequate shutdown with the most reactive rod stuck out of the core as discussed in Sections 14.1, 14.2.5, and 14.2.6.

IP2
FSAR UPDATE

Control rod reactivity requirements at beginning- and end-of-life for Cycle 1 are summarized in Table 3.2-2. The installed worth of the control rods for Cycle 1 is shown in Table 3.2-3. These values will vary from cycle to cycle depending on the reload core design.

The difference is available for excess shutdown upon reactor trip. The control rod requirements are discussed below.

3.2.1.1.1.3 Total Power Reactivity Defect

Control rods must be available to compensate for the reactivity change incurred with a change in power level due to the Doppler effect. The magnitude of this change was determined by measurement during the Cycle 1 Startup test program.

The average temperature of the reactor coolant is increased with power level in the reactor. Since this change is actually a part of the power dependent reactivity change, along with the Doppler effect and void formation, the associated reactivity change must be controlled by rods. The largest amount of reactivity that must be controlled is at the end-of-life when the moderator temperature coefficient has its most negative value. The Cycle 1 moderator density coefficient range is given in Table 3.2-1, line 44, while the cumulative reactivity change for Cycle 1 is shown in the first line of Table 3.2-2. By the end of the fuel cycle, the nonuniform axial depletion causes a severe power peak at low power. The reactivity associated with this peak is part of the power defect.

3.2.1.1.1.4 Operational Maneuvering Band

The control group is operated at full power within a prescribed band of travel in the core to compensate for periodic changes in boron concentration, temperature, or xenon. The band has been defined as the operational maneuvering band. When the rods reach either limit of the band, a change in boron concentration must be made to compensate for any additional change in reactivity, thus keeping the control group within the maneuvering band.

3.2.1.1.1.5 Control Rod Bite

If sufficient boron is present in a chemically shimmed core, the inherent operational control afforded by the negative moderator temperature coefficient is lessened to such a degree that the major control of transients resulting from load variations must be compensated for by control rods. The ability of the plant to accept major load variations is distinct from safety considerations, since the reactor would be tripped and the plant shut down safely if the rods could not follow the imposed load variations. In order to meet required reactivity ramp rates resulting from load changes, the control rods were inserted a given distance into the core. The reactivity worth of this insertion has been defined as control rod bite.

The reactivity insertion rate was sufficient to compensate for reactivity variation due to changes in power and temperature caused either by a ramp load change of 5-percent/min, or by a step load change of 10-percent. An insertion rate of $3 \times 10^{-5} \Delta\rho/\text{sec}$ is determined by the transient analysis of the core and plant to be adequate for the most adverse combinations of power and moderator coefficients.

IP2
FSAR UPDATE

Beginning with Cycle 18, plant operation with Control Bank D at bite position is no longer required. The analysis in support of the stretch power uprate eliminated the need for control rod bite.

3.2.1.1.1.6 Xenon Stability Control

Control rods are capable of suppressing xenon-induced power oscillations in the axial direction, should they occur. Ex-core instrumentation is provided to obtain necessary information concerning power distribution. This instrumentation is adequate to enable the operator to monitor and control xenon-induced power oscillations. Extensive analyses, with confirmation of methods by spatial transient experiments at Haddam Neck, have shown that any induced radial or diametral xenon transients would die away naturally. A full discussion of xenon stability control can be found in Reference 1. In assessing potential power distribution instabilities arising from spatial xenon redistribution and in determining stability indices, primary reliance has been placed on time-dependent digital calculations in three dimensions representing feedback reactivity effects by means of semi-empirically fitted expressions whose coefficients were determined from other calculations using standard design analytical techniques and computer codes (e.g., LEOPARD code).

To assess the level of credibility and range of uncertainty attached to xenon stability analyses, conservative values of the reactivity feedback parameters were used to arrive at a reasonable upper limit for the stability index. This technique gives reasonable assurance that the reactor will in fact be stable toward diametral xenon oscillations. Means are available to increase the moderator temperature feedback term in order to stabilize the reactor response to diametral xenon oscillation (Reference 2). The reference three-dimensional time dependent digital calculations have indicated that the Indian Point Unit 2 reactor is stable against diametral xenon transients.

Cross-coupled transients are discussed in Reference 3 on the basis of full three-dimensional analyses of xenon transients.

"Second overtone" xenon transients from quadrant to quadrant (X-Y transient) are also discussed in Reference 3 in the form of radial transients. That is to say that a power-xenon perturbation is introduced by moving the center control rod. "Second overtone" xenon transients from top-to-bottom (axial transient) have been analyzed with results presented in References 1 and 4. For clarity, such transients are presented here specifically for the Indian Point Unit 2 reactor.

Figure 3.2-1 shows a cross-plot of the axial peaking factor and axial offset for transients at three points in core life. This plot is completely in agreement with such plots shown in Reference 1. In short, the ex-core detector based protection system is capable of detecting (by means of axial offset) transients, which result from perturbations to the "second axial overtone" of the power distribution.

The separation of dimensions is a conceptual artifice, which greatly facilitates analysis of xenon transients. Full three-dimensional transient analyses have been performed, as reported in References 2 and 3. Conclusions relating to power distribution stability against spatial xenon redistribution are based on results of these analyses. Cross-coupling between axial and diametral xenon oscillations are inherently accounted for in the three-dimensional time dependent calculations. Results of these calculations do not reveal any unique problems arising from cross-coupling. See Appendix 3B for additional discussion.

IP2 FSAR UPDATE

If the core was originally operating with a symmetric quadrant-to-quadrant power distribution, the effect of excess xenon poisoning would be to flatten the power distribution because the xenon excess would be greatest where the equilibrium power has been greatest. While this additional power flattening would tend to decrease the stability of the reactor, the analytical evaluation described in Reference 3 had already assumed a power distribution flatter than expected in the actual reactors; thus, an allowance has already been made in the Reference 3 analysis to account for this effect. Furthermore, the high xenon inventory present under the postulated conditions (i.e., maximum xenon buildup) would decrease the required boron concentration and lead to a more stable reactor response from the enhanced negative moderator reactivity feedback effect.

As burnup progresses, the required boron concentration further decreases resulting in an increasingly more stable reactor response to diametral xenon oscillations. This effect is greater than the effect of burnup on radial power flattening.

If the equilibrium power was not balanced from quadrant to quadrant, the effect of the excess xenon poisoning might be to cause the quadrant power to reverse and perhaps to increase in magnitude. If the quadrant power tilt were to reach the limit given in the Technical Specifications, the operator would take action to maintain core thermal margins.

In any event, the excess xenon, which might be present under the conditions postulated would decay naturally and cannot be regarded as a continuing source of power distribution anomalies. Similarly, a top-to-bottom power imbalance could be temporarily increased by the excess xenon poisoning. Such an imbalance cannot be a safety problem because the reactor protection system is cognizant of the axial power imbalance and if necessary will reduce trip setpoints accordingly.

3.2.1.1.1.7 Excess Reactivity Insertion Upon Reactor Trip

The control requirements are nominally based on providing 1-percent shutdown at hot, zero power conditions with the highest worth rod stuck in its fully withdrawn position or to prevent return to criticality following a credible steamline break, whichever is the more limiting. The condition where excess reactivity insertion is most critical is at the end of a cycle when the steam break accident is considered. For example, the excess control available at the end of Cycle 1, hot zero power condition with the highest worth rod stuck out is 2.08-percent $\Delta\rho$ after allowing a 10-percent margin for uncertainty in control rod worth as shown in Table 3.2-3.

3.2.1.1.1.8 Calculated Rod Worths

The complement of 53 full length control rods arranged in the pattern shown in Figure 3.2-2 meets the shutdown requirements. Table 3.2-3 lists the calculated worths of this rod configuration for beginning and end of the first cycle.

The calculated reactivity worths listed are decreased in the design by 10-percent to account for any errors or uncertainties in the calculation. This worth is established for the condition that the highest worth rod is stuck in the fully withdrawn position in the core.

A comparison between calculated and measured rod worths in the operating reactor shows the calculation to be well within the allowed uncertainty of 10-percent.

3.2.1.2 Reactor Core Power Distribution

The accuracy of power distribution calculations has been confirmed through approximately 1000 flux maps during some 20 years of operation under conditions very similar to those expected for the plant described herein. Details of this confirmation are given in Reference 5.

3.2.1.2.1 Definitions

Power distributions are quantified in terms of hot channel factors. These factors are a measure of the peak pellet power within the reactor core and the total energy produced in a coolant channel and are expressed in terms of quantities related to the nuclear or thermal design, namely:

Power density is the thermal power produced per unit volume of the core (kW/liter).

Linear power density is the thermal power produced per unit length of active fuel (kW/ft). Since fuel assembly geometry is standardized, this is the unit of power density most commonly used. For all practical purposes it differs from kW/liter by a constant factor, which includes geometry and the fraction of the total thermal power that is generated in the fuel rod.

Average linear power density is the total thermal power produced in the fuel rods divided by the total active fuel length of all rods in the core.

Local heat flux is the heat flux at the surface of the cladding (BTU-ft⁻²-hr⁻¹). For nominal rod parameters this differs from linear power density by a constant factor.

Rod power or rod integral power is the length integrated linear power density in one rod (kW).

Average rod power is the total thermal power produced in the fuel rods divided by the number of fuel rods (assuming all rods have equal length).

The hot channel factors used in the discussion of power distributions in this section are defined as follows:

F_Q : Heat Flux Hot Channel Factor, is defined as the maximum local heat flux on the surface of a fuel rod divided by the average fuel rod heat flux, allowing for manufacturing tolerances on fuel pellets and rods.

F_Q^N : Nuclear Heat Flux Hot Channel Factor, is defined as the maximum local fuel rod linear power density divided by the average fuel rod linear power density, assuming nominal fuel pellet and rod parameters.

F_Q^E : Engineering Heat Flux Hot Channel Factor, is the allowance on heat flux required for manufacturing tolerances. The engineering factor allows for local variations in enrichment, pellet density and diameter, surface area of the fuel rod, and eccentricity of the gap between pellet and clad. Combined statistically the net effect is a factor of 1.03 to be applied to fuel rod surface heat flux.

IP2
FSAR UPDATE

$F_{\Delta H}^N$ Nuclear Enthalpy Rise Hot Channel Factor, is defined as the ratio of the integral of linear power along the rod with the highest integrated power to the average rod power.

Manufacturing tolerances, hot channel power distribution and surrounding channel power distributions are treated explicitly in the calculation of the DNBR.

It is convenient for the purposes of discussion to define subfactors of F_Q . However, design limits are set in terms of the total peaking factor.

F_Q = total peaking factor (or heat flux hot-channel factor)

$$= \frac{\text{maximum kW / ft}}{\text{average kW / ft}}$$

without densification effects

$$\begin{aligned} F_Q &= F_Q^N \times F_Q^E \\ &= F_{XY}^N \times F_Z^N \times F_Q^E \times F_U^N \end{aligned}$$

where:

F_Q^N and F_Q^E are defined above.

F_U^N = factor for conservatism, assumed to be 1.05.

F_{XY}^N = ratio of peak power density to average power density in the horizontal plane of peak local power

F_Z^N = ratio of the power per unit core height in the horizontal plane of peak local power to the average value of power per unit core height. If the plane of peak local power coincides with the plane of maximum power per unit core height, then F_Z^N is the core average axial peaking factor.

To include the allowance made for densification effects, which are height dependent, the following quantities are defined.

$S(Z)$ = the allowance made for densification effects at height Z in the core.

$P(Z)$ = ratio of the power per unit core height in the horizontal plane at height Z to the average value of power per unit core height.

Then:

$$F_Q = \frac{\text{maximum kW/ft}}{\text{average kW/ft}}$$

Including densification allowance

$$F_Q = \max [F_{XY}^N(Z) \times P(Z) \times S(Z) \times F_U^N \times F_Q^E]$$

3.2.1.2.2 Radial Power Distributions

The power shape in horizontal sections of the core at full power is a function of the fuel and burnable absorber loading patterns, and the presence or absence of a single bank of control rods. Thus, at any time in the cycle, a horizontal section of the core can be characterized as (1) unrodded, or (2) with group D control rods. These two situations combined with burnup effects determine the radial power shapes, which can exist in the core at full power. The effect on radial power shapes of power level, xenon, samarium, and moderator density effects are also considered but these are quite small. The effect of nonuniform flow distribution is negligible. While radial power distributions in various planes of the core are often illustrated, the core radial enthalpy rise distribution as determined by the integral of power up each channel is of greater interest. As an example, Historical Figures 3.2-3 through 3.2-6 show representative radial cycle 1 power distributions for one quarter of the core for representative operating conditions. These conditions are (1) Hot Full Power (HFP) - beginning-of-life (BOL) - unrodded - no xenon, (2) HFP-BOL - Bank D in - equilibrium xenon - unrodded, (3) HFP - end-of-life (EOL) - unrodded - equilibrium xenon, (4) HFP, BOL, no xenon, part-length rods in. Figure 3.2-6 is of historical significance only, since part-length rods have been removed.

Since the position of the hot channel varies from time to time a single reference radial design power distribution is selected for DNB calculations. This reference power distribution is chosen conservatively to concentrate power in one area of the core, minimizing the benefits of flow redistribution. Assembly powers are normalized to core average power.

3.2.1.2.3 Axial Power Distributions

The shape of the power profile in the axial or vertical direction is largely under the control of the operator through either the manual operation of the control rods or automatic motion of rods responding to manual operation of the soluble boron system. Nuclear effects, which cause variations in the axial power shape include moderator density, Doppler effect on resonance absorption, spatial xenon, and burnup. Automatically controlled variations in total power output and rod motion are also important in determining the axial power shape at any time. Signals are available to the operator from the ex-core ion chambers, which are long ion chambers outside the reactor vessel running parallel to the axis of the core. Separate signals are taken from the top and bottom halves of the chambers. The difference between top and bottom signals from each of four pairs of detectors is displayed on the control panel and called the flux difference, ΔI . Calculations of core average peaking factor for many plants and measurements from operating plants under many operating situations are associated with either ΔI or axial offset in such a way that an upper bound can be placed on the peaking factor. For these correlations axial offset is defined as:

$$\text{axial offset} = \frac{\phi_t - \phi_b}{\phi_t + \phi_b}$$

and ϕ_t and ϕ_b are the top and bottom detector readings.

3.2.1.2.4 Local Power Peaking

Fuel densification, which has been observed to occur under irradiation in several operating reactors, causes the fuel pellets to shrink both axially and radially. The pellet shrinkage combined with random hang-up of fuel pellets results in gaps in the fuel column when the pellets below the hung-up pellet settle in the fuel rod. The gaps vary in length and location in the fuel rod. Because of decreased neutron absorption in the vicinity of the gap, power peaking occurs in the adjacent fuel rods resulting in an increased power peaking factor. A quantitative measure of this local peaking is given by the power spike factor $S(Z)$ where Z is the axial location in the core.

The method used to compute the power spike factor is described in Reference 6. Results reported in Reference 14 show that fuel manufactured by Westinghouse will not densify and therefore no power spike penalty should be included in the safety analysis

The power spike factor due to densification is assumed to be a local perturbation applicable to overpower transients. Thus, densification affects F_Q but not $F_{\Delta H}^N$. The magnitude of the increased power peaking increases from no effect at the bottom of the core to a few percent at the top of the core. For fuel produced by a process other than those for which Reference 6 is applicable, specifications will be followed to ensure that the effects of densification will be no greater than has been allowed for in the design. The specifications for qualifying the extent of densification will be based on the NRC report on fuel densification (Reference 7).

Results reported in a Westinghouse Topical Report concerning the spike penalty in LOCA analysis (Reference 8) show that the power spike penalty does not have to be included in the LOCA envelope.

3.2.1.2.5 Limiting Power Distributions

According to the ANS classification of plant conditions, Condition I occurrences are those which are expected frequently or regularly in the course of power operation, maintenance, or maneuvering of the plant. As such, Condition I occurrences are accommodated with margin between any plant parameter and the value of that parameter, which would require either automatic or manual protective action. Inasmuch as Condition I occurrences occur frequently or regularly, they must be considered from the point of view of affecting the consequences of fault conditions (Conditions II, III, and IV). In this regard, analysis of each fault condition described is generally based on a conservative set of initial conditions corresponding to the most adverse set of conditions, which can occur during Condition I operation.

Implicit in the definition of normal operation is proper and timely action by the reactor operator. That is, the operator follows recommended operating procedures for maintaining appropriate power distributions and takes any necessary remedial actions when alerted to do so by the plant instrumentation. Thus, as stated above, the worst or limiting power distribution, which can occur during normal operation is to be considered as the starting point for analysis of Condition II, III, and IV events.

Improper procedural actions or errors by the operator are assumed in the design as occurrences of moderate frequency (Condition II). Therefore, the limiting power shapes, which result from such Condition II events are those power shapes, which deviate from the normal operating condition at the recommended axial offset band, e.g., due to lack of proper action by

IP2
FSAR UPDATE

the operator during a xenon transient following a change in power level brought about by control rod motion. Power shapes, which fall in this category are used for determination of the reactor protection system setpoints so as to maintain margin to overpower or DNB limits.

The means for maintaining power distributions within the required hot channel factor limits are described in the Technical Specifications. A complete discussion of power distribution control in Westinghouse PWRs is included in Reference 9. Detailed background information on the design constraints on local power density in a Westinghouse PWR, on the defined operating procedures, and on the measures taken to preclude exceeding design limits is presented in the Westinghouse topical report on power distribution control and load following procedures (Reference 4). The following paragraphs summarize these reports and describe the calculations used to establish the upper bound on peaking factors.

The calculations used to establish the upper bound on peaking factors, F_Q and $F_{\Delta H}^N$, include all of the nuclear effects, which influence the radial and/or axial power distributions throughout core life for various modes of operation including load follow, reduced power operation, and axial xenon transients.

Radial power distributions are calculated for the full power condition and fuel and moderator temperature feedback effects are included for the average enthalpy plane of the reactor. The steady-state nuclear design calculations are done for normal flow with the same mass flow in each channel and flow redistribution effects neglected. The effect of flow redistribution is calculated explicitly where it is important in the DNB analysis of accidents. The effect of xenon on radial power distribution is small but is included as part of the normal design process. Radial power distributions are relatively fixed and easily bounded with upper limits.

The core average axial profile, however, can experience significant changes, which can occur rapidly as a result of rod motion and load changes and more slowly due to xenon distribution. For the study of points of closest approach to axial power distribution limits, several thousand cases are examined. Since the properties of the nuclear design dictate what axial shapes can occur, boundaries in the limits of interest can be set in terms of the parameters, which are readily observed in the plant. Specifically, the nuclear design parameters, which are significant to the axial power distribution analysis are:

1. Core power level.
2. Core height.
3. Coolant temperature and flow.
4. Coolant temperature program as a function of reactor power.
5. Fuel cycle lifetimes.
6. Rod bank worths.
7. Rod bank overlaps.

Normal operation of the plant assumes compliance with the following conditions:

IP2
FSAR UPDATE

1. Control rods in a single bank move together with no individual rod insertion differing from the bank demand position by more than the Technical Specification limit.
2. Control banks are sequenced with overlapping banks.
3. The control bank insertion limits are not violated.
4. Axial power distribution procedures, which are given in terms of flux difference control and control bank position, are observed.

The axial power distribution procedures referred to above are part of the required operating procedures, which are followed in normal operation. Briefly they require control of the axial offset (flux difference divided by fractional power) at all power levels within a permissible operating band of a target value corresponding to the equilibrium full power value. In the first cycle, the target value changes from about +10 to -3-percent linearly through the life of the cycle. This minimizes xenon transient effects on the axial power distribution since the procedures essentially keep the xenon distribution in phase with the power distribution.

Calculations are performed for normal operation of the reactor including load following maneuvers. Beginning, middle, and end of cycle conditions are included in the calculations. Different histories of operation are assumed prior to calculating the effect of load follow transients on the axial power distribution. These different histories assume base loaded operation and extensive load following. For a given plant and fuel cycle, a finite number of maneuvers are studied to determine the general behavior of the local power density as a function of core elevation.

These cases represent many possible reactor states in the life of one fuel cycle, and they have been chosen as sufficiently definitive of the cycle by comparison with much more exhaustive studies performed on some 20 or 30 different, but typical, plant and fuel cycle combinations. The cases are described in detail in Reference 4, and they are considered to be necessary and sufficient to generate a local power density limit, which, when increased by 5-percent for conservatism, will not be exceeded with a 95-percent confidence level. Many of the points do not approach the limiting envelope. However, they are part of the time histories, which lead to the hundreds of shapes, which do define the envelope. They also serve as a check that the reactor studied is typical of those more exhaustively studied.

Thus, it is not possible to single out any transient or steady-state condition, which defines the most limiting case. It is not even possible to separate out a small number, which form an adequate analysis. The process of generating a myriad of shapes is essential to the philosophy that leads to the required level of confidence. A maneuver, which provides a limiting case for one reactor fuel cycle is not necessarily a limiting case for another reactor or fuel cycle with different control bank worths, enrichments, burnup, coefficients, etc. Each shape depends on the detailed history of operation up to that time and on the manner in which the operator conditioned xenon in the days immediately prior to the time at which the power distribution is calculated.

The calculated points are synthesized from axial calculations combined with radial factors appropriate for rodged and unrodged planes in the first cycle. In these calculations, the effects on the unrodged radial peak of xenon redistribution that occurs following the withdrawal of a control bank (or banks) from a rodged region is obtained from two-dimensional X-Y calculations.

IP2
FSAR UPDATE

A 1.03 factor to be applied on the unrodded radial peak was obtained from calculations in which xenon distribution was preconditioned by the presence of control rods and then allowed to redistribute for several hours. A detailed discussion of this effect may be found in Reference 4. The calculated values have been increased by a factor of 1.05 for conservatism and a factor of 1.03 for the engineering factor F_{Q}^E .

The envelope drawn over the calculated ($[F_Q \times \text{Power}] \text{ max}$) points in Figure 3.2-7 represents an upper bound envelope on local power density versus elevation in the core for Cycles 1 through 12. For Cycles 13 and on, the anticipated normalized F_Q times power versus core height limiting $K(z)$ curve is shown in the Unit 2 COLR. It should be emphasized that this envelope is a conservative representation of the bounding values of local power density. Expected values are considerably smaller and, in fact, less conservative bounding values may be justified with additional analysis or surveillance requirements. Additionally, Figure 3.2-7 is based on a radial power distribution invariant with core elevation.

Finally, as previously discussed, this upper bound envelope is based on procedures of load follow, which require operation within an allowed deviation from a target equilibrium value of axial flux difference. [**Note** - *Per Confirmatory Order for Indian Point Unit 2 of February 11, 1980, (letter from W. J. Cahill, Con Edison, to A. Schwencer, NRC), Indian Point Unit 2 is not operated presently in a load follow mode of operation.*] These procedures are detailed in the Technical Specifications and are followed by relying only upon ex-core surveillance supplemented by the normal monthly incore core map requirement and by computer based alarms on deviation and time of deviation from the allowed flux difference band.

To determine reactor protection system setpoints with respect to power distributions, three categories of events are considered, namely rod control equipment malfunctions, operator errors of commission and operator errors of omission. In evaluating these three categories of events, the core is assumed to be operating within the four constraints described above.

The first category comprises uncontrolled rod withdrawal (with rods moving in the normal bank sequence). Also included are motions of the banks below their insertion limits, which could be caused, for example, by uncontrolled dilution or primary coolant cooldown. Power distributions are calculated throughout these occurrences assuming short term corrective action, that is, no transient xenon effects are considered to result from the malfunction. The event is assumed to occur from typical normal operating situations, which include normal xenon transients.

It is further assumed in determining the power distributions that total core power level will be limited by reactor trip to below 120-percent. Since the study is to determine protection limits with respect to power and axial off-set, no credit is taken for trip setpoint reduction due to flux difference. The peak power density, which can occur in such events, assuming reactor trip at or below 120-percent, is less than that required for centerline melt, including uncertainties and densification effects.

The second category assumes that the operator malpositions the rod bank in violation of the insertion limits and creates short-term conditions not included in normal operating conditions.

The third category assumes that the operator fails to take action to correct a flux difference violation. The resulting F_Q is multiplied by 102-percent power including an allowance for calorimetric error. It should be noted that a reactor overpower accident is not assumed to occur coincident with an independent operator error.

IP2
FSAR UPDATE

Analysis of possible operating power shapes shows that the appropriate hot channel factors F_Q and $F_{\Delta H}^N$ for peak local power density and for DNB analysis at full power are the values addressed in the Technical Specifications.

F_Q can be increased with decreasing power as shown in the Technical Specifications. Increasing $F_{\Delta H}^N$ with decreasing power is permitted by the DNB protection setpoints and allows radial power shape changes with rod insertion to the insertion limits. It has been determined that Technical Specifications are met provided that, during normal operation of the plant, there is compliance with the four conditions listed earlier in this section.

When a situation is possible in normal operation, which could result in local power densities in excess of those assumed as the precondition for a subsequent hypothetical accident, but which would not itself cause fuel failure, administrative controls and alarms are provided for returning the core to a safe condition.

3.2.1.2.6 Power Distribution Anomalies

A discussion of the means provided to monitor and control power distributions anomalies caused by misplaced control rods and xenon oscillations is given in Appendix 3B.

A description of the protective function in the event of axial xenon oscillations, including calculated peaking factors and DNBRs, and the automatic trip setpoint reduction is given in References 1 and 4. Additional information on the response to ex-core ion chambers, including comparison with experimental information, is given in References 2 and 10. X-Y control rods are not required nor are they employed in the Indian Point Unit 2 reactor. A discussion of the consequences of control rod malposition is given in Appendix 3B and in Reference 2.

No automatic protective function is necessary, since even the complete misalignment of a control rod in the most limiting case (see Reference 2) cannot lead to a DNBR less than the applicable safety analysis limit at operating conditions. Furthermore, (1) rod position indicators are provided, (2) the existence of an asymmetric control rod misalignment would be revealed by the ex-core instrumentation, and (3) both asymmetric and symmetric control rod misalignments can readily be detected by the incore thermocouple system as indicated in References 2 and 10.

3.2.1.2.7 Reactivity Coefficients

The response of the reactor core to plant conditions or operator adjustments during normal operation, as well as the response during abnormal or accidental transients, is evaluated by means of a detailed plant simulation. In these calculations, reactivity coefficients are required to couple the response of the core neutron multiplication to the variables, which are set by conditions external to the core. Since the reactivity coefficients change during the life of the core, a range of coefficients is established to determine the response of the plant throughout life and to establish the design of the reactor control and protection system.

3.2.1.2.7.1 Moderator Temperature Coefficient

The moderator temperature coefficient in a core controlled by chemical shim is less negative than the coefficient in an equivalent rodged core. One reason is that control rods contribute a negative increment to the coefficient and in a chemical shim core, the rods are only partially

IP2
FSAR UPDATE

inserted. Also, the chemical poison density is decreased with the water density upon an increase in temperature. This gives rise to a positive component of the moderator temperature coefficient due to boron being removed from the core. This is directly proportional to the amount of reactivity controlled by the dissolved poison.

In order to reduce the dissolved poison requirement for control of excess reactivity, burnable absorber rods have been incorporated in the core design. The result is that changes in the coolant density will have less effect on the density of poison and the moderator temperature coefficient will be reduced. The moderator temperature coefficient is negative at the operating coolant temperature with burnable absorber rods installed.

The original burnable absorber was in the form of borated Pyrex glass rods clad in stainless steel. The rods (1412 in the initial core) in the form of clusters were distributed throughout the initial core in vacant rod cluster control guide tubes as illustrated in Figures 3.2-8 and 3.2-9. Information regarding research, development, and nuclear evaluation of the burnable poison rods can be found in Reference 11. These rods initially controlled 7.2-percent $\Delta\rho$ of the installed excess reactivity and their addition resulted in a reduction of the initial hot zero power boron concentration in the coolant to 1318 ppm.

Starting with Cycle 8, the Wet Annular Burnable Absorber (WABA) design has been used. The WABA design is described in Section 3.2.3.2.1.5.

Starting with Cycle 11, the Integral Fuel Burnable Absorber (IFBA) design has also been used. The IFBA design is described in Section 3.2.3.2.1.5.

The effect of burnup on the moderator temperature coefficient is calculated and the coefficient becomes more negative with increasing burnup. This is due to the buildup of fission products with burnup and dilution of the boric acid concentration with burnup. The reactivity loss due to equilibrium xenon is controlled by boron, and as xenon builds up, boron is taken out. For example, the calculated net effect and the predicted unrodded moderator temperature coefficient equilibrium xenon for Cycle 1 at full power BOL was $-0.55 \times 10^{-4}/^{\circ}\text{F}$. With core burnup, the coefficient became more negative as boron was removed due to the buildup of plutonium and fission products. At Cycle 1 end-of-life with no boron or rods in the core, the moderator coefficient was $-3.0 \times 10^{-4}/^{\circ}\text{F}$.

Variation in moderator temperature can be seen, for example, from the Cycle 1 Figures 3.2-10 through 3.2-12.

3.2.1.2.7.2 Moderator Pressure Coefficient

The moderator pressure coefficient has an opposite sign to the moderator temperature coefficient. Its effect on core reactivity and stability is small because of the small magnitude of the pressure coefficient, a change of 50 psi in pressure having no more effect on reactivity than a one-half degree change in moderator temperature. The calculated Cycle 1 beginning and end-of-life pressure coefficients are specified in Table 3.2-1, line 43.

3.2.1.2.7.3 Moderator Density Coefficient

A uniform moderator density coefficient is defined as a change in the neutron multiplication per unit change in moderator density. The range of the moderator density coefficient for Cycle 1, for example, from BOL and EOL is specified in Table 3.2-1.

3.2.1.2.7.4 Doppler and Power Coefficients

The Doppler coefficient is defined as the change in neutron multiplication [**Note** - *Neutron multiplication is defined as the ratio of the average number of neutrons produced by fission in each generation to the total number of corresponding neutrons absorbed.*] per degree change in fuel temperature. The coefficient is obtained by calculating neutron multiplication as a function of effective fuel temperature. As an example, the Cycle 1 results, using the LEOPARD code (Reference 12), are shown in Figure 3.2-13.

In order to know the change in reactivity with power, it is necessary to know the change in the effective fuel temperature with power as well as the Doppler coefficient. It is very difficult to predict the effective temperature of the fuel using a conventional heat transfer model because of uncertainties in predicting the behavior of the fuel pellets. Therefore, an empirical approach is taken to calculate the power coefficient, based on operating experience of existing Westinghouse cores. As an example, Figure 3.2-14 shows the power coefficient as a function of power for Cycle 1 obtained by this method. The results presented do not include any moderator coefficient even though the moderator temperature changes with power level.

As the fuel pellet temperature increases with power, the resonance absorption in U-238 increases due to Doppler broadening of the resonances. A large temperature drop occurs across the fuel pellet-clad gap. Under certain conditions, this gap may be closed, thus resulting in lower pellet temperature. The net effect is a lower effective fuel temperature, a higher (more negative) Doppler coefficient, and a lower (less negative) power coefficient than that which exists with a pellet-clad gap. For example, the power coefficient for Cycle 1, which was determined using a closed gap model, is shown in Figure 3.2-15.

Calculations indicate the stability of the reactor to xenon oscillations is relatively insensitive to the thermal model used to obtain the power coefficient. The damping factor associated with the fuel Doppler effect is:

$$\alpha_f = \frac{\partial K_{eff}}{\partial T} \times \frac{\partial T}{\partial P}$$

where:

T = fuel temperature

P = power

The quantity $\frac{\partial T}{\partial P}$ is larger for the gap model than for the no gap case but since the Doppler coefficient varies as $T^{-1/2}$ the term $\frac{\partial K_{eff}}{\partial T}$ is smaller.

The net effect is that α_f is relatively insensitive to the thermal model in the range of power 0.5 to 1.5 of core average, which is the range of interest for stability.

3.2.1.3 Nuclear Evaluation of Current Core

Three principal computer codes have been used in the nuclear design on this reload cycle. These are: PHOENIX-P (two-dimensional), ANC (two-dimensional and three-dimensional) and APOLLO (one-dimensional). Descriptions and uses for these codes are given below:

PHOENIX-P is a two dimensional, multi-group transport theory code which utilizes a 70 energy-group cross section library. It provides the capability for cell lattice modeling on an assembly level. In this design, PHOENIX-P is used to provide homogenized, two-group cross sections for nodal calculations and feedback models. Also, PHOENIX-P is used to generate appropriately weighted constants for the baffle/reflector regions.

ANC is an advance nodal code capable of two-dimensional and three-dimensional calculations. In this design, ANC is employed as the reference model for all safety analysis calculations, power distributions, peaking factors, critical boron concentrations, control rod worth, reactivity coefficients, etc. In addition, 3D ANC is used to validate one and two-dimensional results and to provide information about radial (x-y) peaking factors as a function of axial position. It has the capability of calculating discrete pin powers from the nodal information as well.

APOLLO, an advanced version of PANDA, is a two group, one-dimensional diffusion-depletion code. It uses cross sections generated by a radial averaging of the corresponding 3D model cross sections and is used as a one-dimensional axial model. Thermal feedback is included in the calculational models. The axial model is used for computing axial power distributions, differential rod worths, control rod operating limits (insertion limits, return to power limits), etc.

Additional support codes are used for special calculations such as determining fuel temperatures.

3.2.2 Thermal and Hydraulic Design and Evaluation

[Note - A large amount of material has been retained as historical background.]

3.2.2.1 Thermal and Hydraulic Characteristics of the Design

3.2.2.1.1 Central Temperature of the Hot Pellet

The temperature distribution in the pellet is mainly a function of the uranium-dioxide thermal conductivity and the local power density. The absolute value of the temperature distribution is affected by the cladding temperature and the thermal conductance of the gap between the pellet and the cladding.

The gap conductance model is selected such that when combined with the UO₂ thermal conductivity model, the calculated fuel centerline temperatures reflect the inpile temperature measurements. A more detailed discussion of the gap conductance model has been provided in References 83 and 84. The temperature drop across the gap is calculated by assuming an annular gap conductance model of the following form:

$$h = \frac{K_{gas}}{\frac{\delta}{2} + \delta_r}$$

where:

IP2
FSAR UPDATE

- h = contact conductance, Btu/hr-ft²-°F
- K_{gas} = thermal conductivity of the gas mixture including a correction factor (Reference 25) for the accommodation coefficient for light gases, e.g., helium, Btu/hr-ft-°F
- δ = diametral gap size, ft
- δ_r = effective gap spacing due to surface roughness, ft

or an empirical correlation derived from thermocouple and melt radius data.

The larger gap conductance value from the equation above and the empirical correlation is used to calculate the temperature drop across the gap for finite gaps.

For evaluations in which the pellet-clad gap is closed, a contact conductance is calculated. The contact conductance between UO₂ and zircaloy has been measured and found to be dependent on the contact pressure, composition of the gas at the interface, and the surface roughness (References 25 and 26). This information, together with the surface roughness found in Westinghouse fuel, leads to the following correlation:

$$h = 0.6P + \frac{K_{gas}}{\delta_r}$$

- δ_r = effective gap spacing due to surface roughness, ft
- h = contact conductance, Btu/hr-ft²-°F
- P = contact pressure, psi
- K_{gas} = thermal conductivity of gas mixture at the interface including a correction factor (Reference 25) for the accommodation coefficient for light gases, e.g., helium, Btu/hr-ft-°F

The thermal conductivity of uranium-dioxide was evaluated from data reported by Howard, et al.,²⁷ Lucks, et al.,²⁸ Daniel, et al.,²⁹ Feith,³⁰ Vogt, et al.,³¹ Nishijima, et al.,³² Ainscough, et al.,³³ Godfrey, et al.,³⁴ Stora, et al.,³⁵ Bush,³⁶ Asamoto, et al.,³⁷ Kruger,³⁸ and Gyllander.³⁹

At the higher temperatures, thermal conductivity is best obtained by utilizing the integral conductivity to melt, which can be determined with more certainty. From an examination of the data, it has been concluded that the best estimate for the value of $\int_0^{2800^\circ\text{C}} K dt$ is 93 watts/cm. This conclusion is based on the integral values reported by Gyllander,³⁹ Lyons, et al.,⁴⁰ Duncan,⁴¹ Bain,⁴² and Stora.⁴³

The design curve for the thermal conductivity is shown in Figure 3.2-38. The section of the curve at temperatures between 0°C and 1300°C is in excellent agreement with the recommendation of the IAEA panel.⁴⁴ The section of the curve above 1300°C is derived for an integral value of 93 watts/cm.^{39,41,43}

Thermal conductivity for UO₂ at 95-percent theoretical density can be represented best by the following equation:

$$K = \frac{1}{11.8 + 0.0238T} + 8.775 \times 10^{-13} T^3$$

where:

$$K = \text{watt/cm}^2\text{C}$$
$$T = \text{C}$$

Based upon the above considerations, the maximum central temperature of the hot pellet at steady state is shown in Table 3.2-6. This temperature is well below the melting temperatures of the irradiated UO₂, which is taken as 5080°F (Reference 45) unirradiated and decreasing by 58°F per 10,000 MWd/metric ton uranium.

Westinghouse experience with fuel rods operating at high power ratings has been summarized in Appendix A, Indian Point No. 2 Preliminary Safety Analysis Report (Docket 50-247) and in Appendix-Section IX of the Preliminary Safeguards Report for the Saxton Reactor Operating at 35 MWt (Docket 50-146). These reports presented considerable statistical evidence of successful operation of high performance zircaloy clad fuel rods in CVTR (1368 rods) and Shipping port core I Blanket (94,920 rods). Since the date of these reports, a significant amount of additional information has been developed relating to the integrity of free standing zircaloy-clad oxide fuel rods at high power ratings. In addition, a comprehensive experimental program was initiated to extend the operating experience to higher power and to higher exposures for many of these fuel rods. This information is summarized in Figure 3.2-39.

More detailed information about Westinghouse experience with high power fuel rod bars has been provided in Reference 46.

3.2.2.1.2 Heat Flux Ratio and Data Correlation

Departure from nucleate boiling (DNB) is predicted upon a combination of hydrodynamic and heat transfer phenomena and is affected by the local and upstream conditions including the flux distribution. In reactor design, the heat flux associated with DNB and the location of DNB are both important. The W-3 based L-grid DNB correlation was used in design of the LOPAR fuel assemblies. The WRB-1 DNB correlation, Reference 76, is the primary DNB correlation for the analysis of the optimized and VANTAGE+ fuel assemblies. The W-3 DNB correlation⁴⁷ was developed to predict the DNB flux and the location of DNB equally well for uniform and an axially nonuniform heat flux distribution. This correlation replaced the WAPD q" and ΔH DNB correlations published in Nucleonics,⁴⁸ May 1963, in order to eliminate the discontinuity of the latter at the saturation temperature and to provide a single unambiguous criterion of the design margin.

The W-3 correlation, and several modifications of it, have been used in Westinghouse critical heat flux (CHF) calculations. The W-3 correlation was originally developed from single tube data,⁴⁹ but was subsequently modified to apply to the "L" grid⁵⁰ rod bundle data. These modifications to the W-3 correlation have been demonstrated to be adequate for reactor rod bundle design.

The W-3 DNB correlation⁴⁷ incorporates both local and system parameters in predicting the local DNB heat flux. This correlation includes the nonuniform flux effect and the upstream

IP2
FSAR UPDATE

effect, which includes inlet enthalpy or length. The local DNB heat flux ratio (defined as the ratio of the DNB heat flux to the local heat flux) is indicative of the contingency available in the local heat flux without reaching DNB.

The sources of the data used in developing the correlation were:

WAPD-188	(1958)	CU-TR-No. I (NW-208)	(1964)
ASME Paper 62-WA-297	(1962)	CISE-R-90	(1964)
CISE-R-63	(1962)	DP-895	(1964)
ANL-6675	(1962)	AEEW-R-356	(1964)
GEAP-3766	(1962)	BAW-3238-7	(1965)
AEEW-R-213 and 309	(1963)	AE-RTL-778	(1965)
CISE-R-74	(1963)	AEEW-355	(1965)
CU-MPR-XIII	(1963)	EUR-2490.e	(1965)

The comparison of the W-3 measured to predicted DNB flux of this correlation is given in Figure 3.2-40. The local flux DNB ratio versus the probability of not reaching DNB is plotted in Figure 3.2-41. This plot indicates that with a DNBR of 1.3 the probability of not reaching DNB is 95-percent at a 95-percent confidence level. The comparison of the "L"-grid measured to predicted DNB flux is given in Figure 3.2-42.

Rod bundle data without mixing vanes agree very well with the predicted DNB flux as shown in Figure 3.2-43. Rod bundle data with mixing vanes (Figure 3.2-44) show on the average an 8-percent higher value of DNB heat flux than predicted by the W-3 DNB correlation. The L-grid modified spacer factor has been formulated to reflect the improvement in DNB heat flux due to the presence of mixing vanes.

It should be emphasized that the inlet subcooling effect of the W-3 correlation was obtained from both uniform and non-uniform data. The existence of an inlet subcooling effect has been demonstrated to be real and hence the actual subcooling should be used in the calculations. The W-3 correlation was developed from tests with flow in tubes and rectangular channels. Good agreement was obtained when the correlation is applied to test data for rod bundles.

3.2.2.1.3 Definition of Departure From Nucleate Boiling Ratio

The DNB heat flux ratio (DNBR) as applied to the design when all flow cell walls are heated is:

$$DNBR = \frac{q''_{DNB,N} \times F'_{s'} \times 0.986}{q''_{loc}} \quad (\text{for LOPAR Fuel})$$

The DNB heat flux ratio (DNBR) as applied to typical cells (flow cells with all walls heated) and thimble cells (flow cells with heated and unheated walls) is defined as:

$$DNBR = \frac{q''_{DNB,N}}{q''_{loc}}$$

where:

$$q''_{DNB,N} = \frac{q''_{DNB,EU}}{F}$$

IP2
FSAR UPDATE

and $q''_{\text{DNB,EU}}$ is the uniform DNB heat flux as predicted by the WRB-1 DNB Correlation and the W-3 DNB correlation (Reference 47) when all flow cells are heated. The flux shape factor to account for nonuniform axial heat flux distributions is F (Reference 47) with the "C" term modified as in Reference 49.

F_s is the modified spacer factor, which uses an axial grid spacing coefficient, K_s , and a thermal diffusion coefficient, TDC, based on the 20-in. grid spacing data.

q''_{loc} is the actual local heat flux.

The DNBR as applied to the W-3 DNB correlation when a cold wall is present is:

$$\text{DNBR} = \frac{q''_{\text{DNB,N,CW}}}{q''_{\text{loc}}}$$

where:

$$q''_{\text{DNB,N,CW}} = \frac{q''_{\text{DNB,EU,Dh}} \times \text{CWF}}{F}$$

$q''_{\text{DNB,EU,Dh}}$ is the uniform DNB heat flux as predicted by the W-3 cold wall DNB correlation (Reference 49) when not all flow cell walls are heated (thimble cold wall cell).

W-3 Cold Wall Factor:

$$\begin{aligned} \text{CWF} = \frac{q''_{\text{coldwall}}}{q''_{\text{W-3,Dh}}} = & 1.0 - R_u \{ 13.76 - 1.372e^{1.78x} - 4.732 \left(\frac{G}{10^6} \right)^{-0.0535} \\ & - 0.0619 \left(\frac{P}{1000} \right)^{0.14} - 8.509 D_h^{0.107} \} \end{aligned}$$

where:

$$R_u = (D_h - D_e / D_h), \quad q''_{\text{W-3,Dh}} = \text{prediction of W - 3 correlation using } D_h \text{ for } D_e$$

The equivalent uniform DNB flux $q''_{\text{DNB,EU}}$ is calculated for the W-3 equivalent uniform flux DNB correlation as follows:

$$\begin{aligned} \frac{q''_{\text{DNB,EU}}}{10^6} = & \left[(2.022 - 0.0004302p) + (0.1722 - 0.0000984p) e^{(18.177 - 0.004129p)\chi} \right] \\ & \times \left[1.037 + \frac{G}{10^6} (0.1484 - 1.596\chi + 0.1729\chi|\chi|) \right] \times [1.157 - 0.869\chi] \\ & \times [0.2664 + 0.8357e^{-3.151De}] \times [0.8258 + 0.000794 (H_{\text{sat}} - H_{\text{in}})] \end{aligned}$$

The heat flux is in Btu/hr-ft² and the units of the parameters are as listed below. The ranges of parameters for applicability of the W-3 DNB correlation are:

System pressure, $p = 500$ to 2400 psia
Mass velocity, $G = 1.0 \times 10^6$ to 5.0×10^6 lb/hr ft²

IP2
FSAR UPDATE

Equivalent diameter, $D_e = 0.2$ to 0.7 -in.

Quality, $\chi_{loc} = -0.15$ to $+0.15$

Inlet enthalpy, no limit, Btu/lb

Length, $L = 10$ to 168 -in.

$$\frac{\text{Heated perimeter}}{\text{Wetted perimeter}} = 0.88 \text{ to } 1.00$$

Geometries - circular tubes and rectangular channels

Flux = Uniform and non-uniform heat flux converted from non-uniform data by using F-factor of Reference 47.

For the LOPAR fuel, which uses the "L"-grid modified W-3 DNB correlation with the modified spacer factor (Reference 50):

$$F'S = (1.445 - 0.0371L) \left(\frac{P}{225.896} \right)^{.5} \left(e^{(\chi + .2)^2} - .73 \right) + K_S \frac{G}{10^6} \left(\frac{TDC}{.019} \right)^{.35}$$

Where: K_S = spacer factor dependent on grid type and axial spacing

P = inlet pressure, psia

G = inlet mass velocity, lbm/hr-ft²

TDC = thermal diffusion coefficient

L = test length, ft

χ = local quality, fraction

The ranges of the parameters listed above are:

$$1460 \leq P \leq 2430 \text{ psia}$$

$$1.96 \times 10^6 \leq G \leq 3.68 \times 10^6 \text{ lbm/hr-ft}^2$$

$$-0.15 \leq \chi \leq +0.15 \text{ fraction}$$

$$8 \leq L \leq 14\text{-ft}$$

Geometries ("L"-grid correlation) - circular tubes and rectangular channels

Flux = Various nonuniform heat fluxes

Local Nonuniform DNB Flux

The local nonuniform $q''_{DNB,N}$ is calculated as follows:

$$q''_{DNB,N} = \frac{q''_{DNB,EU}}{F}$$

where:

IP2
FSAR UPDATE

$$F = \frac{C}{q''_{\text{local at } \ell_{\text{DNB}}} \times (1 - e^{-C\ell_{\text{DNB}}})} \int_0^{\ell_{\text{DNB}}} q''(z) e^{-C(\ell_{\text{DNB}} - z)} dz$$

ℓ_{DNB} = distance from the inception of local boiling to the point of DNB, in inches.

Z = distance from the inception of local boiling measured in the direction of flow, in inches.

$$C = 0.15 \frac{(1 - \chi_{\text{DNB}})^{4.31}}{(G/10^6)^{0.478}} \text{ in.}^{-1} \quad (\text{Reference 49})$$

Where:

G = mass velocity, lb/hr-ft²

χ_{DNB} = quality of the coolant at the location where DNB flux is calculated

In determining the F-factor, the value of $q''_{\text{local at } \ell_{\text{DNB}}}$ in the above equation for the F-factor was measured as $z = \ell_{\text{DNB}}$, the location where the DNB flux is calculated. For a uniform flux, F becomes unity so that $q''_{\text{DNB,N}}$ reduces to $q''_{\text{DNB,EU}}$ as expected. The criterion for determining the predicted location of DNB is to evaluate the ratio of the predicted DNB flux to the local heat flux along the length of the channel. The location of the minimum DNB ratio is considered to be location of DNB.

3.2.2.1.4 Procedure for Using W-3 L-grid Correlation

In predicting the local DNB flux in a nonuniform heat flux channel, the following two steps are required:

1. The uniform DNB heat flux, $q''_{\text{DNB,EU}}$, is computed with the W-3 L-grid correlation using the specified local reactor conditions.
2. This equivalent uniform heat flux is converted into corresponding nonuniform DNB heat flux, $q''_{\text{DNB,N}}$, for the nonuniform flux distribution in the reactor. This is accomplished by dividing the uniform DNB flux by the F-factor.⁴⁷ Since F is generally greater than unity, $q''_{\text{DNB,N}}$ will be smaller than $q''_{\text{DNB,EU}}$.

To calculate the DNBR of a reactor channel, the values of

$$\frac{q''_{\text{DNB,N}}}{q''_{\text{loc}}}$$

along the channel are evaluated and the minimum value is selected as the minimum DNBR incurred in that channel.

The W-3 L-grid correlation depends on both local and inlet enthalpies of the actual system fluid, and the upstream conditions are accommodated by the F-factor. Hence, the correlation provides a realistic evaluation of the safety margin on heat flux.

3.2.2.1.5 The WRB-1 DNB Correlation

The WRB-1⁷⁶ correlation was developed based exclusively on the large bank of mixing vane grid rod bundle critical heat flux data (in excess of 1100 points) that Westinghouse has collected. The WRB-1 correlation, based on local fluid conditions, represents the rod bundle data with better accuracy over a wide range of variables than the previous correlation used in design (namely the W-3 correlation). This correlation accounts directly for both typical and thimble cold wall cell effects, uniform and non-uniform heat flux profiles, and variations in rod heated length and in grid spacing.

The applicable range of variables is:

Pressure	$1440 \leq P \leq 2490$ psia
Local Mass Velocity	$0.9 \leq \bar{G}_{loc}/10^6 \leq 3.7$ lb/ft ² -hr
Local Quality	$-0.2 \leq \chi_{loc} \leq 0.3$
Heated Length, Inlet to CHF Location	$L_h \leq 14$ feet
Grid Spacing	$13 \leq g_{sp} \leq 32$ inches
Equivalent Hydraulic Diameter	$0.37 \leq d_e \leq 0.60$ inches
Equivalent Heated Hydraulic Diameter	$0.46 \leq d_h \leq 0.68$ inches

Figure 3.2-44A shows measured critical heat flux plotted against predicted critical heat flux using the WRB-1 correlation.

A correlation limit DNBR of 1.17 for the WRB-1 correlation has been approved by the NRC for the 15x15 fuel.

3.2.2.1.6 The W-3 DNB Correlation

The W-3 DNB correlation^{47, 49 and 95} is used for both fuel types where the primary DNB correlation is not applicable. The WRB-1 correlation is developed based on mixing vane data and therefore is only applicable in the heated rod spans above the first mixing vane grid. The W-3 correlation, which does not take credit for mixing vane grids, is used to calculate DNBR values in the heated region below the first mixing vane grid. In addition, the W-3 correlation is applied in the analysis of accident conditions where the system pressure is below the range of the primary correlation. For system pressure in the range of 500 to 1000 psia, the W-3 correlation is 1.45⁸⁹. For system pressure greater than 1000 psia, the W-3 correlation is limited to 1.30. A cold wall factor⁵⁰ is applied to the W-3 DNB correlation to account for the pressure of the unheated thermal surface.

3.2.2.1.7 Film Boiling Heat Transfer Coefficient

Heat transfer after departure from nucleate boiling was conservatively assumed to be limited by film boiling immediately, and the period of transition boiling neglected.

The correlation used to evaluate these film boiling heat transfer coefficients was developed by Tong, Sandberg and Bishop⁵¹ and is shown in Figure 3.2-45.

$$\left(\frac{hD}{k}\right)_f = 0.0193 \left(\frac{DG}{\mu}\right)_f^{0.80} \left(\frac{C_p \mu}{k}\right)_f^{1.23} \left(\frac{\rho_g}{\rho_b}\right)^{0.68} \left(\frac{\rho_g}{\rho_\ell}\right)^{0.068}$$

where: $\rho_b = \rho_g \alpha + \rho_\ell (1 - \alpha)$ and

IP2
FSAR UPDATE

C_p = heat capacity at constant pressure, Btu/lb-°F
 D = equivalent diameter of flow channel, ft
 h = heat transfer coefficient, Btu/hr-ft²-°F
 G = mass flow rate, lb/hr-ft²
 k = thermal conductivity, Btu/hr-ft-°F
 α = void fraction
 ρ = density, lbs/ft³
 μ = viscosity, lbs/ft-hr

Subscripts:

g = Evaluation of the property at the saturated vapor condition
 ℓ = Evaluation of the property at the saturated liquid condition
 f = Evaluation of the property at the average film temperature
 w = Evaluation of the property at the wall temperature
 b = Evaluation of the property at the average bulk fluid condition

The heat transfer correlation was developed for flow rates equal or greater than 0.8×10^6 lb/hr ft² over a pressure range of 580 to 3190 psia, for qualities as high as 100-percent, and heat flux from 0.1 to 0.65×10^6 Btu/hr ft².

3.2.2.2 Hot Channel Factors

The total hot channel factors for heat flux and enthalpy rise are defined as the maximum-to-core average ratios of these quantities. The heat flux factor considers the local maximum linear heat generation rate at a point (the "hot spot"); the enthalpy rise hot channel factor involves the maximum integrated value along a channel (the "hot channel").

3.2.2.2.1 Definition of Engineering Hot Channel Factor

Each of the total hot channel factors is composed of a nuclear hot channel factor describing the neutron flux distribution and an engineering hot channel factor, which allows for variations in flow conditions and fabrication tolerances. The engineering hot channel factors are made up of subfactors, which account for the influence of the variations of fuel pellet diameter, density, enrichment and eccentricity; fuel rod diameter; inlet flow distribution; flow redistribution; and flow mixing.

3.2.2.2.2 Heat Flux Engineering Subfactor, F_Q^E

The heat flux engineering hot channel factor is used to evaluate the maximum linear heat generation rate in the core. This subfactor is determined by statistically combining the fabrication variations for fuel pellet diameter, density, enrichment and variation in fuel rod diameter, and has a value of 1.03 to be applied to the fuel rod surface heat flux. As shown in Reference 52, no DNB penalty need be taken for the short relatively low intensity heat flux spikes caused by variations in the above parameters or fuel pellet eccentricity

IP2
FSAR UPDATE

3.2.2.2.3 Enthalpy Rise Engineering Subfactor, $F_{\Delta H}^E$

The effect of variations in flow conditions and fabrication tolerances on the hot channel enthalpy rise in reload analysis is directly considered in the Westinghouse version of VIPRE-01 Code^{100,101} thermal subchannel analysis under any reactor operating condition (refer to Section 3.2.2.4, DNB Analysis Method for VIPRE description). The items presently considered contributing to the enthalpy rise engineering hot channel factor are discussed below:

1. Pellet diameter, density and enrichment.

Variation in pellet diameter, density and enrichment are considered, statistically, in establishing the limit DNBR's (see section 3.2.2.4) for the Revised Thermal Design Procedure⁹⁷ employed in this application. Uncertainties in the variables are determined from sampling of manufacturing data.

2. Inlet Flow Maldistribution.

Data have been considered from several one-seventh scale hydraulic reactor model tests (References 53, 54, and 55) in arriving at the core inlet flow maldistribution criteria to be used in the THINC⁵⁶ analyses. THINC analyses made, using these data, have indicated that a conservative design basis is to consider a 5-percent reduction in the flow to the hot assembly (Reference 78). The design basis of 5% flow reduction to the hot assembly is also used in the VIPRE analysis for the 1.4% power uprate.

3. Flow Redistribution.

The flow redistribution accounts for the reduction in flow in the hot channel resulting from the high flow resistance in the channel due to the local or bulk boiling. The effect of the nonuniform power distribution is inherently considered in the VIPRE analysis for every operating condition, which is evaluated.

4. Flow Mixing.

The mixing vanes incorporated in the spacer grid design induce additional flow mixing between the various flow channels in a fuel assembly as well as between adjacent assemblies. This mixing reduces the enthalpy rise in the hot channel resulting from local power peaking or unfavorable mechanical tolerances. The subchannel mixing model now incorporated in the VIPRE code and used in reload reactor design is based on experimental data (Reference 57).

3.2.2.3 Core Pressure Drop and Hydraulic Loads

Core and vessel pressure losses are calculated by equations of the form:

$$\Delta P_L = \left(K + F \frac{L}{D_e} \right) \frac{\rho V^2}{2 g_c (144)}$$

where:

$$\Delta P_L = \text{unrecoverable pressure drop, lb}_f/\text{in.}^2$$

IP2
FSAR UPDATE

ρ	= fluid density, lb _m /ft ³
L	= length, ft
D _e	= equivalent diameter, ft
V	= fluid velocity, ft/sec
g _c	= 32.174, lb _m -ft/lb _f -sec ²
K	= form loss coefficient, dimensionless
F	= friction loss coefficient, dimensionless

Fluid density is assumed to be constant at the appropriate value for each component in the core and vessel. Because of the complex core and vessel flow geometry, precise analytical values for the form and friction loss coefficients are not available. Therefore, experimental values for these coefficients are obtained from geometrically similar models.

The results of full scale tests of core components and fuel assemblies are utilized in developing the core pressure loss characteristic in reload reactor design. The pressure drop for the vessel has been obtained by combining the core loss with correlation of one-seventh scale model hydraulic test data on a number of vessels (References 53 and 54) and form loss relationships (Reference 58). Moody (Reference 59) curves have been used to obtain the single phase friction factors.

The fuel assembly holddown springs are designed to keep the fuel assemblies in contact with the lower core plate under all Condition I and II events, with the exception of the turbine overspeed transient associated with a loss of external load. The holddown springs are designed to tolerate the possibility of an over deflection associated with fuel assembly liftoff for this case and provide contact between this transient. More adverse flow conditions occur during a loss-of-coolant accident. Hydraulic loads at normal operating conditions are calculated considering the best estimate flow and accounting for the minimum core bypass flow based on manufacturing tolerances. Core hydraulic loads at cold plant startup conditions are based on the best estimate flow, but are adjusted to account for the coolant density difference. Conservative core hydraulic loads for a pump overspeed transient, which could possibly create flow rates 20-percent greater than the best estimate flow, are evaluated to be approximately twice the fuel assembly weight. The hydraulic forces are not sufficient to lift a rod control cluster during normal operation even if the rod cluster is detached from its coupling.

3.2.2.4 Thermal and Hydraulic Design Parameters

The thermal and hydraulic design parameters are given in Table 3.2-6, Sheets 1-3. Sheet 3 shows parameters over a range of vessel average temperatures, giving flexibility to operate at full licensed power at various plant operating conditions.

DNB Design Basis

There will be at least a 95-percent probability that departure from nucleate boiling (DNB) will not occur on the limiting fuel rods during normal operation and operational transients and any transient conditions arising from faults of moderate frequency (Condition I and II events), at a 95-percent confidence level. Historically, this has been conservatively met by adhering to the following thermal design basis: there must be at least a 95-percent probability that the minimum departure from nucleate boiling ratio (DNBR) of the limiting power rod during Condition I and II events is greater than or equal to the DNBR limit of the DNB correlation being used. The DNBR limit for the correlation is established based on the variance of the correlation such that there is

IP2
FSAR UPDATE

a 95-percent probability with 95-percent confidence that DNB will not occur when the calculated DNBR is at the DNBR limit.

DNB Analysis Method

The THINC IV ^{77, 78} computer program, beginning in Cycle 10, was used to perform the thermal/hydraulic calculations for both fuel types. The THINC IV code is used to calculate coolant density, mass velocity, enthalpy, void fractions, static pressure and DNBR distributions along flow channels within a reactor core under all expected operating conditions. References 77 and 78 contain details of the THINC IV computer program, including models and correlations used. The Westinghouse version of the VIPRE-01 (VIPRE) code is used. The VIPRE code is equivalent to the THIC-VI (THINC) code and has been approved by the NRC for licensing applications to replace the THINC code. The use of VIPRE is in full compliance with the conditions specified in the NRC Safety Evaluation Report (SER) on WCAP-14565-P-A (Reference 101). The design method employed for both fuel types to meet the DNB design basis is the Revised Thermal Design Procedure.⁹⁷ Uncertainties in plant operating parameters, nuclear and thermal parameters, and fuel fabrication parameters are considered statistically such that there is at least a 95-percent probability that the minimum DNBR will be greater than or equal to the limit DNBR for the limiting power rod. Plant parameter uncertainties are used to determine the plant DNBR uncertainty. The DNBR uncertainty, combined with the DNBR limit, establishes a design DNBR value, which must be met in plant safety analyses. Since the parameter uncertainties are considered in determining the design DNBR value, the plant safety analyses are performed using values of input parameters without uncertainties. In addition, the limit DNBR values are increased to values designated as the safety analysis limit DNBR's. The plant allowances available between the safety analysis limit DNBR values and the design limit DNBR values is not required to meet the design basis. This allowance will be used for flexibility in the design and operation of this plant.

For this design, the WRB-1 correlation is used for analysis of the Vantage+ fuel assemblies with a correlation limit of 1.17 (both typical and thimble cells).

The design method employed for both fuel types to meet the DNB design basis is the Revised Thermal Design Procedure (RTDP)⁹⁷. With the RTDP methodology, uncertainties in plant operating parameters, nuclear and thermal parameters, fuel fabrication parameters, computer codes and DNB correlation predictions are considered statistically to obtain DNB uncertainty factors. Based on the DNB uncertainty factors, RTDP design limit DNBR values are determined such that there is at least a 95% probability at a 95% confidence level that DNB will not occur on the most limiting fuel rod during normal operation and operational transients and during transient conditions arising from faults of moderate frequency (Condition I and II events as defined in ANSI N18.2)

To maintain DNBR margin to offset DNB penalties such as those due to fuel rod bow (see section 3.2.2.6) and potential transition core (see 3.2.2.5.1), the safety analyses were performed to DNBR limits higher than the design limit DNBR values. The difference between the design limit DNBRs and the safety analysis limit DNBRs results in available DNBR margin. The net DNBR margin, after consideration of all penalties, is available for operating and design flexibility. The Standard Thermal Design Procedure (STDP) is used for those analyses where RTDP is not applicable. In the STDP method the parameters used in analysis are treated in a conservative way from a DNBR standpoint. The parameter uncertainties are applied directly to the plant safety input values to give the lowest minimum DNBR. The DNBR limit for STDP is

the appropriate DNB correlation limit increased by sufficient margin to offset the applicable DNBR penalties.

For this design, the WRB-1 correlation is used for analysis of both fuel types with a correlation limit of 1.17 (both typical and thimble cells). When the core condition is outside the range of the WRB-1 correlation, the W-3 correlation is applied with a correlation limit of 1.30 (both cell types).

DNB With Physical Burnout

Westinghouse⁶⁰ has conducted DNB tests in a 25-rod bundle where physical burnout occurred with one rod. After this occurrence, the 25-rod test section was used for several days to obtain more DNB data from the other rods in the bundle. The burnout and deformation of the rod did not affect the performance of neighboring rods in the test section during the burnout or the validity of the subsequent DNB data points as predicted by the W-3 correlation. No occurrences of flow instability or other abnormal operations were observed.

DNB With Return to Nucleate Boiling

Additional DNB tests have been conducted by Westinghouse⁶¹ in 19 and 21 rod bundles. In these tests, DNB without physical burnout was experienced more than once on single rods in the bundles for short periods of time. Each time, a reduction in power of approximately 10-percent was sufficient to reestablish nucleate boiling on the surface of the rod. During these and subsequent tests, no adverse effects were observed on this rod or any other rod in the bundle as a consequence of operating in DNB.

Hydrodynamic and Flow Power Coupled Instability

Thermohydrodynamic instabilities will not occur under Condition I and II modes of operation for Westinghouse PWR reactor designs. A large power margin exists to predicted inception of such instabilities. Analysis has been performed which shows that minor plant to plant differences in Westinghouse reactor designs such as fuel assembly arrays, core power to flow ratios and fuel assembly length will not result in gross deterioration of the above power margins.

3.2.2.5 Hydraulic Compatibility

3.2.2.5.1 Transition Core Effects

This section describes the thermal and hydraulic design of the Indian Point Unit 2 during transition cores with Westinghouse VANTAGE+ and 15x15 Upgrade fuel assemblies, and a full 15x15 Upgrade fuel core. DNB performance when transitioning cores, and the hydraulic compatibility of Westinghouse VANTAGE+ and 15x15 Upgraded fuel, will be addressed in this discussion.

3.2.2.5.2 DNB Performance When Transitioning Cores

This section describes the impact on DNB performance when transitioning from VANTAGE+ fuel to 15x15 Upgraded fuel. The Westinghouse transition core DNB methodology is given in References 90, 91 and 92 and has been approved by the NRC via Reference 93 and 94. Using this methodology, transition cores are analyzed as if the entire core consists of one assembly type (full VANTAGE+ fuel or full 15x15 Upgraded fuel).

Beginning with Cycle 17, 15x15 Upgraded fuel assembly regions will be used to refuel the core. The 15x15 Upgraded fuel design incorporates the I-spring mid-grid design and the enhanced IFM. Both types of grids are longer and thinner than the grids in the Vantage+ fuel design. The transition core DNB effect is dependent on the fuel assembly hydraulic characteristics. Since there are changes in the hydraulic parameters in the 15x15 upgraded fuel, there is a transition core impact. Transition core analyses for a mixed core of Vantage+ fuel and 15x15 Upgraded fuel have been performed using VIPRE-01 code. The analyses show that the transition core effect on DNB margin is predicted to be within the acceptable range with the final grid loss coefficients determined for 15x15 Upgraded fuel.

3.2.2.5.3 Compatibility

Hydraulic testing of VANTAGE+ and 15x15 Upgraded fuel assemblies was performed in order to determine their hydraulic resistance and compatibility when in a mixed core. The VANTAGE+ and 15x15 Upgraded fuel designs have been shown to be compatible in Reference 85.

The major hardware differences between the 9 grid 15x15 VANTAGE+ assembly and the 9 grid 15x15 Upgraded assembly are:

1. I-Spring design mid-grids – taller, thinner and greater dimple clad contact area
2. Intermediate Flow Mixer (IFM) grids with increased contact length and balanced vane pattern – Enhanced IFM (EIFM)
3. Tube-in-tube ZIRLO guide thimbles

The hydraulic resistance of the two assemblies is based on full scale hydraulic flow test data. The design hydraulic loss coefficients were verified with a confirmatory hydraulic test in the Fuel Assembly Compatibility Test System (FACTS). The results were evaluated to determine the values of the pressure drop loss coefficients. Test results of the VANTAGE+ fuel are available to compare against. The same test plan used for that testing was applied to the test of the 15x15 Upgraded fuel design.

A fuel assembly vibration test was conducted to confirm that the 15x15 Upgraded fuel assembly does not experience flow-induced vibration. The hydraulic vibration test was performed in the FACTS test loop. The 15x15 Upgraded fuel assembly design did not experience resonant fuel assembly vibration over the range of expected in-core flow rates.

A side-by-side (15x15 Upgraded versus VANTAGE+) 500 hour VIPER test was performed. Test results were used to demonstrate the acceptable fretting behavior of the 15x15 Upgraded fuel design and that the crossflow-induced fuel rod fretting wear between the two designs is insignificant.

A crossflow analysis between the 15x15 Upgraded fuel and VANTAGE+ fuel using the THINC code has been completed to determine the crossflow velocity profile in the transition core from the VANTAGE+ fuel to the 15x15 Upgraded fuel design in the IP2 plant conditions. The crossflow is caused by the midgrid and IFM pressure drop mismatch between adjacent fuel assemblies. The calculated crossflow velocities are bounded by Westinghouse transition core experience.

3.2.2.6 Effects of Rod Bow on DNBR

The phenomenon of fuel rod bowing, as described in Reference 80 must be accounted for in the DNBR safety analysis of Condition I and Condition II events for each plant application. Applicable generic credits for margin resulting from retained conservatisms in the evaluation of DNBR can be used to offset the effects of rod bow.

For safety analysis of Indian Point Unit 2, sufficient margin was maintained in the design of the fuel [**Note** - *Margin maintained between design limit DNBR and safety analysis limit DNBR +As a result of analyses performed for OFA transition, maintaining plugging devices in core is optional.*] to accommodate full and low flow rod bow DNBR penalties (less than 1-percent for the worst cast, which is at a burnup of 24,000 MWd/MTU identified in Reference 81) with the incorporation of the L^2/I scaling factor (I =bending moment of inertia, L =span length) to account for the 9-grid fuel span lengths. The rod bow DNBR penalties in the Intermediate Flow Mixer (IFM) grid spans are less than those in the mixing vane grid spans.

The maximum rod bow penalties accounted for in the design safety analysis are based on an assembly average burnup of 24,000 MWd/MTU. At burnups greater than 24,000 MWd/MTU, credit is taken for the effect of F-delta-H burndown, due to the decrease in fissionable isotopes and the buildup of fission product inventory, and no additional rod bow penalty is required.

3.2.3 Mechanical Design And Evaluation

The reactor core and reactor vessel internals are shown in cross-section in Figure 3.2-46 and in elevation in Figure 3.2-47. The core, consisting of the fuel assemblies, control rods, source rods, burnable poison rods, and plugging devices+, provides and controls the heat source for the reactor operation.

The internals, consisting of the upper and lower core support structure, are designed to support, align, and guide the core components, direct the coolant flow to and from the core components, and to support and guide the incore instrumentation. A listing of the core mechanical design parameters is given in Table 3.2-7.

The fuel assemblies are arranged in a checkerboard and/or roughly circular zoned pattern. The fuel assemblies contain fuel of different enrichments depending on the location of the assembly within the core.

The fuel is in the form of slightly enriched uranium-dioxide ceramic pellets. The pellets are stacked to an active height of 144-in. (previously 142 in.) within ZIRLO™ (previously Zircaloy-4) tubular cladding, which is plugged and seal welded at the ends to encapsulate the fuel. The enrichments of the fuel for the first three regions in the core are given in Table 3.2-7. Reload fuel enrichment may vary up to the maximum value allowed in the Technical Specifications. Heat generated by the fuel is removed by demineralized light water, which flows upward through the fuel assemblies and acts as both moderator and coolant.

The core is divided into fuel assembly regions of different enrichments. The loading arrangement for the initial cycle is indicated on Figure 3.2-48. In the past refueling took place generally in accordance with an inward loading schedule. Starting from Cycle 6 a low leakage loading pattern for core refueling design has been adopted and starting from Cycle 13, a low, low leakage loading pattern was used. This will reduce neutron fluence at the reactor vessel wall.

The control rods, designated as rod cluster control assemblies, consist of groups of individual absorber rods, which are held together by a spider assembly at the top end and actuated as a group. In the inserted position, the absorber rods fit within hollow guide thimbles in the fuel assemblies. The guide thimbles are an integral part of the fuel assemblies and occupy locations within the regular fuel rod pattern where fuel rods have been deleted. In the withdrawn position, the absorber rods are guided and supported laterally by guide tubes, which form an integral part of the upper core support structure. Figures 3.2-49 and 3.2-50 show a typical rod cluster control assembly in a fuel assembly. As shown in Figure 3.2-47, the fuel assemblies are positioned and supported vertically in the core between the upper and lower core plates. The core plates are provided with pins, which index into closely fitting mating holes in the fuel assembly top and bottom nozzles. The pins maintain the fuel assembly alignment, which permits free movement of the control rods from the fuel assembly into the guide tubes in the upper support structure without binding or restriction between the rods and their guide surfaces.

Operational or seismic loads imposed on the fuel assemblies are transmitted through the core plates to the upper and lower support structures and ultimately to the internals support ledge at the pressure vessel flange in the case of vertical loads or to the lower radial support and internals support ledge in the case of horizontal loads. The internals also provide a form fitting baffle surrounding the fuel assemblies, which confine the upward flow of coolant in the core area to the fuel bearing region.

3.2.3.1 Reactor Internals

3.2.3.1.1 Design Description

The reactor internals are designed to support and orient the reactor core fuel assemblies and control rod assemblies, absorb the control rod dynamic loads, and transmit these and other loads to the reactor vessel flange, provide a passageway for the reactor coolant, and support incore instrumentation. The reactor internals are shown in Figure 3.2-47.

The internals have been designed to withstand the forces due to weight, preload of fuel assemblies, control rod dynamic loading, vibration, and earthquake acceleration. The internals were analyzed in a manner similar to Connecticut Yankee, San Onofre, Zorita, Saxton, and Yankee. Under the loading conditions, including conservative effects of design earthquake loading, the structure satisfies stress values prescribed in Section III, ASME Nuclear Vessel Code.

The reactor internals are equipped with bottom-mounted incore instrumentation supports. These supports are designed to sustain the applicable loads outlined above.

The components of the reactor internals are divided into three parts consisting of the lower core support structure (including the entire core barrel and thermal shield), the upper core support structure, and the incore instrumentation support structure.

3.2.3.1.1.1 Lower Core Support Structure

The major component and support member of the reactor internals is the lower core support structure, shown in Figure 3.2-51. This support structure assembly consists of the core barrel, the core baffle, the lower core plate and support columns, the thermal shield, the intermediate diffuser plate, and the bottom support plate, which is welded to the core barrel. All the major

IP2
FSAR UPDATE

material for this structure is type 304 stainless steel. The core support structure is supported at its upper flange from a ledge in the reactor vessel head flange and its lower end is restrained in its transverse movement by a radial support system attached to the vessel wall. Within the core barrel are axial baffle and former plates, which are attached to the core barrel wall and form the enclosure periphery of the assembled core. The lower core plate is positioned at the bottom level of the core below the baffle plates and provides support and orientation for the fuel assemblies.

The lower core plate is a 2-in. thick member through which the necessary flow distributor holes for each fuel assembly are machined. Fuel assembly locating pins (two for each assembly) are also inserted into this plate. Columns are placed between this plate and the lower core support of the core barrel in order to provide stiffness and to transmit the core load to the lower core support. Intermediate between the support plate and lower core support plate a perforated plate is positioned to diffuse uniformly the coolant flowing into the core.

The one-piece thermal shield is fixed to the core barrel at the top with rigid bolted connections. The bottom of the thermal shield is connected to the core barrel by means of axial flexures. This bottom support allows for differential axial growth of the shield with respect to the core barrel but restricts radial or horizontal movement of the bottom of the shield. Rectangular tubing, in which vessel material samples can be inserted and irradiated during reactor operation, are welded to the thermal shield and extend to the top of the thermal shield. These samples are held in the rectangular tubing by a preloaded spring device at the top and bottom.

The lower core support structure and principally the core barrel serve to provide passageways and control for the coolant flow. Inlet coolant flow from the vessel inlet nozzles proceeds down the annulus between the core barrel and the vessel wall, flows on both sides of the thermal shield, and then into a plenum at the bottom of the vessel. It then turns and flows up through the lower support, passes through the intermediate diffuser plate and then through the lower core plate. The flow holes in the diffuser plate and the lower core are arranged to give a very uniform entrance flow distribution to the core. After passing through the core, the coolant enters the area of the upper support structure and then flows generally radially to the core barrel outlet nozzles and directly through the vessel outlet nozzles.

A small amount of water also flows between the baffle plates and core barrel to provide additional cooling of the barrel. Similarly, a small amount of the entering flow is directed into the vessel head plenum to provide cooling of the head. Both these flows eventually are directed into the upper support structure plenum and exit through the vessel outlet nozzles.

Vertically downward loads from weight, fuel assembly preload, control rod dynamic loading, and earthquake acceleration are carried by the lower core plate partially into the lower core plate support flange on the core barrel shell and partially through the lower support columns to the lower core support and then through the core barrel shell to the core barrel flange supported by the vessel head flange. Transverse loads from earthquake acceleration, coolant cross flow, and vibration are carried by the core barrel shell to be distributed to the lower radial support to the vessel wall, and to the core barrel flange. Transverse acceleration of the fuel assemblies is transmitted to the core barrel shell by direct connection of the lower core plate to the barrel wall and by a radial support type connection of the upper core plate to slab-sided pins pressed into the core barrel.

The main radial support system of the core barrel is accomplished by "key" and "keyway" joints to the reactor vessel wall. At equally spaced points around the circumference, an Inconel block

IP2
FSAR UPDATE

is welded to the vessel inside diameter. Another Inconel block is bolted to each of these blocks, and has a "keyway" geometry. Opposite each of these is a "key", which is attached to the internals. At assembly, as the internals are lowered into the vessel, the keys engage the keyways in the axial direction. With this design, the internals are provided with a support at the furthest extremity, and may be viewed as a beam fixed at the top and simply supported at the bottom.

Radial and axial expansions of the core barrel are accommodated but transverse movement of the core barrel is restricted by this design. With this system, cycle stresses in the internal structures are within the ASME Section III limits. This eliminates any possibility of failure of the core support.

In the event of downward vertical displacement of the internals, energy absorbing devices limit the displacement by contacting the vessel bottom head. The load is transferred through the energy devices of the internals.

The energy absorbers, cylindrical in shape, are contoured on their bottom surface to the reactor vessel bottom head geometry. Their number and design are determined so as to limit the forces imposed to less than yield. Assuming a downward vertical displacement, the potential energy of the system is absorbed mostly by the strain energy of the energy absorbing devices.

The free fall in the hot condition is on the order of 0.50-in. and there is an additional strain displacement in the energy absorbing devices of approximately 0.75-in. Alignment features in the internals prevent cocking of the internals structure during this postulated drop. The control rods are designed to provide assurance of control rod insertion capabilities under this assumed drop of internals condition. The drop distance of about 1.25-in. is not enough to cause the tips of the shutdown group of rod cluster control assemblies to come out of the guide tubes in the fuel assemblies.

3.2.3.1.1.2 Upper Core Support Assembly

The upper core support assembly, shown in Figure 3.2-52, consists of the top support plate, deep beam sections, and upper core plate between which are contained 48 support columns and 61 guide tube assemblies. The support columns establish the spacing between the top support plate, deep beam sections, and the upper core plate. They are fastened at top and bottom to these plates and beams. The support columns transmit the mechanical loadings between the two plates and serve the supplementary function of supporting thermocouple guide tubes. The guide tube assemblies, shown on Figure 3.2-53, sheath and guide the control rod drive shafts and control rods and provide no other mechanical functions. They are fastened to the top support plate and are guided by pins in the upper core plate for proper orientation and support. Additional guidance for the control rod drive shafts is provided by the control rod shroud tube, which is attached to the upper support plate and guide tube.

The upper core support assembly, which is removed as a unit during refueling operation, is positioned in its proper orientation with respect to the lower support structure by flat-sided pins pressed into the core barrel, which in turn engage in slots in the upper core plate. At an elevation in the core barrel where the upper core plate is positioned, the flat-sided pins are located at angular positions of 0, 90, 180, and 270 degrees. Four slots are milled into the core plate at the same positions. As the upper support structure is lowered into the main internals, the slots in the plate engage the flat-sided pins in the axial direction. Lateral displacement of the plate and of the upper support assembly is restricted by this design. Fuel assembly locating

pins protrude from the bottom of the upper core plate and engage the fuel assemblies as the upper assembly is lowered into place. Proper alignment of the lower core support structure, the upper core support assembly, the fuel assemblies and control rods is thereby assured by this system of locating pins and guidance arrangement. The upper core support assembly is restrained from any axial movements by a large circumferential spring, which rests between the upper barrel flange and the upper core support assembly and is compressed by the reactor vessel head flange.

Vertical loads from weight, earthquake acceleration, hydraulic loads, and fuel assembly preload are transmitted through the upper core plate via the support columns to the deep beams and top support plate and then to the reactor vessel head. Transverse loads from coolant cross flow, earthquake acceleration, and possible vibrations are distributed by the support columns to the top support plate and upper core plate. The top support plate is particularly stiff to minimize deflection.

3.2.3.1.1.3 Incore Instrumentation Support Structures

The incore instrumentation support structures consist of an upper system to convey and support thermocouples penetrating the vessel through the head and a lower system to convey and support flux thimbles penetrating the vessel through the bottom.

The upper system utilizes the reactor vessel head penetrations. Instrumentation port columns are slip-connected to inline columns that are in turn fastened to the upper support plate. These port columns protrude through the head penetrations. The thermocouples are carried through these port columns and the upper support plate at positions above their readout locations. The thermocouple conduits are supported from the columns of the upper core support system. The thermocouple conduits are sealed stainless steel tubes.

In addition to the upper incore instrumentation, there are reactor vessel bottom port columns, which carry the retractable, cold-worked stainless steel flux thimbles that are pushed upward into the reactor core. Conduits extend from the bottom of the reactor vessel down through the concrete shield area and up to a thimble seal line. The minimum bend radii are about 144-in. and the trailing ends of the thimbles (at the seal line) are extracted approximately 15-ft during refueling of the reactor in order to avoid interference within the core. The thimbles are closed at the leading ends and serve as the pressure barrier between the reactor pressurized water and the containment atmosphere.

Mechanical seals between the retractable thimbles and the conduits are provided at the seal line. During normal operation, the retractable thimbles are stationary and move only during refueling or for maintenance, at which time a space of approximately 15-ft above the seal line is cleared for the retraction operation. Sections 7.4 and 7.6 contain more information on the layout of the incore instrumentation system. The incore instrumentation support structure is designed for adequate support of instrumentation during reactor operation and is rugged enough to resist damage or distortion under the conditions imposed by handling during the refueling sequence.

3.2.3.1.2 Evaluation of Core Barrel and Thermal Shield

The internals design is based on analysis, test, and operational information. Troubles in previous Westinghouse PWRs have been evaluated and information derived has been considered in this design. For example, the Westinghouse design uses a one-piece thermal

IP2
FSAR UPDATE

shield, which is attached rigidly to the core barrel at one end and flexured at the other. The early designs that malfunctioned were multi-piece thermal shields that rested on vessel lugs and were not rigidly attached at the top.

Early core barrel designs that have malfunctioned in service, now abandoned, employed threaded connections such as tie rods, joining the bottom support to the bottom of the core barrel, and a bolted connection that tied the core barrel to the upper barrel. The malfunctioning of core barrel designs in earlier service was believed to have been caused by the thermal shield, which was oscillating, thus creating forces on the core barrel. Other forces were induced by unbalanced flow in the lower plenum of the reactor. In today's rod cluster control design there are no fuel followers to necessitate a large bottom plenum in the reactor. The elimination of these fuel followers enabled Westinghouse to build a shorter core barrel.

The Connecticut Yankee reactor and the Zorita reactor core barrels are of the same construction as the Indian Point Unit 2 reactor core barrel. Deflection measuring devices employed in the Connecticut Yankee reactor during the hot functional test, and deflection and strain gauges employed in the Zorita reactor during the hot-functional test provided important information that was used in the design of the present day internals, including that for Indian Point. When the Connecticut Yankee thermal shield was modified to the same design as for Southern California Edison, it, too, operated satisfactorily as was evidenced by the examination after the hot-functional test. After hot-functional tests on all of these reactors, a careful inspection of the internals was examined for any differential movement; upper core plate inside supports were examined, and the thermal shield attachments to the core barrel, including all lockwelds on the devices used to lock the bolt, were checked; no malfunctions were found.

Substantial scale model testing was performed at WAPD. This included tests, which involved a complete full-scale fuel assembly, which was operated at reactor flow, temperature, and pressure conditions. Tests were run on a one-seventh scale model of the Indian Point Unit 2 reactor. Measurements taken from those tests indicated very little shield movement, on the order of a few mils when scaled up to Indian Point Unit 2. Strain gauge measurements taken on the core barrel also indicated very low stresses. Testing to determine thermal shield excitation due to inlet flow disturbances was included. Information gathered from these tests was used in the design of the thermal shield and core barrel. It was concluded, from the experience gained during the testing program and the analyses, that the design as employed on the Indian Point Unit 2 plant is adequate.

In order to confirm the internals design, deflection gauges were mounted on the thermal shield top and bottom for the hot-functional test. Gauges were mounted in the top of the thermal shield equidistant from the fixed supports, and at the bottom of the thermal shield, equidistant from the six flexures, and next to the flexure supports. The internals inspection, just before the hot-functional test, included looking at mating bearing surfaces, main welds, and welds that are used on bolt locking devices. At the conclusion of the hot-functional test, measurement readings were taken from the deflectometers on the shield and the internals were re-examined at all key areas for any evidence of malfunction.

3.2.3.2 Core Components

3.2.3.2.1 Design Description

3.2.3.2.1.1 Fuel Assembly

The overall configuration of the VANTAGE+ fuel assembly is shown in Figures 3.2-54 and 3.2-56B. The Vantage+ fuel assembly with Performance+ enhancements is shown in Figure 3.2-61B. The 15x15 Upgraded fuel assembly, introduced in Cycle 17, is shown in Figure 3.2-61C. The assemblies are square in cross section, nominally 8.426-in. on a side, and have an overall height of approximately 159.975 inches. The fuel rods in a fuel assembly are arranged in a square array with 15 rod locations per side and a nominal centerline-to-centerline pitch of 0.563-in. between rods. Of the total possible 225 rod locations per assembly, 20 are occupied by guide thimbles for the rod cluster control rods and one for incore instrumentation. The remaining 204 locations contain fuel rods. In addition to fuel rods, a fuel assembly is composed of a top nozzle, a bottom nozzle, ten grid assemblies (plus 3 intermediate flow mixing grids starting with Cycle 13), 20 absorber rod guide thimbles, and one instrumentation thimble.

The guide thimbles in conjunction with the grid assemblies and the top and bottom nozzles comprise the basic structural fuel assembly skeleton. The grid assemblies are bulge attached to the guide thimbles at each location along the height of the fuel assembly at which lateral support for the fuel rods is required. Within this skeletal framework the fuel rods are contained and supported and the rod-to-rod centerline spacing is maintained along the assembly.

The original fuel design for Indian Point 2 was the Westinghouse High Parasitic (HIPAR) fuel assembly. This consisted of Zircaloy clad fuel rods, 9 Inconel grids and stainless steel instrumentation and guide thimbles. Burnable absorbers used were pyrex glass.

Starting with Cycle 5, the Westinghouse Low Parasitic (LOPAR) fuel assembly was introduced. This design consisted of Zircaloy-4 clad fuel rods, 9 Inconel grids and Zircaloy-4 instrumentation and guide thimbles.

For the Cycle 8, Wet Annular Burnable Absorbers (WABA) were introduced.

For Cycle 10, the Westinghouse Optimized Fuel Assembly (OFA) was introduced. This consisted of Zircaloy-4 clad fuel rods, 2 Inconel grids (top & bottom), 7 Zircaloy-4 grids and Zircaloy-4 instrumentation and guide thimbles. In addition, thimble plugs were removed from the core this cycle based on analysis performed to support removal. The assembly top nozzle design was changed to a Reconstitutable Top Nozzle (RTN) design to facilitate reconstitution of failed fuel.

For Cycle 11, the OFA fuel assembly design incorporated Debris Filter Bottom Nozzles (DFBN) and Integral Fuel Burnable Adsorbers (IFBA).

For Cycle 13, the Westinghouse Vantage+ fuel design was introduced. This design included ZIRLO clad fuel rods, 2 Inconel grids, 7 low pressure drop (LPD) Zircaloy-4 grids, 3 Zircaloy Integral Flow Mixing grids (IFM), ZIRLO instrumentation and guide thimbles, annular axial blankets along with the DFBN, IFBA and RTN. Use of WABAs was continued. See Reference 13.

IP2
FSAR UPDATE

For Cycle 15, the Vantage+ fuel assembly design incorporated Performance+ features of ZIRLO grids and IFMs and a hardened coating of zirconium oxide on the bottom section of the fuel rod clad to increase debris resistance.

For Cycle 16, the Vantage+ fuel assembly design was further enhanced with Performance+ features that include debris mitigation features of an additional grid located at the bottom end plug of the fuel rod, a longer fuel rod end plug and a revised DFBN. Other performance+ enhancements include longer fuel rods and longer annual axial blankets.

In addition to the above fuel design changes, the design burnup of the fuel assemblies has also been increasing to 62,000 MWD/MTU lead rod burnup for Cycle 16. See References 15, 16 and 17.

For Cycle 17, the 15x15 Upgraded fuel assembly design was used. This design has features to address grid-to-rod fretting fuel failures. These include I-spring mid-grids, enhanced IFMs and balanced mixing vanes. In addition, the tube-in-tube thimble design was incorporated with a single-dashpot, which improves straightness.

For Cycle 18, solid axial blanket pellets were introduced for the non-IFBA fuel rods.

Bottom Nozzle

Two types of nozzle designs were used for the HIPAR fuel assemblies. One type, which is square in cross section, is fabricated from type 304 stainless steel consisting of four side plates, 12 cross bars and four pads or feet. The side plates are welded together at the corners to form a plenum for inlet coolant to the fuel assembly. The cross bars are welded at each end to the top edges of the side plate and function as the bottom end support for the fuel rods. The bottom support surface for the fuel assembly is formed by the four pads, which are welded to the side plates in the corners. This design was used in a majority of the first core fuel assemblies. The previously used LOPAR and OFA fuel incorporate an equivalent bottom nozzle design utilizing a square perforated plate rather than the cross bars and side plate. On both designs, their respective cross bars and perforated plate prevent the fuel rods from falling through the bottom nozzles of the assembly.

Coolant flow to the fuel assembly is directed from the plenum in the bottom nozzle upward to the interior of the fuel assembly and to the channel between assemblies.

Axial loads imposed on the assembly, as well as the weight of the assembly are distributed through the guide thimble and the bottom nozzle to the lower core support plate. Indexing and positioning of the fuel assembly in the core is controlled through two holes in diagonally opposite pads, which mate with locating pins in the lower core plate. Lateral loads imposed on the fuel assembly are also transferred to the core support structures through the locating pins.

The OFA and VANTAGE+ bottom nozzle uses the reconstitutable feature found on the previously installed LOPAR fuel design, which uses a locking cup to lock the thimble screws on the guide thimble assembly, instead of the lockwire used in earlier LOPAR designs. The OFA nozzle assembly is shorter when compared to the previously installed LOPAR assembly to enhance fuel rod growth allowances.

The two bottom nozzle designs used in the OFAs are both square in cross section and fabricated from 304 stainless steel. The design used in earlier regions consists of a perforated

IP2
FSAR UPDATE

plate, four angle legs, and four pads of feet. The angle legs are fastened to the plate forming a plenum space for the coolant inlet to the fuel assembly.

The remaining OFA regions and the VANTAGE+ and 15x15 Upgraded fuel regions (starting with Cycle 13, Region 15) incorporate an equivalent bottom nozzle design denoted as the Debris Filter Bottom Nozzle (DFBN). This nozzle adds side plates or "skirts" to the previous design increasing structural capability for abnormal loads and providing a more defined plenum space below the nozzle. Additionally, the relatively large adapter plate flow holes of the earlier design are replaced with a new pattern of smaller flow holes. The decrease in size of the holes provides a "screen" for larger debris particles, which would otherwise cause damage if allowed to pass into the assembly.

In both designs, the adaptor plates prevent accidental downward ejection of the fuel rods from the fuel assembly. The nozzles are fastened to the assembly guide tubes by stainless steel screws, which penetrate through the nozzle and mate with a threaded plug in each guide tube (Figure 3.2-57). The screw possesses a circular locking cup around the screw head, which is crimped into mating detentes (lobes) on the bottom nozzle, preventing the screw from loosening.

Top Nozzle

The Reconstitutable Top Nozzle (RTN) used in both the OFA, VANTAGE+ and 15x15 Upgraded fuel assemblies is a box-like structure, which functions as the fuel assembly upper structural element and forms a plenum space where the heated fuel assembly discharge coolant is mixed and directed toward the flow holes in the upper core plate. The nozzle is comprised of an adaptor plate enclosure, top plate, clamps, hold-down leaf springs and assorted hardware. Each nozzle has four sets of leaf springs. All parts, with the exception of the springs and their hold-down bolts/screws, are constructed of type 304 stainless steel. The springs are made from age hardenable Inconel 718 and the bolts/screws from Inconel 600 for Region 16 and earlier regions, and from shotpeened Inconel 718 for Regions 17 and 18.

The adaptor plate portion of the nozzle is square in cross section, and is perforated by machined slots to provide for coolant flow through the plate. At assembly, the top ends of the LOPAR thimble stainless sleeves are fitted through individual bored holes in the plate and welded to the plate around the circumference of each hole. In the OFA removable top nozzle design, a groove is provided in each thimble thru-hole in the nozzle plate into which a stainless steel nozzle insert is mechanically connected by means of a preformed circumferential bulge near the top of the insert. Thus, the adaptor plate acts as the fuel assembly top end plate, and provides a means of distributing evenly among the guide thimbles any axial loads imposed on the fuel assemblies.

The nozzle enclosure is actually a square tubular structure, which forms the plenum section of the top nozzle. The bottom end of the enclosure is pinned and welded to the periphery of the adaptor plate and the top end is welded to the periphery of the top plate.

The top plate is square in cross section with a square central hole. The hole allows clearance for the rod cluster control absorber rods to pass through the nozzle into the guide thimbles in the fuel assembly and for coolant exit from the fuel assembly to the upper internals area. Two pads containing axial through-holes, which are located on diametrically opposite corners of the top plate provide a means of positioning and aligning the top of the fuel assembly. As with the bottom nozzle, alignment pins in the upper core plate mate with the holes in the top nozzle

plate. Hold-down forces of sufficient magnitude to oppose the hydraulic lifting forces on the fuel assembly are obtained by means of the leaf spring sets, which are mounted on the top plate. The springs are fastened in pairs to the top plate at the two corners where alignment holes are not used and radiate out from the corners parallel to the sides of the plate. Fastening of each pair of springs is accomplished with a clamp, which fits over the ends of the springs and two bolts/screws (one per spring set), which pass through the clamp and spring, and thread into the top plate. At assembly, the spring mounting bolts/screws are torqued sufficiently to preload against the maximum spring load and then lockwelded to the clamp, which is counterbored to receive the bolt/screw head. The spring load is obtained through deflection of the spring pack by the upper core plate. The spring pack form is such that it projects above the fuel assembly and is depressed by the core plate when the internals are loaded into the reactor. The free end of the spring pack is bent downward and captured in a key slot in the top plate to guard against loose parts in the reactor in the event (however remote) of spring fracture. The capture of the loose end has been deleted in latter designs.

Starting with Cycle 14, Region 16, the fuel has a cast top nozzle. This is a two-piece design incorporating a machined stainless steel adapter plate welded to a low-cobalt investment casting. The cast top nozzle is functionally interchangeable with the previous design and meets design criteria for the top nozzle.

In addition to its plenum and structural functions, the nozzle provides a protective housing for components, which mate with the fuel assembly. In handling a fuel assembly with a control rod inserted, the control rod spider is contained within the nozzle. During operation in the reactor, the nozzle protects the absorber rods from coolant cross flows in the unsupported span between the fuel assembly adaptor plate and the end of the guide tube in the upper internals package. Plugging devices, [*Note - As a result of analyses performed for OFA transition, maintaining plugging devices in the core is optional.*], which fill the ends of the fuel assembly thimble tubes at unrodded core locations and the source rods and burnable absorber rods, are all contained within the fuel top nozzle.

For the RTN design, a stainless steel nozzle insert is mechanically connected to the top nozzle adaptor plate (Figure 3.2-58A) via the engagement of the preformed circumferential bulge near the top of the insert and the mating groove in the wall of the adapter plate thimble tube through-hole. The insert has four equally spaced axial slots, which allow the insert to deflect inwardly at the elevation of the bulge, thus permitting the installation and removal of the nozzle. The insert bulge is positively held in the adapter plate mating groove by placing a lock tube with a uniform OD identical to that of the thimble tube into the insert. The lock tube is secured in place by a top flare, which creates a tight fit and six non-yielding projections on the OD, which interface with the concave side of the insert to preclude escape during core component transfer. The adaptor plate acts as the fuel assembly top end plate and provides a means of evenly distributing any axial loads imposed on the fuel assemblies to the guide thimbles.

Guide Thimbles

The control rod guide thimbles in the fuel assemblies provide guided channels for the absorber rods during insertion and withdrawal of the control rods. Up to and including Region 18 (VANTAGE+), they are fabricated from a single piece of tubing, which is drawn to two different diameters. The OFA thimbles are Zircaloy-4 and the VANTAGE+ thimble material ZIRLO™. The larger inside diameter at the top provides a relatively large annular area for rapid insertion during a reactor trip and accommodates a small amount of upward cooling flow during normal operations. The bottom portion of the guide thimble has two sections of reduced diameter

IP2
FSAR UPDATE

producing a "double dashpot" action when the absorber rods near the end of travel in the guide thimbles during a reactor trip. The transition zones at the dashpot sections are conical in shape so that there are no rapid changes in diameter in the tube.

Starting with Region 19 (15x15 Upgraded fuel design), the guide thimbles incorporate the tube-in-tube dashpot design. The tube-in-tube design utilizes a separate dashpot tube assembly that is inserted into the guide thimble assembly pulled to a press fit over the thimble end plug and bulged into place. To maintain the same diametrical clearance between the guide thimble ID and the dashpot OD, the 15x15 upgraded nominal dashpot thickness was reduced from 0.0165 to 0.0160 inches. As the dashpot tube in the design can provide additional lateral support in that bottom thimble span, it is expected that there will be additional resistance to lateral deformation and Incomplete Rod Insertions as a result of the design modification. The 15x15 Upgraded fuel thimbles are ZIRLO™.

Flow holes are provided just above the first dashpot transition to permit the entrance of cooling water during normal operation, and to accommodate the outflow of water from the dashpot during reactor trip.

The dashpot is open at the bottom by means of the drainage hole in the thimble screws that secure the bottom nozzle to the welded end plugs of the guide thimbles. This geometry is shown in Figure 3.2-57.

The top ends of the thimble tubes are mechanically attached to the sleeve of the top grid. An insert is also bulge attached to the thimble and the insert upper end is in turn mechanically attached to the top nozzle as shown in Figure 3.2-58A.

VANTAGE+ Grids

Prior to Region 18, the VANTAGE+ assembly has twelve grids. Starting with Region 18, a thirteenth grid, the protective grid (P-grid), was added to the VANTAGE+ assembly. The top and bottom grids, as in the OFA assembly, and the P-grid are Inconel 718 non-mixing vane grids. The top and bottom grids are Inconel-718 non-mixing vane grids. Low Pressure Drop (LPD) Zircaloy grids are used for the middle grids with Zircaloy IFMs located in the three uppermost middle grid spans. The VANTAGE+ fuel assembly with PERFORMANCE+ options has ZIRLO™ grids for the 3IFMs and 7 mid grids. The LPD grids have mixing vanes, diagonal springs and a reduced grid height, relative to the OFA grids. The LPD grid cells use the standard four dimples and two springs per cell for support locations. The IFMs provide mid-span flow mixing in the hottest fuel assembly spans. Each IFM cell contains four dimples, which are designed to prevent midspan channel closure and fuel rod contact with the mixing vanes. With the additional Performance+ enhancements added to the fuel starting with Region 18, a new Protective Bottom Grid (PBG) has been added. The PBG is a wider, extra grid at the very bottom of the fuel assembly that protects the fuel from debris. Its purpose is to filter out debris and hold it at an elevation below the bottom of the active core. The PBG is not a structural grid. The bottom of the PBG lies below the tops of the lower end plugs within the fuel rod. This means that any debris caught in the PBG cannot fret through the cladding and expose fuel pellets.

All VANTAGE+ outside grid straps contain mixing vanes, which also act as guides during fuel handling. The grids are also attached to the thimble tubes via the bulging mechanism as shown in Figure 3.2-61A. Top grid nozzle attachment is shown in Figure 3.2-58A. All grids employ the anti-snag outer strap design. A mixing vane grid is shown in Figure 3.2-59.

15x15 Upgraded Design Grids

The 15x15 Upgraded fuel design still contains twelve grids with the top and bottom grids unchanged from the Vantage+ design. The middle grids have changed to an I-spring design. The changes were made to improve fuel rod fretting margin. In addition to the spring change the size of the dimples was increased. The strap thickness was decreased to help offset pressure drop increase due to the I-spring and increased grid strap height. The strap height increased to create space to accommodate the increased dimples and the I-spring. The IFM grid design was enhanced to increase contact area also.

Fuel Rods

The fuel rods consist of uranium-dioxide ceramic pellets in slightly cold worked ZIRLO™ tubing, which is plugged and seal welded at the ends to encapsulate the fuel. Sufficient void volume and clearances are provided within the rod to accommodate fission gases released from the fuel, differential thermal expansion between the cladding and the fuel, helium released from poison burnup (IFBA rods), and fuel swelling due to accumulated fission products without overstressing of the cladding or seal welds. Shifting of the fuel within the cladding is prevented during handling or shipping prior to core loading by a stainless steel helical compression spring, which bears on the top of the fuel.

At assembly, the pellets are stacked in the cladding to the required fuel height. The compression spring is then inserted into the top end of the fuel and the end plugs pressed into the ends of the tube and welded. A hold-down force of approximately four times the weight of the fuel is obtained by compression of the spring between the top end plug and the top of the fuel pellet stack. All fuel rods are internally pressurized with helium in order to minimize compressive clad stresses and creep due to coolant operating pressures.

The fuel pellets are in the form of a right circular cylinder and consist of slightly enriched uranium-dioxide powder, which is compacted by cold pressing and sintering to the required density. The ends of each pellet are dished slightly to allow the greater axial expansion at the center of the pellets to be taken up within the pellets themselves and not in the overall fuel length. The VANTAGE+ and 15x15 Upgrade fuel has mid-enriched annular (IFBA) and solid (non-IFBA) pellets in the axial blanket region of the fuel rod and optimized plenum spring to maximize the available plenum volume for increased burnup. The Vantage+ fuel with Performance+ enhancements and the 15x15 Upgrade fuel have a longer fuel rod to allow higher fission gas release due to longer cycles. This is allowable due to the ZIRLO cladding, which has less rod growth on irradiation.

For the first core, the pellets in the outer region had a density of approximately 10.3 g/cm³ (94-percent of theoretical density) while those in the two inner regions (checkerboard pattern, see Figure 3.2-48) had a density of 10.4 g/cm³ corresponding to 95-percent of theoretical density. Lower pellet densities were used to compensate for the effects of the higher burnup, which the fuel experienced in those regions.

Reload cores contain 15x15 Upgraded fuel and VANTAGE+ assemblies arranged in a zoned and/or checkerboard pattern. Different fuel enrichments, as listed in Table 3.2-7, are used for each of the core regions for all core loadings.

Each fuel rod is marked with a permanent traceability code. This aids in ensuring that rods of the proper enrichment will be loaded into each fuel assembly. The identification numbers on the

IP2
FSAR UPDATE

fuel assembly top nozzles will then maintain the enrichment identity and ensure that the assemblies with the correct enrichment are loaded into the proper core region.

Each assembly is assigned a core loading position. A record is then made of the core loading position, serial number, and enrichment. During the core loading, two independent checks are made to ensure that the actual loading position agrees with the position assigned.

During initial core loading and subsequent refueling operations, detailed handling and checkoff procedures are used throughout the sequence. The initial core was loaded in accordance with the core loading diagram similar to Figure 3.2-48, which shows the location for each of the three enrichment types of fuel assemblies used in the loading.

3.2.3.2.1.2 Rod Cluster Control Assemblies

The control rods or rod cluster control assemblies consist of a group of individual absorber rods fastened at the top end to a common hub or spider assembly. These assemblies, one of which is shown in Figure 3.2-49, are provided to control the reactivity of the core under operating conditions. The absorber material used in the control rods is silver-indium-cadmium alloy, which is essentially "black" to thermal neutrons and has sufficient additional resonance absorption to increase its worth significantly. The alloy is in the form of extruded single-length rods, which are sealed in stainless steel tubes to prevent the rods from coming in direct contact with the coolant.

The overall control rod length is such that when the assembly has been withdrawn through its full travel, the tips of the absorber rods remain engaged in the guide thimbles so that alignment between rods and thimbles is always maintained. Since the rods are long and slender, they are relatively free to conform to any small misalignments with the guide thimble. Prototype tests have shown that the rod cluster control assemblies are very easily inserted and not subject to binding even under conditions of severe misalignment.

The spider assembly is in the form of a center hub with radial vanes supporting cylindrical fingers from which the absorber rods are suspended. Handling detents and detents for connection to the drive shaft are machined into the upper end of the hub. A spring pack is assembled into a skirt integral to the bottom of the hub to stop the rod cluster control assembly and absorb the energy from the impact at the end of a trip insertion. The radial vanes are joined to the hub and the fingers are joined to the vanes by furnace brazing. A centerpost, which holds the spring pack and its retainer is threaded into the hub within the skirt and welded to prevent loosening in service. All components of the spider assembly are made from type 304 stainless steel except for the springs, which are Inconel X-750 alloy and the retainer, which is of 17-4 pH material.

The absorber rods are secured to the spider so as to ensure trouble free service. The rods are first threaded into the spider fingers and then pinned to maintain joint tightness, after which the pins are welded in place. The end plug below the pin position is designed with a reduced section to permit flexing of the rods to correct for small operating or assembly misalignments.

In construction, the silver-indium-cadmium rods are inserted into cold-worked stainless steel tubing, which is then sealed at the bottom and the top by welded end plugs. Sufficient diametral and end clearance are provided to accommodate relative thermal expansions and to limit the internal pressure to acceptable levels.

IP2
FSAR UPDATE

The bottom plugs are made bullet-nosed to reduce the hydraulic drag during a reactor trip and to guide smoothly into the dashpot section of the fuel assembly guide thimbles. The upper plug is threaded for assembly to the spider and has a reduced end section to make the joint more flexible. Stainless steel clad silver-indium-cadmium alloy absorber rods are resistant to radiation and thermal damage thereby ensuring their effectiveness under all operating conditions. Rods of similar design have been successfully used in a number of operating nuclear plants.

3.2.3.2.1.3 Neutron Source Assemblies

Six neutron source assemblies were utilized in the first cycle core. These consisted of two assemblies with four secondary source rods each, and four assemblies with one secondary source rod and one primary source rod each. The rods in each assembly were fastened to a spider at the top end. The spider for the four secondary source rod assemblies was similar to the rod cluster control assembly spiders, while the primary source assembly spider was similar to that of the burnable poison and plugging device assemblies. Various source assembly designs are used in the reload cycles.

In the first cycle core, the neutron source assemblies were inserted into the rod cluster control guide thimbles in fuel assemblies at unrodded locations. The location and orientation of each of the assemblies in the core is shown in Figure 3.2-62.

The primary and secondary source rods both utilize the same type of cladding material as the absorber rods (cold-worked type 304 stainless steel tubing). The secondary source rods contain Sb-Be pellets. The primary source rods contained capsules of Pu-Be source material in the initial core loading; for reload cores, this material may vary. Design criteria similar to that for the fuel rods is used for the design of the source rods; i.e., the cladding is free standing, internal pressures are always less than reactor operating pressure, and internal gaps and clearances are provided to allow for differential expansions between the source material and cladding.

3.2.3.2.1.4 Plugging Devices

In order to limit bypass flow through the rod cluster control guide thimbles in fuel assemblies, which do not contain either control rods, source assemblies or burnable absorber rods, the fuel assemblies at those locations were fitted with plugging devices. The plugging devices consist of a flat plate with short rods suspended from the bottom surface and a spring pack assembly. At installation in the core, the plugging devices fit with the fuel assembly top nozzles and rest on the adaptor plate. The short rods project into the upper ends of the thimble tubes to reduce the bypass flow area. The spring pack is compressed by the upper core plate when the upper internals package is lowered into place. Similar short rods are also used on the source assemblies to fill the ends of all vacant fuel assembly guide thimbles. All components in the plugging device, except for the springs, are constructed from type 304 stainless steel. The springs are wound from an age hardenable nickel base alloy to obtain higher strength.

Coincident with implementation of the Indian Point Unit 2 OFA transition, removal of thimble plugging devices from the core was allowed. This included the removal of the thimble plugs from the OFA assemblies, previously installed LOPAR assemblies, and all new core component clusters (burnable absorbers and sources).

As part of the implementation of the power uprate, Cycle 17 core will contain thimble plugs for all assemblies that do not contain inserts e.g. RCCAs, WABAs or secondary sources.

IP2
FSAR UPDATE

3.2.3.2.1.5 Burnable Absorber Rods

The burnable absorber rods are statically suspended and positioned in vacant rod cluster control thimble tubes within the fuel assemblies at nonrodded core locations. The absorber rods in each fuel assembly are grouped and attached together at the top end of the rods by a flat plate, which fits with the fuel assembly top nozzle and rests on the top adaptor plate.

The plate with the absorber rods is held down and restrained against vertical motion with a spring pack, which is attached to the plate and is compressed by the upper core plate when the reactor upper internals package is lowered into the reactor. This ensures that the absorber rods cannot be lifted out of the core by flow forces.

The absorber rods used during Cycles 1 through 7 consisted of borated Pyrex glass tubes contained within type 304 stainless steel tubular cladding, which was plugged and seal welded at the ends to encapsulate the glass. The glass was also supported along the length of its inside diameter by a thin-wall type 304 stainless steel tubular inner liner.

Starting in Cycle 8, Wet Annular Burnable Absorber (WABA) rods were used and are described in Reference 74. As shown in Figures 3.2-69 and 3.2-70, WABA rods are composed of annular pellets containing aluminum oxide-boron carbide ($Al_2O_3 - B_4C$) burnable absorber material contained within two concentric Zircaloy tubes. The Zircaloy tubes are plugged and seal welded at the ends to enclose the annular stack of absorber material. The tubes are also the inner and outer cladding of the annular burnable absorber rod. A holddown device is placed on top of the pellet stack to hold the stack in position and to allow for pellet stack growth. The holddown device is a C-shape Zircaloy polygonal ring clip. Within the rod is an annular plenum to allow for helium gas release from the absorber material during boron depletion. Reactor coolant flows through the inner tube and outside the outer tube of the annular rod. The annular rods are grouped and attached at the top end to a holddown assembly and retaining plate in the same way as the borosilicate glass absorber rod. WABA rods are used in preference to standard BPRAs to provide smaller residual burnup penalty.

Starting with Cycle 11, Integral Fuel Burnable Absorbers (IFBA) were used in conjunction with the WABA rods. The IFBA features a zirconium diboride coating on the fuel pellet surface on the central portion of the enriched UO_2 pellets. IFBA's provide power peaking and moderator temperature coefficient control. IFBA's are described in Reference 88.

3.2.3.2.2 Evaluation of Core Components

3.2.3.2.2.1 Fuel Evaluation

The fission gas release and the associated buildup of internal gas pressure in the fuel rods are calculated by overall fuel rod design models, which incorporate time-dependent fuel densification (References 68 and 69). The increase of internal pressure in the fuel rod due to this phenomena is included in the determination of the maximum cladding stresses at the end of core life when the fission product gap inventory is a maximum. Modifications to the initial core fuel design and evaluations are given in the Indian Point Unit 2 Fuel Densification Reports^{70 and 71}. The VANTAGE+ fuel rod design bases and evaluation are given in Reference 88. The fuel rod design has not been changed as part of the 15x15 Upgraded fuel design.

The maximum allowable tensile strain in the cladding during steady-state operation, considering the combined effects of internal gas pressure, external coolant pressure, fuel pellet swelling and

IP2
FSAR UPDATE

thermal expansion, and cladding creep is less than 1% from the unirradiated condition throughout core life. For Condition II transients, the total tensile strain during the transient is less than 1% from the pre-transient value. The associated stresses are below the yield strength of the material under steady-state and Condition II transient conditions.

To assure that manufactured fuel rods meet a high standard of excellence from the standpoint of functional requirements, many inspections and tests are performed both on the raw material and the finished product. These tests and inspections include chemical analysis, tensile testing of fuel tubes, dimensional inspection, X-ray of both end plug welds, ultrasonic testing, and helium leak tests.

In the event of cladding defects, the high resistance of uranium-dioxide fuel pellets to attack by hot water protects against fuel deterioration or decrease in fuel integrity. Thermal stress in the pellets, while causing some fracture of the bulk material during temperature cycling, does not result in pulverization or gross void formation in the fuel matrix. As shown by operating experience and extensive experimental work in the industry, the thermal design parameters conservatively account for any changes in the thermal performance of the fuel element due to pellet fracture.

The consequences of a breach of cladding are greatly reduced by the ability of uranium-dioxide to retain fission products including those, which are gaseous or highly volatile. This retentiveness decreases with increasing temperature or fuel burnup, but remains a significant factor even at full power operating temperature in the maximum burnup element.

Data on fuel behavior in high burnup uranium-dioxide show that it is possible to conservatively define the fuel swelling as a function of burnup and as-fabricated uranium-dioxide porosity (References 68 and 69).

Actual fuel rod damage limits depend upon neutron exposure and normal variation of material properties and are greater than the design limits. For the life of the fuel rod, the actual stresses and strains are below the design limits. Thus, significant margins exist between actual operating conditions and the damage limits.

The other parameters having an influence on cladding stress and strain are as follows:

1. Internal gas pressure.

The maximum rod internal pressure under nominal conditions will be substantially less than the calculated pressure at the design limits. The end-of-life internal gas pressure is dependent upon the fuel rod power history and will not exceed the design limit defined in Section 3.1.2.1 (item 3).

2. Cladding temperature.

The strength of the fuel cladding is temperature dependent. The minimum ultimate strength reduces to the design yield strength at an average cladding temperature of approximately 850°F. The maximum average cladding temperature during normal operating conditions is given in Table 3.2-6.

3. Burnup.

Fuel burnup results in fuel swelling, which, along with fuel thermal expansion, causes tensile cladding strain. Since rod power levels, and hence fuel temperature, decreases with burnup, the fuel pellet diameter increase with burnup is somewhat mitigated by the reduced thermal expansion. The strain design limits and stress design limits are met throughout the burnup lifetime of the fuel. These strain and stress design limits are below the cladding damage limits.

4. Fuel temperature and kW/ft.

The fuel is designed so that the maximum fuel temperature will not exceed 4700°F during normal operating conditions or unanticipated malfunction transients (Condition II events).

3.2.3.2.2.2 Evaluation of Burnable Absorber Rods

The burnable absorber rods are positioned in the core inside rod cluster control assembly guide thimbles and held down in place by attachment to a retainer assembly compressed beneath the upper core plate and, hence, cannot be the source of any reactivity transient. Due to the low heat generation rate and the conservative design of the rods, there is no possibility for release of the poison as a result of helium pressure or clad heating during accident transients including loss-of-coolant.

3.2.3.2.2.3 Effects of Vibration and Thermal Cycling on Fuel Assemblies

Analyses of the effect of cyclic deflection of the fuel rods, grid spring, rod cluster control rods, and burnable absorber rods due to hydraulically induced vibrations and thermal cycling show that the design of the components is good for an infinite number of cycles.

In the case of the fuel rod grid spring support, the amplitude of a hydraulically induced motion of the fuel rod is extremely small (approximately 0.001-in.), and the stress associated with the motion is significantly small (<100 psi). Likewise, the reactions at the grid spring due to the motion is much less than the preload spring force and contact is maintained between the fuel clad and the grid spring and dimples. Fatigue of the clad and fretting between the clad and the grid support is not anticipated.

The effect of thermal cycling on the grid-clad support is a slight relative movement between the grid contact surfaces and the clad. Since the number of cycles of the occurrence is small over the life of a fuel assembly (approximately 3 years), negligible wear of the mating parts is expected. Incore operation of assemblies in the Yankee Rowe and Saxton reactors using similar clad support have verified the calculated conclusions. Additional test results under simulated reactor environment in the Westinghouse Reactor Evaluation Channel also support these conclusions.

The dynamic deflection of the control rods and the burnable absorber rods is limited by their fit with the inside diameter of either the upper portion of the guide thimble or the dashpot. With this limitation, the occurrence of truly cyclic motion is questionable. However, an assumed cyclic deflection through the available clearance gap results in an insignificantly low stress in either the clad tubing or in the flexure joint at the spider or retainer plate. The above

consideration assumes the rods are supported as cantilevers from the spider or the retainer plate in the case of the burnable absorber rods.

A calculation assuming the rods are supported by the surface of the dashpots and at the upper end by the spider or retainer results in a similar conclusion.

3.2.3.3 Transition Cores

Beginning with Cycle 17, 15x15 Upgraded fuel assembly regions will be used to refuel the core. The 15x15 Upgraded fuel design incorporates the I-spring mid-grid design and the enhanced IFM. Both types of grids are longer and thinner than the grids in the Vantage+ fuel design. The transition core DNB effect is dependent on the fuel assembly hydraulic characteristics. Since there are changes in the hydraulic parameters in the 15x15 Upgraded fuel, there is a transition core impact. Transition Core analyses for a mixed core of Vantage+ fuel and 15x15 Upgraded fuel have been performed using VIPRE-01 code. The analyses show that the transition core effect on DNB margin is predicted to be within the acceptable range with the final grid loss coefficients determined for 15x15 Upgraded fuel.

3.2.3.4 Control Rod Drive Mechanism Design Description

3.2.3.4.1 Full Length Rods

The control rod drive mechanisms are used for withdrawal and insertion of the rod cluster control assemblies into the reactor core and to provide sufficient holding power for stationary support.

Fast total insertion (reactor trip) is obtained by simply removing the electrical power allowing the rods to fall by gravity. Design scram time is 2.4 seconds from gripper release to dashpot entry.

The complete drive mechanism, shown in Figure 3.2-65, consists of the internal (latch) assembly, the pressure vessel, the operating coil stack, the drive shaft assembly, and the rod position indicator coil stack.

Each assembly is an independent unit, which can be dismantled or assembled separately. Each mechanism pressure housing is threaded onto an adaptor on top of the reactor pressure vessel and seal welded. The operating drive assembly is connected to the control rod (directly below) by means of a grooved drive shaft. The upper section of the drive shaft is suspended from the working components of the drive mechanism. The drive shaft and control rod remain connected during reactor operation including tripping of the rods.

Main coolant fills the pressure containing parts of the drive mechanism. All working components and the shaft are immersed in the main coolant and depend upon it for lubrication of sliding parts.

Three magnetic coils, which form a removable electrical unit and surround the rod drive pressure housing, induce magnetic flux through the housing wall to operate the working components. They move two sets of latches, which lift, lower, and hold the grooved drive shaft.

The three magnets are turned on and off in a fixed sequence by solid-state switches for the full length rod assemblies.

IP2
FSAR UPDATE

The sequencing of the magnets produces step motion over the full length of normal control rod travel.

The mechanism develops a lifting force approximately two times the static lifting load. Therefore, extra lift capacity is available for overcoming mechanical friction between the moving and the stationary parts. Gravity provides the drive force for rod insertion and the weight of the whole rod assembly is available to overcome any resistance.

The mechanisms are designed to operate in water at 650°F and 2485 psig. The temperature at the mechanism head adaptor will be much less than 650°F because it is located in a region where there is limited flow of water from the reactor core while the pressure is the same as in the reactor pressure vessel. A multiconductor cable connects the mechanism operating coils to the 125-V DC power supply. The power supply is described in Section 7.3.2.

3.2.3.4.1.1 Latch Assembly

The latch assembly contains the working components, which withdraw and insert the drive shaft and attached control rod. It is located within the pressure housing and consists of the pole pieces for three electromagnets. They actuate two sets of latches, which engage the grooved section of the drive shaft.

The upper set of latches move up or down to raise or lower the drive rod by 5/8-in. The lower set of latches have a 1/16-in. axial movement to shift the weight of the control rod from the upper to the lower latches.

3.2.3.4.1.2 Pressure Vessel

The pressure vessel consists of the pressure housing and rod travel housing. The pressure housing is the lower portion of the vessel and contains the latch assembly. The rod travel housing is the upper portion of the vessel. It provides space for the drive shaft during its upward movement as the control rod is withdrawn from the core.

3.2.3.4.1.3 Operating Coil Stack

The operating coil stack is an independent unit, which is installed on the drive mechanism by sliding it over the outside of the pressure housing. It rests on a pressure housing flange without any mechanical attachment and can be removed and installed while the reactor is pressurized.

The three operating coils are made of round copper wire, which is insulated with a double layer of filament type glass yarn.

The design operating temperature of the coils is 200°C. Average coil temperature can be determined by resistance measurement. Forced air cooling along the outside of the coil stack maintains a coil casing temperature of approximately 120°C or lower.

3.2.3.4.1.4 Drive Shaft (Drive Rod) Assembly

The main function of the drive shaft is to connect the control rod to the mechanism latches. Grooves for engagement and lifting by the latches are located throughout the 144-in. of control

rod travel. The grooves are spaced 5/8-in. apart to coincide with the mechanism step length and have 45-degree-angle sides.

The drive shaft is attached to the control rod by the coupling. The coupling has two flexible arms, which engage the grooves in the spider assembly.

A 0.25-in. diameter disconnect rod runs down the inside of the drive shaft. It uses a locking button at its lower end to lock the drive rod assembly and control rod assembly together. At its upper end there is a disconnect assembly for remote disconnection of the drive rod assembly from the control rod assembly.

During plant operation, the drive shaft assembly remains connected to the control rod at all times. It can be attached and removed from the control rod only when the reactor vessel head is removed.

3.2.3.4.1.5 Position Indicator Coil Stack

The position indicator coil stack slides over the rod travel housing section of the pressure vessel. It detects drive rod position by means of a cylindrically wound differential transformer, which spans the normal length of the rod travel (144-in.).

3.2.3.4.1.6 Drive Mechanism Materials

All parts exposed to reactor coolant, such as the pressure vessel, latch assembly, and drive rod, are made of metals, which resist the corrosive action of the water.

Three types of metals are used exclusively: stainless steels, Inconel-X, and cobalt-based alloys. Wherever magnetic flux is carried by parts exposed to the main coolant, 400 series stainless steel is used. Cobalt-based alloys are used for the pins, latch tips, and bearing surfaces.

Inconel-X is used for the springs of both latch assemblies and type 304 stainless steel is used for all pressure containment. Hard chrome plating provides wear surfaces on the sliding parts and prevents galling between mating parts (such as threads) during assembly.

Outside of the pressure vessel, where the metals are exposed only to the reactor containment environment and cannot contaminate the main coolant, carbon and stainless steels are used. Carbon steel, because of its high permeability, is used for flux return paths around the operating coils. It is zinc-plated approximately 0.001-in. thick to prevent corrosion.

3.2.3.4.1.7 Principles of Operation

The drive mechanisms, shown schematically in Figure 3.2-66, withdraw and insert their respective control rods as electrical pulses are received by the operator coils.

ON and OFF sequence, repeated by switches in the power programmer, causes either withdrawal or insertion of the control rod. Position of the control rod is indicated by the transformer action of the position indicator coil stack surrounding the rod travel housing. The transformer output changes as the top of the ferromagnetic drive shaft assembly moves up the rod travel housing. Generally during plant operation the drive mechanisms hold the control rods

IP2
FSAR UPDATE

withdrawn from the core in a static position and only one coil, the stationary gripper coil, is energized on each mechanism.

Control Rod Withdrawal

The control rod is withdrawn by repeating the following sequence:

1. Movable Gripper Coil - ON.

The movable gripper armature raises and swings the movable gripper latches into the drive shaft groove.
2. Stationary Gripper Coil - OFF.

Gravity causes the stationary gripper latches and armature to move downward until the load of the drive shaft is transferred to the movable gripper latches. Simultaneously, the stationary gripper latches swing out of the shaft groove.
3. Lift Coil - ON.

The 5/8-in. gap between the lift armature and the lift magnet pole closes and the drive rod raises one step length.
4. Stationary Gripper Coil - ON.

The stationary gripper armature raises and closes the gap below the stationary gripper magnetic pole, swings the stationary gripper latches into a drive shaft groove. The latches contact the shaft and lift it 1/16-in. The load is so transferred from the movable to the stationary gripper latches.
5. Movable Gripper Coil - OFF.

The movable gripper armature separates from the lift armature under the force of three springs and gravity. Three links, pinned to the movable gripper armature, swing the three movable gripper latches out of the groove.
6. Lift Coil - OFF.

The gap between the lift armature and the lift magnet pole opens. The movable gripper latches drop 5/8-in. to a position adjacent to the next groove.

Control Rod Insertion

The sequence for control rod insertion is similar to that for control rod withdrawal:

1. Lift Coil - ON.

The movable gripper latches are raised to a position adjacent to a shaft groove.

IP2
FSAR UPDATE

2. Movable Gripper Coil - ON.

The movable gripper armature raises and swings the movable gripper latches into a groove.

3. Stationary Gripper Coil - OFF.

The stationary gripper armature moves downward and swings the stationary gripper latches out of the groove.

4. Lift Coil - OFF.

Gravity separates the lift armature from the lift magnet pole and the control rod drops down 5/8-in.

5. Stationary Gripper Coil - ON.

6. Movable Gripper Coil - OFF.

The sequences described above are termed as one step or one cycle and the control rod moves 5/8-in. for each cycle. Each sequence can be repeated at a rate of up to 72 steps/min and the control rods can therefore be withdrawn or inserted at a rate of up to 45-in./min. The sequence timing has been modified to preclude the rod withdrawal event described in NRC Generic Letter 93-04.

Control Rod Tripping

If power to the movable gripper coil is cut off, as for tripping, the combined weight of the drive shaft and the rod cluster control assembly is sufficient to move the latches out of the shaft groove. The control rod falls by gravity into the core. The tripping occurs as the magnetic field, holding the movable gripper armature against the lift magnet, collapses and the movable gripper armature is forced down by the weight acting upon the latches.

3.2.3.4.2 Part-Length Rods

Deleted

3.2.3.5 Fuel Assembly and Rod Cluster Control Assembly Mechanical Evaluation

To confirm the mechanical adequacy of the fuel assembly and full length rod cluster control assembly, functional test programs have been conducted on a full scale Indian Point Unit 2 prototype 12-ft canless fuel assembly and control rod. The prototype assembly was tested under simulated conditions of reactor temperature, pressure, and flow for approximately 1000 hr. The prototype mechanism accumulated 2,260,892 steps and 600 scrams. At the end of the test the control rod drive mechanism was still operating satisfactorily. A correlation was developed to predict the amplitude of flow excited vibration of individual fuel rods and fuel assemblies. Inspection of the fuel assembly and drive line components did not reveal significant fretting. The wear of the absorber rods, fuel assembly guide thimbles, and upper guide tubes was minimal. The control rod free fall time against 125-percent of nominal flow was less than 1.5 sec to the dashpot (10-ft of travel). Additional tests had previously been made on a full scale San Onofre mockup version of the fuel assembly and control rods (Reference 73).

3.2.3.5.1 One-Seventh Scale Mockup Tests

A one-seventh scale model of the Indian Point Unit 2 internals was designed and built for hydraulic and mechanical testing. The tests provided information on stresses and displacements at selected locations on the structure due to static loads, flow induced loads, and electromagnetic shaker loads. Flow distribution and pressure drop information were obtained. Results of the static tests indicated that mean strains in the upper core support plate and upper support columns are below design limits. Strains and displacements measured in the model during flow tests verified that no damaging vibration levels were present. Additional information gained from the tests was the natural frequency and damping of the thermal shield and other components in air and water. Model response can be related to the full scale plant for most of the expected exciting phenomena, but across-the-board scaling is not possible. Specifically exciting phenomena, which are strongly dependent on Reynolds number cannot be scaled. In areas where Reynolds number may be important, either (1) the measured vibration amplitudes were many times lower than a level that would be damaging, or (2) full scale vibration data have been obtained.

3.2.3.5.2 Loading and Handling Tests

Tests simulating the loading of the prototype fuel assembly into a core location have also been successfully conducted to determine that proper provisions had been made for guidance of the fuel assembly during refueling operation.

3.2.3.5.3 Axial and Lateral Bending Tests

Axial and lateral bending tests have been performed in order to simulate mechanical loading of the assembly during refueling operation. Although the maximum column load expected to be experienced in service is approximately 1000 lb, the fuel assembly was successfully loaded to 2200 lb axially with no damage resulting. This information is also used in the design of fuel handling equipment to establish the limits for inadvertent axial loads during refueling.

3.2.4 Fixed Incore Detectors

Eight fixed core neutron detectors are installed within the Unit 2 reactor as shown in Figure 3.2-67. They provide no input to plant instrumentation nor are they needed by the operator. The detectors have been retired and are cut and capped at the seal table.

The detectors are not movable when the primary system is at operating pressure. The assemblies are extracted downward from the core during refueling. The seal table used for the movable detector assemblies is also utilized for the fixed incore detector assemblies.

The installation of the fixed incore detector system is expected to cause no significant reactivity effect. If a fixed detector were to fail, the expulsion of reactor coolant would be accommodated by the charging pumps, which is common for ruptures of a very small cross section. This would enable the operator to execute an orderly shutdown. If a seal were to fail at the seal table, flow from the reactor coolant system would be through the annulus defined by the O.D. of the flux thimble and the I.D. of the conduit (approximately 0.13-in.). The fixed incore detector system is designed to Class I standards such that the likelihood of a failure causing a loss of coolant will be extremely remote.

3.2.4.1 Core Monitoring

Verification of axial and radial power distribution during full power operation is performed using the movable incore detector system. These movable detector locations are shown in Figure 3.2-68. The axial power distribution during operation is determined for each measured thimble location since the activity level is measured at several axial heights for each thimble. Comparison of the measured power distribution to design predictions provides confirmation of safe operation of the reactor and confidence in design predictions. To obtain temperature maps of the core, 65 fuel assembly outlet thermocouples are located as shown in Figure 3.2-68. These thermocouples are located in the upper coolant internals package above the corresponding assemblies. Based on the average activity determined for each thimble, the measured radial power distribution can be determined.

3.2.5 Plant Computer

The computer system provided for Indian Point Unit 2 is a DS&S Plant Integrated Computer System known as "PICS". It is provided as an adjunct to the normal control room instrumentation to assist the operator in the operation of the reactor by monitoring reactor performance and displaying it in a consistent, well-ordered, usable form. The computer system performs functions such as scanning, signal converting, calculating, indicating, recording, and alarm annunciating. This system is not required for safety, and operation of the reactor is not in any way dependent upon the availability of the computer.

Briefly, the analog scanning includes reading all inputs in a pre-established manner, checking the readings, converting values to engineering units, storing them for future use, updating information, and checking alarm conditions. Some inputs are scanned once every second and status placed in memory; other inputs are not scanned periodically but are given immediate attention. The alarm program compares the values of the inputs against the fixed or variable alarm limits and indicates when off-normal conditions exist.

3.2.6 Current Operating Cycle

Indian Point Unit 2 is currently operating in the eighteenth cycle. The core for this cycle uses 15x15 Upgraded and VANTAGE+ with Performance+ enhancements fuel. In order to reduce neutron fluence to the reactor vessel shell, a low-low leakage loading pattern, shown in Figure 3.2-68A, is utilized. Integrated fuel burnable absorbers (IFBA) and wet annular burnable absorber (WABA) assemblies, described in References 74 and 88, are used. Figures 3.2-68 and 3.2-68B show the locations of core components and instrumentation. The cycle is designed for a burnup of 25,077 MWd/MTU which includes a power coastdown. The methodology and computer codes described in Reference 75, 82, 87, 96, and 97 were utilized for analysis of the current operating cycle. Fuel Temperatures were calculated using the fuel thermal models of References 69 and 84 (prior to Cycle 16 the analysis was done with Reference 83).

Beginning with Cycle 11, replacement fuel had debris filter bottom nozzles and integral fuel burnable absorbers. To prevent debris from reaching the core, the nozzles have a larger number of smaller holes than previous designs. The integral fuel burnable absorber (IFBA) has a thin layer of zirconium diboride or enriched zirconium diboride coated directly onto selected fuel pellets to control power peaking.

IP2
FSAR UPDATE

A three dimensional model is used to track and predict core operating characteristics. The code predictions are compared to startup physics test results, measured core flux distributions, and critical boron concentrations as a function of core burnup. It has been shown to provide a suitable and accurate means for predicting core operating conditions.

REFERENCES FOR SECTION 3.2

1. Westinghouse Electric Corporation, "Power Distribution Control in Westinghouse Pressurized Water Reactors," WCAP-7208 (Proprietary), 1968.
2. R. F. Barry, et al., "Power Maldistribution Investigations," WCAP-7407-L (Proprietary), Westinghouse Electric Corporation.
3. F. B. Skogen and A. F. McFarlane, "Xenon-Induced Spatial Instabilities in Three-Dimensions," WCAP-3680-22, Westinghouse Electric Corporation, September 1969.
4. T. Morita, et al., "Power Distribution Control and Load Following Procedures," WCAP-8385 (Proprietary), September 1974 and WCAP-8403 (Non-Proprietary), Westinghouse Electric Corporation, September 1974.
5. F. L. Langford and R. J. Nath, "Evaluation of Nuclear Hot Channel Factor Uncertainties," WCAP-7308-L (Proprietary), April 1969 and WCAP-7810 (Non-Proprietary), Westinghouse Electric Corporation, December 1971.
6. J. M. Hellman, (Ed), "Fuel Densification Experimental Results and Model for Reactor Application," WCAP-8218-P-A (Proprietary), Westinghouse Electric Corporation, March 1975 and WCAP-8219-A (Non-Proprietary), March 1975.
7. R. O. Meyer, "The Analysis of Fuel Densification," Division of Systems Safety, NUREG-0085, U.S. Nuclear Regulatory Commission, July 1976.
8. J. M. Hellman, C. A. Olson, and J. M. Yang, "Effects of Fuel Densification Power Spikes on Clad Thermal Transients," WCAP-8359, Westinghouse Electric Corporation, July 1974.
9. "Power Distribution Control of Westinghouse Pressurized Water Reactors," WCAP-7811 (Non-Proprietary), Westinghouse Electric Corporation, December 1971.
10. R. J. Johnson, "Connecticut-Yankee Tests on Detection of Power Maldistribution," WCAP-9010 (Proprietary), Westinghouse Electric Corporation, February 1969.
11. P. M. Wood, E. A. Bassler, et al., "Use of Burnable Poison Rods in Westinghouse Pressurized Water Resources," WCAP-7113, Westinghouse Electric Corporation, October 1967.
12. R. F. Barry, "The Revised LEOPARD Code - A Spectrum Dependent Non-Spatial Depletion Program," WCAP-2759, Westinghouse Electric Corporation, March 1965.

IP2
FSAR UPDATE

13. VANTAGE+ Fuel Upgrade Reload Transition Safety Report for Indian Point Unit 2, September 1994.
14. Kersting, P.J. et al., "Assessment of Clad Flattening and Densification Power Spike Factor Elimination in Westinghouse Nuclear Fuel," WCAP-13589-A, March 1995.
15. Davidson, S.L. (Ed.) et al., "Extended Burnup Evaluation of Westinghouse Fuel," WCAP-10125-P-A, December 1985.
16. Davidson, S.L (Editor), "Westinghouse Fuel Criteria Evaluation Process," WCAP-12488-A, October 1994.
17. Letter from N.J Liparulo (Westinghouse) to R.J. Jones (NRC) "Westinghouse Interpretation of Staff's Position on Extended Burnup (Proprietary)," NTD-NRC-94-4275, August 29, 1994.
18. Deleted
19. Deleted
20. Deleted
21. Deleted
22. Deleted
23. Deleted
24. Deleted
25. R.A. Dean, "Thermal Contact Conductance Between UO₂ and Zircaloy-2," CVNA-127, May 1962.
26. A.M. Ross and R.D. Stoute, "Heat Transfer Coefficient Between UO₂ and Zircaloy-2," AECL-1552, June 1962.
27. V.C. Howard and T.G. Gulivin, "Thermal Conductivity Determinations on Uranium Dioxide by a Radial Flow Method", UKAEA IG-Report 51, November 1960.
28. C.F. Lucks and H.W. Deem, "Thermal conductivity and Electrical Conductivity of UO₂ in Progress Reports Relating to Civilian Applications," BMI-1448 (Rev) (June 1960); BMI-1489 (Rev.) (December, 1960) and BMI-1518 (Rev.) Battelle Memorial Institute-Columbus (May, 1961).
29. J. L. Daniel, J. Matolich, Jr., and H.W. Deem, "Thermal Conductivity of UO₂," HW-69945, September 1962.
30. A. D. Feith, "Thermal Conductivity of UO₂ by a Radial Heat Flow

IP2
FSAR UPDATE

31. J. Vogt, L. Grandell, and U. Runfors, "Determination of the Thermal Conductivity of Unirradiated Uranium Dioxide," AB Atomenergi Report RMB-527, 1964, Quoted by IAEA Technical Report Series No. 59, "Thermal Conductivity of Uranium Dioxide."
32. T. Nishijima, T. Kawada, and A. Ishihata, "Thermal Conductivity of Sintered UO_2 and Al_2O_3 at High Temperatures," J. American Ceramic Society, Vol. 48, pp. 31-34, 1965.
33. J. B. Ainscough and M.H. Wheeler, "Thermal Diffusivity and Thermal Conductivity of Sintered Uranium Dioxide," in Proceedings of the Seventh Conference of Thermal Conductivity, p. 467, National Bureau of Standards, Washington, 1968.
34. T. G. Godfrey, et al., "Thermal Conductivity of Uranium Dioxide Armco Iron by and Improved Radial Heat Flow Technique," ORNL-3556, June 1964.
35. J. P. Stora, et al., "Thermal Conductivity of Sintered Uranium Oxide Under In-Pile Conditions," EURAE-1095, August 1964.
36. A. J. Bush, "Apparatus for Measuring Thermal Conductivity to 2500°C ," Report 64-1P6-401-43 (Proprietary), Westinghouse Research Laboratories, February 1965.
37. R. R. Asamoto, F.L. Anselin, and A.E. Conti, "The Effect of Density on the Thermal Conductivity of Uranium Dioxide," GEAP-5493, April 1968.
38. O. L. Kruger, "Heat Transfer Properties of Uranium and Plutonium Dioxide," Paper 11-N-68F presented at the Fall Meeting of Nuclear Division of the American Ceramic Society, Pittsburgh, Pa., September 1968
39. J. A. Gyllander, "In-Pile Determination of the Thermal Conductivity of UO_2 in the Range $500\text{-}2500^\circ\text{C}$," AE-411, January 1971.
40. M. F. Lyons, et al., " UO_2 Powder and Pellet Thermal Conductivity During Irradiation," GEAP-5100-1, March 1966.
41. R. N. Duncan, "Rabbitt Irradiation of UO_2 " CVNA-142, June 1962.
42. A. S. Bain, "The Heat Rating Required to Produce Center Melting in Various UO_2 Fuels," ASTM Special Technical Publication No. 306, pp. 30-46, Philadelphia, Pa., 1962.
43. J. P. Storal, "In-Reactor Measurements of the Integrated Thermal Conductivity of UO_2 - Effect of Porosity," Trans. ANS, Vol. 13, 137-138, 1970
44. International Atomic Energy Agency, "Thermal Conductivity of Uranium Dioxide," Report of the Panel held in Vienna, April 1965, IAEA Technical Reports Series No. 59, Vienna, The Agency, 1966.

IP2
FSAR UPDATE

45. J. A. Christensen, R.J. Allio, and A. Biancheria, "Melting Point of Irradiated Uranium Dioxide," WCAP-6065, Westinghouse Electric Corporation, February 1965.
46. W. R. Smalley, "Survey of Experience With High Performance Fuel Rods of PWR Type, WCAP-7125, Westinghouse Electric Corporation, January 1968.
47. L. S. Tong, "Prediction of Departure From Nucleate Boiling for an Axially Non-Uniform Heat Flux Distribution," Journal of Nuclear Energy, Vol. 21, pp. 241-248, 1967.
48. L. S. Tong, H. B. Currin, and A.G. Throp II, "New Correlations Predict DNB Conditions," Nucleonics, May 1963. Also WCAP-1997, 1963.
49. L. S. Tong, "Boiling Crisis and Critical Heat Flux," AEC Critical Review Series, TID-25887, 1972.
50. F. E. Motely and F. F. Cadek, "Application of Modified Spacer Factor to L-Grid Typical and Cold Wall Cell DNB," WCAP-8030-A (Non-Proprietary), Westinghouse Electric Corporation, October, 1972.
51. L. S. Tong, R. P. Sandberg, and A.A. Bishop, "Forced Convection Heat Transfer at High Pressure After the Critical Heat Flux," ASME 65-HT-31 1965.
52. K. W. Hill, F. E. Motley, and F.F. Cadek, "Effect of Local Heat Flux Spikes on DNB in Non-Uniform Heated Rod Bundles," WCAP-8174 (Proprietary), August 1973, and WCAP-8202 (Non-Proprietary), Westinghouse Electric Corporation, August 1973.
53. G. Hetsroni, "Hydraulic Tests of the San Onofre Reactor Model, WCAP-3269-8, June 1964.
54. G. Hetsroni, "Studies of the Connecticut-Yankee Hydraulic Model," NYO-3250-2, June 1965.
55. F. D. Carter, "Inlet Orificing of Open PWR Cores," WCAP-7836, Westinghouse Electric Corporation, January 1972.
56. J. Shefcheck, "Application of the THINC Program to PWR Design," WCAP-7359-L (Proprietary), August 1969, and WCAP-7838 (Non-Proprietary), Westinghouse Electric Corporation, January 1972.
57. F. F. Cadek, "Interchannel Thermal Mixing With Mixing Vane Grids," WCAP-7667-P-A (Proprietary) and WCAP-7755-A (Non-Proprietary), Westinghouse Electric Corporation, January 1975.
58. I.E. Idel'chik, "Handbook of Hydraulic Resistance," AEC-TR-6630, 1960.
59. L.F. Moody, "Friction Factors for Pipe Flow," Transaction of the American Society of Mechanical Engineers, Vol. 66, pp. 671-684, 1944.

IP2
FSAR UPDATE

60. J. Weisman, A. H. Wenzel, L. S. Tong, D. Fitzsimmons, W. Thorne, and J. Batch, "Experimental Determination of the Departure From Nucleate Boiling In Large Rod Bundles at High Pressure," AICHE, Preprint 29, 9th National Heat Transfer Conference, Seattle, Washington, 1967.
61. L. S. Tong, H. Chelemer, J. E. Casterline, and B. Matzner, "Critical Heat Flux (DNB) in Square and Triangular Array Rod Bundles," JSME, Semi-International Symposium, Paper No. 256, Tokyo, Japan, 1967.
62. Deleted
63. Deleted
64. Deleted
65. Deleted
66. Deleted
67. Deleted
68. J. V. Miller (Ed), "Improved Analytical Models Used in Westinghouse Fuel Rod Design Computations," WCAP-8785, Westinghouse Electric Corporation, October 1976.
69. R. A. Weiner, et al., "Improved Fuel Performance Models for Westinghouse Fuel Rod Design and Safety Evaluations," WCAP-11873-A, Westinghouse Electric Corporation, August 1988.
70. "Fuel Densification--Indian Point Nuclear Generating Station Unit No.2," WCAP-8062, Westinghouse Electric Corporation, January 1973.
71. "Addendum to Densification - Indian Point Nuclear Generating Station Unit No. 2," WCAP-8062-Addendum, Westinghouse Electric Corporation, dated March 22, 1973.
72. Deleted
73. Westinghouse Electric Corporation, "Large Closed Cycle Water Reactor Research and Development Program Quarterly Progress Reports for the Period January 1963 through June 1965," WCAP-3738, 3739, 3743, 3750, 3269-2, 3269-5, 3269-6, 3269-12 and 3269-13.
74. Westinghouse Electric Corporation, "Westinghouse Wet Annular Burnable Absorber Evaluation Report," WCAP-10021-P-A, Rev.1 (Proprietary), October 1983.
75. Davidson, S. L. (Ed), et al, "Westinghouse Reload Safety Evaluation Methodology," WCAP-9273-NP-A, Westinghouse Electric Corporation, July 1985.

IP2
FSAR UPDATE

76. Motley, F. E., Hill, K. W., Cadek, F. F. and Shefcheck, J., "New Westinghouse Correlation WRB-1 for Predicting Critical Heat Flux in Rod Bundles with Mixing Vane Grids," WCAP-8762-P-A, July 1984 (Proprietary) and WCAP-8763, July 1976 and July 1985.
77. H. Chelemer, et al, "THINCIV-An Improved Program for Thermal-Hydraulic Analysis of Rod Bundle Cores," WCAP-7956, June 1973.
78. Hochreiter, L. E., et al, "Application of THINCIV Program to PWR Design," WCAP-8054, September 1973.
79. Chelemer, H., et al, "Improved Thermal Design Procedure," WCAP-8567, July 1975.
80. Skaritka, J., et al, "Fuel Rod Bow Evaluation," WCAP-8691, Rev. 1 (Proprietary), WCAP-8692, Rev. 1 (non-Proprietary) July 1979.
81. Letter from C. Berlinger (NRC) to E. P. Rahe, Jr. (Westinghouse), "Request for Reduction in Fuel Assembly Burn-Up Limit for Calculation of Maximum Rod Bow Penalty," June 18, 1986.
82. Liu, Y. S., et al, "ANC: A Westinghouse Advanced Nodal Computer Code," WCAP-10965-P-A and WCAP-10966-A, September 1986.
83. Leech, W. J., et al, "Revised PAD Code Thermal Safety Model," WCAP-8720 Addendum 2 (Proprietary), October 1982.
84. Slage, W.H. (Ed.), "Westinghouse Improved Performance Analysis and Design Model (PAD 4.0)," WCAP-15063-P-A, Rev.1 w/errata July 2000.
- 84a. Gergos, B. W. and Slagle W. H., "Reload Safety Evaluation Indian Point Nuclear Plant Unit 2 Cycle 11", Attachment to THFL-91-371, Westinghouse Electric Corporation, June 1991.
85. MD2-04-25, "15x15 Upgrade Fuel Assembly – Design Closeout Package (DR02-3)", 5/24/04.
86. Chelemer, H., et al, "Improved Thermal Design Procedure," WCAP-8568-A February 1989.
87. Nguyen, T. Q., et al, "Qualification of the PHOENIX-P/ANC Nuclear Design System for Pressurized Water Reactor Core", WCAP-11596-P-A, November 1987.
- 87a. Davidson, S. L., "Reference Core Report VANTAGE 5 Fuel Assembly," WCAP-10444, Addendum 1, December 1985, WCAP-10445-NP-A, September 1985.
88. Davidson, S. L., Nuhfer, D. L. (Eds), "VANTAGE+ Fuel Assembly Reference Core Report", WCAP-12610-P-A and Appendices A through G, April, 1995.

IP2
FSAR UPDATE

89. Letter from A. C. Thadani (NRC) to W. J. Johnson (Westinghouse), January 31, 1989, Subject: Acceptance for Referencing of Licensing Topical Report, WCAP-9226-P/9227-NP, "Reactor Core Response to Excessive Secondary Steam Releases."
90. Davidson, S. L., Iorii, J. A., "Reference Core Report - 17x17 Optimized Fuel Assembly," WCAP-9500-A, May 1982.
91. Letter from E. P. Rahe (Westinghouse) to J. R. Miller (NRC), "WCAP-9500 and WCAP-9401/9402 NRC SER Mixed Core Compatibility Items," NS-EPR-2573, March 19, 1982.
92. Schueren, P. and McAtee, K. R., "Extension of Methodology for Calculating Transition Core DNBR Penalties," WCAP-11837-P-A, January 1990.
93. Letter from C. O. Thomas (NRC) to E. P. Rahe (Westinghouse), "Supplemental Acceptance No. 2 for Referencing Topical Report WCAP-9500," January 1983.
94. Letter from A. C. Thadani (NRC) to W. J. Johnson (Westinghouse), "Acceptance for Referencing of Licensing Topical Report WCAP-11837", October 1989.
95. Tong L. S., Critical Heat Flux in Rod Bundles, Two Phase Flow and Heat Transfer in Rod Bundles," Annual Winter Meeting ASME, November 1968, Page 3146.
96. Friedland, A. J. and Ray, S. "Improved THINC-IV Modeling for PWR Core Design", WCAP-12330-P, August 1989.
97. Friedland, A. J. and Ray, S. "Revised Thermal Design Procedure", WCAP 11397-P-A, April 1989.
98. Slagle, W.H., "Westinghouse Fuel Assembly Reconstitution Evaluation Methodology," WCAP-13061-NP-A, July 1993.
99. "ARMP-02 Documentations: Part II, Chapter 11 - NODE-P2 Computer Code Manuals, Vol. I and II," EPRI NP-4574-CCM, Electric Power Research Institute, Palo Alto, CA, October 1988.
100. Stewart, C.W. et al., "VIPRE-01: A Thermal-Hydraulic Code for Reactor Cores." Volumes 1-3 (Revision 3, August 1989) Volume 4 (April 1987), NP-2511-CCM-A, Electric Power Research Institute.
101. WCAP-14565-P-A/WCAP-15306-NP-A, "VIPRE-01 Modeling and Qualification for Pressurized Water Reactor Non-LOCA Thermal-Hydraulic Safety Analysis," October 1999, Sung, Y. et al.

IP2
FSAR UPDATE

TABLE 3.2-1 (Sheet 1 of 3)
Nuclear Design Data
Cycle 1 Values

STRUCTURAL CHARACTERISTICS

1.	Fuel weight (UO ₂), lbs	217,800
2.	Zircaloy weight, lbs	44,600
3.	Core diameter, in.	132.75
4.	Core height, in.	
	Reflector thickness and composition	144
5.	Top water plus steel, in.	~ 10
6.	Bottom water plus steel, in.	~ 10
7.	Side water plus steel, in.	~ 15
8.	H ₂ O/U, (cold) core	3.91
9.	Number of fuel assemblies	193
10.	UO ₂ rods per assembly	204

PERFORMANCE CHARACTERISTICS

11.	Heat output, MWt (initial rating)	2758
12.	Heat output, MWt (maximum calculated turbine rating)	3216
13.	Fuel burnup, MWd/metric ton uranium	16,100
	First cycle enrichments, w/o	
14.	Region 1	2.21
15.	Region 2	2.80
16.	Region 3	3.20
17.	Equilibrium enrichment	3.2
18.	Nuclear heat flux hot channel factor, F_{Q1}^T	2.32
19.	Nuclear enthalpy rise hot channel factor, $F_{\Delta H}^N$	1.55

IP2
FSAR UPDATE

TABLE 3.2-1 (Sheet 2 of 3)
Nuclear Design Data
Cycle 1 Values

CONTROL CHARACTERISTICS

	Effective multiplication (Beginning-of-Life) with rods in, no Boron	
20.	Cold, no power, clean	1.113
21.	Hot, no power, clean	1.057
22.	Hot, full power, clean	1.031
23.	Hot, full power, Xe and Sm equilibrium	1.001
24.	Material	5-percent Cd; 15-percent In; 80-percent Ag
25.	Full length rod cluster control assemblies, number	53
26.	Part length rod cluster control assemblies (removed)	
27.	Number of absorber rods per rod cluster control assemblies	7,8,9,12,16, or 20
28.	Total rod worth, BOL, percent	(See Table 3.2-2)
	Boron concentration for first core cycle loading with burnable poison rods	
29.	Fuel loading shutdown; rods in (k = .86)	2000 ppm
	(k = .90)	1615 ppm
30.	Shutdown (k = .99) with rods inserted, clean, cold	849 ppm
31.	Shutdown (k = .99) with rods inserted, clean, hot	572 ppm
32.	Shutdown (k = .99) with no rods inserted, clean, hot	1405 ppm
33.	Shutdown (k = .99) with no rods inserted, clean, cold	1370 ppm

IP2
FSAR UPDATE

TABLE 3.2-1 (Sheet 3 of 3)
Nuclear Design Data
Cycle 1 Values

Boron concentration to maintain $k = 1$ at hot full power,
No rods inserted:

34.	Clean	1160 ppm
35.	Xenon	860 ppm
36.	Xenon and Samarium	780 ppm
37.	Shutdown, all but one rod inserted, clean, cold ($k = .99$)	915 ppm
38.	Shutdown, all but one rod inserted, clean, hot ($k = .99$)	677 ppm

BURNABLE POISON RODS

39.	Number and material	1412 Borated Pyrex Glass
40.	Worth hot Δp	8.2-percent
41.	Worth cold Δp	5.4-percent

KINETIC CHARACTERISTICS

42.	Moderator temperature coefficient at fuel power ($^{\circ}\text{F}^{-1}$)	- 0.25×10^{-4} to - 3.00×10^{-4}
43.	Moderator pressure coefficient (psi^{-1})	+ 0.2×10^{-6} to + 3.00×10^{-6}
44.	Moderator density coefficient, $\Delta k/\text{gm}/\text{cm}^3$	- 0.1 to .30
45.	Doppler coefficient ($^{\circ}\text{F}^{-1}$)	- 1.1×10^{-5} to 1.8×10^{-5}
46.	Delayed neutron fraction, percent	0.50 to .72
47.	Prompt neutron lifetime, sec	1.50×10^{-5} to 2.0×10^{-5}

Note:

1. The total flux hot channel factor (F_Q^T) is a generic limit.
The actual value is presented in the Technical Specifications.

IP2
FSAR UPDATE

TABLE 3.2-1A
Nuclear Design Data
Cycle 18 Values

	Cycle 18
1. Heat output, MWt	3216
2. Fuel loading shutdown boron concentration; rods in ($k \leq 0.95$)	≥ 2050
3. Most positive Moderator Temperature Coefficient (pcm/°F)	-8.99
4. Least Negative Doppler- Only Power Coefficient, Zero to Full Power (pcm/% Power)	-13.88 to -8.55
5. Most Negative Doppler- Only Power Coefficient, Zero to Full Power (pcm/% Power)	-14.88 to -8.98
6. Effective average delayed neutron fraction β_{eff} , percent	0.506 to 0.624
7. Prompt neutron lifetime, μsec	12.27 to 15.01
8. Design bases minimum shutdown ($\% \Delta p$)	1.3
9. Nuclear Heat Flux Hot Channel Factor (F_q) limit	2.5
10. Nuclear Enthalpy Rise Hot Channel Factor (F_dH) limit	1.7

IP2
FSAR UPDATE

TABLE 3.2-2
Reactivity Requirements for Control Rods for Cycle 1₁

<u>Requirements</u>	Percent $\Delta\rho$	
	Beginning-of-Life	End-of-Life
Control		
Power defect	1.90	3.05
Operational maneuvering band	0.40	0.40
Control rod bite	0.10	0.10
X-Y xenon rods	<u>0.20</u>	<u>0.20</u>
Total control	2.60	3.75

Notes:

1. Design values used for performing preoperational calculations and analyses.

IP2
FSAR UPDATE

TABLE 3.2-3
Calculated Rod Worths, $\Delta\rho$ for Cycle 1

<u>Core Condition</u>	<u>Rod Configuration</u>	<u>Worth (Percent)</u>	<u>Less 10-percent₁ (Percent)</u>	<u>Design Reactivity Requirements (Percent)</u>	<u>Shutdown Margin (Percent)</u>
BOL, HFP	53 rods in	8.46			
	52 rods in highest worth rod stuck out	7.43	6.69	2.60	4.09
EOL, HFP	53 rods in	7.98			
	52 rods in; highest worth rod stuck out	6.48	5.83	3.75	2.08 ₂

BOL = Beginning-of-life

EOL = End-of-life

HFP = Hot full power

Notes:

1. Calculated rod worth is reduced by 10-percent to allow for uncertainties.
2. The design basis minimum shutdown margin is 1.95-percent.

IP2
FSAR UPDATE

TABLE 3.2-4
DELETED

TABLE 3.2-5
DELETED

IP2
FSAR UPDATE

TABLE 3.2-6 (Sheet 1 of 3)
Thermal and Hydraulic Design Parameters

	All Hipar Fuel Core ₅	All Lopar Fuel Core ₅	All OFA Fuel Core ₅	All VANTAGE+ Fuel Core ₆
Total heat Output, MWt	2758	2758	3071.4	3216
Total Heat Output, Btu/hr	9,413x10 ⁶	9,413x10 ⁶	10,483x10 ⁶	10,973x10 ⁶
Heat generated in fuel, percent	97.4	97.4	97.4	97.4
Nominal system pressure, psia	2250	2250	2250	2250
Coolant Flow				
Total flow rate, x 10 ⁶ lbs/hr ₁	129.57	128.3	121.72	123.3
Avg velocity along fuel rods, ft/sec	14.8	14.6	13.0	13.80
Avg mass flow, x 10 ⁶ lb/hr-ft ²	2.42	2.39	2.21	2.24
Coolant temperature, °F				
Nominal inlet	541.6	541.3	547.7	538.2
Average rise in vessel	55.8	56.3	64.4	67.6
Average rise in core	58.2	58.7	67.9	71.8
Average in core	571.7	571.7	583.5	575.9
Average in vessel	569.5	569.5	579.7	572.0
Heat transfer				
Active heat transfer surface area, ft ²	51,400	52,100	52,100	52,100
Average heat flux, Btu/hr- ft ²	178,500	176,000	196,000	205,200
Maximum heat flux, Btu/hr-ft ²	414,000	408,300	490,000	513,100

IP2
FSAR UPDATE

TABLE 3.2-6 (Sheet 2 of 3)
Thermal and Hydraulic Design Parameters

	All Hipar Fuel Core ₅	All LOPAR Fuel Core ₅	All OFA Fuel Core ₅	All VANTAGE+ Fuel Core ₆
Heat Transfer (continued)				
Maximum thermal output for normal operation, KW/ft	13.4 ₂	13.4 ₂	15.86 ₃	16.6 ₃
Maximum clad surface temperature for normal operation, °F	657	657	663	NA
Fuel central temperatures for nominal fuel rod dimensions, °F				
Maximum at 100-percent power	<4700	<4700	<4700	<4700
DNB ratio				
Minimum DNB ratio at nominal operating conditions (Thimble)	1.95	1.84	2.45	2.40
Typical	NA	NA	2.33	2.50
Pressure drop, psi				
Across core	24.0	25.5	27.2	29.0
Across vessel, including nozzles	50.0	~51.5	~55.0	NA

IP2
FSAR UPDATE

TABLE 3.2-6 (Sheet 3 of 3)
Thermal and Hydraulic Design Parameters

	<u>3230 MWt</u> (Low Temp Extreme) ₇	<u>3230 MWt</u> (High Temp Extreme) ₇
NSSS Power, MWt	3230	3230
Core Power, MWt	3216	3216
Thermal Design Flow, Loop gpm	80,700	80,700
Reactor Thermal Design Flow, Total, 10 ⁶ lbm/hr	126.8	123.3
Reactor Coolant Pressure, psia	2250	2250
Reactor Coolant Temperature, °F		
Core Outlet	588.1	610.0
Vessel Outlet	583.7	605.8
Core Average	552.6	575.9
Vessel Average	549.0	572.0
Vessel/Core Inlet	514.3	538.2
Zero Load Temperature	547	547
Percent Tube Plugging	10 ₈	10 ₈
Core Bypass Percent	6.5 ₄	6.5 ₄

Notes:

1. The thermal design flow rate for all the all HIPAR core reflects a 5-percent flow reduction (to account for postulated 25-percent steam generator tube plugging). The thermal design flow rate for the all LOPAR core reflects a 6-percent flow reduction (5-percent reduction to account for postulated 25-percent steam generator tube plugging and an additional 1-percent reduction to account for an all LOPAR fuel core). For all OFA and all VANTAGE+ Fuel Cores, the thermal design flow rate reflects a 5-percent flow reduction (to account for postulated 10-percent steam generator tube plugging).
2. This power level is based upon a peaking factor (F_q) of 2.32.
3. This power level is based upon a peaking factor (F_q) of 2.50
4. Increased bypass flow is due to thimble plug deletion, and IFMs.
5. This data is historic only.
6. This data reflects the current core with uprated power of 3216 MWt.
7. This data is for analysis extremes covering a range of vessel average temperatures.
8. The tube plugging level is supported by the Thermal-hydraulic safety analyses.

IP2
FSAR UPDATE

TABLE 3.2-7 (Sheet 1 of 3)
Core Mechanical Design Parameters₁

Fuel assemblies

Number		193
Rod array		15 x 15
Rods per assembly		204 ₂
Rod pitch, in.		0.563
Overall dimensions		8.426 x 8.426 HIPAR ₆ /LOPAR ₆ 8.424 x 8.424 OFA 8.426 x 8.426 VANTAGE+/15x15 Upgraded
Number of grids per assembly	(HIPAR ₆ /LOPAR ₆ /OFA)	9
	(VANTAGE+/15x15 Upgraded)	13
Number of instrumentation thimbles		1
Number of guide thimbles		20
Diameter of guide thimbles, upper	part, in., HIPAR ₆	0.545 O.D. x 0.515 I.D.
Diameter of guide thimbles, lower	part, in., HIPAR ₆	0.484 O.D. x 0.454 I.D.
Diameter of guide thimbles, upper	part, in., LOPAR ₆	0.546 O.D. x 0.512 I.D.
Diameter of guide thimbles, lower	part, in., LOPAR ₆	0.489 O.D. x 0.455 I.D.
Diameter of guide thimbles, upper	part, in., OFA/V+	0.533 O.D. x 0.499 I.D.
Diameter of guide thimbles, lower	part, in., OFA/V+	0.489 O.D. x 0.455 I.D.
Diameter of guide thimbles, upper	part, in., 15x15 Upgraded	0.533 O.D. x 0.499 I.D.
Diameter of guide thimbles, lower	part, in., 15x15 Upgraded	0.487 O.D. x 0.455 I.D.

Fuel rods

Number		39,369 (+3 stainless steel rods)
Outside diameter, in.		0.422
Diametral gap, in.		0.0075
Clad thickness, in.		0.0243
Clad material		Zircaloy (HIPAR ₆ /LOPAR ₆ /OFA) ZIRLO™ (VANTAGE+/15x15 Upgraded)
Overall length		148.6, HIPAR ₆ 151.9, LOPAR ₆ 152.17, OFA 152.55, VANTAGE+ 152.88, V+ w/P+ Enhancements/15x15 Upgraded
Length of end cap, overall, in.		0.688, HIPAR ₆ 0.265, LOPAR ₆ 0.357 OFA/v+ (TOP) 0.430 OFA/V+ (BOTTOM) 0.350, V+w/P+/15x15 Upgraded (TOP)
		0.810, V+w/P+/15x15 Upgraded (BOTTOM)
Length of end cap, inserted in rod		0.250, HIPAR ₆ 0.200, LOPAR ₆ 0.130, OFA/V+/15x15 Upgraded
Active fuel length, in.		142, HIPAR ₆ 144, LOPAR ₆ 144, OFA/V+/15x15 Upgraded

IP2
FSAR UPDATE

TABLE 3.2-7 (Sheet 2 of 3)
Core Mechanical Design Parameters₁

Fuel pellets

Material	UO ₂ sintered
Density (percent of theoretical)	
Region 17C	95.58 VANTAGE+
Region 18A	95.50 VANTAGE+
Region 18B	95.70 VANTAGE+
Region 19A	95.60 15x15 Upgraded
Region 19B	95.50 15x15 Upgraded
Region 20A	95.50 15x15 Upgraded
Region 20B	95.50 15x15 Upgraded
Feed enrichments w/O ₃	
Region 17A	4.80 VANTAGE+
Region 18A	4.59 VANTAGE+
Region 18B	4.95 VANTAGE+
Region 19A	4.00 15x15 Upgraded
Region 19B	4.40 15x15 Upgraded
Region 20A	4.60 15x15 Upgraded
Region 20B	4.95 15x15 Upgraded
Diameter, in.	0.3659
Length, in.	0.4390
	0.500 (Blanket)
<u>Rod cluster control assemblies</u>	
Neutron absorber	5-percent Cd, 15-percent In, 80-percent Ag
Cladding material	Type 304 SS - cold worked
Clad thickness, in.	0.019
Number of clusters	53
Number of control rods per cluster	20
Length of rod control, in.	156.436 (overall)
Length of absorber section, in.	142.00

IP2
FSAR UPDATE

TABLE 3.2-7 (Sheet 3 of 3)
Core Mechanical Design Parameters₁

Core structure

Core barrel	
I.D., in.	148.0
O.D., in.	152.5
Thermal shield	
I.D., in.	158.5
O.D., in.	164.0

Wet Annular Burnable Absorber (WABA) Rods

Number	640
Pellet Stack Length	128"
Pellet Material	Al ₂ O ₃ -B ₄ C
Boron Loading(Natural)	.0243 g/cm
(B-10)	.0060 g/cm
Pellet O.D. /I.D.	.318"/.278"
Tube material	ZIRLO™
Outer tube O.D. /I.D.	.3810"/.3290"
Inner tube O.D. /I.D.	.2670"/.2250"

Integral Fuel Burnable Absorber (IFBA) Rods

Number	5396
Absorber	Zirconium Diboride
B-10 Loading (mg/inch) ₄	2.65 (1.5X)
	2.21 (1.25X)
IFBA Coating Length	120/128inches

Notes:

1. All dimensions are for cold conditions. Data is for all fuel types unless otherwise stated.
2. Twenty-one rods are omitted: Twenty provide passage for control rods and one contains incore instrumentation.
3. Reload fuel regions have variable enrichments depending on energy requirements, the number of assemblies being fed, and the degree of low leakage (i.e. number of feed assemblies on the periphery).
4. Nominal values.
5. Deleted

IP2
FSAR UPDATE

6. Symbol representing old and removed fuel assemblies.

3.2 FIGURES

Figure No.	Title
Figure 3.2-1	Typical Power Peaking Factor Versus Axial Offset
Figure 3.2-2	Rod Cluster Groups - Cycle 1 [Historical]
Figure 3.2-3	Assembly Average Power & Burnup, Cycle 1 Calculations, BOL, Unrodded Core [Historical]
Figure 3.2-4	Assembly Average Power & Burnup, Cycle 1 Calculations, EOL, Unrodded Core [Historical]
Figure 3.2-5	Assembly Average Power Distribution Cycle 1 Calculations, BOL, Group C4 Inserted [Historical]
Figure 3.2-6	Assembly Average Power Distribution Cycle 1 Calculations, BOL Part-Length Rods In [Historical]
Figure 3.2-7	Cycle 1 Maximum F_{σ} X Power Versus Axial Height During Normal Operation [Historical]
Figure 3.2-7A	Deleted – See Unit 2 COLR For Normalized K (Z) – Fq Vs. Axial Height For Cycle 17
Figure 3.2-8	Burnable Poison & Source Assembly Locations - Cycle 1
Figure 3.2-9	Burnable Poison Rod Locations - Cycle 1 [Historical]
Figure 3.2-10	Moderator Temperature Coefficient Vs Moderator Temperature - EOL, Cycle 1 [Historical]
Figure 3.2-11	Moderator Temperature Coefficient Vs Moderator Temperature - BOL, Cycle 1 Full Power [Historical]
Figure 3.2-12	Moderator Temperature Coefficient Vs Moderator Temperature - BOL, Cycle 1 Zero Power [Historical]
Figure 3.2-13	Doppler Coefficient Vs Effective Fuel Temperature - Cycle 1 [Historical]
Figure 3.2-14	Power Coefficient Vs Percent Power - Cycle 1 [Historical]
Figure 3.2-15	Power Coefficient - Closed Gap Model
Figure 3.2-16	Deleted
Figure 3.2-17	Deleted
Figure 3.2-18	Deleted
Figure 3.2-19	Deleted
Figure 3.2-20	Deleted
Figure 3.2-21	Deleted
Figure 3.2-22	Deleted
Figure 3.2-23	Deleted
Figure 3.2-24	Deleted
Figure 3.2-25	Deleted
Figure 3.2-26	Deleted
Figure 3.2-27	Deleted
Figure 3.2-28	Deleted
Figure 3.2-29	Deleted
Figure 3.2-30	Deleted
Figure 3.2-31	Deleted
Figure 3.2-32	Deleted
Figure 3.2-33	Deleted

IP2
FSAR UPDATE

Figure 3.2-34	Deleted
Figure 3.2-35	Deleted
Figure 3.2-36	Deleted
Figure 3.2-37	Deleted
Figure 3.2-38	Typical Thermal Conductivity Of UO ₂
Figure 3.2-39	High Power Fuel Rod Experimental Program
Figure 3.2-40	Typical Comparison Of W-3 Prediction And Uniform Flux Data
Figure 3.2-41	Typical W-3 Correlation Probability Distribution Curve
Figure 3.2-42	Comparison Of "L" Grid Typical And Thimble Cold Wall Cell Rod Bundle DNB Data For Non-Uniform Axial Heat Flux With Predictions Of W-3 X F' _{SL}
Figure 3.2-43	Typical Comparison Of W-3 Correlation With Rod Bundle DNB Data (Simple Grid Without Mixing Vane)
Figure 3.2-44	Typical Comparison Of W-3 Correlation With Rod Bundle DNB Data (Simple Grid With Mixing Vane)
Figure 3.2-44A	Typical Measured Versus Predicted Critical Heat Flux-WRB-1 Correlation
Figure 3.2-45	Typical Stable Film Boiling Heat Transfer Data And Correlation
Figure 3.2-46	Core Cross Section
Figure 3.2-47	Reactor Vessel Internals
Figure 3.2-48	Core Loading Arrangement - Cycle 1 [Historical]
Figure 3.2-49	Typical Rod Cluster Control Assembly
Figure 3.2-50	Rod Control Cluster Assembly Outline
Figure 3.2-51	Core Barrel Assembly
Figure 3.2-52	Upper Core Support Structure
Figure 3.2-53	Guide Tube Assembly
Figure 3.2-54	Fuel Assembly And Control Cluster Cross Section - HIPAR, LOPAR, And OFA And VANTAGE+
Figure 3.2-55	HIPAR Fuel Assembly
Figure 3.2-56	LOPAR Fuel Assembly
Figure 3.2-56A	OFA Fuel Assembly
Figure 3.2-56B	VANTAGE+ Fuel Assembly
Figure 3.2-57	Guide Thimble To Bottom Nozzle Joint
Figure 3.2-58	LOPAR Top Grid To Nozzle Attachment
Figure 3.2-58A	OFA And VANTAGE+ Top Grid To Nozzle Attachment
Figure 3.2-59	Spring Clip Grid Assembly
Figure 3.2-60	Mid-Grid Expansion Joint Design Plan View
Figure 3.2-61	Elevation View - LOPAR Grid To Thimble Attachment
Figure 3.2-61A	Elevation View-VANTAGE+ Grid To Thimble Attachment
Figure 3.2-61B	Vantage+ Fuel Assembly With Performance+ Enhancements
Figure 3.2-61C	15x15 Upgraded Fuel Assembly
Figure 3.2-62	Cycle 1 - Neutron Source Locations [Historical]
Figure 3.2-63	HIPAR Burnable Poison Rod
Figure 3.2-64	LOPAR Burnable Poison Rod
Figure 3.2-65	Control Rod Drive Mechanism Assembly

IP2
FSAR UPDATE

Figure 3.2-66	Control Rod Drive Mechanism Schematic
Figure 3.2-67	Thimble Location - Fixed Incore Detectors
Figure 3.2-68	Cycle 14 Incore Detector, Thermocouple And Flow Mixing Device Locations
Figure 3.2-68A	Cycle 18 Region And Fuel Assembly Locations
Figure 3.2-68B	Cycle 18 Core Components And Fresh IFBA Locations
Figure 3.2-69	Comparison Of Borosilicate Glass Absorber Rod With WABA Rod
Figure 3.2-70	Wet Annular Burnable Absorber Rod

3.3 TESTS AND INSPECTIONS

3.3.1 Reactivity Anomalies

To eliminate possible errors in the calculations of the initial reactivity of the core and the reactivity depletion rate, the predicted relation between fuel burnup and the boron concentration, necessary to maintain adequate control characteristics, must be adjusted (normalized) to reflect actual core conditions. When full power is reached initially, and with the control rod groups in the desired positions, the boron concentration is measured and the predicted curve adjusted to this point. As power operation proceeds, the measured boron concentration is compared with the predicted concentration and the slope of the curve relating burnup and reactivity was compared with that predicted. This process of normalization is completed before a cycle burnup of 60 Effective Full Power Days (EFPDs) is reached. Thereafter, actual boron concentration is compared with prediction, and the reactivity status of the core can be continuously evaluated. Any reactivity anomaly greater than 1-percent would be unexpected, and its occurrence would be thoroughly investigated and evaluated. The methods employed in calculating the reactivity of the core versus burnup and the reactivity worth of boron versus burnup are given in Section 3.2.1.

3.3.2 Thermal And Hydraulic Tests And Inspections

General hydraulic tests on models were used to confirm the design flow distributions and pressure drops.^{1,2} Fuel assemblies and control and drive mechanisms were also tested. Onsite measurements were made to confirm the design flow rates.

Vessel and internals inspections were also reviewed to check such thermal and hydraulic design values as bypass flow. As part of startup physics testing, a series of core power distribution measurements were made over the entire range of operation in terms of design control rod configuration by means of the core movable detector system. These measurements were analyzed and the results compared with the analytical predictions upon which the safety analysis was based with regard to both radial and axial power distribution. The design hot-channel factors were used as criteria for acceptable results.

3.3.3 Core Component Tests And Inspections

To ensure conformance of all materials, components, and assemblies to the design requirements, a release point program is established with the assembly manufacturer, which requires upgrading of all raw materials, special processes (i.e., welding, heat treating, nondestructive testing, etc.) and those characteristics of detail parts, which directly affect the

IP2
FSAR UPDATE

assembly and alignment of the reactor internals. The upgrading is accomplished by the issuance of an inspection release by quality control after conformance has been verified.

A resident quality control representative performs a surveillance/audit program at the manufacturer's facility and witnesses the required tests and inspections and issues the inspection releases. An example is the radiographic examination of the welds joining core barrel shell courses.

Components and materials supplied by Westinghouse to the assembly manufacturer are subjected to a similar program. Quality control engineers develop inspection plans for all raw materials, components, and assemblies. Each level of manufacturing is evaluated by a qualified inspector for conformance, i.e., witnessing the ultrasonic testing of core plant raw material. Upon completion of specified events, all documentation is audited prior to releasing the material or component for further manufacturing. All documentation and inspection releases are maintained in the quality control central records section. All materials are traceable to the mill heat number.

In conclusion, a set of "as-built" dimensions are taken to verify conformance to the design requirements and assure proper fit-up between the reactor internals and the reactor pressure vessel.

3.3.3.1 Quality Assurance Program

The quality assurance program plan of the Westinghouse Nuclear Fuel Division is summarized in Reference 3.

The program provides for control over all activities affecting product quality, commencing with design and development and continuing through procurement, materials handling, fabrication, testing and inspection, storage, and transportation. The program also provides for the indoctrination and training of personnel and for the auditing of activities affecting product quality through a formal auditing program.

Westinghouse drawings and product, process, and materials specifications identify the inspections to be performed.

3.3.3.2 Quality Control

Quality control philosophy is generally based on the following inspections being performed to a 95-percent confidence that at least 95-percent of the product meets specification, unless otherwise noted.

1. Fuel system components and parts

The characteristics inspected depend upon the component parts; the quality control program includes dimensional and visual examinations, check audits of test reports, material certification, and nondestructive examination, such as X-ray and ultrasonic.

All material used in this core is accepted and released by quality control.

IP2
FSAR UPDATE

2. Pellets

Inspection is performed for dimensional characteristics such as diameter, density, length, and squareness of ends. Additional visual inspections are performed for cracks, chips, and surface conditions according to approved standards.

Density is determined in terms of weight per unit length and is plotted on zone charts used in controlling the process. Chemical analyses are performed on a specified sample basis throughout pellet production.

3. Rod inspection

The fuel rod inspection consists of the following nondestructive examination techniques and methods, as applicable:

- a. Each rod is leak tested using a calibrated mass spectrometer, with helium being the detectable gas.
- b. Rod welds are inspected by ultrasonic test or X-ray in accordance with a qualified technique and Westinghouse specification.
- c. All rods are dimensionally inspected prior to final release. The requirements include such items as length, camber, and visual appearance.
- d. All fuel rods are inspected by gamma scanning or other approved methods to ensure proper plenum dimensions.
- e. All fuel rods are inspected by gamma scanning, or other approved methods to ensure that no significant gaps exist between pellets.
- f. All fuel rods are active gamma scanned to verify enrichment control prior to acceptance for assembly loading.
- g. Traceability of rods and associated rod components is established by quality control.

4. Assemblies

Each fuel assembly is inspected for compliance with drawing and/or specification requirements. Other incore control component inspection and specification requirements are given in paragraph 4.2.3.4 of Reference 3.

5. Other inspections

The following inspections are performed as part of the routine inspection operation:

- a. Tool and gauge inspection and control, including standardization to primary and/or secondary working standards. Tool inspection is performed at prescribed intervals on all serialized tools. Complete records are kept of calibration and conditions of tools.

IP2
FSAR UPDATE

- b. Audits are performed of inspection activities and records to ensure that prescribed methods are followed and that records are correct and properly maintained.
- c. Surveillance inspection, where appropriate, and audits of outside contractors are performed to ensure conformance with specified requirements.

6. Process control

- a. To prevent the possibility of mixing enrichments during fuel manufacture and assembly, strict enrichment segregation and other process controls are exercised.

The uranium-dioxide powder is kept in sealed containers. The contents are fully identified both by descriptive tagging and preselected color coding. A Westinghouse identification tag completely describing the contents is affixed to the containers before transfer to powder storage. Isotopic content is confirmed by analysis.

Powder withdrawal from storage can be made by only one authorized group, which directs the powder to the correct pellet production line. All pellet production lines are physically separated from each other and pellets of only a single nominal enrichment and density are produced in a given production line at any given time.

Finished pellets are placed on trays identified with the same color code as the powder containers and transferred to segregated storage racks within the confines of the pelleting area. Samples from each pellet lot are tested for isotopic content and impurity levels prior to acceptance by quality control. Physical barriers prevent mixing of pellets of different nominal densities and enrichments in this storage area. Unused powder and substandard pellets are returned to storage in the original color-coded containers.

Loading of pellets into the clad is performed in isolated production lines, and again only one enrichment and density loaded on a line at a time.

A serialized traceability code is placed on each fuel tube to provide unique identification. The end plugs are inserted and then inert-welded to seal the tube. The fuel tube remains coded and traceability identified until just prior to installation in the fuel assembly.

At the time of installation into an assembly, the traceability codes are removed and a matrix is generated to identify each rod in its position within a given assembly. The top nozzle is inscribed with a permanent identification number providing traceability to the fuel contained in the assembly.

Similar traceability is provided for burnable poison, source rods, and control rodlets, as required.

REFERENCES FOR SECTION 3.3

IP2
FSAR UPDATE

1. G. Hetsroni, "Hydraulic Tests of the San Onofre Reactor Model, "WCAP-3269-8, Westinghouse Electric Corporation, 1964.
2. G. Hetsroni, "Studies of the Connecticut-Yankee Hydraulic Model, "WCAP-2761, Westinghouse Electric Corporation, 1965.
3. J. Moore, "Nuclear Fuel Division Quality Assurance Program Plan;" WCAP-7800, Revision 5, Westinghouse Electric Corporation, November 1979.

Appendix 3A
EXPERIMENTAL VERIFICATION OF CALCULATIONS
FOR BORON BURNABLE POISON RODS

A number of experiments were performed at the Westinghouse Reactor Evaluation Center to investigate the reactivity worth of Pyrex glass tubing similar to that employed in the Indian Point Unit 2 core as burnable poison rods. Several configurations with and without glass burnable poison rods and with fuel loadings representative of power reactors were tested. The reactor used was a rectangular core 4-ft high with 29 or 30 fuel rods on a side. In each case the water height was adjusted until the reactor was just critical.

Analyses were performed for each of the configurations measured to determine the adequacy of the methods used to calculate burnable poison rod worths in the design of the Indian Point Unit 2 core. The results of the calculations for the different experimental configurations are listed in Table 3A-1. In each case the eigenvalue should be compared to the appropriate reference eigenvalue (core with fuel only) to eliminate the systematic bias, which appears in the clean core calculation. The discrepancy between the eigenvalue calculated for the unpoisoned and poisoned cases has been related to the fractional error in the neutron current into the boron. This error is also given in Table 3A-1.

The burnable poison rods used in Indian Point Unit 2 correspond to the thick-walled tubes and in these cases the agreement is generally better than 5-percent.

IP2
FSAR UPDATE

TABLE 3A-1 (Sheet 1 of 2)
Calculations and Burnable Poison Rod Worths₁

<u>Case</u>	<u>Configuration</u>	<u>Loading</u>	<u>Just Critical Water Height, cm</u>	<u>Calculated K_{eff} For Critical Core</u>	<u>Error in Poison Absorption, Percent</u>
1	No inserts - clean	25 ² = 625	64.10		
2	One solid glass rod	25 ² -1 = 624	70.00		
3	No inserts clean core	29 ² = 841	43.25	.996915 ₂	
4	Uniform thin wall glass	29 ² -25 = 816	69.61	.994633	4.6
5	Uniform thick wall glass	29 ² -25 = 816	83.81	.994800	3.5
6	Central assembly pattern - 72 water holes	29 ² -72 = 769	39.52	1.000085	
7	Central assembly pattern - 36 thin wall glass 36 water holes	29 ² -72 = 769	83.76	.996162	1.4
8	Central assembly pattern - 36 thick wall glass 36 water holes	29 ² -72 = 769	114.95	.996392	0.8
9	4 water holes array	29 ² -16 = 825	42.25		
10	No inserts - clean	30 ² = 900	40.69	.996596 ₂	

IP2
FSAR UPDATE

TABLE 3A-1 (Sheet 2 of 2)
Calculations and Burnable Poison Rod Worths₁

<u>Case</u>	<u>Configuration</u>	<u>Loading</u>	<u>Just Critical Water Height, cm</u>	<u>Calculated K_{eff} For Critical Core</u>	<u>Error in Poison Absorption, Percent</u>
11	Uniform water holes	30 ² -36 = 864	38.91	.99777	
12	Uniform voids (SS cladding)	30 ² -36 = 864	42.62		
13	Uniform thin wall glass tubes	30 ² -36 = 864	67.18	.993915	4.8
14	Uniform thick wall glass tubes	30 ² -36 = 864	82.56	.994875	2.5
15	Uniform - .260-in. Ag-In-Cd	30 ² -32 = 868	92.34		
16	Alternate thin wall glass tubes	30 ² -18 = 882	49.42	.994963	6.2
17	Alternate thick wall glass tubes	30 ² -18 = 882	51.90	.994965	5.1
18	Alternate solid glass rods - bare	30 ² -18 = 882	54.91	.995925	1.8
19	Alternate pattern - Ag-In-Cd (.260)	30 ² -18 = 882	53.89		
20	Alternate pattern - Ag-In-Cd (.330)	30 ² -18 = 882	59.94		
21	Four assembly pattern - water holes	30 ² -80 = 820	37.13	.999352	
22	Four assembly pattern - 40 thick wall glass 40 water holes	30 ² -80 = 820	68.73	.997573	1.8

Notes:

1. Reactivity data of glass rods, encased in 0.020-in. SS 0.395-in. I.D., 0.435-in. O.D.
Nominal glass rod data: solid rod, 0.396-in. O.D., L = 48-in.; thick wall I.D. = 0.228-in., O.D. = 0.375-in.,
L = 48-in. thin wall I.D. = 0.316-in., O.D. = 0.394-in., L = 48-in.
2. Reference case.

IP2
FSAR UPDATE

Appendix 3B
POWER DISTRIBUTION CONTROL

3B.1 GENERAL

The spatial stability of the xenon distribution in large PWRs has been the subject of extensive investigation by Westinghouse. General studies (performed in part under the Euratom Xenon Program) are reported in WCAP-3680-20, 21, 22, and 23¹⁻⁴ and specific studies related to the Indian Point Unit 2 reactor are reported in WCAP-7407-L⁵ (Westinghouse Proprietary). Confidence that the reactor can be maintained within thermal limits (design nuclear hot channel factors) is provided by the following:

1. Results of the extensive analytical investigation of potential spatial instability arising from redistribution of xenon in the Indian Point Unit 2 reactor lead to the conclusions that (a) the reactor may be unstable toward axial spatial oscillations and (b) is stable toward radial or diametral (quadrant to quadrant) xenon spatial oscillations.
2. Stability towards diametral (X-Y) xenon oscillations was demonstrated during Cycle 1 startup tests per a report submitted by Con Edison to the NRC (Reference 6).
3. Continuous monitoring and appropriate alarm functions of both axial and diametral power tilts, using signals from the eight ex-core ion chambers, with additional information provided by the core exit thermocouples and moveable incore flux detectors.
4. Since the core is expected to be X-Y stable, automatic protection against diametral transients is not required. However, an alarm function is provided to alert the operator to the existence of such tilts before a limiting value on diametral power tilt is reached.

Stability toward diametral oscillations was verified at startup. As burnup progresses, the reactor becomes increasingly stable toward diametral oscillations due to the decreasing soluble boron concentration and hence the continuously increasing moderator temperature coefficient feedback effect.

5. Control rod cluster malpositioning even under the most limiting case will not lead to a DNBR = 1.30 at operating conditions. Means for detecting such a misalignment are also provided.

3B.2 SPATIAL XENON STABILITY

3B.2.1 AXIAL XENON STABILITY

The potential existence of axial power distribution anomalies due to xenon redistribution have been reported in WCAP-7208.⁷ Results of these studies have shown that the reactor will be unstable toward xenon oscillations in this dimension; consequently, power shaping devices (i.e., control rods) and automatic protection (i.e., trip setpoint reduction with excessive axial power imbalance) are provided. Operating philosophy and procedures for monitoring and controlling axial power anomalies have been described in References 7 and